Universitat de València
DEPARTAMENTO DE FÍSICA ATÓMICA
MOLECULAR Y NUCLEAR

Breakdown studies for high gradient RF warm technology in: CLIC and hadron therapy linacs

DOCTORADO EN FÍSICA
JORGE GINER NAVARRO

Directores:
Ángeles Faus Golfe
Nuria Catalán Lasheras

Diciembre de 2016

Dra. ÁNGELES FAUS GOLFE, Científico Titular del Consejo Superior de Investigaciones Científicas (CSIC),
Dra. NURIA CATALÁN LASHERAS, Staff Scientist de la European Organization for Nuclear Research (CERN),

CERTIFICAMOS:

Que la presente memoria *Breakdown studies for high gradient RF warm technology in: CLIC and hadron therapy linacs* ha sido realizada bajo nuestra dirección en el Departamento de Física Atómica Molecular y Nuclear de la Universitat de València por Jorge Giner Navarro y constituye su Tesis Doctoral.

Y para que así conste, firmamos el presente Certificado.

Firmado: Ángeles Faus Golfe

Firmado: Nuria Catalán Lasheras

Resumen

Los últimos veinte años han marcado un importante progreso en el desarrollo de futuros colisionadores lineales. Los estudios de NLC/JLC (Next/Japanese Linear Collider) y CLIC (Compact Linear Collider) han permitido alcanzar gradientes de aceleración en el rango de 20 a 100 MV/m con estructuras aceleradoras de radiofrecuencia (RF) de conductividad normal operando a frecuencias entre 12 y 30 GHz. El estudio de CLIC consiste en el desarrollo de un colisionador lineal electrón-positrón con una energía de centro de masas en el rango de 0.5 a 5 TeV y una luminosidad máxima de 10^{35} $\mathrm{cm}^{-2}\mathrm{s}^{-1}$, haciendo uso de estructuras aceleradoras con gradientes de 100 MV/m. Las limitaciones de gradiente en la operación de aceleradores lineales vienen dadas por la formación de *breakdowns* o descargas, debido a los intensos campos electromagnéticos a los que las superficies están sometidas, que pueden afectar seriamente en la aceleración y transmisión del haz de partículas que lo atraviesa. El avance de los últimos años en el gradiente de aceleración se ha conseguido gracias a un mejor entendimiento de los fenómenos de RF a alta potencia, a un progreso significativo en los métodos de diseño de estructuras con avanzados códigos de simulación electromagnética, y al perfeccionamiento en las técnicas de fabricación de dichas estructuras.

El estudio de CLIC ha llevado a cabo la construcción en el CERN (European Organization for Nuclear Research) de tres laboratorios de alta potencia RF en la banda X (12 GHz) para la realización de tests de nuevos diseños de estructuras aceleradoras de alto gradiente, así como para dar soporte al desarrollo de fuentes y componentes RF de alta potencia como, por ejemplo, *klystrons* y compresores de pulso. Estos laboratorios son conocidos como Xbox-1, Xbox-2 y Xbox-3, estando el primero integrado en el sistema de CTF3 (CLIC Test Facility) del CERN. Las instalaciones comprenden un equipo de diagnóstico avanzado para la detección y el análisis de sucesos de *breakdowns* en las estructuras aceleradoras, con el fin de estudiar fenomenológicamente la formación y consecuencias de estas descargas durante la operación del acelerador. CLIC dispone también del laboratorio DC Spark en el CERN, en el cual se realiza un estudio complementario de fenomenología de *breakdowns* con un equipo experimental más económico y flexible. Se trata del Large Electrode System (LES) en el que se generan pulsos de alto voltaje en corriente

continua entre un par de electrodos producidos con técnicas de fabricación similares a las estructuras de RF. Este sistema permite estudiar el comportamiento de la superficie, en términos de *breakdowns*, cuando están sometidos a campos eléctricos comparables a los de las estructuras aceleradoras de CLIC.

Existe un gran número de aplicaciones en las cuales se pretende aprovechar las ventajas de los aceleradores lineales de alto gradiente. La tranferencia de esta tecnología a diferentes campos es crucial para dar continuidad a su futuro desarrollo, así como para el beneficio de otros campos científicos. Por un lado, la construcción de aceleradores de electrones para láseres de electrones libres (Free Electron Laser, FEL) y de retrodispersión Compton, para la producción de rayos X y gamma de alta energía e intensidad, son de gran importancia para el estudio de procesos atómicos y nucleares, así como para los estudios fotónicos en ciencias de materiales, biología o química. El uso de la tecnología de alto gradiente da lugar a un diseño compacto del acelerador que facilitaría su construcción en entornos tecnológicos más reducidos así como en las universidades.

Otra de las aplicaciones más prometedoras de esta tecnología es en el campo de la hadronterapia para el tratamiento del cáncer. El uso de haces acelerados de protones o iones de carbono, los cuales presentan una deposición de energía muy localizada, permite realizar una cirugía del tumor muy precisa que trata de evitar el daño de los tejidos sanos que lo rodean. Existe un número relativamente pequeño de espacios que ofrecen actualmente este servicio en todo el mundo, y suelen tratarse de grandes instalaciones que disponen de un sincrotrón, ciclotrón o sincrociclotrón para distribuir los haces de hadrones acelerados en múltiples salas de tratamiento. El concepto de aceleradores lineales comienza a cobrar interés en la última década gracias a sus ventajas de modularidad y rapidez en el control de la energía final del haz, el cual permite realizar técnicas innovadoras en sesiones de tratamiento de menor duración. El uso de aceleradores de alto gradiente facilitaría el servicio público a la hadronterapia con la construcción de instalaciones médicas más compactas que podrían incluso adaptarse a centros hospitalarios especializados.

En este contexto, la presente tesis se centra en el estudio de las limitaciones en el rendimiento de aceleradores de alto gradiente debido a fenómenos de *breakdowns* en estructuras aceleradoras diseñadas para CLIC y aceleradores de hadronterapia. El objetivo consiste en el desarrollo de esta tecnología de alto gradiente de conductividad normal para su aplicación en los diferentes campos multidisciplinares que pretenden aprovechar sus ventajas. Esta tesis se puede estructurar en tres partes fundamentales.

La primera parte consiste en una introducción a los conceptos básicos de los aceleradores lineales de alto gradiente y se han definido sus parámetros más importantes. El gradiente de aceleración corresponde al potencial axial por unidad de longitud que proporciona una ganancia de energía a una partícula cargada al atrave-

sar la estructura aceleradora, y viene dado por la intensidad de los campos eléctricos presentes en el eje axial. Además, el factor de calidad Q y la *shunt impedance* R de la estructura son magnitudes que indican la eficiencia con la que las estructuras construyen este gradiente de potencial en la cavidad por la que pasa el haz de partículas a costa de la potencia eléctrica consumida. El diseño de la geometría de la estructura es de vital importancia para conseguir la mayor eficiencia energética posible para la operación del acelerador. El diseño de referencia de las estructuras aceleradoras de CLIC para un colisionador lineal de 3 TeV consiste en estructuras *traveling-wave* de 23 cm de longitud, fabricadas en cobre, que operan a una frecuencia de 12 GHz (banda X) y que permiten alcanzar gradientes de 100 MV/m. La potencia RF se acopla fuertemente con el haz de electrones acelerado, distribuido en pulsos de 1.2 A de corriente y 156 ns de anchura, y produce el efecto conocido como *beam-loading* (estructura cargada con el haz). Este acoplamiento produce la modificación de los campos electromagnéticos en el volumen de la estructura y la reducción del gradiente de aceleración, que debe compensarse con el suministro de mayor potencia RF.

Los aceleradores que disponen de tecnología de alto gradiente de conductividad normal presentan diferentes diseños de estructuras aceleradoras de alta frecuencia, usualmente en la banda S (3 GHz) y en la banda C (5.7 GHz). Entre ellos se encuentran los aceleradores de electrones de FELs, como por ejemplo son SwissFEL (Suiza), SACLA (Japón) y PAL-XFEL (Corea del Sur), y de retrodispersión Compton, como son ELI-NP (Rumanía) o ThomX (Francia). Los diseños en estudio de aceleradores lineales destinados para la hadronterapia exploran también el uso de estas bandas de frecuencia, como son por ejemplo los prototipos de LIBO (3 GHz) y CABOTO (5.7 GHz), alcanzando un gradiente de aceleración máximo de 15.8 y 34 MV/m respectivamente.

El estudio de los fenómenos de *breakdowns* asociados a estructuras de RF ha permitido un mejor entendimiento de las limitaciones de los aceleradores de alto gradiente. Diferentes experimentos y simulaciones moleculares dan a entender que los sucesos de *breakdowns* se desencadenan en protuberancias microscópicas existentes a lo largo de la superficie metálica de las paredes de la estructura aceleradora. Estas formas geométricas particulares originan campos eléctricos localizados más intensos y, en consecuencia, la emisión de una corriente de electrones detectable por efecto de *enhanced field-emission* (emisión de campo aumentada). Esta fuente emisora puede llegar a fundirse por calentamiento resistivo y producir, de manera descontrolada, fuertes descargas eléctricas que acaban en la formación de pequeños cráteres visibles en el microscopio. El límite de rendimiento del acelerador se suele juzgar con el llamado *breakdown rate* (BDR), el cual nos da la fracción de pulsos en la cual una unidad de longitud del acelerador produce una descarga. Esta magnitud se expresa en términos de *breakdowns* por pulso por metro, [bpp/m], y se mide por el número

de descargas que se producen en una estructura aceleradora durante un intervalo de pulsos de potencia RF. Experimentalmente, se ha observado una fuerte dependencia del BDR con el gradiente, E_{acc}, y con la anchura temporal del pulso, t_p, dado por la ley de escala BDR $\propto E_{acc}^{30} \cdot t_p^5$. Esta dependencia puede explicarse, en principio, con la existencia de defectos y dislocaciones en la superficie de la estructura sometidos a fuertes tensiones debido al campo eléctrico y que permiten el crecimiento de nuevos emisores que pueden desencadenar sucesos de *breakdowns*.

Contrariamente al criterio de Kilpatrick comúnmente utilizado para el diseño de estructuras aceleradoras, el campo eléctrico superficial no permite predecir el límite de gradiente que una estructura puede alcanzar, a pesar de la importancia de esta magnitud en el mecanismo de formación de *breakdowns*. Un análisis estadístico de diferentes prototipos desarrollados por CLIC y NLC/JLC muestra una gran dispersión entre los máximos niveles de campo eléctrico en la superficie, en el rango de 60 a 300 MV/m. Por esta razón, se tienen en cuenta otras restricciones a la hora de diseñar estructuras de alto gradiente. Por un lado, el calentamiento de la superficie producido por los pulsos de alta potencia origina una degradación de la superficie (efecto conocido como 'fatiga') la cual acaba haciéndose más rugosa y aumenta las probabilidades de *breakdowns*, especialmente en las regiones donde el campo magnético es más intenso y donde se disipa mayor energía en forma de calor. Por otro lado, se utiliza una nueva magnitud conocida como el vector de Poynting modificado, S_c, el cual consiste en una combinación entre la densidad de potencia real e imaginaria del vector de Poynting. Esta magnitud tiene en cuenta el acoplamiento de la potencia RF disipada en los emisores de campo superficiales y los campos no-lineales generados por *field-emission*. El límite en gradiente de los diferentes prototipos muestran mayor correlación con el vector de Poynting modificado que con el campo eléctrico superficial.

La segunda parte de esta memoria de tesis consiste en la descripción detallada de los diferentes estudios experimentales realizados en las instalaciones de alto gradiente en el CERN para el estudio de CLIC, conocidos como las Xboxes. Los nuevos prototipos de CLIC han sido estudiados en los laboratorios de RF de alta potencia para evaluar el gradiente de aceleración que pueden alcanzar en condiciones de anchura de pulso de 180 ns y con el requisito de un máximo BDR de 3×10^{-7} bpp/m. El sistema está equipado de la instrumentación necesaria para la medida de la potencia incidente, reflejada y transmitida en la estructura, así como para la detección y localización de *breakdowns*. Tras pasar por todo el proceso de fabricación y tratamiento de limpieza, los nuevos prototipos no son capaces de soportar altos gradientes desde el principio, sino que deben sufrir un proceso de adaptación conocido como *conditioning*. El gradiente y la anchura de pulso se hacen crecer gradualmente con la acumulación de pulsos de RF, pero manteniendo a la vez un nivel de BDR bajo para evitar daños irreversibles producidos por *breakdowns*. Tras el *conditioning*, se

realizan medidas de BDR a diferentes gradientes de aceleración y anchuras de pulso, que permiten verificar las leyes de escala experimentales. Al mismo tiempo, se realizan medidas de corriente oscura con *Faraday cups* emitida desde la superficie interna de la estructura aceleradora por *field-emission*. El objetivo es estudiar el comportamiento de los emisores existentes en la superficie y encontrar indicadores del mecanismo de formación de *breakdowns*.

Uno de los estudios realizados en este trabajo de tesis es el desarrollo de diferentes técnicas de localización de *breakdowns* en el interior de la estructura para evaluar su rendimiento durante el *conditioning* y las medidas de BDR. Los métodos se basan en el análisis de las señales de pulsos RF incidente, reflejada y transmitida en la estructura y la comparación de tiempos de propagación y avance de fase desde el origen de la descarga hasta los detectores. Como resultado, una distribución uniforme de *breakdowns* a lo largo de la estructura es síntoma de un buen rendimiento, puesto que todas las celdas presentan prácticamente la misma probabilidad de desencadenar un suceso de *breakdown*. Sin embargo, también es posible encontrar una única celda, llamada *hot cell*, que produzca la mayoría de los sucesos y la cual afecta negativamente al rendimiento global de la estructura.

Otro estudio ha consistido en el análisis estadístico del número de pulsos producidos entre sucesos de *breakdowns*. Este análisis permite evaluar el comportamiento de los fenómenos de *breakdowns* en términos de una función de densidad de probabilidad. Los resultados muestran que los sucesos no corresponden a una distribución de probabilidad de Poisson, es decir, que no son sucesos aleatorios descorrelacionados sino que existen excitaciones correlacionadas entre sucesos. La función de probabilidad obtenida parece indicar la existencia de dos procesos que presentan diferentes BDR. Una hipótesis que podemos extraer de estos resultados consiste en la distinción entre sucesos primarios y secundarios, siendo los últimos producidos en un intervalo de hasta unos 3000 pulsos debido al daño residual ocasionado por un suceso primario. El análisis de localización de *breakdowns* ha permitido comprobar que la mayor parte de los *breakdowns* más inmediatos (secundarios) se concentran en la misma región que el predecesor.

El proceso de *conditioning* es también de especial interés, puesto que constituye una gran parte del tiempo empleado para el test de las estructuras en las Xboxes. El nivel de *conditioning* se ha evaluado normalizando el gradiente y el BDR haciendo uso de las leyes de escala experimentales. La comparación de la historia de *conditioning* en prototipos fabricados a partir del mismo diseño RF señalan una progresión similar del nivel de *conditioning* con el número de pulsos acumulados, a pesar de haber utilizado diferentes estrategias de operación y de haber acumulado una cantidad distinta de sucesos de *breakdowns*. Este resultado demuestra que el proceso de *conditioning* depende del número de pulsos acumulados y no del número de *breakdowns*, y que los pulsos que no desencadenan descargas tienen un papel importante

en el comportamiento dinámico de la estructura aceleradora. La comparación de las historias de *conditioning* se ha extendido a diferentes diseños de prototipos, y muestra una correlación más fuerte cuando el nivel de *conditioning* se describe en términos del vector de Poynting modificado, tal y como se espera para predecir el gradiente alcanzable en la estructura.

A pesar de disponer de las leyes de escala experimentales entre el BDR, el gradiente de aceleración y la anchura de pulso, todavía no es clara la dependencia del BDR con la forma del pulso. El uso de compresores de pulso en aceleradores lineales proporciona un mayor pico de potencia durante el pulso comprimido, pero deja un exceso de potencia antes y después debido a la carga y descarga de las cavidades del compresor. Este exceso puede afectar negativamente en el comportamiento de la estructura aceleradora. Se han analizado los efectos de la forma del pulso en el calentamiento de la estructura, mostrando un exceso de aproximadamente un 4 %. Las primeras medidas en la Xbox-2 del BDR en una estructura alimentada con un pulso rectangular y con un compresor de pulso muestran un ligero incremento del BDR en el último caso.

Se ha realizado también el experimento de *beam-loading* en la Xbox-1 y haciendo uso del haz de electrones del acelerador lineal de CTF3. En este experimento se ha hecho acelerar el haz de electrones en un prototipo de alto gradiente de CLIC para estudiar si la alteración de los campos electromagnéticos en su interior produce un efecto en su comportamiento en cuanto a la formación de *breakdowns*. La mayor parte del trabajo ha consistido en la adaptación del sistema de RF y del programa de control para la operación de este experimento, así como para garantizar la estabilidad del sistema requerida para las medidas de BDR. Los primeros resultados demuestran que el ritmo de sucesos de *breakdown* se mantiene a pesar de que el haz de electrones hace disminuir el gradiente de aceleración efectivo, y que estos *breakdowns* se concentran en las celdas donde los campos electromagnéticos son más intensos. La confirmación de estos resultados serán importantes para la optimización de los futuros diseños de las estructuras de CLIC.

La tercera y última parte de esta tesis se centra en las actividades llevadas a cabo en el CERN y el Instituto de Física Corpuscular (IFIC) para el desarrollo de aceleradores médicos destinados a la terapia de hadrones. CLIC participa en el diseño de nuevas estructuras para aceleradores lineales de protones con el fin de aumentar el gradiente hasta los 50 MV/m. Esto permitiría reducir considerablemente el tamaño del acelerador y así poder ser instalado directamente en el cabezal rotatorio que dirige el haz hacia el paciente, tal y como se propone en el proyecto TULIP (Turning Linac for Proton Therapy) por la Fundación TERA. El transporte de potencia del *klystron* al cabezal se ha demostrado con la fabricación en el CERN y el test de alta potencia en CTF3 de una guía de ondas rotatoria, que permite transmitir la RF a diferentes ángulos sin pérdidas de potencia ni variaciones de fase significativas. En

este mismo contexto, el IFIC está llevando a cabo la construcción de un laboratorio de RF de alto gradiente, en la banda S (2.998 GHz), para el estudio fenomenológico de *breakdowns* en estructuras aceleradoras con aplicaciones en, principalmente, aceleradores lineales médicos de hadronterapia. Este laboratorio cuenta con la experiencia adquirida para la operación y diagnóstico de estructuras aceleradoras de CLIC en las Xbox del CERN, y sus experimentos y resultados serán de especial interés para la comunidad científica en el campo de los aceleradores lineales de alto gradiente.

Abstract

The present thesis is focused on the study of the breakdown limitations for the high-gradient (HG) performance of normal-conducting Radio-Frequency (RF) accelerating structures. The formation of vacuum arcs perturbs the electromagnetic fields of the cavities and affects in the quality of the accelerating beam. The Compact Linear Collider (CLIC) project studies the feasibility of a multi-TeV e^+e^- linear collider and develops the current state-of-the-art HG structures to achieve accelerating gradients of 100 MV/m with a maximum breakdown rate of 3×10^{-7} breakdowns per pulse per meter. A wide experimental programme is established by CLIC for the design and test of efficient and compact accelerating structures, thanks to the construction of three X-band high-power test stands, also known as Xboxes, and the pulsed-DC Large Electrode system dedicated to breakdowns studies.

Chapter 1 introduces the basic concepts related to linear accelerators and the classification of different designs of RF accelerating structures. The advantages that HG technology offers are also described for different applications, such as Future Linear Colliders, hadron therapy linacs, Free Electron Lasers and Compton backscattering light sources. A bibliographic description of the current understanding of breakdown phenomena and their consequences in the designs of HG accelerating structures is made in Chapter 2.

In Chapter 3, we describe in detail the existing HG test facilities operated for the sake of advancing in the design and construction of HG accelerators, as well as for the better understanding of the RF breakdown mechanisms. Different breakdown studies are presented in Chapter 4, which have been carried out at the Xboxes and pulsed-DC Large Electrode system. The techniques used for the localization of breakdowns in RF structures at the Xboxes is presented in detail with experimental results. A statistical study of breakdown occurrences is also made to understand the underlying random process of these events and the formu-

lation of a double breakdown rate model is presented in agreement with the observations. The study of the RF conditioning in HG accelerating structures is made based on a comparative analysis of different conditioning histories of prototypes tested at CERN and KEK, which have led to new insights that may allow to efficiently reduce the time to achieve their best performance. A preliminary study is performed in Xbox-2 to analyse the possible negative effect of the use of a pulse compressor on the breakdown performance of HG prototypes, due to the excess of RF power that is driven before and after the compressed rectangular-shaped pulse. Experimental data is compared with simulations of possible candidates that may affect in the breakdown rate results.

Chapter 5 is focused on the description and first experimental results of the beam-loading experiment, which aims at studying the effect of the presence of the beam on the breakdown rate in a CLIC HG accelerating structure due to the alteration of the longitudinal gradient profile.

Finally, Chapter 6 summarizes the current activities in the development of HG hadron therapy linacs at CERN. This chapter also describes the infrastructure and future plans of the new IFIC HG RF laboratory that is under construction in Valencia for the study of the phenomenology of breakdowns in S-band HG accelerators.

Contents

Chapter 1

Introduction to high-gradient warm RF in linear accelerators

The interest of exploring the high-energy range in particle physics has lead to important progress in particle accelerators. They have become larger and more sophisticated over the last decades to enhance the experimental conditions of beam collisions. The high energy physics (HEP) community states that several phenomena in nature and experimental results are still not explained based on the current paradigm, also known as the Standard Model. The exploration of the physics beyond the Standard Model requires the study of high energy interactions, in the TeV range, performed in hadronic or leptonic colliders. New developments are being carried out in accelerator technology to give the most reliable solutions for future colliders and dig deeply in HEP studies. In parallel, this technology is being transferred to other experimental facilities that could provide a public service, for example hadron therapy accelerators for cancer irradiation. In this chapter, we will focus on the characteristics of high-gradient accelerators and the main applications that may benefit from them.

1.1 High-gradient in compact accelerators

Linear accelerators, also known as linacs, constitute an important component of the wide family of accelerators. Unlike circular accelerators such as synchrotrons, which keep the path of the particles in a closed orbit, linacs perform the acceleration along a straight line. The absence of bending dipoles implies that the energy loss by the emission of synchrotron radiation is negligible. However, the accelerating cavities in a linac see the passage of each bunch of particles only once and the acceleration needs to be done in a single shot. High-gradient (HG) technology plays a key role in the development of linacs aiming to build compact and efficient accelerators.

1.1.1 Particle acceleration

Accelerating structures store the electromagnetic energy in a certain volume in the term of electric and magnetic fields, as shown in the drawing of Fig. 1.1, which oscillate in time with a frequency f as a sinusoidal function. Linacs typically operate at working frequencies of MHz to GHz, in the radio-frequency (RF) range. A particle that travels through an accelerating structure interacts with these RF fields and gains kinetic energy according to the Panofsky equation [1]:

$$\Delta W = q\langle E_{acc}\rangle TL\cos(\phi_s) \tag{1.1}$$

Here, ΔW is the **energy gain**; q denotes the charge of the particle that interacts with the field; $\langle E_{acc}\rangle$ represents the average accelerating gradient; the transit time factor T takes into account the finite speed of the particle and how the RF fields vary while it crosses the structure; ϕ_s is the so-called *synchronous* phase, which represents the relative phase of the RF field with respect to the beam; and L is the length of the structure.

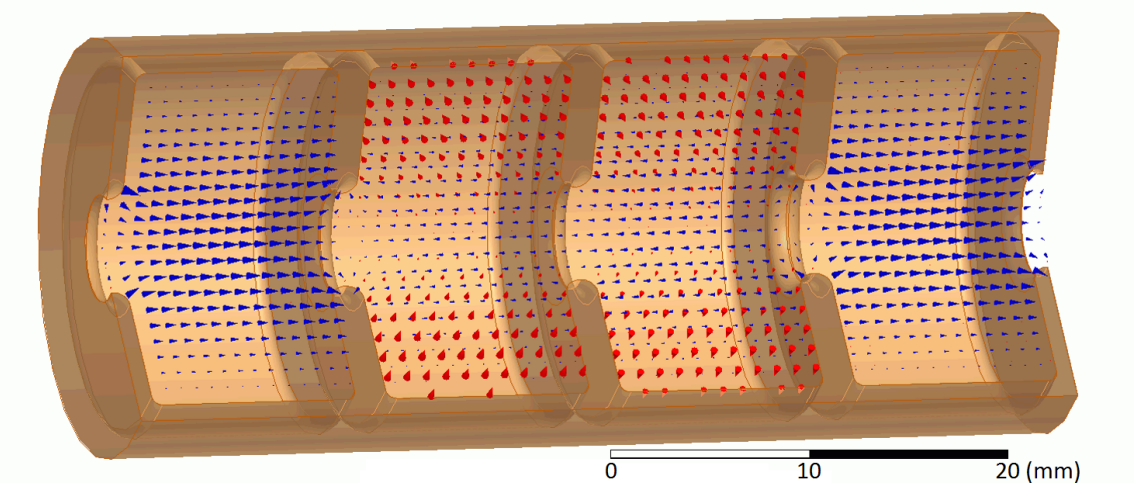

Figure 1.1: Drawing of a coupled-cell $2\pi/3$-mode accelerating structure. Blue and red arrows represent electric and magnetic fields, respectively. Courtesy of [2]

The gradient is directly related to the longitudinal electric field E_z on axis, which can be written in terms of the longitudinal position z and time t as follows:

$$E_z(z,t) = E_{acc}(z)\cos(\omega t(z) + \phi_s) \tag{1.2}$$

where $\omega = 2\pi f$ is the angular frequency. Since the particles going through have a finite velocity, they see how the fields are varying while traveling, and therefore the intensity of interaction changes in time and position. Assuming a constant particle

velocity v, the time when the particle is at position z is $t(z) = z/v$, then one can determine the energy gain of a charged particle crossing a gap of length L:

$$\Delta W = q \int_{-L/2}^{L/2} E_{acc}(z) \cos(\omega z/v + \phi_s) dz \tag{1.3}$$

If we define the longitudinal RF voltage in the gap:

$$V_0 \equiv \langle E_{acc} \rangle L = \int_{-L/2}^{L/2} E_{acc}(z) dz \tag{1.4}$$

we can write the transit time factor, introduced in Eq. (1.1), as follows

$$T \equiv \frac{1}{V_0} \int_{-L/2}^{L/2} E_{acc}(z) \cos(\omega z/v + \phi_s) dz \tag{1.5}$$

The transit time factor [3] represents an efficiency factor of the energy gain ΔW and becomes lower when the speed of the particle is smaller, i.e. when the particle takes more time to cross the gap compared to the RF field cycle. As a example, electrons and positrons travel near the speed of light from only 1 MeV kinetic energy, while 100 MeV protons travel at 40% of the speed of light. For this reason, the transit time factor is usually close to one for the accelerating structures of electron or positron linacs (except at injection), while in proton machines the transit time factor becomes smaller for the same gap dimensions.

According to Eq. (1.4), the accelerating gradient $\langle E_{acc} \rangle$ corresponds to the axial potential per unit of length that makes a charged particle gain energy when it interacts with the fields of an accelerating structure. For linacs, this gradient becomes a very important parameter of the machine since it determines the length of the accelerator for the desired final energy. For a particular energy goal, the higher the accelerating gradient the shorter the machine will be, and therefore the cost of the accelerator will be reduced.

The HG regime is considered above 10 MV/m. Such high gradients demand large surface electric fields on the walls of the structures which produces non-linear effects and triggers vacuum discharges. These are well-known in the literature as vacuum arcs or breakdowns. There is a great interest of understanding the formation of such breakdowns and how to diminish them during operation, and this will be the main topic of the present manuscript.

1.1.2 Main characteristics of RF structures

Accelerating structures are generally made of a series of periodic units, called cells, aligned in a straight line and coupled by irises of a certain aperture (see Fig. 1.1).

Each cell stores the electromagnetic energy and provides a longitudinal voltage given by the gradient and cell length $V_{cell} = \langle E_{acc} \rangle L_{cell}$. The accelerating gradient E_{acc} is directly determined by the amount of power that is fed into the cell. Its performance in terms of gradient and efficiency is determined by the geometry, the material and the working RF frequency f, and it is described by some parameters summarized in this section.

The intrinsic **quality factor** Q is defined as the ratio of the **stored energy** in the cell U over the dissipated energy in one RF cycle due to electrical resistance in the walls, also expressed as:

$$Q = \frac{\omega U}{P_d} \tag{1.6}$$

where P_d is the dissipated power in the walls by ohmic losses. This corresponds to an equivalent definition of the quality factor of a resonator, since a cavity can be described as a resonant circuit of resistors, capacitors and inductors [4].

Since these structures also include coupling holes where power P_{ext} can exit, an external quality factor Q_{ext} is equivalently defined:

$$Q_{ext} = \frac{\omega U}{P_{ext}} \tag{1.7}$$

The total dissipation of power $P_{tot} = P_d + P_{ext}$ defines then the loaded quality factor Q_{load}:

$$Q_{load} = \frac{\omega U}{P_d + P_{ext}} \tag{1.8}$$

which is related to the intrinsic and external quality factors by the expression:

$$\frac{1}{Q_{load}} = \frac{1}{Q} + \frac{1}{Q_{ext}} \tag{1.9}$$

A structure loses its stored energy $U(t)$ following the time differential equation:

$$\frac{dU(t)}{dt} = -P_d - P_{ext} = -\frac{\omega U(t)}{Q_{load}} \tag{1.10}$$

that can be solved by considering an initial stored energy U_0:

$$U(t) = U_0 \exp\left(-\frac{\omega t}{Q_{load}}\right) \tag{1.11}$$

In the latter expression one can notice that the quality factor represents the number of RF cycles, with a factor 2π, that a cell takes to lose a factor $1/e$ of its stored energy.

Another important parameter that concerns the power efficiency is the **shunt impedance** R, which describes how effective the structure is providing an axial voltage V_0 for a given dissipated power P_d through the walls [3]:

$$R = \frac{V_0^2}{P_d} \tag{1.12}$$

The shunt impedance scales linearly with the length of the structure L for identical cells, thus it can be normalized as $R' = R/L$. Equivalently, the effective shunt impedance per unit of length R'_{eff} is commonly used to maximize the particle energy gain ΔW of Eq. (1.1) at $\phi_s = 0$ for the same dissipated power, and is defined by:

$$R'_{eff} = \frac{1}{L}\frac{(\Delta W/q)^2}{P_d} = \frac{1}{L}RT^2 = R'T^2 \tag{1.13}$$

where the squared transit time factor acts as a effective factor of the shunt impedance per unit of length. R'_{eff} scales with the working RF frequency as $f^{1/2}$ for normal-conducting structures and as f^2 for superconducting structures [3], which makes the use of high-frequency structures interesting for the sake of a good power efficiency.

The ratio R'/Q between the shunt impedance and the intrinsic quality factor, commonly known as the **normalized shunt impedance** or the R-over-Q value, is a parameter that only depends on the cavity geometry, and not on the material. Consequently, combining Eqs. (1.6) and (1.12), the normalized shunt impedance gives a relationship between the accelerating gradient $\langle E_{acc} \rangle = V_0/L$ and the stored energy per unit of length $U' = U/L$:

$$U' = \frac{\langle E_{acc} \rangle^2}{\omega(R'/Q)} \tag{1.14}$$

1.1.3 Traveling Wave and Standing Wave structures

Accelerating structures can be classified according to different criteria, such as the electromagnetic modes (TE, TM or TEM), the electrical conductivity of the material (normal or superconducting) and operation mode (traveling or standing wave structures). The design of an accelerating structure always depends on the application of the accelerator complex and the beam properties that are required for the facility, which needs a dedicated pre-study in order to optimize the efficiency and cost of the machine. Different classifications of structure designs can be found in [4], but we will focus here on the classification between Traveling Wave (TW) and Standing Wave (SW) structures.

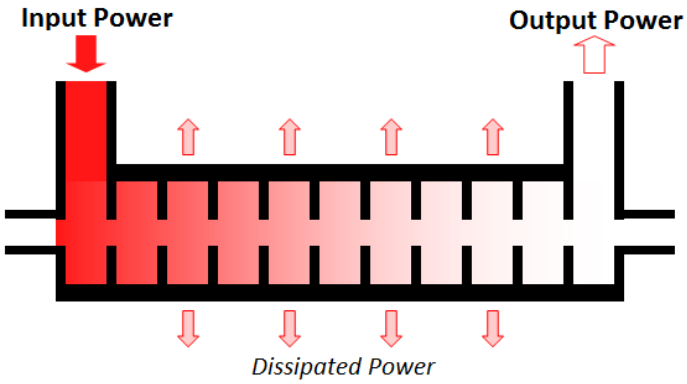

(a)

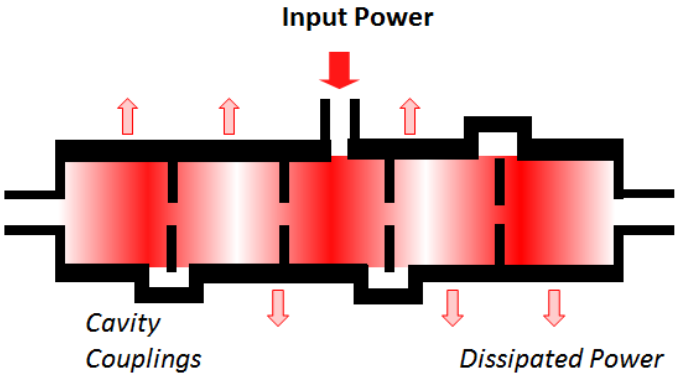

(b)

Figure 1.2: Schematic illustration of a (a) traveling wave and (b) standing wave structure.

Traveling Wave

TW accelerating structures are broadband waveguides with periodically-loaded irises [3], as illustrated in Fig. 1.2(a), in which the RF power flows through each cell from an input to an output coupler. The cell iris aperture defines the Brillouin dispersion relation of each propagation mode between the RF frequency f and the wave-number k, shown in Fig. 1.3. In this way, the speed of the accelerated particles is synchronized with the RF **phase velocity**:

$$v_{ph} = \frac{\omega}{k} = 2\pi\frac{f}{k} \tag{1.15}$$

Once the operating frequency of the structure is chosen, the dimensions of the cells are determined for a given phase advance per cell:

$$\Delta\varphi = k(f) \cdot L_{cell} \tag{1.16}$$

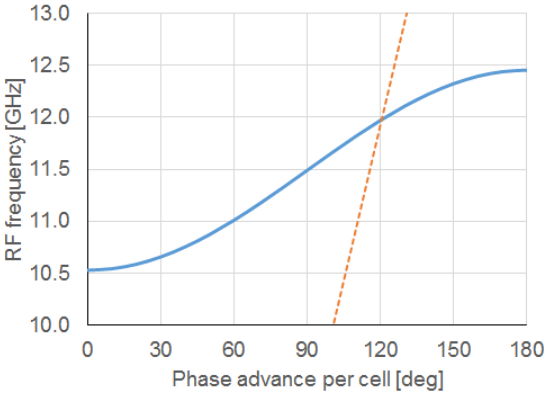

Figure 1.3: Brillouin diagram (solid blue line) of a X-band TW accelerating structure that operates at 12 GHz frequency and 120 degrees phase advance. As a reference, the dispersion curve $\omega = ck$ of a plane wave traveling at speed of light c (dashed orange line) is also shown, representing the phase velocity of the beam particles that will be accelerated.

where L_{cell} is the length of the cell or the distance between two irises.

The speed at which the RF power transmits through the TW structure is the **group velocity**, and is given by:

$$v_g = \frac{d\omega}{dk} = 2\pi L_{cell} \frac{df}{d(\Delta\varphi)} \tag{1.17}$$

The power P_{in} is attenuated by ohmic losses as it traverses the cells of the structure. TW structures with identical cell geometries are known as 'constant-impedance' structures, in which the accelerating gradient decays towards the end since the stored energy per unit of length U' becomes smaller:

$$U' = \frac{P_{in}}{v_g} \tag{1.18}$$

In order to achieve a 'constant-gradient' profile, the structure is tapered making the iris aperture smaller towards the end cells so that the reduction of the group velocity compensates the loss of RF power and, consequently, the stored energy per cell is approximately maintained.

The group velocity also determines the **filling time** of each cavity cell. A general TW structure of length L tapered with a group velocity profile $v_g(z)$ presents a filling time:

$$t_{fill} = \int_0^L \frac{dz}{v_g(z)} \tag{1.19}$$

And for a constant-impedance structure, with constant group velocity, the filling time is given by $t_{fill} = L/v_g$.

Standing Wave

In the case of SW structures, also referred to as resonant cavities, a single coupler is used to feed a certain number of cells. As represented in Fig. 1.2(b), both ends of the structure are closed and the multiple wave reflections build standing wave patterns which correspond to discrete electromagnetic eigenmodes. The cavity cells are coupled each other via coupling holes or side coupling cavities. For a SW structure made of N cells, the frequencies of the eigenmodes, represented by the integer n, are given by:

$$f_n = \frac{f_0}{\sqrt{1+\beta_c \cos\left(n\pi/N\right)}} \quad n = 0, 1, ..., N \tag{1.20}$$

where β_c is called the cell-to-cell coupling factor and f_0 is the frequency of the 0-mode. The fields configuration of each mode correspond to a phase advance per cell of $n\pi/N$.

There is no net power flow in SW structures and the cavity cells are filled uniformly in time. In this case, the filling time is given by the quality factor loaded by the external coupling:

$$t_{fill} = \frac{Q_{load}}{\omega} \tag{1.21}$$

Note that the superconducting SW cavities have large filling times due to their high quality factor, and also allow to efficiently accelerate long beam trains since they require low power in average to achieve high gradients. On the other hand, normal-conducting SW structures need smaller filling times before injecting the beam, thus they are capable of operating with short pulses and reach higher gradients.

1.1.4 Current design of high-gradient RF accelerating structures

Table 1.1 summarizes some of the relevant RF parameters previously discussed for several different accelerating structure designs, applied for linear colliders, Free Electron Lasers and Compton backscattering light sources, distinguishing between normal-conducting copper-made structures and superconducting-niobium cavities operating at a temperature of 2 K. The latter group presents higher quality factor, because of its very low resistive losses, and it is operated with longer RF pulses due to the slow rise time given by the high Q.

Accelerating structures working at high frequencies have smaller dimensions and are able to produce a very high gradient minimizing breakdown phenomena. HG structures have been made at S-band (3 GHz), C-band (5.7 GHz) and X-band (12 GHz) with typical gradients in the 20–100 MV/m range. Nevertheless, the small wavelength of high frequencies requires very precise geometries for the same phase

errors. Mechanical tolerances for X-band structures become very tight and require ultra-precision machining which increases significantly the final cost.

The shunt impedance of HG structures is increased by closing the iris around the beam, which has the negative effect of producing strong wakefields affecting beam stability. For SW structures, the shunt impedance is already very large and can be reduced without major impact to avoid wakefields affecting the beam.

1.1.5 Beam loading of the accelerating structure

When a bunch of charged particles enters into a structure, it induces electromagnetic fields that change the field distribution present in the cavity. This effect is called 'beam-loading' and implies a reduction of the accelerating gradient ΔE_{acc} (and voltage) in the structure. Using Eq. (1.14), the loss of stored energy per unit of length in one cell after the passage of the beam is:

$$\Delta U' = \frac{(E_{acc} - \Delta E_{acc})^2}{\omega(R'/Q)} - \frac{(E_{acc})^2}{\omega(R'/Q)} \tag{1.22}$$

According to the fundamental theorem of beam loading [5], the accelerating voltage gained by the beam in the cavity is half the voltage that it leaves behind. As a consequence, the energy gained per unit of length by the bunch with charge q is:

$$\Delta W' = q \cdot \left(E_{acc} - \frac{1}{2}\Delta E_{acc} \right) \tag{1.23}$$

Due to energy conservation, the energy lost by the cavity is gained by the beam:

$$\Delta U' + \Delta W' = 0 \tag{1.24}$$

and the reduction of the accelerating gradient results:

$$\Delta E_{acc} = \frac{1}{2}\omega(R'/Q)q \tag{1.25}$$

Notice that this reduction depends on the bunch charge but not on the stored energy already present in the structure. The induced voltage by the beam fulfills the field superposition principle, and the beam-loaded voltage $V_0^{load} = E_{acc}^{load} L$ in the structure consists of the combination of the intrinsic cavity gradient E_{acc}^{unload} and the beam-induced gradient E_{acc}^{beam} with a RF to beam phase difference ϕ_s:

$$E_{acc}^{load} = E_{acc}^{unload} + E_{acc}^{beam} \cos(\phi_s) \tag{1.26}$$

The power absorbed by the beam during acceleration is given by:

$$P_{beam} = I_{beam} \frac{\Delta W}{q} \tag{1.27}$$

Table 1.1: Design parameters of different HG accelerating structures and linac specifications applied to linear colliders (CLIC and ILC), free-electron lasers (LCLS-II, SwissFEL, SACLA and PAL-XFEL) and Compton backscattering light sources (ELI-NP, ThomX and cERL). The photon beam energy of the light sources is also included.

Parameter	Unit	CLIC [6]	SwissFEL [7]	SACLA [8]	PAL-XFEL [9]	ELI-NP [10]	ThomX [11]	ILC [12]	LCLS-II	European XFEL	cERL
Facility		Collider	FEL	FEL	FEL	Compton	Compton	Collider	FEL	FEL	Compton
Technology		Normal-conducting						Superconducting			
Material		Copper						Niobium			
RF frequency f	[GHz]	11.994	5.712	5.712	2.856	5.712	2.998	1.3	1.3	1.3	1.3
Gradient E_{acc}	[MV/m]	100	28	35	27	33	18.2	31.5	16	23.6	15
Structure Length L	[m]	0.233	1.924	1.869	3.120	1.8	4.5	1.309	1.039	1.309	1.039
Number of cells		26	113	91	84	102	135	9	9	9	9
Iris aperture diameter	[mm]	4.7–6.3	10.8–14.4	13.6–17.3		11.6–13.6		70	70	70	70
Cell diameter	[mm]	16.7–17.5	43.8–44.8	44.0–45.7				210	210	210	210
Operating mode		TW	TW	TW	TW	TW	TW	SW	SW	SW	SW
Phase advance per cell	[rad]	$2\pi/3$	$2\pi/3$	$3\pi/4$	$2\pi/3$	$2\pi/3$	$2\pi/3$	π	π	π	π
Shunt impedance R'/Q	[kΩ/m]	14.6–17.9	7.23–8.70	5.4	4.1	7.9	0.95–1.1	0.998	0.998	0.998	0.998
Quality factor Q		5536–5738	9951–10036	10000	13000	8850	14800	1×10^{10}	2.7×10^{10}	1×10^{10}	$> 1 \times 10^{10}$
Group velocity v_g/c	[%]	0.83–1.65	1.19–3.10	2	1.2	1.4–2.5	1.1	–	–	–	–
RF Pulse length t_p	[μs]	0.242	0.350	0.6	1	0.820	6	1650	CW	1400	CW
Repetition rate	[Hz]	50	100	60	60	100	50	5	CW	10	CW
Operating temperature T	[K]	303	313	303	303	303	303	2	2	2	2
Linac length	[m]	21000	500	400	700	60	4.5	11000	550	1700	2.4
Maximum beam energy	[GeV]	1500	5.8	8.3	10	0.74	0.07	250	4	17.5	0.035
Photon energy (light sources)	[keV]	–	0.25–12	5–15	0.28–20	1000–20000	$<$90	–	0.2–25	0.26–25	6.9

where I_{beam} is the beam current and $\Delta W = qE_{acc}L\cos(\phi_s)$ is the beam energy gain. This term contributes in the total power consumption $P_{tot} = P_d + P_{ext} + P_{beam}$. A beam coupling coefficient is defined as:

$$\beta_{beam} = \frac{P_{beam}}{P_d + P_{ext}} \tag{1.28}$$

which is equal to 1 in critical coupling conditions. The quality factor Q^*_{load} of the cavity loaded by the beam is:

$$Q^*_{load} = \frac{Q_{load}}{1 + \beta_{beam}} \tag{1.29}$$

The ratio between the energy absorbed by the beam $\Delta W = P_{beam}t_{beam}$ and the RF energy consumed $U_{RF} = P_{tot}t_{RF}$ gives the RF to beam efficiency:

$$\eta_{RF-beam} = \frac{\Delta W}{U_{RF}} = \frac{P_{beam} \cdot t_{beam}}{P_{tot} \cdot t_{RF}} \tag{1.30}$$

Using Eq. (1.28) and considering the filling time of the structure to build the fields before the entrance of the beam $t_{RF} = t_{fill} + t_{beam}$:

$$\eta_{RF-beam} = \frac{\beta_{beam}}{1 + \beta_{beam}} \frac{t_{beam}}{t_{fill} + t_{beam}} \tag{1.31}$$

This efficiency is an important parameter in the cost optimization for the operation of an accelerating machine. The use of superconducting structures guarantees lower ohmic losses in the structure, but they require high filling times (due to their high quality factors) and extra cooling power from cryogenics in order to keep the superconducting state. Normal-conducting structures present lower filling times but the ohmic losses become more important. Every design needs a compromise between beam requirements and power consumption in the accelerator with a careful optimization of the power efficiency.

As explained before, in TW structures the RF power flows through each cell and the remaining power is extracted to the output coupler. An analytical calculation of the power flow and accelerating gradient in traveling wave structures is made in [13] for both transient and steady state when beam loads the structure. Considering a structure with a group velocity $v_g(z)$, an intrinsic cell quality factor $Q(z)$ and normalized shunt impedance per unit of length $(R'/Q)(z)$ profile along the axial cell position z, the power flow is:

$$P(z,t) = U'(z,t)v_g(z) \tag{1.32}$$

where $U'(z,t)$ is the stored energy per unit of length related with accelerating gradient by Eq. (1.14). The energy conservation gives the following differential equation:

$$\frac{\partial P(z,t)}{\partial z} + \frac{\partial U'(z,t)}{\partial t} = -\frac{\omega U'(z,t)}{Q_0} - E_{acc}(z,t) I_{beam}(t) \tag{1.33}$$

The first term on the left-hand side represents the variation of the power flow which is damped cell by cell through the structure, while the second term considers the time-variation of the stored energy in each cell, which is zero in steady state. On the right-hand side, the first term corresponds to the ohmic losses of the structure and the second one takes into account the loading by the presence of beam current $I_{beam}(t)$. The analytical solution, presented in [13], of the accelerating gradient along the structure is decomposed by the unloaded E_{acc}^{unload} and beam-induced gradient E_{acc}^{beam} as in Eq. (1.26):

$$E_{acc}^{unload}(z,t) = E_{acc}\left(0, t-\tau(z)\right) g(z) H\left(t-\tau(z)\right) \tag{1.34}$$

$$E_{acc}^{beam}(z,t) = -\omega g(z) \int_0^z \frac{(R'/Q)(z')}{2 v_g(z') g(z')} I_{beam}\left(t-\tau(z)+\tau(z')\right) H\left(t-\tau(z)+\tau(z')\right) dz' \tag{1.35}$$

where $H(t)$ is the Heaviside step function, $E_{acc}(0,t)$ is the accelerating gradient at the first cell of the structure, related to the input power $P_{in}(t)$ by:

$$E_{acc}(0,t) = \sqrt{\frac{\omega (R'/Q)(0)}{v_g(0)} P_{in}(t)}, \tag{1.36}$$

$g(z)$ is the unloaded profile defined by:

$$g(z) \equiv \sqrt{\frac{v_g(0)}{v_g(z)}} \sqrt{\frac{(R'/Q)(z)}{(R'/Q)(0)}} \exp\left(-\int_0^z \frac{\omega}{2 v_g(z') Q(z')} dz'\right), \tag{1.37}$$

and $\tau(z)$ is the filling time to the cell of position z:

$$\tau(z) \equiv \int_0^z \frac{1}{v_g(z')} dz' \tag{1.38}$$

For a constant beam current I_{beam}, the steady state solution is given by:

$$E_{acc}^{load}(z) = E_{acc}(0) g(z) - g(z) \int_0^z \frac{I_{beam}}{g(z')} \frac{\omega (R'/Q)(z')}{2 v_g(z')} dz' \tag{1.39}$$

Figure 1.4 shows the application of these calculations on a 23 cm-long constant-gradient TW structure, made up of 26 regular cells and 2 coupling cells with a total

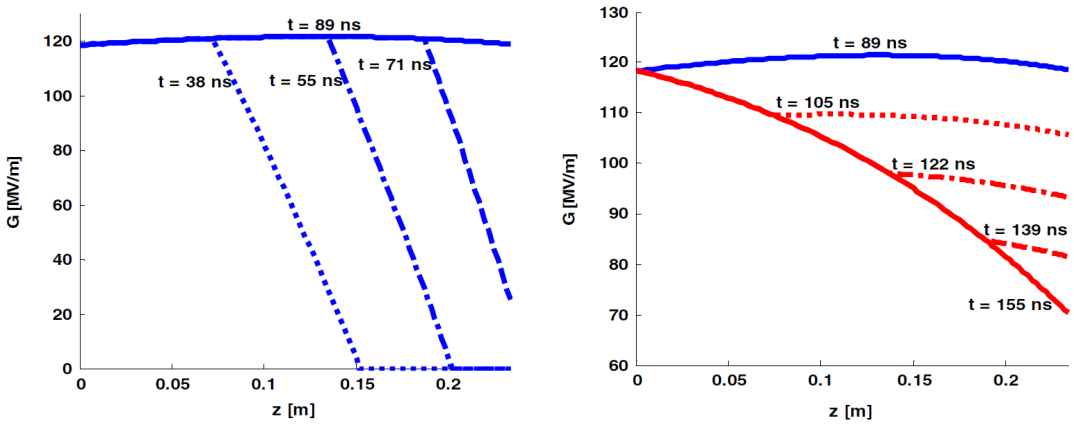

(a) (b)

Figure 1.4: Analytical calculations made in [13] of the accelerating gradient profile in a CLIC-G TW structure (a) during the energy filling (from 0 to 89 ns) and (b) when a beam current of 1.2 A enters to the structure (after $t = 89$ ns). Blue and red lines correspond to unloaded and loaded gradient profiles, respectively. Solid lines correspond to steady state profile, while dashed lines represent transients.

filling time of 67 ns, fed up with an input power of 61.3 MW and loaded with a beam current of 1.2 A after 89 ns. In Fig. 1.4(a) one can see how the structure is being filled with RF power from the input coupler cell ($z = 0$) to the output of the structure ($z = 23$ cm) according to the group velocity profile of 0.83–1.65% of the speed of light. The gradient is built up during a certain transient of 22 ns from the moment that the power has reached the cell, which is given by the cell Q factor. At $t = 89$ ns, the gradient achieves a steady state (blue solid line), in which the gradient of all the cells remains invariant in time. This structure is designed to keep a constant gradient profile in steady state at 120 MV/m for an input power of 61.3 MW.

If the beam traverses the structure when the steady state is achieved, at $t = 89$ ns, part of the stored RF energy is absorbed by the beam while more power comes into the structure through the input coupler. Consequently, the gradient profile is altered as shown in Fig. 1.4(b), affecting first the front cells and being propagated to the end of the structure. A new steady state is reached (red solid line) one filling time after the start of the beam pulse. In this case, the gradient at the first cell is larger than the last one, the average gradient is reduced to 100 MV/m compared to the unloaded profile and therefore the beam energy gain is in average smaller.

1.2 Applications of high-gradient RF warm technologies

With the recent developments in production and performance of normal-conducting RF accelerating structures, a wide range of potential applications are considered in accelerator facilities that could benefit from the advantages of high-gradient in terms of dimensions and cost. This section will give a summary of the current applications of interest of linacs with HG warm RF technology.

1.2.1 Future Linear Colliders for HEP

The Large Hadron Collider (LHC), at CERN, is currently carrying through the Run 2 colliding two beams of protons at a centre-of-mass energy of 13 TeV. This run would complete the results obtained in the previous Run 1 in 2012, when a Higgs-like boson was discovered at a mass energy of 125 GeV [14, 15]. Such discovery, together with many experimental results, has represented an important progress in the field of Particle Physics confirming the Standard Model in newly explored energy scales. A more fundamental theory underlying the Standard Model may involve additional particles to be discovered in the TeV scale that would extend the role of the Higgs boson in nature.

The discovery of the Higgs boson entailed the start of a major programme to perform precise measurements of this particle's properties in order to validate the Standard Model and to search for further new physics at the energy frontier. The efforts are focused on the full power operation of the LHC and its perspective of high-luminosity upgrade of the accelerator and detectors, by around 2030, that will allow to collect ten times more data than foreseen in the initial design. An important parameter that takes into account the optimization of the center-of-mass collider is the luminosity, defined by:

$$\mathcal{L} = H_D \frac{N_1 N_2}{4\pi\sigma_x\sigma_y} n_b f_r \tag{1.40}$$

where N_1 N_2 are the number of particles per bunch of each beam, n_b is the number of bunches per beam pulse, $\sigma_{x,y}$ are the horizontal and vertical beam sizes at the interaction point, f_r is the beam repetition rate and H_D is the enhancement factor that takes into account the influence between the two bunches with opposite charge when they collide at the interaction point. The integrated luminosity $\mathcal{L}_{int} = \int \mathcal{L}(t)dt$ is directly proportional to the number of collision events in the machine, and therefore the number of produced particles of experimental interest. This means that if we consider to have a Higgs boson factory, luminosity must be maximized.

There is a scientific interest in an electron-positron (e^+e^-) collider that can complement the LHC results capable of studying the properties of the Higgs boson and

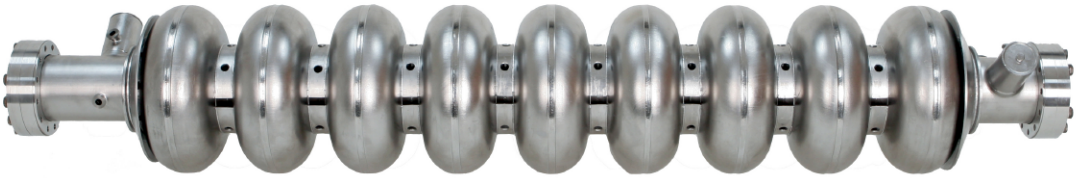

(a)

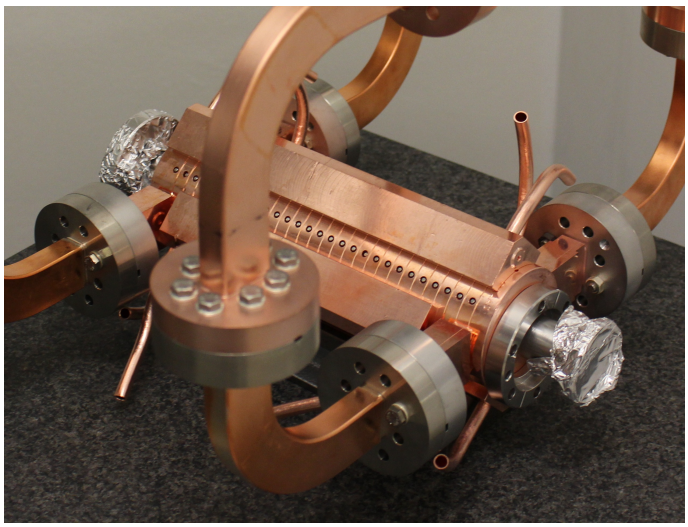

(b)

Figure 1.5: Pictures of two HG accelerating structures: (a) TESLA 9-cell niobium-made prototype for the ILC, with a total length of 1.25 m (taken from [17]); (b) CLIC-G TD26CC copper-made prototype for the CLIC Main Linac, with a total length of 23 cm (courtesy of A. Solodko).

other particles with unprecedented precision. The construction and reliable operation of a linear collider has been investigated during the last twenty years by an extensive group of researchers worldwide. Two e^+e^- linear collider projects have been proposed: the International Linear Collider (ILC) and the Compact Linear Collider (CLIC). The two collaborations were merged in 2012 under a unique Linear Collider collaboration [16] to share the efforts on the technical issues that are common to both.

International Linear Collider

The ILC is a 200-500 GeV center-of-mass high-luminosity e^+e^- linear collider, to be hosted in Japan, under a strong international collaboration. The acceleration is

based on 1.3 GHz superconducting RF technology, as recommended by the International Technology Recommendation Panel (ITRP) and the International Committee for Future Accelerators (ICFA) in 2004. An international collaboration was formed by research institutes involved in linear collider R&D to define the basic parameters and layout of the ILC machine. The detailed design study and cost estimate was published in the ILC Reference Design Report [18] in 2007. This was followed by an engineering design study that was consolidated in 2013 with the publication of the ILC Technical Design Report [17], which presents the matured technology design and construction plan for the ILC. An schematic layout of the accelerator complex is shown in Fig. 1.6.

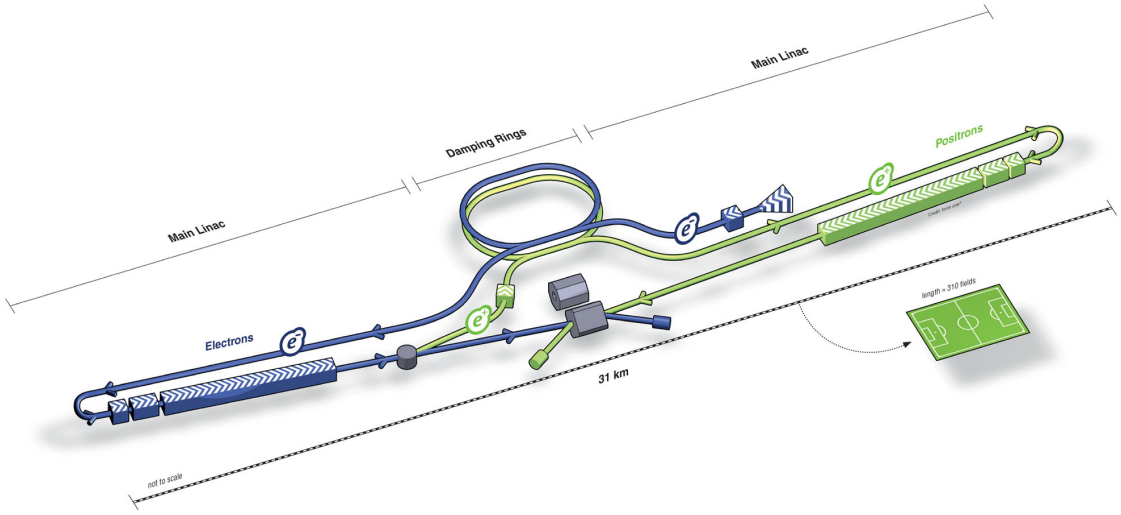

Figure 1.6: Schematic layout of the ILC.

Beam test facilities are employed for critical technical demonstrations, including accelerating gradient, precision beam handling and beam dynamics, and also to train scientific and engineering staff and regional industry. The Accelerator Test Facility (ATF) at the High Energy Accelerator Research Organization (KEK), in Japan, was built to address ultra-low emittance beam challenges. The ATF2 facility, which uses the beam extracted from ATF damping ring, aims at focusing beams to nanometer scale using an ILC-like final focus and providing nanometer stability. Research is also focused on ILC Damping Rings, essential to achieve ultra-low emittance beams, and their challenges such as suppression of electron cloud instabilities undertaken at the Cornell Electron-Positron Storage Ring Test Accelerator (CesrTA), and the demonstration of the ultra-low vertical emittance operation and fast injection-extraction developed at ATF.

The baseline design for the ILC linac is the TESLA 9-cell superconducting cavity [12], made of high-purity niobium, operating at an RF frequency of 1.3 GHz

and a nominal accelerating gradient of 31.5 MV/m. A picture of an accelerating prototype is shown in Fig. 1.5(a) and its design parameters are included in Table 1.1. An industrialization effort has been made to achieve a HG performance of 35 MV/m, with a permissible spread of up to ±20%, at an intrinsic quality factor above 0.8×10^{10}. Vertical-test results of several prototypes have demonstrated to overcome the required yield. The Free-Electron Laser in Hamburg (FLASH) at DESY is the only operating electron linac where it is possible to run close to reference design gradients with nominal ILC beams. The industralization of the superconducting RF technology is demonstrated by the ongoing construction of the European X-ray Free-Electron Laser (XFEL) project at DESY (Hamburg), foreseen to be finished in September 2016, which is completing the production of a total of 808 ILC-type superconducting cavities in 101 cryomodules (8 cavities per module), that will operate at a gradient of 23.6 MV/m. Furthermore, the Linac Coherent Light Source (LCLS) at SLAC (USA) has started the upgrade to LCLS-II with a 4 GeV continuous-wave superconducting linac made of 35 cryomodules. The fabrication of a total of 280 ILC-type structures strengthens the industrialization in USA in favor of the mass production for ILC.

Compact Linear Collider

The CLIC study is an international collaboration that is developing the concept of a multi-TeV e^+e^- linear collider with a centre-of-mass energy range from 0.5 to 5 TeV, optimised for a nominal energy of 3 TeV. The construction of the collider is foreseen to be done at CERN in three stages with center-of-mass energies of 380 GeV, 1.5 TeV and 3 TeV. The first stage, well above the top quark pair production threshold ($\sim$ 350 GeV), is proposed for precise top quark and Higgs physics measurements. The 1.5 TeV stage will allow the study of additional Higgs and top quark properties and the potential discovery of new physics phenomena. The last stage of 3 TeV will give access to the discovery and more precise measurements of pair-produced particles lighter than 1.5 TeV. A schematic layout of CLIC a this last stage is shown in Fig. 1.7.

The construction and operation of a realistic and cost efficient machine in the 3 TeV range requires HG linacs, aiming at an accelerating gradient of 100 MV/m. Since superconducting technology is fundamentally restricted to lower gradients (below approximately 35 MV/m), only normal-conducting RF structures are likely to achieve such gradients. The design of the electron and positron linacs are based on X-band (12 GHz) copper-made TW structures. The RF parameters of the current baseline design of CLIC Main Linac structures are included in Table 1.1. A picture of a CLIC baseline design prototype, nicknamed as TD26CC, is also shown in Fig. 1.5(b).

Normal-conducting technology requires high peak power to reach the nominal

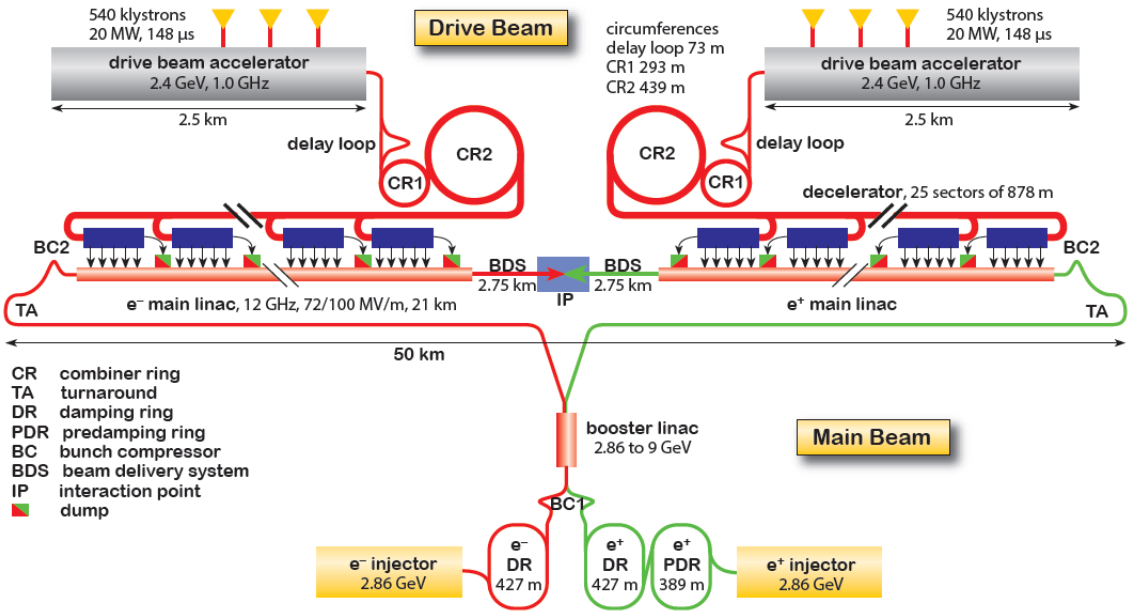

Figure 1.7: Schematic layout of the CLIC accelerator complex for a center-of-mass energy of 3 TeV.

gradient. The pioneer proposal of the 'two-beam acceleration' scheme is adopted to optimize the efficiency of RF power production, as an alternative to the classical klystron powering for linacs. A high-current low-energy electron beam, called Drive Beam (DB), runs in parallel to the Main Linac (ML) beam and is decelerated in Power Extraction and Transfer Structures (PETS) where the RF power is obtained and transfered by waveguides to the ML accelerating structures. Both beams can be generated in a central injector complex and are transported along the linac. The CLIC Test Facility CTF3 was built at CERN by the international collaboration to demonstrate the key feasibility issues of the two-beam acceleration technology and test the ML accelerating structures at nominal gradient. The CLIC Conceptual Design Report [19] was published in 2012 to summarize the concept of a Linear Collider based on the CLIC technology and results of the CTF3 studies. An updated baseline document is being composed [20] in 2016 with new optimized parameters and developments.

As already discussed, high power levels flowing through the ML structures build extremely high electric fields on the copper surfaces and non-linear effects may create vacuum discharges that perturb the operation. These breakdowns reduce the integrated luminosity of the collider since they cause transverse kicks to the beam which increases the angular divergence [21]. Consequently, a dedicated study of breakdown phenomena on different accelerating prototypes is crucial to understand how

to minimize the possible arcs. The NLC (Next Linear Collider) [22] and JLC/GLC (Japan/Global Linear Collider) [23] projects developed X-band (11.4 GHz) normal-conducting RF technology, with a target gradient of 50 MV/m, for e^-e^+ linear colliders in the TeV scale. A collaboration between SLAC and KEK led to important advances in RF design and assembly techniques of accelerating structures that allowed to achieve very high accelerating gradients, that would be later developed for the CLIC study [24].

1.2.2 Hadron therapy linacs

Cancer represents one of the leading causes of death in the world. Patients suffering from cancer have the possibility of different treatment techniques, such as chemotherapy, external radiotherapy, brachytherapy (or internal radiotherapy) and surgery. Accelerators have been an important tool for the development of external radiotherapy techniques.

External radiotherapy

Since the discovery of the X-rays in 1895 by C. Röntgen, which were first applied for imaging and medical diagnostics, high-energy photon beams were developed along with the accelerator technology for radiotherapy. Beams of charged particles started later to be used for radiotherapy due to their physical advantages in energy deposition to the tumor tissue, as shown in the comparison between X-ray and particle beams of Fig. 1.8. X-ray beams dose is distributed in a wide depth area, while using charged particles, like protons and carbon ions, most of its energy is transferred to a narrow region called Bragg peak, where the beam has maximum destructive effect. No radiation is left behind this peak since all the charges have lost their energy and been stopped, which reduces the irradiation of healthy organs in the vicinities of the tumor.

The use of proton and heavy ion beams, like Helium and Carbon, for cancer treatment is commonly known as hadron therapy. The fact that most of the energy is deposited in the Bragg peak implies that the tumor can be precisely irradiated with high control and keeping the surrounding healthy tissues safe.

Since the Bragg peak of proton and carbon ion beams is very narrow, a few millimeters thick, beam must be modulated in amplitude and energy in order to cover the whole size of the tumor. The penetration depth of the beam into the body is directly determined by the particle energy. The superposition of the different modulated beams define the spread out of the Bragg peak (SOBP) shown in Fig. 1.8. The irradiation of the localized tumor from different positions around the patient implies a considerable reduction of the dose absorbed by the healthy tissues. To do so, a rotating gantry is responsible for directing the beam to the tumor from

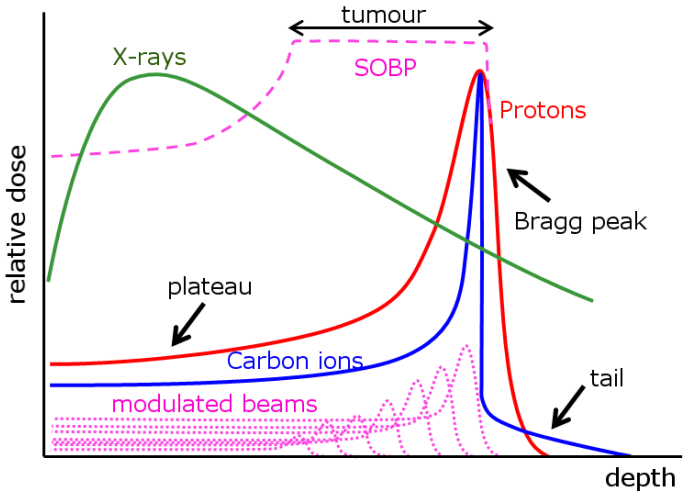

Figure 1.8: Dose distribution in water depth of monoenergetic proton (red), carbon ion (blue) and X-ray (green) beams. SOBP (pink) is the deposited dose covered on the whole tumor by modulating the proton beams with different current and energy. Courtesy of [25].

different angles. The trajectory of the hadron beams needs to be bent, thus the size of these gantries become important due to the high magnetic rigidity $B\rho$, where B is the magnetic field of the dipole and ρ is the bending radius, meaning that higher magnetic fields are needed to bend the beam with smaller radius. Typical magnetic rigidities for hadron therapy beams are 2.5 Tm for protons and 6.3 Tm for carbon ions.

Different beam delivery techniques are used to modulate the beams and form the SOBP: passive spreading and active scanning systems.

- In passive systems, the beam is spread by inserting scattering material before the patient that provides the needed dose depth distribution. Elements of variable thickness are employed, like ridge filters, modulator wheels and range shifters. A combination of these elements with collimators determine the aperture of the beam and the transverse irradiation of the tumor.

- Active scanning consists in controlling the dose deposition depth by modulating the beam energy in the accelerator. An advanced technique called "pencil-beam" method scans the tumor with a spot beam by controlling two scanning dipole magnets placed at the output of the accelerator. In this way, the tumour is precisely painted voxel-by-voxel with the desired dose. In combination with a 3D imaging feedback system, it would also be possible to perform an accurate irradiation on moving organs.

Linacs in hadron therapy

To the present day, a total of 62 facilities worldwide of particle radiotherapy are operational [26], based on proton and carbon ion beams, and other 34 are under construction foreseen from 2016 and 2018. Proton beams of energy between 200 and 250 MeV and carbon ion beams of energy between 300 and 400 MeV per nucleon are suitable to penetrate the body and irradiate the tumor. Beam currents around 1 nA for protons and 0.1 nA for carbon ions are usually needed.

The existing hadron therapy facilities employ cyclotrons, synchrocyclotrons or synchrotrons. Cyclotrons and synchrocyclotrons provide fixed energy beams, so passive absorbers are needed to irradiate different depths of the tumor. Synchotrons can deliver beams with different energies, but the slow beam extraction between each energy step (in the order of 1-2 s) leads to long sessions of therapy.

The use of linacs in such facilities is now being actively considered and has been studied over the last 20 years [27]. Linacs comprise a sequence of modules of accelerating structures and klystron power sources. This modularity allows to control each module individually, both in amplitude and phase, so that the final beam energy can be adjusted pulse-to-pulse through changes only in the low-level RF electronics stage. Variations of energies are possible in 2-5 ms using high repetition rate systems, typically between 200 and 400 Hz, and they allow to perform active spot scanning on the tumor with the pencil-beam method. These systems are capable of irradiating the whole volume in therapy sessions of few minutes.

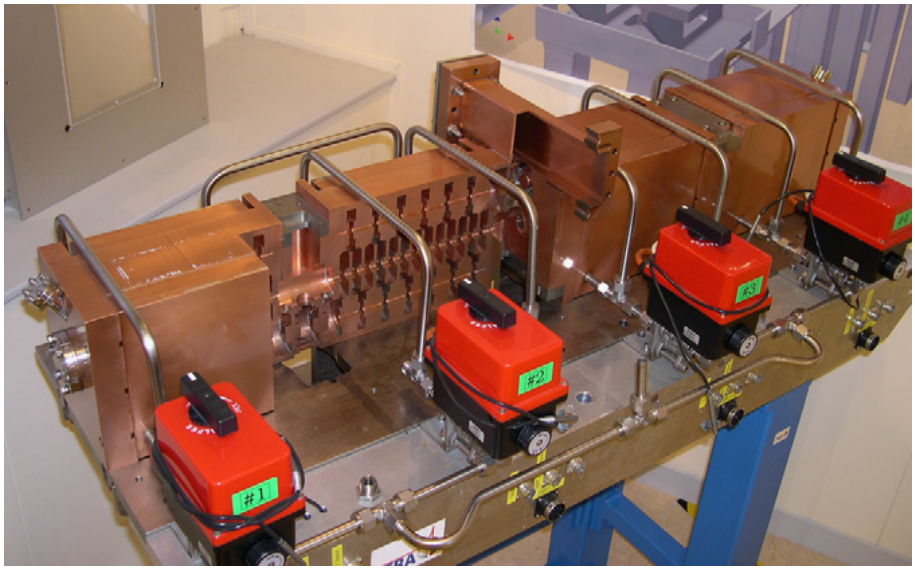

Figure 1.9: Four tank units of the LIBO S-band copper-made prototype and cut-away of one of them which shows the accelerating and coupling cells, courtesy of [28]. The structures were tested at a nominal gradient of 15.8 MV/m.

A first proposal of using a proton linac for cancer therapy was made in 1991 [29], based on an 'all-linac' design, which consists of a 70 MeV Drift Tube Linac (DTL) and a 3 GHz Cell Coupled Linac (CCL), capable of accelerating protons to 250 MeV. A 'cyclinac' approach for proton therapy was first proposed in [30], which combines a 30 MeV cyclotron followed by a 200 MeV linac. This concept was developed by TERA (Fondazione per Adroterapia Oncologica) in collaboration with CERN and INFN (Insituto Nazionale di Fisica Nucleare), carrying out the design and test of a 3 GHz CCL called LIBO (Linear Booster) [31], with a nominal accelerating gradient of 15.8 MV/m. A picture of a LIBO prototype made of 4 tank units is shown in Fig. 1.9. A.D.A.M. (Application of Detectors and Accelerators to Medicine) is a commercial company [32] which started the construction of an 'all-linac' accelerator for proton therapy, named LIGHT (Linac for Image Guided Hadron Therapy), based on the LIBO design. For carbon ion linacs for cancer therapy, the design of CABOTO (Carbon Booster for Therapy in Oncology) [33] consists of a cyclinac made up of a 150 MeV/u cyclotron and a 5.7 GHz 24 m-long linac operating at a high gradient up to 34 MV/m and a repetition rate up to 300 Hz, with a maximum final energy of 410 MeV/u.

The fundamental goal of high-gradient is to make more compact linacs, and this started to become relevant in the first linac designs for proton therapy accelerators. The limitation in gradient comes from the occurrences of vacuum arcs that perturb and interrupt the beam that treats the patient. The study of breakdown phenomenology in normal-conducting accelerating structures is crucial for the future of hadron therapy facilities, since HG linacs offer numerous advantages in terms of cost and operation. They open the possibility to build smaller facilities that can be easily integrated in hospitals.

1.2.3 Other potential high-gradient applications

The compactness that HG linacs offers can be exploited for other applications. Here we will mention the development of Free Electron Lasers (FEL) and Compton backscattering sources.

Free Electron Lasers

The so-called fourth generation light sources, based on linac-driven FELs [34], have brought an important advance in photon science involving multiple disciplines as biology, chemistry and material science. An electron beam is accelerated to the GeV energy range which goes through an undulator, a periodical magnetic structure that makes the electron trajectory oscillate. The beam emits a coherent X-ray radiation with optimum properties for photon experiments. Compared to synchrotron light

sources based on storage rings, FELs provide a much brighter, monochromatic, X-ray beam which allows image reconstruction down to the atomic scale. The light source also provides very short pulses of the order of 100 fs for the imaging of fast molecular processes.

A big fraction of the FEL facility cost comes from the linear acceleration of the beam. The use of HG technology considerably reduces the cost and dimensions of the FEL easing their construction and funding in international research institutes. Usually, S-band linacs (3 GHz) are used for existing FELs and some new C-band linacs (5.7 GHz) offer higher accelerating gradients.

The different linac designs of some existing X-ray FELs in the world are summarized in Table 1.1, in which we include: the Linac Coherent Light Source (LCLS-II) [35], at SLAC laboratory (USA); the SPring-8 Angstrom Compact free electron LAser (SACLA) [36], at RIKEN (Japan); and the Pohang Accelerator Laboratory X-ray Free electron Laser (PAL-XFEL), at PAL (Korea). The first one is an upgrade of the first hard X-ray FEL, the LCLS [37], which now makes use of superconducting RF technology in a 4 GeV electron linac with higher repetition rate. The SwissFEL [38] at PSI (Switzerland) and the European XFEL [39] at DESY (Germany) are currently under construction using normal-conducting technology. High gradients above 15 MV/m eases the construction of compact accelerators, as it is the case of SACLA which accelerates a 8.3 GeV electron beam in a 400 m-long linac. As an example, a picture of the accelerating structure of the SwissFEL C-band linac is shown in Fig. 1.10

Figure 1.10: Picture of a C-band 2 m-long (113 cells) accelerating structure for the SwissFEL facility, operating in TW $2\pi/3$ mode at 5.7 GHz and 28 MV/m gradient.

The X-band FEL collaboration [40] is composed by 12 international institutes which promotes the use of X-band technology (12 GHz) to construct the next generation of FELs aiming at optimum cost and dimensions, as well as power efficiency. This collaboration would benefit from the CLIC developments in hardware and

linac design, since they share similar beam specifications. The possibility of applying the CLIC's X-band state-of-the-art accelerating structures, with gradients near 100 MV/m, would allow the construction of unique small-dimension FELs.

Compton backscattering sources

Studies in nuclear physics and other subatomic processes are also performed using Compton backscattering gamma ray sources. The inverse Compton process consists of the scattering of low energy photons with very energetic electron beams that produce photons in the keV-MeV range. Typically, electron beams of the order of 10's to 100's of MeV are needed in Compton sources. Table 1.1 includes the details of some existing and on construction Compton backscattering facilities that make use of HG technology to accelerate the electron beams.

The Extreme Ligh Infrastructure for Nuclear Physics (ELI-NP) [41] is an advanced high-brilliance high-energy gamma ray source based on Compton backscattering under construction at IFIN-HH (Horia Hulubei National Institute for R&D in Physics and Nuclear Engineering) in Bucharest (Romania). An electron beam accelerator comprises a 60 m-long RF linac that delivers the beam with an energy range between 75 and 740 MeV and is capable of producing gamma rays up to 20 MeV by Compton backscattering interaction. The linac system comprises C-band 5.7 GHz warm accelerating structures (see Fig. 1.11) operating at a maximum gradient of 33 MV/m [10].

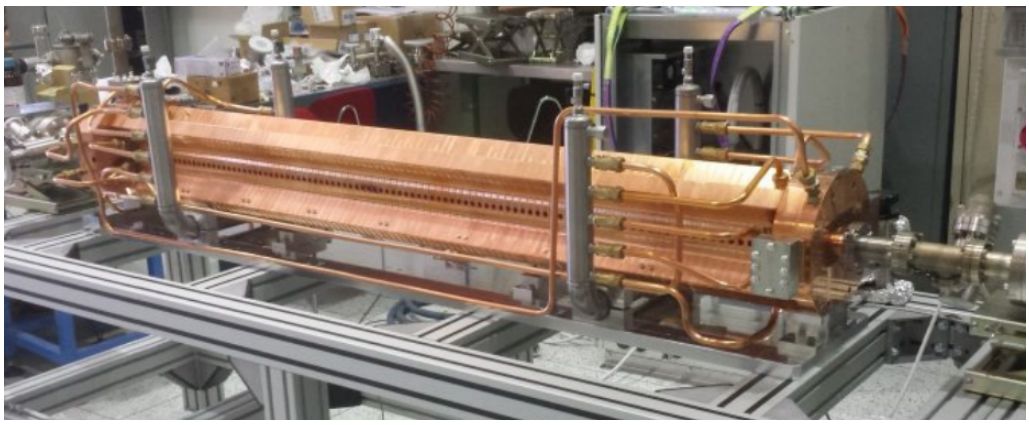

Figure 1.11: Accelerating structure for the ELI-NP C-band linac section, operating in TW $2\pi/3$ mode at 5.7 GHz and 33 MV/m gradient, made of 102 cells with a total length of 1.8 m.

The ThomX project [11] is a compact Compton-based hard X-ray source (up to 90 keV) under construction at LAL (Laboratoire de l'Accélérateur Linéaire), in Orsay (France). The accelerator complex incorporates a 4.5 m-long electron linac

that achieves energies in the range of 50-70 MeV, which acts as the injector of a storage ring where the beam is recirculated and interacts with the laser at high collision frequency. The RF linac is made up of S-band TW accelerating structures operating at room-temperature with a maximum gradient of 18.2 MV/m.

The Compact Energy Recovery Linac (cERL) [42], at KEK (Japan), makes use of ERL design for a X-ray light source in which the beam accelerated in the main linac is recovered with a recirculation loop. The cERL linac comprises two 1.3 GHz superconducting ILC-type cavities operated at a gradient of 15 MV/m. This section accelerates the 1 mA continuous-wave beam to a nominal energy of 35 MeV in a 2.4 m-long cryomodule, which later interacts with a laser to obtain 6.9 keV X-rays.

This represents again a good application of HG technology, which enables compact and economical gamma ray sources and facilitates their use in research institutes and university laboratories interested in nuclear physics studies.

Chapter 2

Phenomenology of breakdowns in high-gradient RF accelerating structures

The performance of HG linacs is mainly limited by the occurrences of vacuum arcs due to intense electromagnetic fields that are present on the walls of the structures. In this chapter we will review the current understanding of breakdown phenomena and their consequences in RF accelerating structures.

2.1 Motivation in breakdown studies

High voltage systems occasionally experience failures due to electric discharges that consist of a sudden release of energy in the system. This is the case of HG RF accelerating structures, where surface electric fields of hundreds of [MV/m] are present, and breakdown arcs take place in the vacuum volume of the accelerating structures with a certain statistical probability that reduces performance of the accelerator.

When a breakdown happens inside the accelerating structure, a surge of current is emitted from the walls forming a plasma that rapidly raises the vacuum pressure levels. The interference of this current with the entering power and the resonant cavity itself produces important non-linearities in the system that seriously affects the acceleration of the beam. Consequently, the breakdown can disturb the trajectory of the beam and its emittance, resulting in luminosity loss and possibly beam loss. Breakdowns in HG linacs may force the accelerator to stop and cause operation down-times.

The performance of the accelerating structures is hence assessed by the **breakdown rate** (BDR), and is given by the fraction of the pulses the accelerator breaks

down. The breakdown rate per unit of length of accelerator is defined as:

$$\mathrm{BDR} = \frac{\text{Number of breakdowns}}{\text{Number of pulses} \times \text{Length}} \tag{2.1}$$

and is expressed in units of [1/pulse/m] (or equivalently [bpp/m], breakdowns per pulse per meter).

In Future Linear Colliders, the luminosity is a crucial parameter of the accelerator design that needs to be maximized in order to achieve the maximum number of particle collisions. The limitation in repetition rate of linear colliders to about 100 Hz, compared to circular collider rates of about 10 kHz, requires an efficient performance of the linac with very low BDR in order to optimize the luminosity. The CLIC study established a BDR goal of 3×10^{-7} bpp/m for the accelerating structures of the Main Linac operating at a gradient of 100 MV/m, which is required for a maximum luminosity loss up to 1% over the $\sim$ 30 km of accelerating structures in both linacs of the collider.

HG technology in hadron therapy accelerators is also concerned about the development of vacuum arcs during operation [25]. These events cause the interruption of beam delivery to the patient and the loss of control in deposited dose into the tumor. A maximum BDR of the order of 10^{-6} bpp/m is usually considered as a limit operation in a hadron therapy linac in order to guarantee an efficient operation of the accelerator complex without breakdowns during the whole treatment session. BDR also needs to be lowered to reasonable levels for HG linacs installed in FEL and Compton backscattering sources for the sake of providing the best experimental conditions.

Several experimental programs, together with simulation studies, are being carried out to understand the formation of vacuum arcs in different systems such as RF accelerating structures. The phenomena of breakdowns is a very complex and multidisciplinary problem which involves studies in RF, surface machining and cleaning, material science and plasma physics, among others. The interest of minimizing the occurrences of vacuum arcs and their effects would allow the development of HG technologies in linear accelerators for numerous applications.

2.2 Surface field emitters

During normal operation of HG accelerating structures, a detectable current emission is observed coming from the high electric field areas of the cavity walls. This current is known as **field emission** (FE) since the electrons are emitted from the metallic walls induced by the electric field. Other types of electron current emission from metallic surfaces can be described by: thermionic emission, in which thermal energy given to the electrons eases their extraction from the atoms; photo-emission,

induced by the incidence of photons above a certain energy via the photoelectric effect; and secondary electron emission, produced by the incidence of other electrons to the metal atoms above a certain energy threshold capable to pull out more electrons. Because of the extremely high fields, FE mechanism dominates and is one of the key steps in the breakdown process in HG accelerating structures. Field emission studies are essential to understand not only vacuum arcs phenomenology but also their precursors.

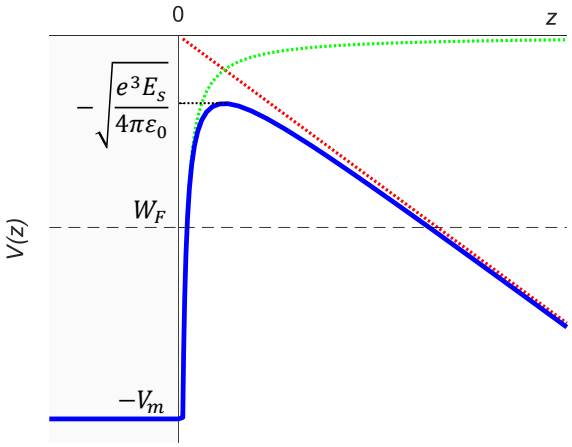

Figure 2.1: Effective potential barrier $V(z)$ (blue) seen by the conducting electrons of the metallic surface, with a Fermi energy level W_F, due to the electrostatic interaction with its image charge (green) and the external electric field E_s (red).

Field emission can be explained by the modification of the potential barrier that the conduction electrons are subject to when an external electric field E_s is applied on the surface, as seen in Fig. 2.1. The effective potential energy $V(z)$ along the normal direction to the metallic surface is given by:

$$V(z) = \begin{cases} -V_m & z < 0 \\ -\frac{e^2}{16\pi\varepsilon_0 z} - eE_s z & z > 0 \end{cases} \tag{2.2}$$

where $\varepsilon_0 = 8.854 \times 10^{-12}$ [F/m] is the vacuum permittivity, $e = 1.602 \times 10^{-19}$ [C] is the electron charge and V_m is the potential energy of the electron inside the metal. For $z > 0$, the first component correspond to the classical screening energy of a perfectly conducting semi-infinite metal, and the second one is the potential of the electric field. The resulting potential barrier is shown in Fig. 2.1, with an effective potential height that is reduced by the field as:

$$V_{eff} = V_m - \sqrt{\frac{e^3 E_s}{4\pi\varepsilon_0}} \tag{2.3}$$

The barrier also presents a finite width that electrons are capable of traversing by quantum tunneling [43]. Assuming that the distribution of conducting electrons follows Fermi-Dirac statistics with a certain Fermi energy level W_F, and considering an external DC field E_s, quantum mechanics calculations gives an electron current density j_{FE} that is transmitted through the barrier [44]:

$$j_{FE}[\mathrm{A/m^2}] = (1.54 \times 10^{-6}) \cdot 10^{4.52\phi[\mathrm{eV}]^{-0.5}} \cdot \frac{E_s[\mathrm{V/m}]^2}{\phi[\mathrm{eV}]} \exp\left(-\frac{6.53 \times 10^9 \phi[\mathrm{eV}]^{1.5}}{E_s[\mathrm{V/m}]}\right) \quad (2.4)$$

where ϕ is the work function of the metal atoms.

Despite the fact that the FE theory explains the strong dependence of the emitted current with the field, an excess of current is always present that may come from the existence of different features in the surface. The extensive progress in machining techniques allows to achieve roughness of the order of 25 nm, but smaller irregularities together with the presence of impurities act as source of enhanced field emission (EFE). Small protrusions grow up on the surface and modify the electric field locally with an enhancement factor β_{FE} which is defined by:

$$\beta_{FE} \equiv \frac{E_{local}}{E_s} \quad (2.5)$$

where E_{local} is the peak surface electric field on such protrusion. This factor depends on the microscopic geometry of the tip (see Fig. 2.2), and a large number of them with different geometries can be distributed all over the surface. The local field can be magnified 1-4 orders of magnitude. Since the emitted current in Eq. (2.4) is strongly sensitive to the field intensity, these tips are the main contribution of electron emission.

The nature of the fields emitters described above can be explained by different scenarios. On the one hand, machining, cleaning and other thermal-chemical processes can leave traces and small features which develop field emitters on the surface. Contamination from different materials employed during the mechanical fabrication and cleaning are also likely to be deposited on the surface and produce small tips and irregularities. On the other hand, recent theoretical models [45] rely on the formation of micro-protrusions by the tensile stresses originated by the high electric fields, which can lead to dislocations and disorientation of the bulk material and consequently the formation of internal voids and external tips. This model would explain the dynamic conditioning of the accelerating structures.

Integrating Eq. (2.4) over an effective area A_e of field emitters, and substituting the global surface field by the local field $\beta_{FE}E_s$, the field emission current yields:

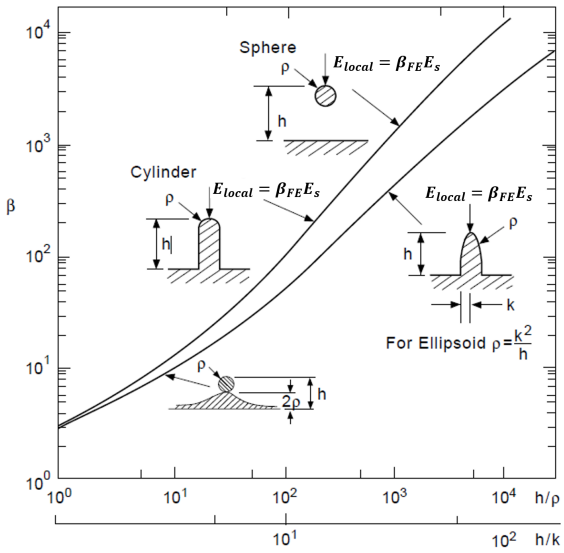

Figure 2.2: Field enhancement factor β_{FE} for different geometrical tip dimensions and configurations on a metallic surface, defined by geometrical factors: h (height), ρ (tip rounding) and k (width). Taken from [44].

$$I_{FE}[\mathrm{A}] = (1.54 \times 10^{-6}) \cdot 10^{4.52\phi[\mathrm{eV}]^{-0.5}} \cdot \\ \cdot A_e[\mathrm{m}^2] \frac{(\beta_{FE} E_s[\mathrm{V/m}])^2}{\phi[\mathrm{eV}]} \exp\left(-\frac{6.53 \times 10^9 \phi[\mathrm{eV}]^{1.5}}{\beta_{FE} E_s[\mathrm{V/m}]}\right) \quad (2.6)$$

In accelerating structures the metallic surface is subject to RF fields that rapidly oscillate in time as $E_s \sin(2\pi f t)$. An equivalent formula is obtained in [44] for RF fields by averaging the field emission current of Eq. (2.6) in a single RF cycle:

$$I_{FE}[\mathrm{A}] = (5.7 \times 10^{-12}) \cdot 10^{4.52\phi[\mathrm{eV}]^{-0.5}} \cdot \\ \cdot A_e[\mathrm{m}^2] \frac{(\beta_{FE} E_s[\mathrm{V/m}])^{2.5}}{\phi[\mathrm{eV}]^{1.75}} \exp\left(-\frac{6.53 \times 10^9 \phi[\mathrm{eV}]^{1.5}}{\beta_{FE} E_s[\mathrm{V/m}]}\right) \quad (2.7)$$

As can be observed in Fig. 2.3(a), the sensitivity of the current with the field becomes much stronger for emitters with higher β_{FE}. Data can be represented as $\log_{10}(I_{FE}/E_s^{2.5})$ versus $1/E_s$ in the so-called Fowler-Nordheim plot, shown in Fig. 2.3(b). In this plot, we could obtain β_{FE} by calculating the inverse of the slope

(derivative) and using the following formula:

$$\beta_{FE} = -\frac{(2.84 \times 10^9) \cdot \phi[\mathrm{eV}]^{1.5}}{\frac{\mathrm{d}(\log_{10}(I_{FE}[\mathrm{A}]/E_s[\mathrm{V/m}]^{2.5})}{\mathrm{d}(1/E_s[\mathrm{V/m}])}} \tag{2.8}$$

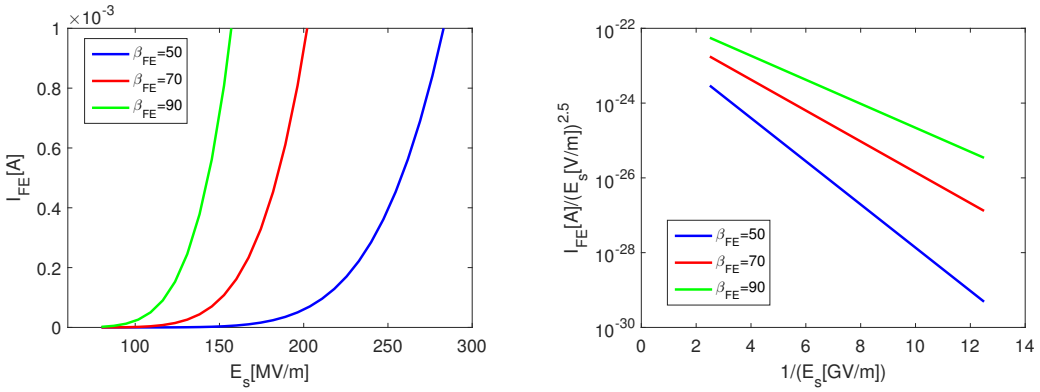

(a) (b)

Figure 2.3: Calculations of the (a) field emission current dependence with surface electric field and (b) Fowler-Nordheim plot, using Eq. (2.7), for a copper-made RF accelerating structure with different field enhancement factors $\beta_{FE} = 50$, 70 and 90, with a tip effective area of 100 nm^2.

Both DC and RF experiments show a good correspondence, once the factor β_{FE} is introduced, with EFE theory for high fields regime. Thermionic emission can be also activated [46] and enhances emitted current since electrons with higher thermal energy than the Fermi level needs to tunnel through weaker and narrower potential barriers, as it is the case for RF guns.

Microscopic field emitters are considered to be the sites where vacuum arcs are more likely to be ignited, due to the large amount of current that is released by field emission. The origin of formation of this features presents special interest to understand the probability of experiencing breakdown discharges. To the present, no clear evidence of breakdown precursors have been found yet. Precise and statistical measurements of field emission current immediately before the discharge are needed to verify the mechanism of breakdowns.

2.3 Description of surface breakdown phenomena

Starting from the existence of emitters that release a significant current of electrons, simulations of the dynamics of such protrusions have been performed to explain the

triggering of vacuum breakdowns in the current model. Variations in the geometry of the emitters can be understood by the molecular interactions with the external field and the self-emitted current.

When the electric field is present, high currents flow through the protrusion and heat it up because of resistive heating. The strong stresses applied by the field deform the tip and modify the local field enhancement factor. This process may lead to a growth of the emitter and the local electric field that raises the field emission. The ignition of a breakdown is triggered by the excess of current density and temperature at the tip above a certain threshold that defines the emitter instability until it gets finally melted.

Different stages are used to describe the arc mechanism, from its initiation to its mitigation [47]. This process is clearly visualized in Fig. 2.4 [48]:

- In the early stage, together with the field emission of electrons, the strong heating of the emission area leads to the melting and evaporation of neutral atoms and ions from the surface [49], assisted by the local electric field and thermal effects. The presence of the first neutral atoms by evaporation is found to be essential to develop the arc discharge.

- The accumulation of neutrals and electrons brings on the ionization of the atoms in avalanche by collisions that produce the formation of a plasma of ions. This plasma consists of a gas of free positive and negative charges interacting among them. A balanced quasi-neutral plasma sheath is formed on top of the original emitter site. This stage is known as the *burning* phase, which lasts around 1-5 ns.

- At the same time, the ionized atoms are attracted to the surface and this is continuously bombarded. Consequently, more neutrals and ions are sputtered and maintain the plasma volume within a longer time scale. Sputtering leads to the surface erosion and the formation of a crater on the surface.

- The cratering implies a rearrangement of the emitter that may create new field emitters around the resulting crater. Current heating melts and evaporate these secondary tips and further craters may be created.

- The plasma is extincted by expansion cooling few microseconds after the external field is switched off.

In RF accelerating structures, a breakdown results in an impedance mismatch and consequently the reflection of the RF power that feeds the structure. The impedance mismatch is the result of the very high electron currents emitted by the plasma spot formed during breakdown. Inside the plasma spot the current is driven

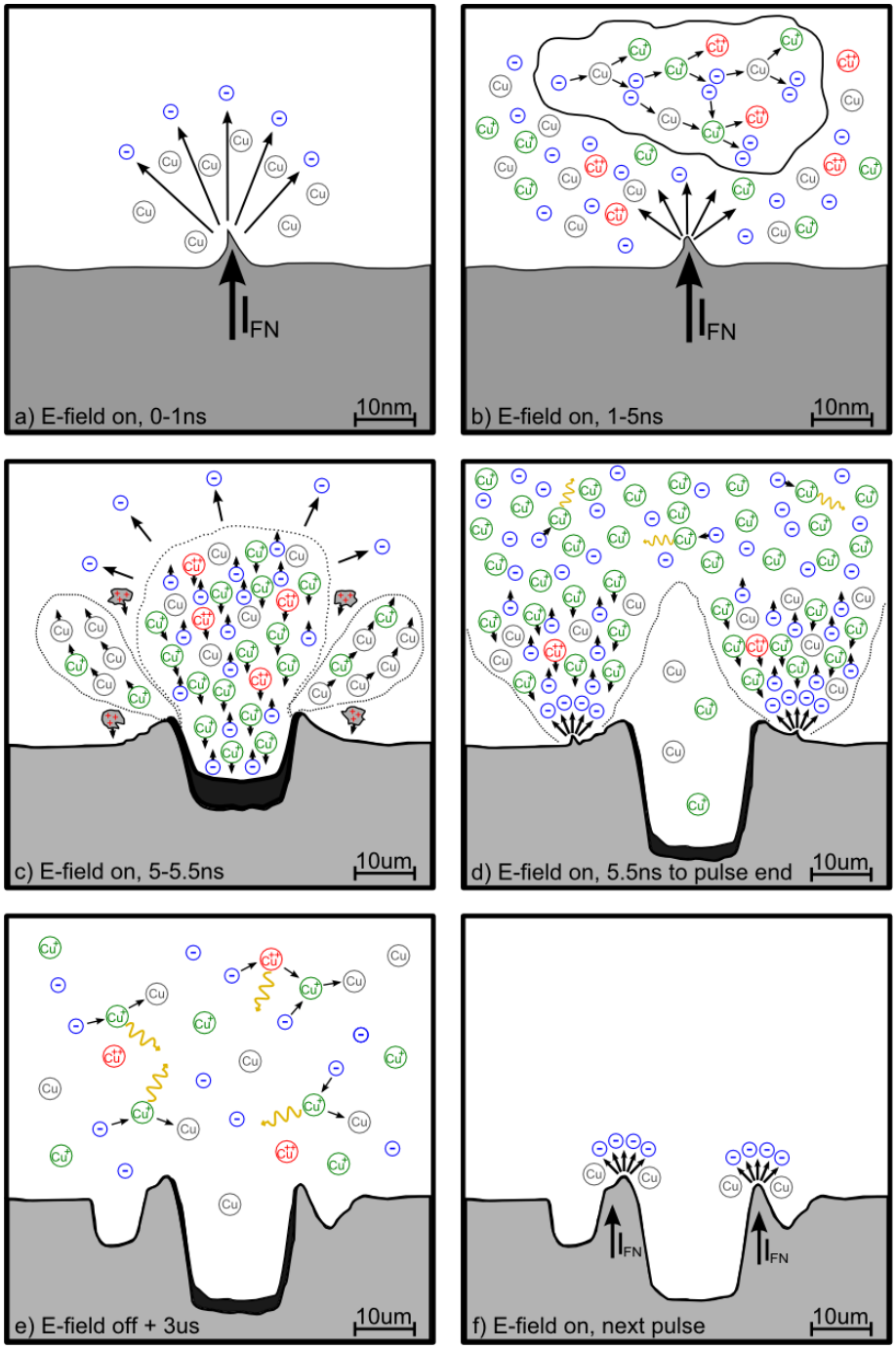

Figure 2.4: Illustrative description of the different stages during the vacuum arc formation. Taken from [48].

by the strong fields in the plasma sheath which forms between the plasma and the metal surface [47]. The emitted current from the plasma is accelerated by the incoming RF fields giving the impedance mismatch. The currents occurring during breakdown can be measured by Faraday cups placed at the ends of the structure and the reflected power can be measured through waveguide directional couplers. RF breakdown experiments at CERN are further discussed in Chapter 4.

Resulting craters have been observed in post-mortem analysis of HG RF accelerating structures and other high-voltage DC systems, by microscopic observation of the damaged surface (see Fig. 2.5).

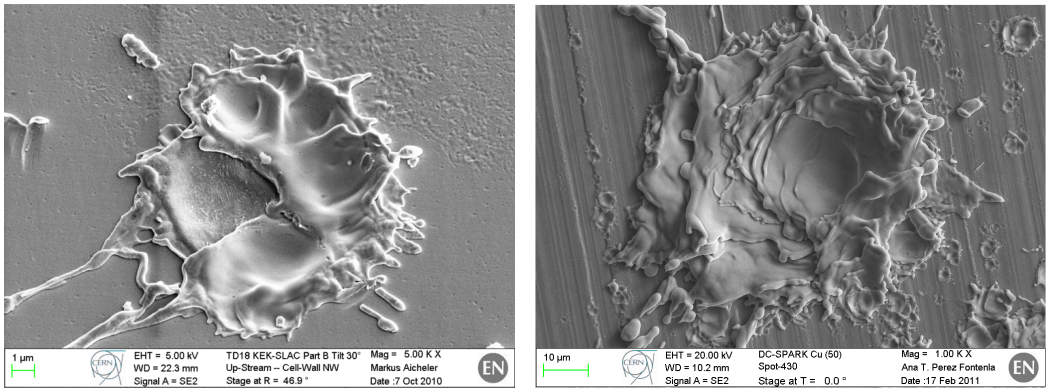

(a) (b)

Figure 2.5: Breakdown crater observed by SEM (Scanning Electron Microscope) on the surface of a (a) CLIC TD18 accelerating structure fabricated at SLAC and tested at KEK, and (b) copper-made sample of the DC-Spark experiment at CERN, taken from [50].

2.4 Breakdown rate performance and scaling laws

The performance of HG RF structures is evaluated by their breakdown probability while they operate in the accelerator at a specified gradient level. This is quantified by the BDR, defined in Eq. (2.1), which has been observed to be strongly dependent on the accelerating gradient E_{acc} and the length of the RF pulse t_p [51–55]. A collection of high-gradient tests data of several RF copper-made prototypes for NLC, JLC/GLC and CLIC with operating frequencies of 12 and 30 GHz is presented in [54]. Measurements of BDR at different gradients, represented in Fig. 2.6, shows a good correspondence between data and the following power law:

$$\mathrm{BDR} \propto E_{acc}^{30} \tag{2.9}$$

The exponent 30 is only adopted to be the most suitable parameter that fits the set of experimental data. This fit does not assume any physical mechanism that would predict breakdown probabilities. Since the peak surface electric field E_s on the metallic walls of the structure is proportional to the gradient, an analogous scaling law BDR $\propto E_s^{30}$ can be determined between BDR and surface field, as it is found in DC experiments [56].

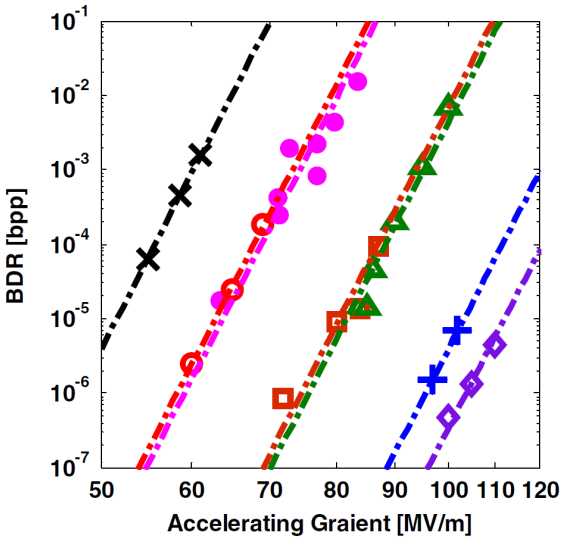

Figure 2.6: Measurements of BDR dependence with the accelerating gradient and power fit of different HG prototypes, taken from [54].

The probability of triggering a breakdown is also influenced by the length of the RF pulse, being more likely to arc for longer pulses. A power law dependence with the breakdown rate at a fixed gradient is found in high-power RF experiments [52, 57, 58]:

$$\text{BDR} \propto t_p^5 \tag{2.10}$$

Combining Eqs. (2.9) and (2.10), a general equation can be derived:

$$\frac{\text{BDR}}{E_{acc}^{30} t_p^5} = \text{constant} \tag{2.11}$$

This equation corresponds to an empirical scaling law that correlates the three relevant parameters of the performance of an accelerating structure in a HG linac: BDR, gradient and pulse length. BDR shows a much stronger dependence on the accelerating gradient rather than the pulse length, thus the scaling $E_{acc} \propto t_p^{-1/6}$ for a fixed BDR is found. In order to achieve the required BDR, the length of the RF pulse needs to be lowered so that the structure can sustain higher gradients. For this

reason, this equation offers an important limit criterion for the optimization of HG linear accelerators, which needs to find the best compromise between the gradient and the length of the train of bunches that fulfills the required power efficiency and beam specifications.

Defect-stress model

A theoretical model is proposed in [45] to explain the physical mechanism that leads to the observed scaling laws between BDR and the surface fields. The model assumes a growth of potential breakdown sites and field emitters induced by the tensile stresses on the surface originated by the external electric field E_s. Dislocations form at locations where there are crystallographic defects and voids, and may produce the mass transport that leads to the formation of micro-protrusions on the external surface.

The probability of experiencing a vacuum arc is assumed to be proportional to the production rate of defects, which is given by thermodynamical statistics. As a result, BDR depends exponentially on the squared electric field:

$$\mathrm{BDR} \propto \exp\left(\frac{\varepsilon_0 E_s^2 \Delta V}{k_B T}\right) \tag{2.12}$$

where $\varepsilon_0 E_s^2$ corresponds to field-induced stress on the metal surface, ΔV is the relaxation volume of the defect, T is the temperature and $k_B = 1.381 \times 10^{-23}$ [J/K] is the Boltzmann constant.

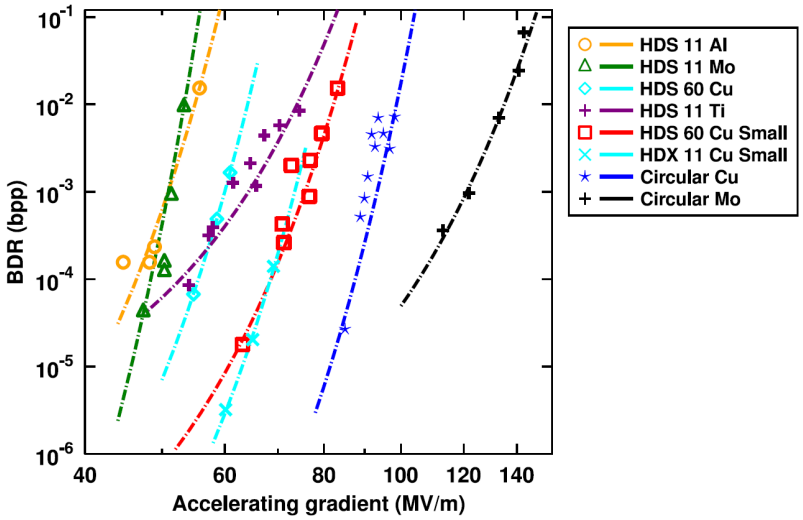

Figure 2.7: Fit of the defect-stress model on the measured BDR at different accelerating gradient of a set of HG prototypes, taken from [45].

The defect-stress model shows a good agreement with the BDR dependence observations both in DC experiments and RF accelerating structures [25,45,59], see the latter in Fig. 2.7. The fitted parameters reveal an average defect size of 8-40 nm, consistent with expected tip sizes that are measured via the field enhancement factor β_{FE}.

In contrast to the power law fit of Eq. (2.9), this model predicts a nonzero BDR at $E_s = 0$ due to the presence of defect concentration even without any field stress, but breakdown does not evolve since plasma is not produced. Nevertheless, it can explain the strong dependence of BDR on the measured fields equivalently as E_{acc}^{30}. In addition, the model includes the influence of the material temperature and suggests the idea of steeper dependence for structures operating at lower temperatures [60].

2.5 Breakdown constraints in RF accelerating structures

The effort to achieve higher gradients in room-temperature accelerating structures has brought a better understanding of vacuum arcs phenomenology and important developments in the optimum design and fabrication of such structures. Recent progress in ultra-precision machining allowed to achieve extremely high quality surfaces of the cavity walls, as well as fulfilling the strict geometrical tolerances of high-frequency structures.

In this section we will review the current design constraints used in the RF design of normal-conducting structures to minimize the occurrences of breakdowns when operating at very high gradients.

2.5.1 Surface electric field

In view of its direct role in the field electron emission, the electric field level is considered to be one of the main causes of vacuum breakdowns. Kilpatrick [61] established an empirical relation to distinguish the no-spark and the possible-spark regime in the operation of RF accelerating structures, depending on the electric field intensity and the RF frequency f. The limit of the surface electric field E_K that follows Kilpatrick's criterion is given by the following expression, reformulated in [62]:

$$f[\mathrm{MHz}] = 1.64 \;\; E_K[\mathrm{MV/m}] \exp\left(-\frac{8.5}{E_K[\mathrm{MV/m}]}\right) \tag{2.13}$$

The Kilpatrick criterion does not include the concept of BDR to assess the sparking probability, and no pulse length dependence can be extracted. As it can be seen

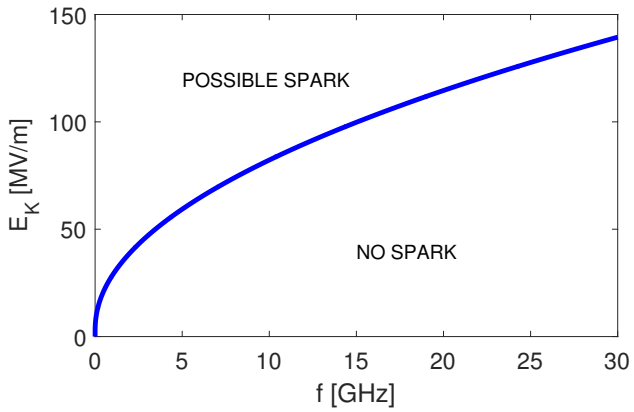

Figure 2.8: Boundary between the no-spark and the possible-spark region according to Kilpatrick's criterion, Eq. (2.13).

in Fig. 2.8, this criterion suggests that higher fields can be achieved at higher frequencies. New techniques in surface machining and cleaning, together with more powerful vacuum systems, allowed to reach higher fields than Kilpatrick's observations, up to a factor 2. Nevertheless, this relation is still used as reference in the design of the field and frequency of some accelerating structures, especially with high-duty cycle or CW systems well below 1 GHz.

The breakdown field E_b is commonly defined as the electric field threshold from which the surface starts to breakdown, and gives the operation limit of a HG accelerating structure. The breakdown field was measured on a set of processed samples with different materials in a pulsed-DC experiment [63], shown in Fig. 2.9, to study the material dependence of such limit. A potential explanation of these results is given in [64], based on a correlation with the crystal structure of the material. In the case of pure fcc (face-centered cubic) metals, the dislocation mobility is higher than bcc (body-centered cubic) and hcp (hexagonal closest packing) metals, being the latter stronger to sustain higher fields due to their very low dislocation mobility. For the same reason, the measured field enhancement factors β_{FE} are lower in hcp metals such as cobalt.

The collected test results, presented in [54], from a wide number of X-band and K-band HG copper-made structures for NLC, JLC/GLC and CLIC shows a large range of maximum achievable gradient. For a pulse length operation of 200 ns and BDR of 10^{-6} bpp/m, gradients from 20 to 140 MV/m were accomplished. The peak surface electric field, which is different for the various cell geometries, was initially considered to limit the maximum achieved gradient. However, a large measured spread of the maximum surface fields, from 60 to 300 MV/m, is observed which indicates that other quantities are giving the limit. For this reason, despite the

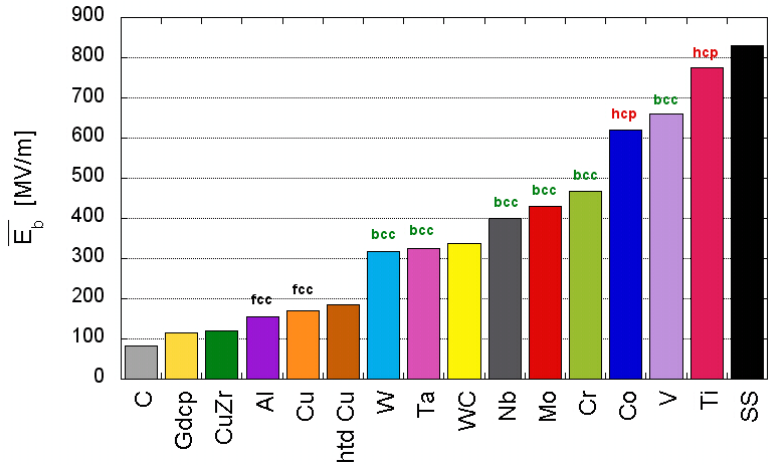

Figure 2.9: Material dependence of the breakdown field E_b measured in the DC Spark system at CERN, taken from [64].

strong influence of the electric field on breakdown phenomena, it is suggested that this magnitude should not be used as the only critical RF constraint in the design of accelerating structures and other quantities are necessary to be considered as predictor of the gradient performance.

2.5.2 Pulsed surface heating and fatigue

Despite the fact that the surface magnetic field is not a relevant magnitude in the field-emission mechanism, it is the responsible of high currents flowing through the metallic walls of the RF structures. Resistive heating of the metallic surface by ohmic dissipation of the RF power is a consequence of its finite electrical conductivity. The cyclic thermal stress degrades the quality of the surface, causing a severe roughening that influences negatively the performance of the structure [65]. Figure 2.10 shows the evidence of accumulated fatigue observed in post-mortem (after the high-power test) at the high magnetic field areas of the RF structure.

For this reason, the **surface temperature rise** ΔT is considered to be a limiting factor of the performance of HG RF structures. A dependence with the fields is found by solving the one-dimensional heat conduction equation for a semi-infinity body [67]:

$$\frac{\partial^2 T(z,t)}{\partial z^2} + \frac{1}{\kappa}\frac{\partial}{\partial z}\left(\frac{dP}{dA}\right) = \frac{1}{\alpha_D}\frac{\partial T(z,t)}{\partial t} \qquad 0 \leq z < \infty \tag{2.14}$$

where T stands for temperature, z represents the normal direction to the metal surface, (dP/dA) is the power density per unit of area absorbed by the conductor,

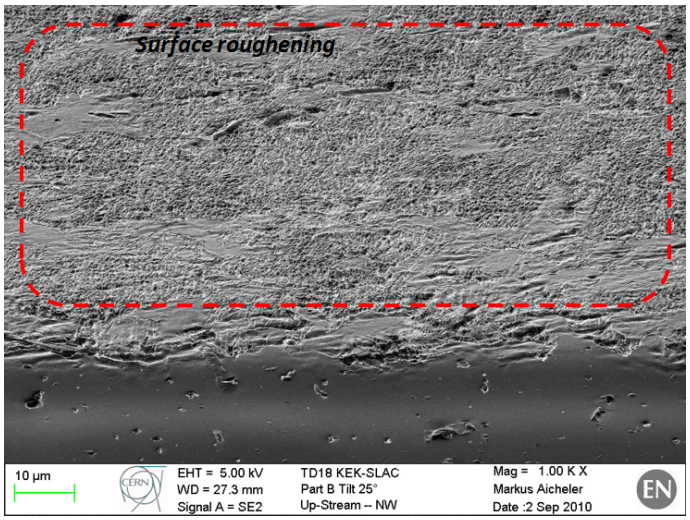

Figure 2.10: Post-mortem observation by SEM on the surface of a CLIC TD18 accelerating prototype tested at KEK, taken from [66]. Roughening by fatigue of the surface is observed at the upper region, produced by the pulse heating of numerous RF cycles.

κ is the thermal conductivity, and α_D represents the thermal diffusivity that can be expressed as:

$$\alpha_D = \frac{\kappa}{\rho c_s} \tag{2.15}$$

where ρ is the material density and c_s is its specific heat.

Since the metallic surface is not a perfect conductor, the electromagnetic fields (E_s and H_s) can penetrate the metal into a certain depth following an exponential decay as $\exp(-z/\delta)$, where δ is known as the **skin depth** and is given by:

$$\delta = \frac{1}{\sqrt{\pi f \mu_0 \sigma}} \tag{2.16}$$

being $\mu_0 = 4\pi \times 10^{-7}$ [H/m] the vacuum permeability and σ the electrical conductivity. Defining $R_s = 1/(\delta\sigma)$ as the surface resistance, the absorbed power density can be evaluated as [68]:

$$\frac{dP}{dA} = \frac{1}{2} R_s H_s^2 \tag{2.17}$$

Equation (2.14) can be solved assuming skin depths much smaller than diffusion length $\delta \ll \sqrt{\alpha_D \Delta t}$, being Δt the length of the arbitrary pulse. On the surface interface, i.e. $z = 0$, the temperature rise results [67]:

$$\Delta T(t) \equiv T(0,t) - T(0,0) \simeq \frac{R_s}{2\rho c_s \sqrt{\pi \alpha_D}} \int_0^t \frac{H_s^2(t')}{\sqrt{t-t'}} dt' \tag{2.18}$$

For the particular case of a flat-rectangular pulse (H_s constant) of length t_p, the maximum temperature rise is given by:

$$\Delta T \simeq \frac{R_s H_s^2 \sqrt{t_p}}{\rho c_s \sqrt{\pi \alpha_D}} \tag{2.19}$$

High-power test results from NLC, JLC/GLC and CLIC indicate that the maximum pulsed surface heating that a structure should accept to operate at reasonable BDR is 56 K [19]. An updated re-baseline of the RF design constraints [69] after pulsed surface heating experiments at SLAC suggested a more restrictive limit of 50 K.

The pulsed surface heating is directly proportional to the **power flow** P and the square root of the pulse length t_p. If the BDR had a dependence on the temperature rise, the following scaling law would be expected for a fixed breakdown probability:

$$P \cdot t_p^{1/2} = \text{constant} \tag{2.20}$$

This relation differs from the scaling $P \cdot t_p^{1/3}$ observed experimentally for copper-made RF structures at a constant BDR, given by Eq. (2.11) and using $P \propto E_{acc}^2$.

2.5.3 Power flow and modified Poynting vector

The high-gradient community aims to search for physically relevant quantities that would predict the maximum gradient a structure is capable to operate stably, since the surface electric field results to be unsatisfactory to explain the experimental results. A limit is proposed in [70] to be the most adequate constraint for the design of a HG TW copper-made structure to ensure a low BDR performance:

$$\frac{P \cdot t_p^{1/3}}{C} < \text{constant} \tag{2.21}$$

where P is the power that flows through the structure, normalized by the minimum circumference C of the structure (iris). The factor $t_p^{1/3}$ is included to fulfill the scaling law of Eq. (2.11) observed experimentally between power (or gradient) and pulse length for a fixed BDR. The scaling of the minimum circumference C compensates the fact that higher peak surface fields are achieved for structures with lower iris aperture and therefore lower input power. From the experimental results of TW prototypes presented in [70], this criterion shows a smaller spread for structures of the same frequency. A limit of 18 and 12 [MW ns$^{1/3}$/mm] is observed for structures operated at 12 and 30 GHz, respectively.

However, the magnitude of Eq. (2.21) can not explain the limits in gradient achieved in SW structures, in which there is no net power flow through the irises. A

new model is proposed in [54] to explain the limiting conditions of the operation of HG RF structures assuming the existence of field emitters generated by microscopic tips on the surface that locally enhances the electric field by a factor β_{FE}. The field emission current, described in Eq. (2.7), heats the tip and may melt it above a certain current threshold, leading to the material evaporation that triggers the breakdown mechanism.

The RF power density is described by the Poynting vector $\vec{S} = \vec{E} \times \vec{H}$. The magnetic field that is induced in the vicinities of the field emitter is proportional to the emitted current $H \propto I_{FE}$. The power flow density that is lost locally by field emission at the tip is:

$$S_{FE} \propto E(t) \cdot I_{FE}(t) \propto (E(t))^3 \exp\left(\frac{6.53 \times 10^9 \phi^{1.5}}{\beta_{FE} E(t)}\right) \tag{2.22}$$

where Eq. (2.7) has been applied.

Due to the non-linearity of the field emission current with the field, a **modified Poynting vector** S_c is defined in [54] as:

$$S_c = \|\mathrm{Re}(\vec{S})\| + g_c \|\mathrm{Im}(\vec{S})\| \tag{2.23}$$

where a coupling factor $g_c = 1/6$ is adopted to take into account the average phase coupling of FE and RF fields. The active power density $\mathrm{Re}(\vec{S})$ corresponds to the net flux of power that traverses the structure in TW mode, and the reactive part $\mathrm{Im}(\vec{S})$ takes into account the cyclic energy transfer between electric and magnetic field. Weighted by the coupling factor g_c, it explains better than the P/C criterion the breakdown limitation in both TW and SW structures.

In addition, results of different types of HG structures seems to present better consistency with an achieved S_c between 2 and 6 [MW/mm^2] for 200 ns pulses, and a smaller statistical spread of $\sqrt{S_c}$ than the peak surface electric field E_s.

Equation (2.23) represents a local field quantity that can be evaluated with electromagnetic field simulations during the cavity geometry design. This allows to study locally the effect of breakdown phenomena in the regions of intense S_c levels, in contrast to the P/C criterion which is an integral parameter. The following scaling law, equivalent to Eq. (2.11), is observed:

$$\mathrm{BDR} \propto S_c^{15} \cdot t_p^5 \tag{2.24}$$

S_c is used as an extra RF constraint for the design of CLIC Main Linac structures [69], limiting it at 5 [MW/mm^2] for an operation with 200 ns pulse length. Other HG structure designs applied for hadron therapy linacs made also use of this quantity [25, 59] for lower RF frequencies (S-band and C-band) and longer pulses. In this case, the modified Poynting vector also shows good predictions of the breakdown performance as in X-band and K-band HG structures.

2.5.4 RF design constraints for CLIC X-band accelerating structures

Several prototypes have been designed to fulfill the CLIC Main Linac requirements of operation at 100 MV/m gradient, with 180 ns flat-top pulse length, and restricting the BDR to be below 3×10^{-7} bpp/m. The RF design is made with simulation tools as ANSYS HFSS (High Frequency Structural Simulator) [71], a 3D electromagnetic finite-element simulator that computes numerically the electric and magnetic fields of any device. The geometry of the cavity cells is optimized to reduce the limiting quantities, presented in this section, that are potentially related to the performance limit by breakdown events. The optimization of the cavity geometry also includes beam dynamics effects (wakefields) and other RF issues like RF-to-beam efficiency.

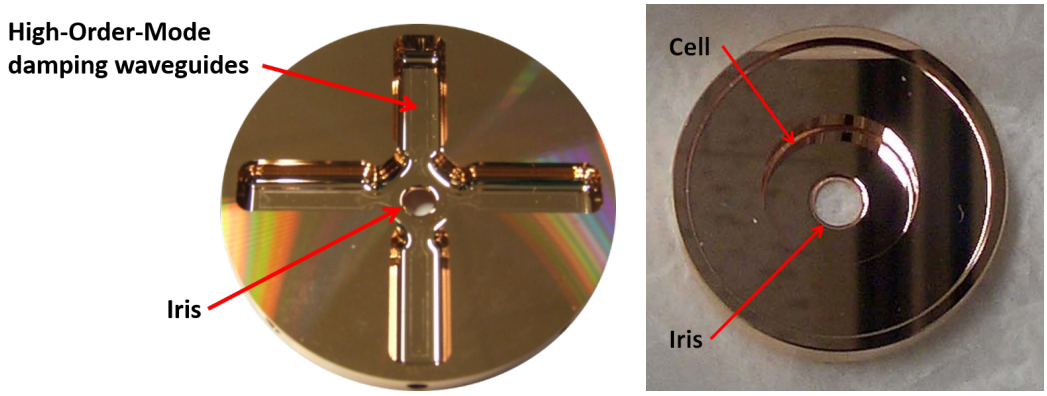

(a) (b)

Figure 2.11: Picture of a single disk sample that conforms a cavity cell of a (a) CLIC-G (damped) and (b) CLIC-G-T24 (undamped) prototype. The iris, cell contour and high-order-mode damping waveguides have been labeled.

The geometry of one cell of a CLIC-G accelerating prototype can be seen in Fig. 2.11(a). The small iris aperture guarantees the low group velocity required to achieve high gradients, and four high-order-mode (HOM) waveguides are included for the suppression of long-range transverse wakefields which are expected from slight misalignments of the CLIC beams. A picture of a one cell disk of a CLIC-G-T24 structure is also shown in Fig. 2.11(b), which does not include the HOM damping waveguides.

As can be observed with HFSS numerical simulations in Fig. 2.12 for the CLIC-G design, the most intense surface electric fields and modified Poynting vector are located at the iris, and the magnetic field, thus the temperature rise, is stronger at the corners of the damping waveguides which delimits the volume of the main

cell. For the undamped version, the surface electric and magnetic fields are also concentrated at the iris and the cell outer boundaries, respectively.

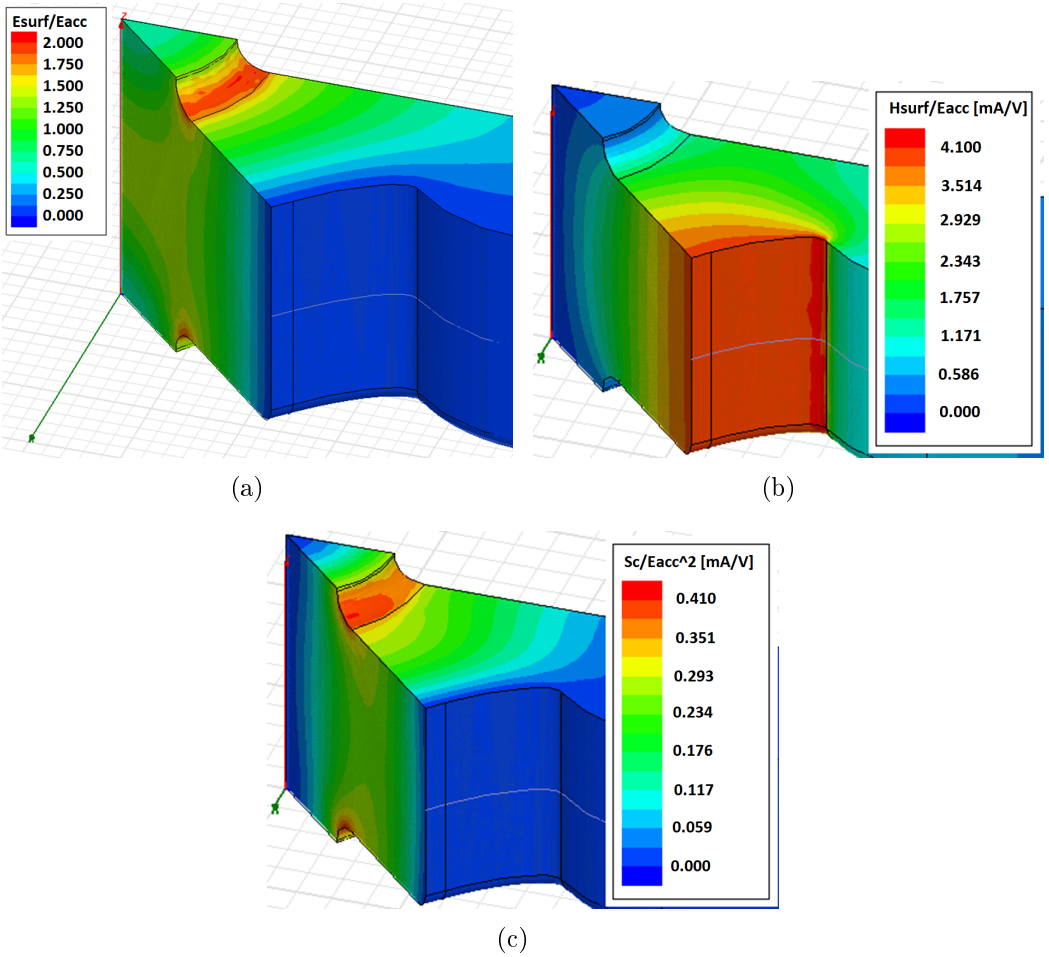

Figure 2.12: Section of the design of a CLIC-G structure with the (a) surface electric fields, (b) surface magnetic fields and (c) modified Poynting vectors, normalized to the accelerating gradient on-axis, simulated by ANSYS HFSS. Taken from [72].

A special effort is being made to design the most efficient geometry of the accelerating structure cells, aiming at minimizing the maximum surface fields when operating at 100 MV/m, as well as the RF power flow to fulfill the P/C criterion. At the same time, high shunt impedances are required for the sake of power efficiency, as the feeding power to build the nominal gradient is optimized. Table 2.1 summarizes the mentioned parameters of different RF designs for CLIC 3 TeV Main Linacs, with the same iris aperture radius of 2.35–3.15 mm, to compare the quantities when operating at nominal average unloaded gradient of 100 MV/m. High-power tests

of undamped structures, such as CLIC-G-T24, generally show better performances than damped ones, such as CLIC-G baseline design. The most notable difference between both designs is the pulsed surface heating. A recent re-baseline of the CLIC-G, called CLIC-G* [73], aims to optimize the production costs of structures made by disks that includes the HOM damping waveguides. The CLIC-G-OPEN design was made to build undamped accelerating structures in two halves, which eases the machining and joining of the pieces and may reduce significantly the fabrication cost.

In the following, a simplified nomenclature of the prototype, without the CLIC-G reference at the beginning, will be used.

Table 2.1: Limiting quantities of CLIC RF designs, at 100 MV/m average unloaded gradient, which are relevant for breakdown activity. The designs correspond to tapered structures with iris aperture radius of 3.15 mm at first cell and 2.35 mm at last cell.

Parameter	**Units**	**CLIC-G** [6]	**CLIC-G*** [73]	**CLIC-G-T24** [74]	**CLIC-G-OPEN** [75]
HOM damping		Yes	Yes	No	No
Input Power	[MW]	43.3	42.5	37.2	44.4
Peak E_s	[MV/m]	190	204	219	267
Peak S_c	[MW/mm^2]	3.9	3.8	3.4	5.3
Maximum ΔT	[K]	22.4	29.7	8.5	23.7

2.6 Conditioning process on high-field surfaces

A fresh structure that has passed through the whole fabrication process of machining, assembly and cleaning is not capable of sustaining the highest fields from the beginning of operation. A process of high-power conditioning is needed so that the structure adapts to high field pulses. Experiments show that after some time of operation the surface presents lower probability to trigger a breakdown at the same field level.

The conditioning strategy consists of gradually increasing the accelerating gradient and the pulse length but keeping a low rate of vacuum arcs in the structure in order to prevent any irreversible damage from breakdowns. An example of a conditioning process performed on a TD26CC structure at CERN [76] is shown in Fig. 2.13. The structure was initially conditioned with a pulse length of 50 ns and the accelerating gradient was slowly increased up to 105 MV/m using an automatic algorithm that keeps the BDR at a fixed value of 7×10^{-5} bpp. Then, the accelerating gradient was backed-off about 10%, the pulse length was incremented 50 ns and the accelerating gradient was increased keeping a BDR target of 2×10^{-5} bpp. When the gradient exceeded 100 MV/m, the process was repeated with a longer

pulse. The active conditioning period was followed by a run with constant input power conditions, 100 MV/m and 250 ns, and the BDR decreased steadily.

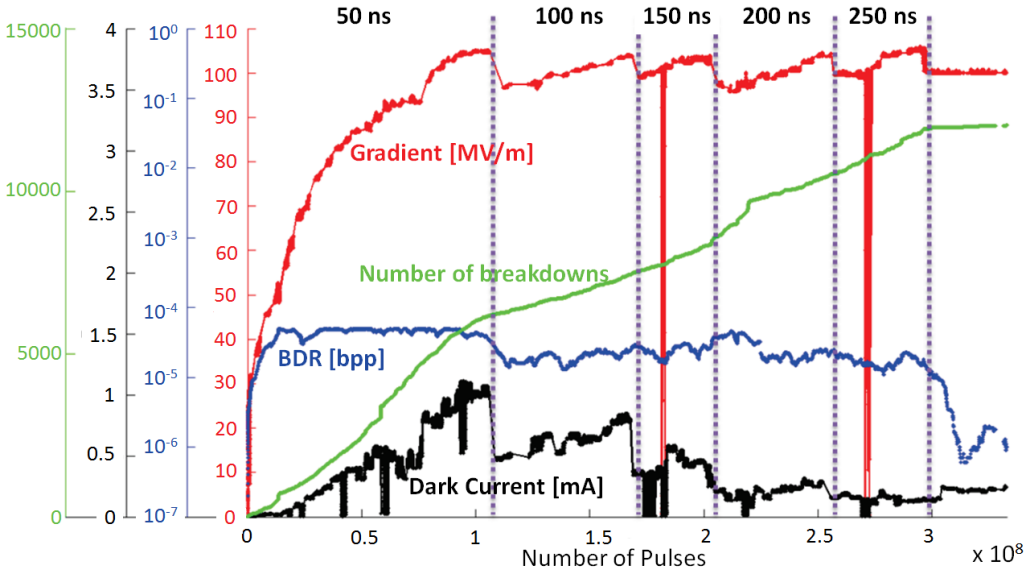

Figure 2.13: Conditioning history of a TD26CC prototype tested at Xbox-1 (CERN), taken from [76]. The plot represents the accelerating gradient (red), BDR (blue), dark current measured at Faraday cups (black) and the cumulative number of breakdowns (green) with respect to the number of triggered pulses, at different pulse lengths indicated on top.

During the initial operation of the structure, vacuum activity is recorded due to a process of out-gassing from the cavity walls. The first breakdowns that take place at low gradients are probably responsible of the removal of surface contaminants such as particles and oxide layers. Higher field emission currents are observed as well at the early stages due to a higher concentration of microscopic emitters and imperfections on the surface that are likely to ignite vacuum arcs. As the structure receives more RF pulses, the distribution of emitters changes dynamically over the surface and enhances considerably its quality, which allows to sustain higher fields.

Vacuum arcs are believed to help positively in blowing micro-protrusions away and reduce the number of potential breakdown sites. However, new insights [77] show that the stresses generated by those RF pulses that do not trigger any breakdown contribute even more to the enhancement of the structure performance. This evidence supports the existence of dislocation by the defect-stress model that dynamically changes the micro-structure of the surface.

Chapter 3

High-gradient test facilities at CERN

The challenge of achieving significantly higher gradients in normal-conducting RF accelerating structures than the current state-of-the-art demands a dedicated study of vacuum breakdown phenomena. In this chapter, we will present the HG test facilities at CERN, as well as the experimental programme to which these are dedicated. We will describe in detail both the RF test stands and the pulsed DC system that are currently running at CERN and their contribution to HG developments.

3.1 The CLIC high-gradient testing programme

The CLIC study aims at accelerating electron and positron beams up to 1.5 TeV in two compact linacs that require gradients of 100 MV/m. The CLIC baseline design considers the acceleration of trains of 312 bunches, with a maximum charge per bunch of 593 pC and a time separation of 0.5 ns, which corresponds to 1.2 A of average current. The total length of a single train of bunches is 156 ns which are accelerated in the Main Linac at a repetition rate of 50 Hz. In order to accelerate the beam with constant gradient, accelerating structures need around 70 ns filling time for the RF pulse to travel the length of the structure and completely fill it with RF fields. The RF pulse that feeds the structure is approximately rectangular-shaped with a flat-top pulse length of 180 ns. Consequently, the goal of CLIC is to design and fabricate accelerating structures that can operate at 100 MV/m and 180 ns pulse length, with the constraint of low BDR performance which has been established to be below 3×10^{-7} bpp/m.

Several generations of prototypes have been designed to meet the CLIC specifications of gradient, pulse length and BDR, as well as power efficiency and wakefield suppression. High-power test results of such prototypes are summarized in Fig. 3.1. The squared dots represent the BDR that was measured at a specific unloaded gradient (tested without beam) and pulse length, after the structure had been con-

ditioned. The choice of gradient and pulse length for measuring BDR was different for each prototype. In order to directly compare the results, these measurements have been scaled to CLIC nominal specifications using Eq. (2.11). The circle dots describe the scaled gradient that the structure would perform at the same BDR as measured using 180 ns flat-top pulses. The cross dots show the expected gradient that the structure would achieve at nominal pulse length and the maximum BDR of 3×10^{-7} bpp/m required for CLIC.

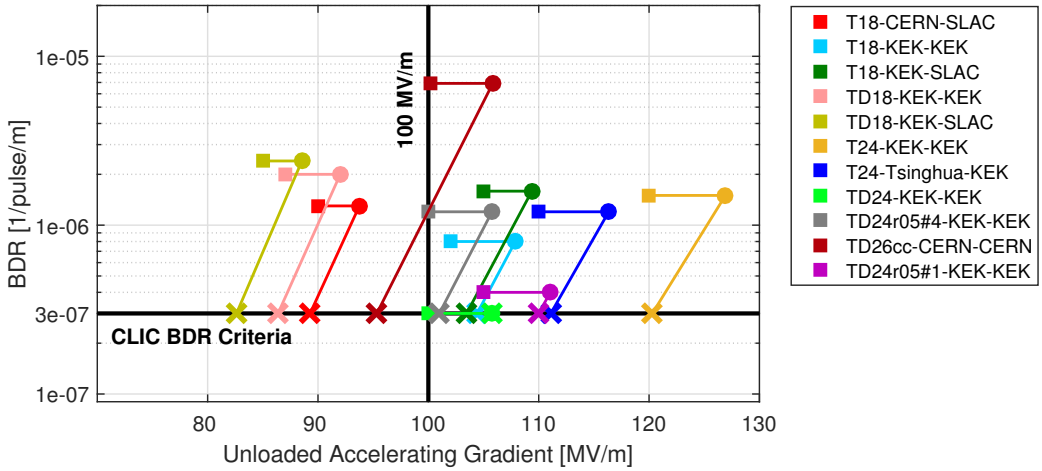

Figure 3.1: Breakdown rate measured against accelerating gradient at a given pulse length (■) for different CLIC prototypes tested at CERN and KEK. Predictions of the expected achievable gradient when scaled to nominal pulse length of 180 ns, using Eq. (2.11), are indicated by (•), and the maximum gradient at CLIC nominal specifications of BDR and pulse length is indicated by (×). The legend uses the nomenclature of the prototype by its nickname design, the institute of fabrication and the institute of high-power testing.

As can be observed, unloaded gradients at CLIC requirements are achieved in the 82-120 MV/m range and a large fraction of prototypes are capable of operating above 100 MV/m. One needs to take into account that the heavy loading of CLIC beam pulses would reduce the average gradient in the structure (see Section 1.1.5), thus unloaded gradients of 120 MV/m would be required for the same input power as the target loaded gradient of 100 MV/m.

The results shown in Fig. 3.1 are part of a major HG testing program to develop CLIC RF structures. The CLIC collaboration also takes advantadge of the existing test facilities based on 11.424 GHz klystrons at SLAC and KEK that were originally constructed for the NLC/GLC project. The Next Linear Collider Test Accelerator (NLCTA) and the Accelerator Structure Test Area (ASTA) at SLAC, and the New X-band Test Facility (NEXTEF) at KEK, have been used to test accelerating structures, PETS and high-power RF components. NEXTEF [78] is

capable of providing up to 90 MW and 300 ns pulses at 50 Hz repetition rate, while NLCTA [51] provided up to 300 MW with typical pulses of 240 ns at 60 Hz repetition rate. In this framework, CERN started the process of building three X-band klystron-based test facilities [79], also called Xboxes, to support the development of HG normal-conducting technology.

The expansion of the X-band high-power infrastructure to test prototypes is valuable in order to advance HG accelerators and better understand the RF breakdown mechanisms. The RF test stands at CERN, which will be described in the following section, are equipped with a high-performance instrumentation for the detection and characterization of breakdown events during the high-power conditioning of a HG RF accelerating structure. Results coming from different tests allow the comparison of different RF designs that are required to fulfill CLIC beam specifications. In addition, various fabrication techniques are tested aiming at an efficient industrialization of the accelerating structures.

The fabrication of these structures is still an expensive procedure due to the very high precision that is required in copper machining (with a roughness of 25 nm), assembly and cleaning. A large and complex RF infrastructure is needed to feed with high-power and test such prototypes. A very long process of RF conditioning requires from 4 to 6 months to complete the test of a single prototype, and constitutes a significant portion of its total cost. For this reason, CERN has also established the development of a more economical facility at the DC Spark laboratory [56]. The Large Electrode System (LES) is a high-repetition rate pulsed DC system that offers the possibility of applying very high surface electric fields, equivalent to those in the CLIC prototypes, between a pair of flat electrodes without the need to fabricate a complete RF structure. Given the existing similarities between RF and DC vacuum arcs, the flexibility of such less-complex system allows complementary breakdown tests [80] to HG RF developments, including surface and material studies. The near equivalence of the high-field and breakdown behavior between RF and pulsed-DC has recently been established and measurements leading to this result are presented in Chapter 4.

The experimental programme

A significant amount of data is produced by the HG facilities, nearly 400 Mbytes per day per structure, and analysed to have a better understanding of the limitations of HG RF structures due to breakdown activity. The examination of the different measurements taken at both RF and DC facilities have led to new insights to design, fabricate and operate these accelerating structures for effective performance. The following measurements are made at the Xbox RF test stands and pulsed DC system and the importance of each field is highlighted:

1. The Xbox test stands evaluate the **accelerating gradient** that is achieved in the structure under test. To do so, the system measures the pulse of RF power that enters into the structure and calculates the corresponding gradient, previously parametrized by a electromagnetic field simulator such as ANSYS HFSS. The shape of the RF pulse is also analysed to determine the **pulse length** and the amount of **RF energy** that is delivered to the structure. Moreover, the system runs under a feedback loop to ensure that the RF power and pulse length are stable during the operation. An equivalent measurement is made at the pulsed DC LES, in which voltage and pulse shape are acquired to determine the surface electric fields at the electrodes.

2. The **measurement of the BDR** gives the overall performance of the HG structure at the Xbox test stand, or the electrodes surface at the DC LES. The way this is measured is that the system runs at constant operation conditions of gradient and pulse length during a certain period of time. Counting the total number of triggered pulses and the number of breakdown events occurred during the reference period, and using Eq. (2.1), one can calculate the BDR to estimate statistically how often breakdowns take place. This is used to evaluate the conditioning state of the structure and, eventually, if its suitability for operation in a linear accelerator at such gradient level.

3. The eventual **detection of breakdowns** during the test operation is currently based on the rise of the reflected power from the structure and the emitted current for RF structures, and the rise of the circuit current between the electrodes of the DC LES. A fast interlock system is implemented in order to inhibit pulsing when a breakdown is detected, hence the acquired signals are read pulse-to-pulse.

4. Measurements of the BDR at different gradients and pulse lengths provide useful **scaling laws** that have been formulated in Eq. (2.11). Scaling laws are used to predict the achievable gradient at the maximum BDR that is specified for the HG linac, as it has already been explained in Fig. 3.1. The scaling laws that have been established so far corresponds to RF and DC rectangular-shaped pulses. Other interesting studies are related to the BDR dependence on the pulse shape, in order to observe possible variations of the breakdown probability for non-uniform pulses.

5. The signals acquired at the Xbox test stands are analysed for the **location of breakdowns** in the RF structure. Analysis techniques, based on timing differences of the RF and dark current signals when the vacuum arc is initiated, are used for the longitudinal positioning of the arc source within the structure. Other instruments, such as accelerometer sensors or optical cameras, are under

study to be used as an alternative technique of breakdown localization at the RF and DC facilities. This measurement allows to determine how breakdowns are spatially distributed along the multiple cells of the structure or over the surface of the electrodes. The observation of a 'hot spot', where most of the breakdowns are initiated, would mean that the BDR is dominated by such a small region and, consequently, would be an evidence of a bad performance of the structure. The spatial distribution of breakdowns can be correlated after the test with a visual inspection of the surface under the microscope by looking at the 'craters', 10 μm-sized features formed by the vacuum arcs.

6. **Field emission** studies can be made both in RF and DC facilities by acquiring the signals of dark current that are detected from surface field emitters. Measurements of field emitted current at different gradients and surface fields are made in order to verify the Fowler-Nordheim theory (see Section 2.2) and evaluate the field enhancement factor β_{FE} of the surface emitters using Eq. (2.8). The intensity of the dark current is observed to decrease while conditioning and further analysis of FE measurements is required to better understand the dynamic mechanism of interaction between the fields and the emitters.

7. The RF and DC facilities record the pulse-by-pulse history of the accelerating gradient or surface field, the pulse length and the accumulated number of detected breakdowns during the full test. The achievable gradient becomes higher at a fixed pulse length and BDR as the structure conditions. The comparative analysis of the **conditioning histories** obtained from the test of different RF prototypes or DC electrodes provides new insights in the understanding of the conditioning mechanism. Different strategies of test operation on identically produced structures could lead to find the most effective way to condition the HG RF structures in the future.

8. The detection of a large number of breakdown events is used to evaluate the number of pulses that the RF structure or the electrodes can sustain without arcing. A **distribution of breakdown occurrences** is analysed by counting the number of pulses that have been triggered between two consecutive breakdowns. With a proper statistical analysis, we can figure out the mechanism of arcs that have been excited by other occurrences.

We will present in Chapter 4 some of the analysis techniques and experimental results obtained for the research of this thesis. This work has been focused on the longitudinal localization of breakdowns in RF structures, the statistical distribution of occurrences in time, the analysis of RF and DC conditioning histories and the BDR dependence on different pulse shapes.

3.2 X-band klystron-based test facilities at CERN

CERN proceeded with the construction of three X-band klystron-based test stands at CERN, operating at RF frequency of 11.994 GHz, to support the development of HG accelerating structures in the 100 MV/m range. The infrastructure also serves as high power source, up to 140 MW, to test RF components needed for the CLIC project such as waveguides and loads. Furthermore, the Xbox test stands constitute a prototype of the power source for a linac unit, including low and high-level RF components, which could become an alternative scheme for a klystron-powered first stage of the CLIC Main Linacs.

The three test stands are named as Xbox-1, Xbox-2 and Xbox-3, in order of construction. A detailed description of the design, components and operation of the Xbox test stands can be found in [81]. A summary of the structures tested so far at the Xbox test stands and their final performance is collected in Table 3.1.

Table 3.1: Final performance of the HG structures tested at Xbox-1 and Xbox-2, at CERN. *For the CRAB cavity, the surface electric field is represented.

Test stand	**Structure**	**Gradient** [MV/m]	**Pulse length** [ns]	**BDR** [bpp]	
Xbox-1	TD24R05	94	200	2×10^{-5}	Developed a hot cell
	TD26CC	100	250	1.5×10^{-6}	
	T24	80	190	2×10^{-6}	Developed a hot cell
Xbox-2	CRAB	154*	200	3×10^{-6}	
	T24-OPEN	90	200	1×10^{-5}	

3.2.1 Xbox-1

The first generation of the Xbox test facility is located in the klystron gallery of CTF3 [79]. The Xbox-1 (see picture in Fig. 3.2) was designed to be a standalone complement to the Two-Beam Test Stand (TBTS), also at CTF3, which needs the generation of a high-current Drive Beam to generate the 12 GHz power and works only at a maximum repetion rate of 1 Hz.

The Xbox-1 performed tests of two CLIC HG prototypes in 2013, a TD24R05 and a TD26CC, and the operation procedure is reported in [81, 82]. The test of the TD24R05 structure [83] was stopped during the conditioning process after the discovery of a *hot cell*, i.e. when the majority of breakdown events are coming from a single cell which degrades the overall BDR performance of the structure. The structure was removed for a post-mortem observation of the damage [84] and was replaced by the TD26CC prototype. This structure successfully completed the

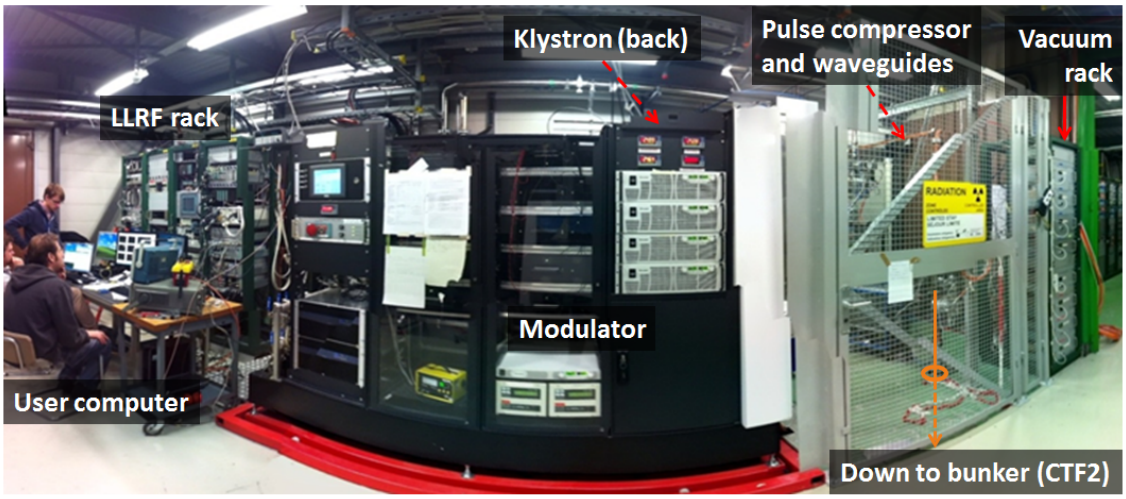

Figure 3.2: Picture of the high-power RF source of the Xbox-1 test stand at the klystron gallery of CTF3. On the left, the low-level RF, control and acquisition systems and the operators. On the center, the Scandinova modulator which hosts a CPI klystron. And on the right, the vacuum controllers and the waveguide network to transport the RF to the bunker.

conditioning process during 4 months [76] in stages of pulse lengths from 50 to 250 ns that were increased in steps of 50 ns (see Fig. 2.13). The TD26CC achieved a maximum gradient of 105 MV/m with 250 ns pulses and a resulting BDR of 8×10^{-5} bpp/m.

Since Xbox-1 is integrated in the CTF3 network, this opens the possibility of testing HG structures with beam. In 2014, the Xbox-1 waveguide network was diverted to the CTF3 dog-leg beam line in order to perform breakdown probability measurements under beam-loading conditions. The experiment started with the test of a T24 prototype, however it also developed a hot cell at the front, most likely due to beam losses caused by a misaligned collimator. The structure was replaced in 2015 by the TD26CC that was already tested by Xbox-1 in CTF2. The setup and results of the beam-loading experiment will be described in more detail in Chapter 5.

RF and controls systems

Figure 3.3 shows the schematic layout of the Xbox-1 test stand and its main subsystems. A detailed diagram of the RF generation, the data acquisition system and the instrumentation for breakdown diagnostics in the RF structure have been included in the figure.

The Xbox-1 makes use of a CPI X-band klystron powered by a Scandinova solid-state modulator, which delivers rectangular pulses of up to 50 MW and 1.5 μs. In

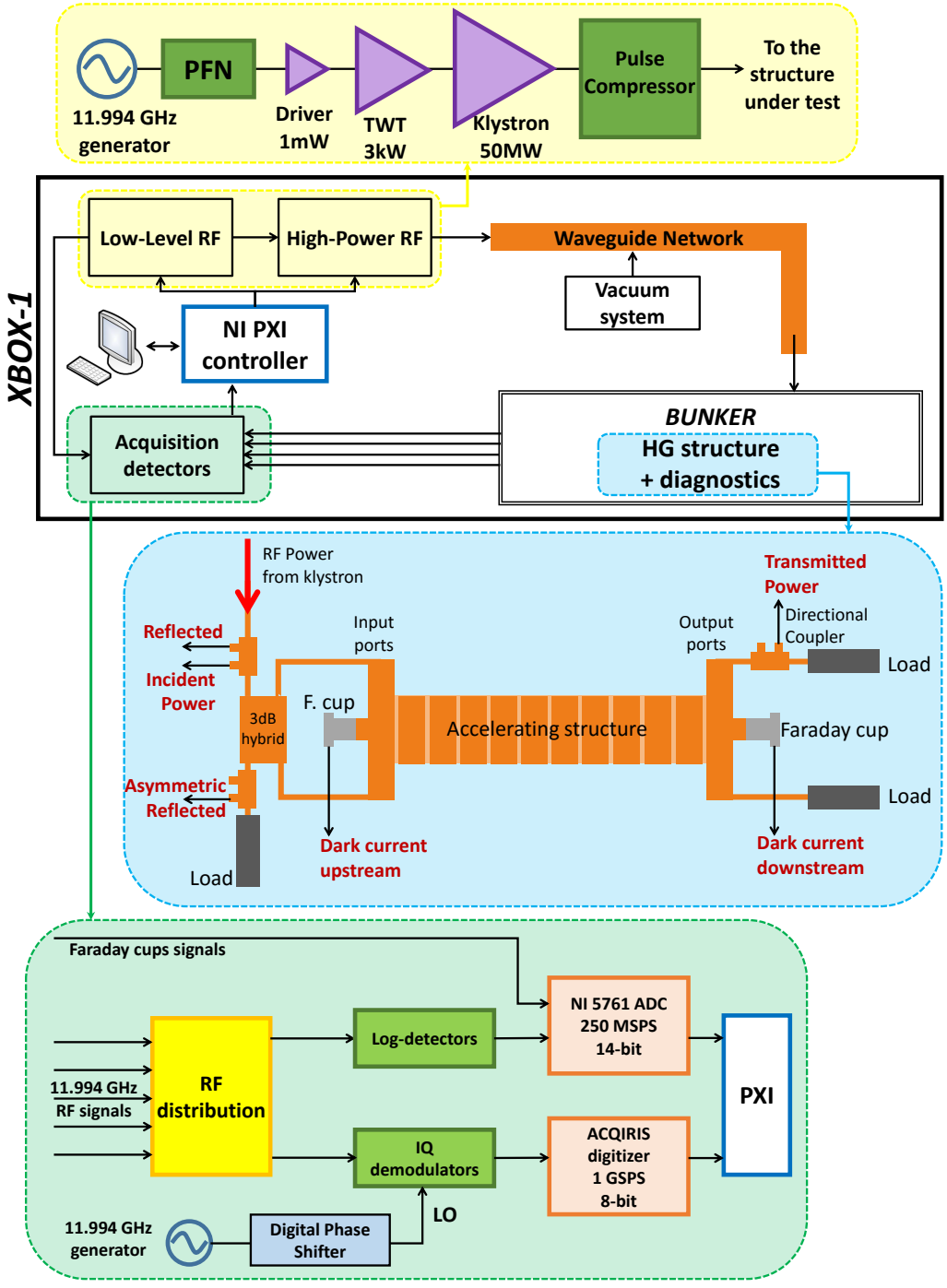

Figure 3.3: Diagram of the Xbox-1 layout and schematic description of the low-level and high-power RF (yellow box), diagnostics (blue box) and acquisition (green box) subsystems.

order to achieve higher peak power, a SLED-I type pulse compressor is installed after the klystron which can form compressed pulses up to 140 MW and 250 ns. The SLED-I pulse compressor [85] stores the RF energy in two high-Q cavities, via a 3 dB-hybrid, and releases it when a phase flip of 180 degrees is applied to the input RF. The RF high-power is delivered through WR-90 rectangular waveguides under vacuum to the device under test, which is hosted at the CTF2 bunker, at the ground floor below the Xbox-1 enclosure.

Regarding the low-level RF system, the reference 11.994 GHz RF signal is generated by the CTF3 master oscillator and is synchronized with the RF system of the CTF3 Drive Beam. A Pulse Forming Network (PFN) generates the waveform with the desired amplitude and phase profile. The PFN consists of a digital phase shifter, to control remotely the reference phase of the pulse, followed by a fast analogue phase shifter which is tuned with a 96 Msamples/s voltage signal in order to produce the phase flip and profile required for the output modulation of the pulse compressor. The RF pulse is then sent to a low-level amplifier, with a remotely tunable output power, and amplified in an Applied Systems Engineering Travelling Wave Tube (TWT) up to 3 kW of power to the klystron.

A National Instruments (NI) PXI controller equipped with FPGA-based digitizers performs the data acquisition of the RF signals and other diagnostics, as well as the detection and data storage of breakdown events in the structure using the acquired signals. The operation of the test stand is controlled and interfaced by a NI LabVIEW programmed software, which allows the user to control the power level, modulate the phase waveform and automatize the conditioning of the structure [81].

Diagnostics and data acquisition

The structure tested in Xbox-1 is equipped by a diagnostics setup that allows the detection and localization of breakdowns. A layout of the experimental setup installed around the TD26CC structure in CTF2 can be seen in Fig. 3.3 (blue box). The RF power of the incident to (INC), reflected from (REF) and transmitted after (TRA) the structure are sampled via 50 dB high-power bi-directional couplers which are part of the waveguide network. The signals are then transmitted to the electronics crate using N-type coaxial cables. Other high-power signals are also extracted with directional couplers to monitor the power delivered to the structure, such as the klystron output power and the reflection from and transmission after the pulse compressor.

Faraday cups upstream and downstream the structure are connected to the structure beampipe to measure dark current signals produced by field-emission and current bursts produced by breakdowns. They also serve as an interlock detector of breakdowns since they can collect the surge of current that is emitted from the arc discharge. The signals (DC-Up and DC-Down) are terminated in 50 Ω and sent to

the electronics crate via 50 Ω coaxial cables.

Figure 3.3 (green box) also shows the diagram of the data acquisition system used at the electronics crate of Xbox-1. The INC, REF and TRA signals are split and sent to logarithmic detectors and IQ demodulators. The log-detectors read the signals in a wide dynamic range so that small differences at lower power levels are easily detected. These are later digitized with NI-5761 ADCs (14-bits, 250 Msamples/s) installed on the PXI crate to be acquired and used as feedback of the power operation of the system. The IQ demodulators down-mix the RF signals to the base-band, using the original 11.994 GHz generator as local oscillator and a digital phase shifter to vary the phase comparator. The RF signal is demodulated in two DC signals, I and Q, that contains information of its amplitude and phase, and they are digitized by ACQUIRIS cards (8-bits, 1 Gsamples/s) that are later sent to the PXI crate. The dark current signals coming from the Faraday cups are also acquired via NI-5761 ADCs integrated in the PXI.

Data is collected and processed by the PXI controller for every pulse, and interlocks the system upon detection of anomalies in the RF reflected and dark current signals, which would be an indication of a breakdown. All signals of each breakdown event and the two previous normal pulses are stored in the hard disk of the PXI. Regular pulses are also stored every minute when no breakdown has been detected. In addition, the history of delivered power to the structure, vacuum levels of the network and other temperature measurements of waveguides are averaged and logged every second. A TDMS-format file is built every 8 hours with all mentioned data for post-processing analysis.

Signal processing

The calibration of the detectors employed to acquire the RF signals is made at the beginning of each test and at various moments during the test. Xbox-1 makes use of logarithmic detectors and IQ demodulators to have a suitable measurement of power amplitude and phase:

1. *Logarithmic detectors.* The voltage signal response $V_{log}(t)$ of the log-detectors is calibrated to determine the actual RF power $P_{RF}(t)$ following an exponential function:

$$P_{RF}(t) = A_{att} \exp\left((V_{log}(t) + V_{offset}) \cdot B_{scale}\right) \tag{3.1}$$

where V_{offset} and B_{scale} are the calibration factors of the detector and A_{att} is an extra calibrated attenuation of the RF network that can be adjusted to the desired power range. The calibration factors V_{offset} and B_{scale} have been obtained by injecting a 12 GHz signal at different power levels and measuring the output voltage from the log-detectors (see calibration curve in Fig. 3.4(a)). An example of the signal calibration of the incident pulse to the structure in

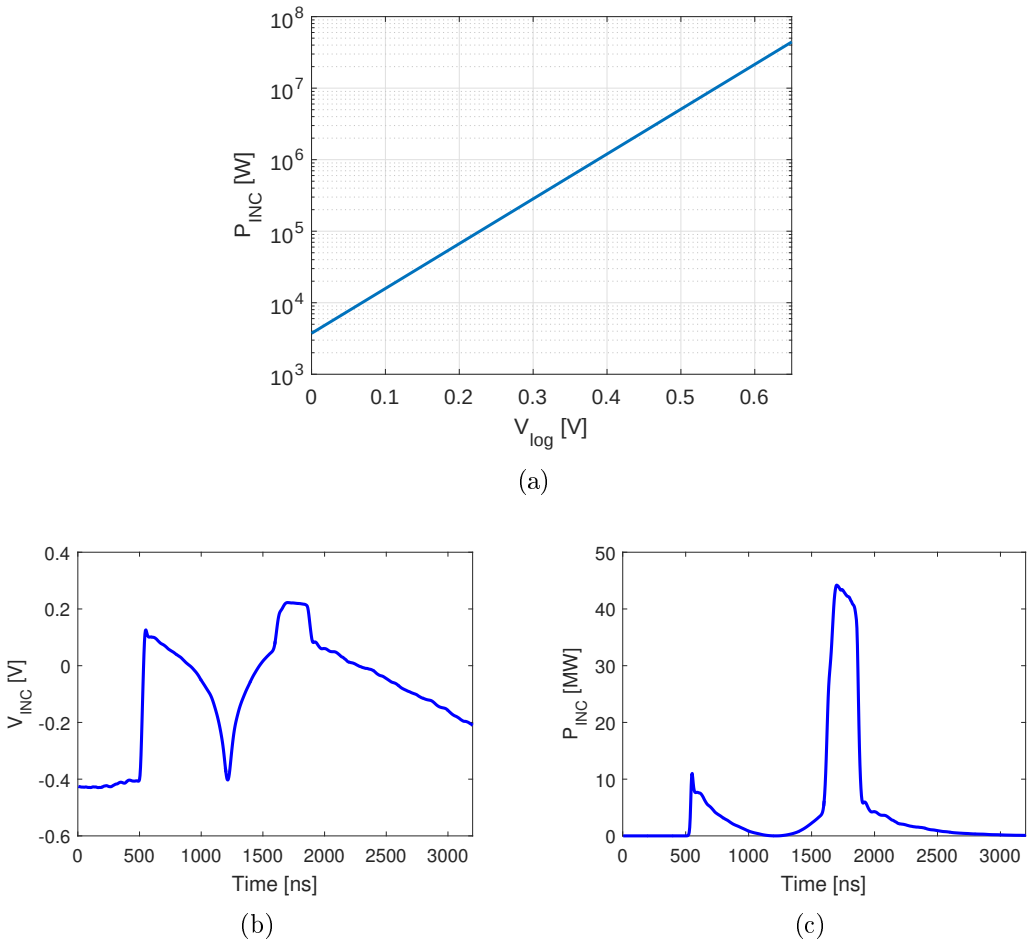

Figure 3.4: Calibration of the incident power channel of the logarithmic detector in Xbox-1: (a) calibration curve for conversion from detector voltage to calibrated power, using the calibration factors $V_{offset} = 0.5381$, $B_{scale} = 14.43$ and $A_{att} = 1.585$, and example of an RF pulse to the TD26CC structure represented by (b) the raw signal and (c) the calibrated power signal.

Xbox-1 is shown in Figs. 3.4(b) and 3.4(c). The detector is more sensitive to the low-power variations as can be seen during the filling of the pulse compressor cavities.

2. *IQ demodulators.* The RF signal $\sqrt{P_{RF}(t)}\cos(\omega t + \phi(t))$ is down-mixed with two 12 GHz local oscillators that differ by 90 degrees phase, and two DC

signals are obtained:

$$I(t) \equiv a\sqrt{P_{RF}(t)}\cos\left(\phi(t)\right) \tag{3.2}$$
$$Q(t) \equiv a\sqrt{P_{RF}(t)}\sin\left(\phi(t)\right) \tag{3.3}$$

where a is the sensitivity factor to be calibrated between the I-Q signals and the amplitude. The power and phase signals can be extracted solving the system of equations:

$$P_{RF} = \frac{1}{a^2}(I^2 + Q^2) \tag{3.4}$$
$$\phi = \arctan\left(\frac{Q}{I}\right) \tag{3.5}$$

Since a realistic demodulator device may include a different error between the acquired I and Q signals, we assume the following response:

$$I' \equiv a\sqrt{P_{RF}}\left(\alpha\cos\left(\phi\right) + \beta_I\right) \tag{3.6}$$
$$Q' \equiv a\sqrt{P_{RF}}\left(\sin\left(\phi + \psi\right) + \beta_Q\right) \tag{3.7}$$

where $\beta_{I,Q}$ are the offset of each signal, α is the amplitude error and ψ is the phase error between the two signals. These factors are calibrated by making a sweep in phase with the input RF signal at a fixed amplitude and measuring the

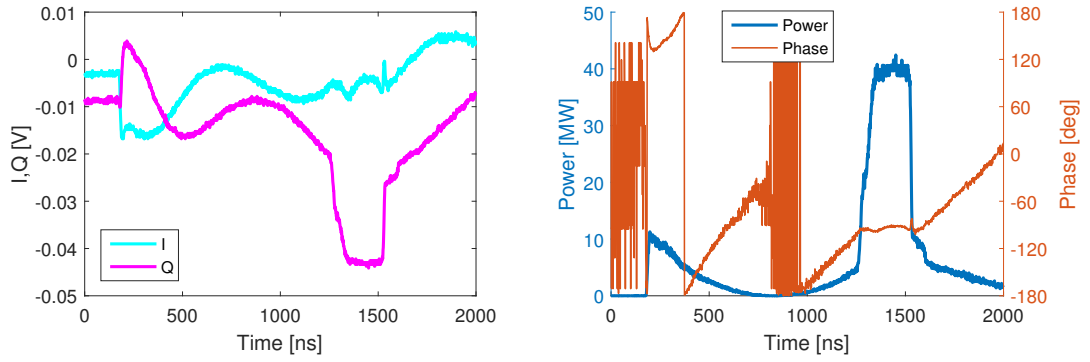

(a) (b)

Figure 3.5: Incident power signal to the TD26CC structure in Xbox-1 represented by (a) the raw I and Q signals and (b) the calibrated power and phase, using the calibration factors $a^2 = 2.93 \times 10^{-11}$ V/W, $\alpha = 0.978$, $\psi = 3.026$ deg, $\beta_I = -3.823$ V and $\beta_Q = -8.780$ V.

output I' and Q', which needs to be corrected using an inverse transformation [86]:

$$\begin{pmatrix} I \\ Q \end{pmatrix} = \begin{pmatrix} 1/\alpha & 0 \\ -\tan(\psi)/\alpha & 1/\cos(\psi) \end{pmatrix} \begin{pmatrix} I' - \beta_I \\ Q' - \beta_Q \end{pmatrix} \tag{3.8}$$

Figure 3.5 shows the calibrated incident power and phase to the TD26CC structure in Xbox-1 from the raw data of the employed IQ demodulators. The phase signal has a worse signal-to-noise ratio when the RF power is very small. A stable phase profile is observed during the compressed pulse given by the output of the pulse compressor in order to flatten the RF power amplitude.

3.2.2 Xbox-2

The Xbox-2 standalone test stand was built and commissioned in 2014 to expand the testing capabilities of CLIC HG prototypes. The new system has fully independent control of the low and high-level components. The autonomy of the electricity and water-cooling systems allows it to avoid the annual CTF3 shutdowns and maximize the up-time of operation of the test stand. Figure 3.6 shows a picture of the Xbox-2 environment at CERN building 150 where the low-level RF system, the klystron and modulator units and the bunker are integrated.

The commissioning of Xbox-2 was completed with the high-power test, from October 2014 to June 2015, of a CLIC Crab cavity [81,87], a deflecting-mode structure that is designed to apply a 2.55 MV transverse kick to the beam in the final stage of

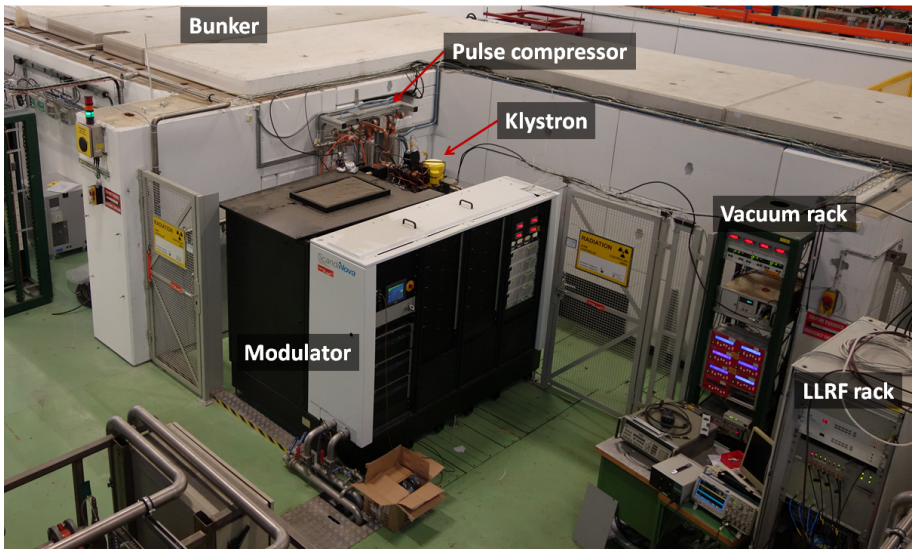

Figure 3.6: Picture of the high-power RF source and bunker site of the Xbox-2 test stand at CERN building 150.

the collider. The nominal power of 13.4 MW with 200 ns pulse length for the operation of this cavity was achieved resulting in an acceptable BDR of 2×10^{-6} bpp, and was later processed up to 51 MW 100 ns-long pulses and a BDR of 3×10^{-5} bpp. The Xbox-2 is currently operating from September 2015 the high-power test of a T24-OPEN structure, designed at CERN and built at SLAC from the machining and brazing of two halves.

RF and controls systems

As in Xbox-1, the Xbox-2 uses a CPI X-band klystron and a Scandinova solid-state modulator that generates high-power RF pulses up to 50 MW and 1.5 μs, at a repetition rate of 50 Hz. A compact SLED-I type pulse compressor, designed and built at CERN, is used to provide 3 times higher peak power in shorter pulses of 250 ns.

A schematic layout of the full Xbox-2 facility can be seen in Fig. 3.7, including a detailed description of the low-level and high-power RF components, the instrumentation for breakdown diagnostics and the data acquisition system. A new design of the low-level RF system is used based on the experience acquired during the operation of Xbox-1. The RF generation, trigger of components and data acquisition is managed by a NI PXI controller. A 2.4 GHz oscillator generated at the PXI is vector-modulated with a user-defined amplitude and phase profile, and is later up-mixed with a 9.6 GHz local oscillator generated from the frequency multiplication of the previous 2.4 GHz oscillator. After the up-mixing stage, a 12 GHz modulated pulse is obtained and sent to an Applied Systems Engineering TWT, which amplifies the signal up to 3 kW to drive the 50 MW klystron. The PXI controller distributes the trigger of the high-power components to be synchronized with the low-level RF generation and the data acquisition system. A new LabVIEW interface, based on the existing one in Xbox-1, has been programmed to control the power level and phase profile that is sent to the structure under test and monitor the acquired signals of the network.

Diagnostics and data acquisition

The experimental setup for breakdown diagnostics is slightly different than the previously described setup for Xbox-1. A layout of the diagnostics used for the T24-OPEN structure at the Xbox-2 bunker is shown in Fig. 3.7 (blue box), which was an upgrade of the existing instrumentation that was used for breakdown measurements during the test of the CLIC Crab cavity [81].

Directional couplers installed before and after the prototype are used to extract the RF signals of the incident (INC) to, reflected (REF) from and transmitted (TRA) through the structure. Killer Bee SMA cables were chosen to deliver the signal to the

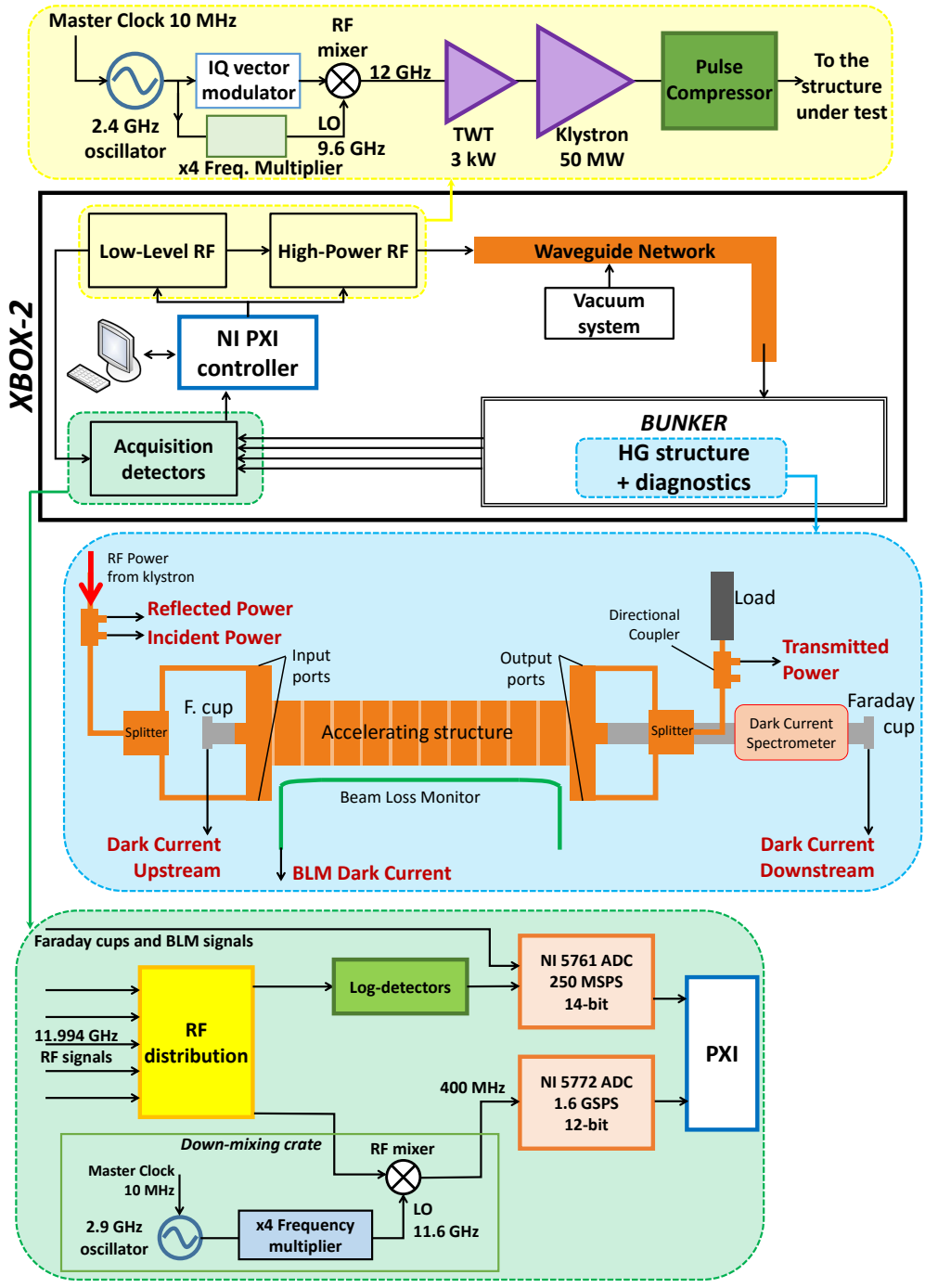

Figure 3.7: Diagram of the Xbox-2 layout and schematic description of the low-level and high-power RF (yellow box), diagnostics (blue box) and acquisition (green box) subsystems.

acquisition electronics due to their high stability. More directional couplers are used after the klystron and the pulse compressor to monitor their performance in power delivery. Faraday cups are also connected upstream and downstream the structure to make field-emission measurements and detect breakdown current bursts. The dark current signals are terminated and sent to the acquisition panel via 50 Ω coaxial cables. A Beam Loss Monitor (BLM) optic fiber [88] is installed and extended in parallel to the structure in order to detect, by Cherenkov radiation, the emission of electrons. This fiber provides an alternative measurement of field-emission and breakdown current. In addition, a spectrometer was installed downstream the structure, consisting of a dipole magnet, a collimator and a screen. The spectrometer is used for the imaging, in position and energy, of the emitted dark current during breakdown events [89].

The signals are acquired in the electronics crate as shown in Fig. 3.7 (green box). An RF distributor panel splits the signals to the logarithmic detectors, as in Xbox-1, and down-mixing crates for reading amplitude and phase. On one side, the log-detector signals are digitized with NI-5761 ADCs (14-bits, 250 Msamples/s) at the PXI crate. They also provide an interlock output signal that is sent to the PXI to stop the system when reflections are higher than a certain threshold. On the other side, the signals are down-mixed to 400 MHz using a 11.6 GHz local oscillator triggered in synchronicity by the same master clock than the 12 GHz generation crate. The down-mixed signals are digitized in NI-5772 ADCs (12-bits, 1.6 Gsamples/s) integrated in the PXI controller to convert them via software demodulation in amplitude and phase. Extra channels of the NI-5761 ADCs are used to acquire the dark current signals from the Faraday cups and the BLM.

As in Xbox-1, data is stored in a TDMS-format file per day at the hard disk of the PXI, with the signals from all breakdown events and the ones from regular pulses every minute if no breakdown is detected. At the same time, the delivered power, maximum dark current, vacuum levels and waveguide temperature measurements are recorded every second.

3.2.3 Xbox-3

Xbox-3 is a novel cost-effective solution for a multi-structure test stand that provides up to four testing slots for HG components [81,90,91]. An schematic diagram of the facility is shown in Fig. 3.8, in which the RF systems have been described.

The facility, located in the same building and enclosure as Xbox-2, makes use of four Toshiba X-band klystrons powered by four solid-state Scandinova modulators. Each unit provides RF power up to 7 MW with 3 μs-long pulses, running at a maximum repetition rate of 400 Hz. The power combination in pairs of these four units, together with CERN-made SLED-I pulse compressors, as outlined in Fig. 3.8, allows

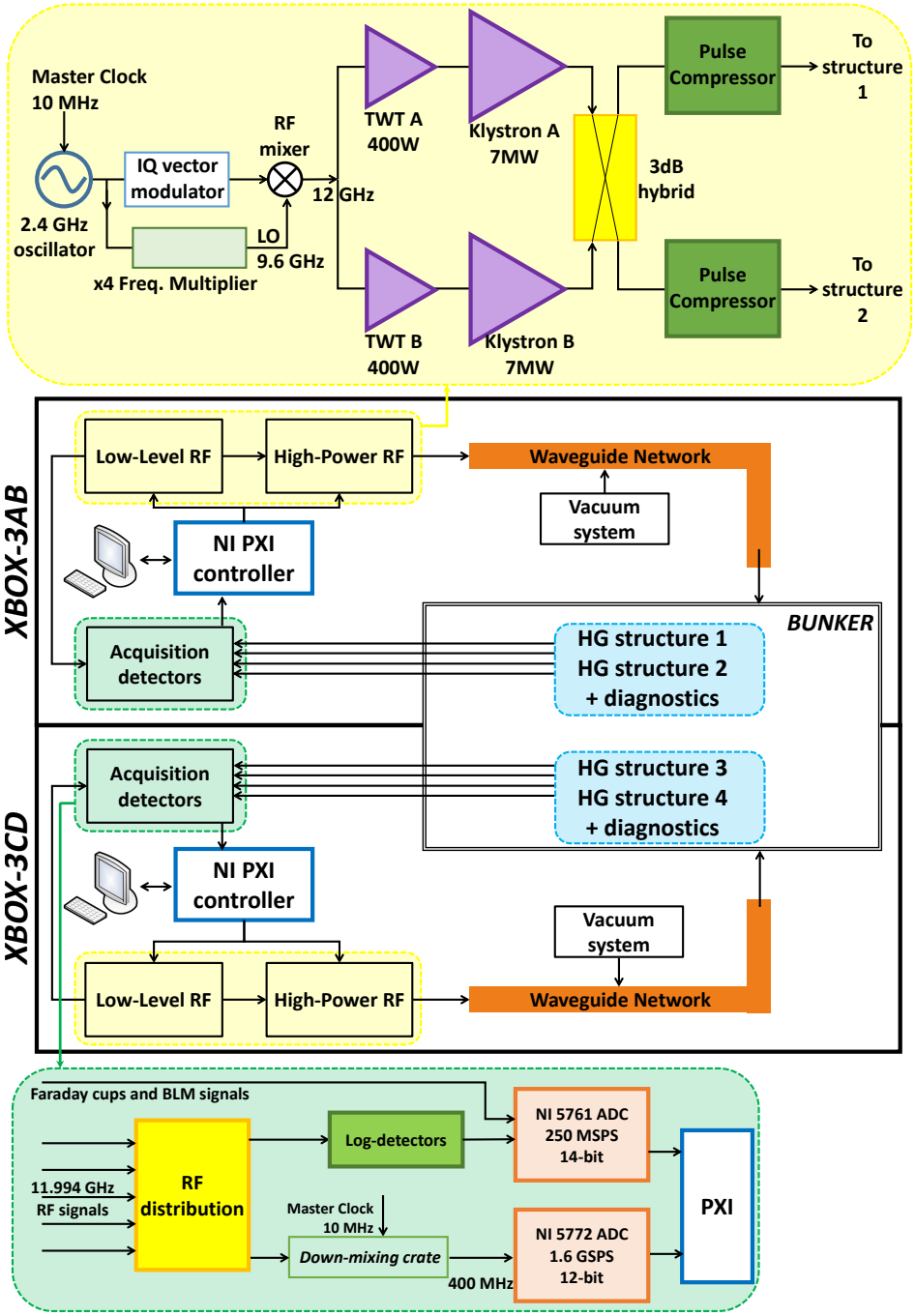

Figure 3.8: Diagram of the Xbox-3 layout and schematic description of the low-level RF and high-power RF combination (yellow box) of the Xbox-3AB subsystem, identical for Xbox-3CD, and the data acquisition system (green box).

a maximum power of 56 MW with 250 ns-long pulses for each device under test. A 3 dB hybrid is used for the power combination and alternating distribution to each branch. The distribution is controlled by the low-level RF system by changing the phase difference between the two klystrons by 90 and 270 degrees. The 12 GHz pulse generation is based on the Xbox-2 up-mixing design and split to the four subsystems. The control of the low-level RF system and the data acquisition will be carried out by a National Instruments PXI controller fully equipped with RF generator and FPGA-based digitizers, which will allow the pulse waveform configuration that is sent to each branch of the network. The data acquisition system is a replica of the existing one in Xbox-2, duplicated for subsystems AB and CD, and adapted by the PXI controller to alternate the acquisition of the signals for each structure.

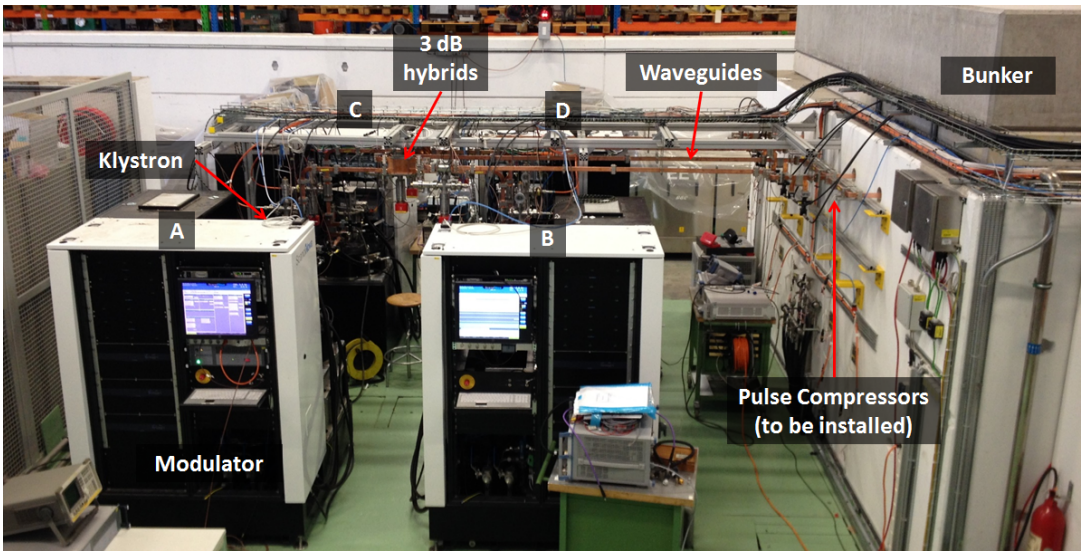

Figure 3.9: Picture of the high-power RF source and bunker site of the Xbox-3 test stand at CERN building 150.

The Xbox-3 has been under commissioning since August 2016. The first priority is to test the network and software by sending power to water-cooled RF loads installed in the bunker, which is shared with Xbox-2. A picture of the current status of Xbox-3 is shown in Fig. 3.9.

The Xbox-3 design results in an important improvement in the testing capabilities of HG structures at CERN since it will carry through the test of four times more structures than Xbox-1 or Xbox-2. Moreover, the fact that these klystron units are able to run at high repetition rate increases by a factor 8 the speed of testing structures. Typically, HG structures need around 4-6 months to be conditioned and fully tested in 50 Hz repetition rate systems as Xbox-1, Xbox-2 and NEXTEF (KEK, Japan). Xbox-3 may reduce the testing time efficiently to less than two months

with an effective repetition rate of 200 Hz per structure. This infrastructure is also beneficial concerning the industrialization of CLIC Main Linac structures, since it would reduce the time spent during the conditioning process, which implies an extra cost for the structure fabrication.

3.3 The DC Large Electrode System at CERN

A very complex infrastructure is required to test the breakdown performance of HG RF prototypes, which are fabricated following an expensive process of ultra-precision machining, cleaning and assembly. The Large Electrode System (LES) is a simpler and more economical setup, hosted at the DC Spark laboratory, which is dedicated to the study of DC breakdowns and is complementary to the RF high-power test results.

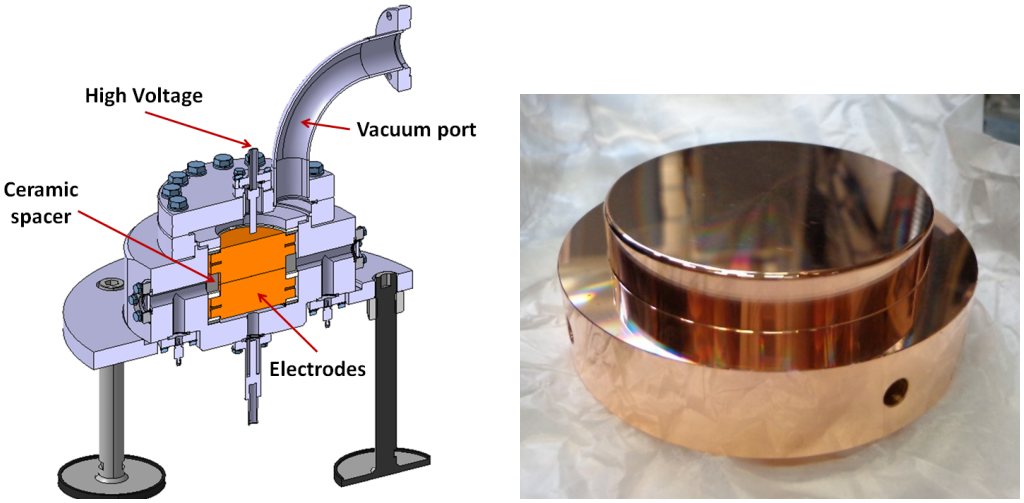

(a) (b)

Figure 3.10: (a) Drawing of the cross-section of all the components that constitute the LES, and (b) picture of one copper electrode machined with ultra-precision diamond tools.

A drawing of the cross-section of the LES can be found in Fig. 3.10(a). The design of the system [56] consists of two copper-made, circular electrodes of 60 mm diameter (see picture in Fig. 3.10(b)) which are held by a ring-shaped ceramic spacer. This spacer ensures the parallelism between both electrodes with high precision at a known gap size to get a uniform electric field from the voltage along the entire surface. Three different ceramic spacers were designed to fix a gap distance d of 20, 40 and 60 μm. When a high-voltage pulse V is applied to the cathode, the surface

electric field in the gap is:

$$E_s = \frac{V}{d} \tag{3.9}$$

For a gap distance of $d = 20$ μm, a voltage of 4 kV is required to obtain 200 MV/m surface fields, as typically achieved in CLIC HG structures. A primary vacuum pump group is connected to the vacuum port to maintain a pressure below 10^{-8} mbar during the high-field operation and to recover the vacuum after breakdown events.

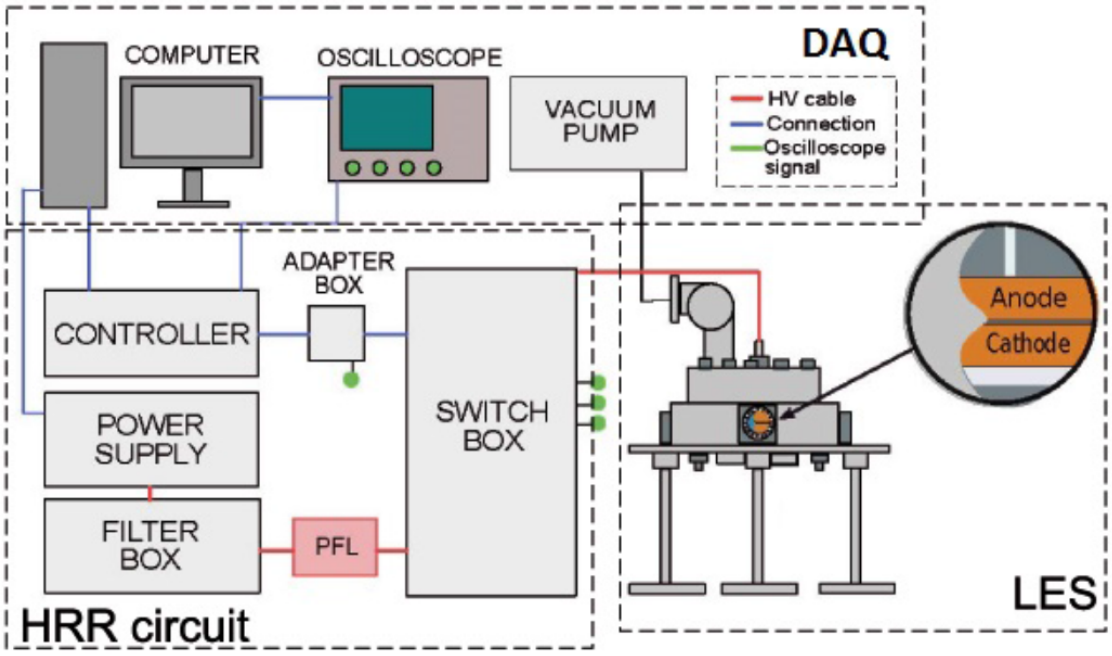

Figure 3.11: Scheme of the high-repetition rate circuit integrated in the Large Electrode System. Taken from [80].

The system is operated by a high-repetition rate (HRR) pulse forming circuit [56] and a schematic is shown in Fig. 3.11. A FuG power supply [92] provides up to 12 kV voltage to the circuit. A Pulse Forming Line (PFL), which consists of a 200 m-long capacitive cable and a low-pass filter, stores up to 1.5 J of energy to be released to the LES. The PFL guarantees the reflection-free discharge of the stored energy after a vacuum arc goes to zero impedance in the LES in order to protect the power supply. A solid-state MOSFET switch is in charge of forming the high-voltage pulse during a defined pulse length. A series resistance dissipates the remaining energy to a bleed resistor when the circuit is open. The switch is capable of triggering pulses to the LES with a repetition rate of 1 kHz. A current transformer and a voltage probe are also included to measure the voltage and current between the two electrodes. When a breakdown takes place, the circuit is short-circuited in the gap

and produces a current rise and a voltage drop. These signals are recorded by a LeCroy oscilloscope for post-processing data analysis.

A controller, designed and built at CERN [48], is used to control the pulse triggering of the switch, its pulse length and repetition rate, and the automatic pulsing interruption in case of the detection of a breakdown based on current measurements. A LabVIEW program [56] is used as a user interface to set the desired parameters to run the experiment, by communicating with the controller and the power supply.

A second upgrade version of the LES has been recently constructed at the DC

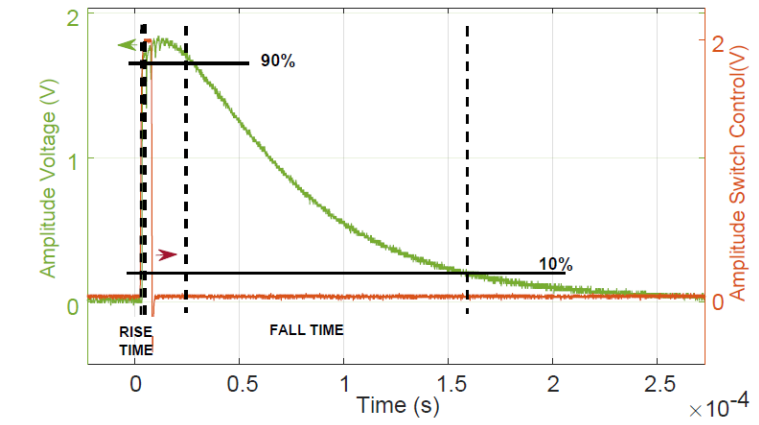

(a)

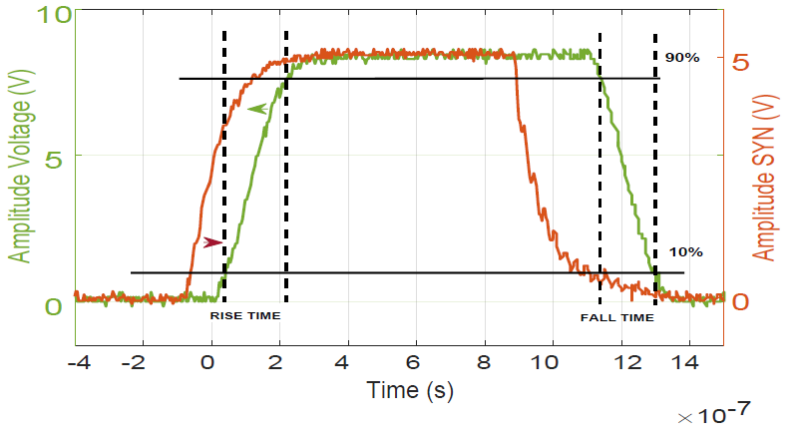

(b)

Figure 3.12: Comparison of the pulse shapes provided by the (a) HRR circuit and (b) Marx Generator circuit of the LES. The red line corresponds to the switch trigger signal and the green line is the resulting voltage signal, measured by a high-voltage probe, that is applied to the electrodes. Taken from [80].

Spark laboratory in which the HRR circuit has been replaced by a Marx Generator circuit [80]. This system has been designed to provide rectangular-shaped pulses similar to the envelope of the RF pulses, with sharper falling edge at the end of the pulse. A comparison of the pulse shape provided by the HRR and the Marx Generator circuit is illustrated in Fig. 3.12, that can be also compared with a typical RF pulse shown in Fig. 3.4(c).

The LES is a simple but important source of data for breakdown studies that is used to complement the results from RF structures. Thanks to the HRR circuit, the system is capable of collecting 20 times more data than Xbox-1 and Xbox-2, and even 5 times faster than the future Xbox-3. This allows more experimental setups to be measured including many pairs of electrodes, with different configurations and materials, and even verify the repeatability of the measurements. Furthermore, this also allows the very-long-term behaviour of the conditioning of copper surfaces to be studied, for example, in order to find whether there is a saturation in the maximum fields that can be sustained. Moreover, the field area of the electrodes of 28 cm^2 is much higher than in CLIC RF structures, in which about 6 cm^2 concentrate above the 95% of the peak surface electric field, and therefore the relevant extension where breakdowns may take place is bigger. A direct comparison between DC and RF breakdowns can be made, showing the multiple similarities of conditioning, statistics of the events, field-emission current measurements and post-mortem breakdown damage analysis.

Chapter 4

Experimental studies of breakdowns in X-band RF test stands at CERN

An extensive analysis of the available data taken with the Xbox-1 and Xbox-2 test stands at CERN has been made during this thesis work with the objective to evaluate and qualitatively understand the performance of the CLIC HG structures. Different studies and measurements are presented in this chapter concerning the limitations of such structures by breakdown occurrences. In particular, this chapter will cover the experimental results obtained from the analysis of breakdown localization in RF structures, conditioning histories, statistics of breakdown occurrences and BDR measurements for different pulse shapes.

4.1 RF breakdown localization in high-gradient tests

The study presented in this section is focused on the localization of breakdowns, in order to evaluate whether the structure conditions uniformly in all the cells or there are regions which are more likely to trigger breakdowns than others. An optimum RF design of the accelerating structure aims at a uniform distribution of breakdowns. A 'hot cell' would limit the conditioning and performance of the whole structure, since BDR would be dominated by such a cell. Hence, the localization of breakdowns allows to evaluate the HG performance of the structure.

4.1.1 Breakdown localization techniques

The RF incident (INC), reflected (REF) and transmitted (TRA) signals and the dark current measurements are used to identify the source position of a breakdown in TW structures. Three methods, described in [93], are used based on the signal

timings and phase measurements when the breakdown is detected. These are known as the 'edge', 'correlation' and 'breakdown phase' methods.

Edge method

When a vacuum arc is initiated at one of the irises of the structure, a plasma spot forms which emits large currents (in the [kA] level) which interfere with the electromagnetic fields. RF power is no longer transmitted through the structure which causes the output power to drop and the reflected power to rise. A typical breakdown event is shown in Fig. 4.1.

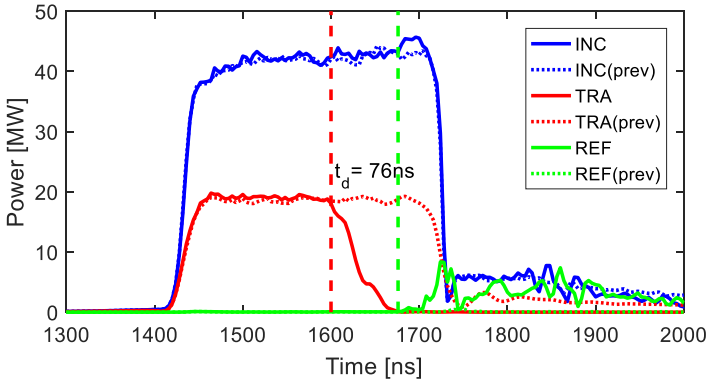

Figure 4.1: Signals of the incident, reflected and transmitted power recorded as a breakdown event (solid lines) and its previous pulse (dotted lines) during the test of the TD26CC at Xbox-1 in 2013. Transmitted signal has been shifted back one filling time (67 ns) to be aligned with the incident and reflected. The green and red vertical dashed lines indicate the rising and falling edges of the reflected and transmitted signal, respectively.

One method of breakdown localization consists of determining the difference of timing between the falling edge of transmitted power t_{TRA} and the rising edge of reflected power t_{REF} and compare the time that the wave needs to travel from the breakdown position to the input and output couplers, assuming that the change in transmitted and reflected power occurs at the same time. Since both signals are extracted from two different directional couplers, placed before and after the structure, we include one filling time t_{fill} of the structure to ensure the same time origin. We define this time difference as:

$$t_d^{\text{edge}} \equiv t_{REF} - t_{TRA} + t_{fill} \tag{4.1}$$

From the group velocity profile $v_g(n_{cell})$ of the structure one can translate the time difference t_d information into a measurement of the breakdown cell number n_{BD}. By comparing the time that the reflected and transmitted power needs to

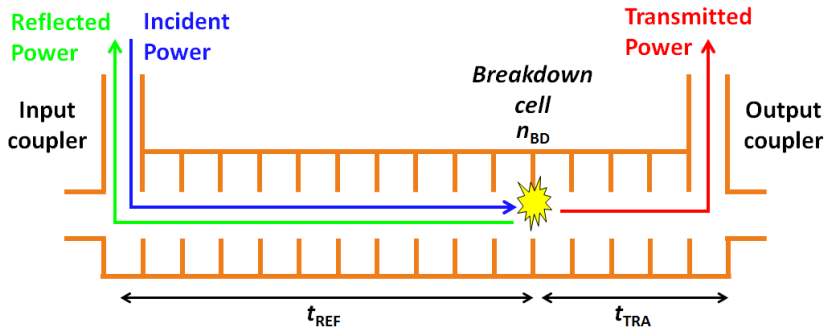

Figure 4.2: Scheme of the RF signals traveling through a TW structure when a breakdown occurs at cell n_{BD}, and time delays of the reflected and transmitted power from the breakdown source to the input and output couplers, which are used for the edge method.

travel from this cell to each directional coupler at the input and output ports, as schematized in Fig. 4.2, the following expression can be derived:

$$t_d^{\text{edge}} = \sum_{n_{cell}=1}^{n_{BD}} \left(\frac{L_{cell}}{v_g(n_{cell})} \right) - \sum_{n_{cell}=n_{BD}}^{N} \left(\frac{L_{cell}}{v_g(n_{cell})} \right) + t_{fill} \tag{4.2}$$

where L_{cell} is the length of one cell, which is 8.33 mm for the CLIC TW structure with a frequency of 11.994 GHz and 120 deg phase advance, and N is the total number of cells in the structure.

The group velocity profile of the TD26CC structure tested in Xbox-1 is shown in Fig. 4.3, together with the corresponding breakdown cell positions for different

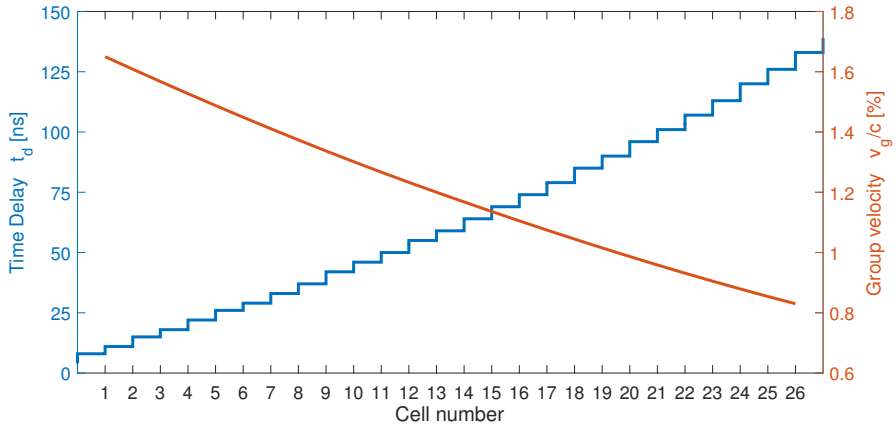

Figure 4.3: Group velocity profile (red) along the 26 cells of the TD26CC structure installed at Xbox-1, and corresponding breakdown cell n_{BD} for the measured time delay t_d (blue).

values of time delays t_d^{edge}. This structure is made of 26 regular cells and 2 coupling cells to the input and output couplers. Measuring these time differences one obtains the cell number of the breakdown by interpolating Eq. (4.2). Measurements fall between 0 and $2t_{fill}$ if the breakdown is triggered inside the structure. Since the RF group velocity decreases towards the end of the structure, the time resolution required to distinguish the position of a breakdown between two consecutive cells is smaller for the first cells (about 3 ns) than for the last ones (about 6 ns).

Correlation method

The second method consists of correlating particular features in the pulse of the reflected and incident power signals, since part of the incident power is reflected backwards from the breakdown cell (see scheme in Fig. 4.4).

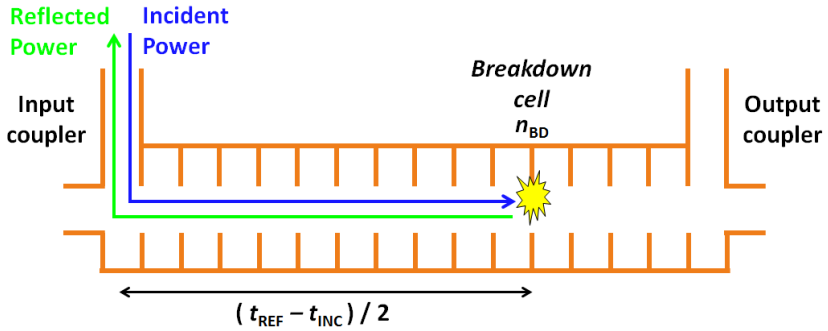

Figure 4.4: Scheme of the incident and reflected RF signals traveling through a TW structure when a breakdown occurs at cell n_{BD}, and time delays used for the correlation method.

When a breakdown is detected with the rising edge of the reflected signal, this shows a pattern that can be correlated with the incident. This effect is particularly clear at the tail of the pulses that have been amplified with a pulse compressor, as shown in Fig. 4.5. When the feeding RF power pulse from the klystron ends, the remaining power at the cavities of the pulse compressor is released exponentially with a slow decay. The incident wave has ripples from multiple reflections along the waveguide network caused by the vacuum arc. These ripples are repeated in the reflected signal after a certain delay t_d^{corr}, which can be translated to the breakdown cell, and with an attenuation factor a_0 due to power losses in each cell:

$$P_{REF}(t) \sim a_0 P_{INC}(t - t_d^{\text{corr}}) \tag{4.3}$$

A two-parameter fit is made to find the best pair (a_0, t_d^{corr}) that minimizes the error difference between both P_{INC} and P_{REF} signals. From the time delay and the

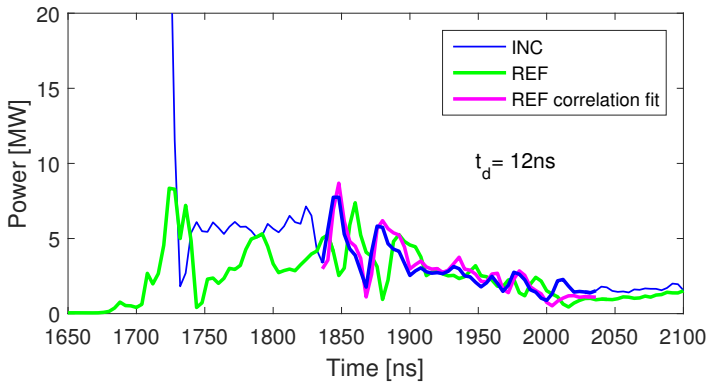

Figure 4.5: Signals of the incident (blue) and reflected (green) power of a breakdown event, zoomed-in at the tail of the compressed pulse, recorded during the test of the TD26CC at Xbox-1 in 2013. Reflected signal has been correlated (pink) in time and attenuation with the incident power to obtain the time delay.

group velocity profile $v_g(n_{cell})$ of the TW structure, one can find the breakdown cell number n_{BD} by interpolating from the following expression:

$$t_d^{\text{corr}} = 2 \sum_{n_{cell}=1}^{n_{BD}} \left(\frac{L_{cell}}{v_g(n_{cell})} \right) \tag{4.4}$$

Using the definition of the filling time t_{fill}:

$$t_{fill} = \sum_{n_{cell}=1}^{N} \left(\frac{L_{cell}}{v_g(n_{cell})} \right) = \sum_{n_{cell}=1}^{n_{BD}} \left(\frac{L_{cell}}{v_g(n_{cell})} \right) + \sum_{n_{cell}=n_{BD}}^{N} \left(\frac{L_{cell}}{v_g(n_{cell})} \right) \tag{4.5}$$

and inserting it into Eq. (4.2):

$$\begin{aligned} t_d^{\text{edge}} = & \sum_{n_{cell}=1}^{n_{BD}} \left(\frac{L_{cell}}{v_g(n_{cell})} \right) - \sum_{n_{cell}=n_{BD}}^{N} \left(\frac{L_{cell}}{v_g(n_{cell})} \right) \\ & + \sum_{n_{cell}=1}^{n_{BD}} \left(\frac{L_{cell}}{v_g(n_{cell})} \right) + \sum_{n_{cell}=n_{BD}}^{N} \left(\frac{L_{cell}}{v_g(n_{cell})} \right) = \\ & = 2 \sum_{n_{cell}=1}^{n_{BD}} \left(\frac{L_{cell}}{v_g(n_{cell})} \right) = t_d^{\text{corr}} \end{aligned} \tag{4.6}$$

we find that one can derive the same expression as the edge method for the conversion of the correlation time delay to breakdown cell number. Consequently, the same interpolation shown in Fig. 4.3 can be made to obtain the breakdown cell position.

Breakdown phase method

A third method is used to be combined with the previous two in order to provide better resolution in breakdown localization. It is based on the phase measurement of the reflected RF signal compared to the incident one, assuming that the reflection is always produced from the same place in the cell and breakdown phases of two consecutive cells are spaced 120 degrees in CLIC TW structures. The breakdown phase [94] is calculated as the average difference between the measured phase of the incident signal and the phase of the delayed reflection, from the instant that the breakdown is triggered:

$$\phi_{BD} = \langle \phi_{REF}(t + t_d) - \phi_{INC}(t) \rangle \tag{4.7}$$

Figure 4.6 shows an example of a breakdown event and the phase measurements of the incident and reflected signals. The phase difference between both signals, previously aligned in time with a delay t_d, remains constant and provides the mea-

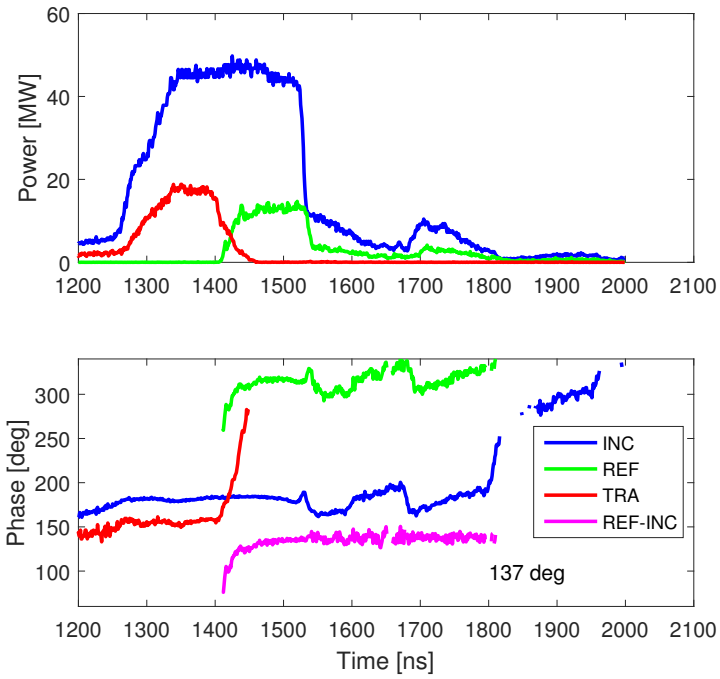

Figure 4.6: Incident and reflected amplitude and phase signals of a breakdown event detected with IQ demodulators during the test of the TD26CC structure in Xbox-1, and phase difference between both correlated signals to measure the breakdown phase. The noisy parts of the phase signals that correspond to a power below 1 MW have been removed for a better visualization.

surement of the breakdown phase. A drift of this phase is often observed [93] and a stable value can not be determined. This drift may be produced due to a possible expansion of the breakdown region to the adjacent cells, or the occurrence of a secondary breakdown within the same pulse triggered upstream of the original cell. In order to obtain a suitable measurement of the breakdown phase, the reflected power needs to be strong enough so that the phase signals could be processed. The phase difference between reflected and incident signal is averaged over slices of 40 ns from the peak value of the reflected signal, to check that it does not drift within a standard deviation of ±10 deg. Only about 25% of the recorded signals of breakdown events in Xbox-1 offers a suitable measurement of the breakdown phase.

The resulting phase of the breakdown corresponds to the accumulated phase advance by the RF power until it is reflected backwards at the breakdown cell number and traverses the same cells, thus it satisfies the following expression:

$$\phi_{BD} = 2 \sum_{n_{cell}=1}^{n_{BD}} (\Delta\varphi(n_{cell})) + \phi_0 = 2\Delta\varphi \cdot n_{BD} + \phi_0 \tag{4.8}$$

where $\Delta\varphi$ is the phase advance per cell, and a constant ϕ_0 has been included to take into account the extra length that the RF power travels through the waveguides and cables until it is detected in the acquisition crate. Since $\Delta\varphi = 120$ deg for CLIC structures, a breakdown phase difference of 240 deg (or equivalently -120 deg) is observed between two consecutive cells.

4.1.2 Experimental results of breakdown localization from the test of a TD26CC prototype

An algorithm has been developed in LabVIEW [95] to analyse the acquired signals with log-detectors and IQ demodulators of all the breakdowns registered by the Xbox-1 system. It has been included in the control and acquisition system of the test stand to evaluate the position distribution of the breakdowns that have been accumulated during a defined period. The algorithm implements the three methods described above, edge, correlation and phase, to localize the source of breakdowns within the structure. The program is commonly used for a daily check of the status of the structure under test. The signature for good performance is a uniform breakdown position distribution, thus it must be periodically verified with sufficient statistics. The experimental results presented in this section correspond to the analysis performed during the test of a TD26CC structure (see picture in Fig. 4.7) during the conditioning process, from August to December 2015, installed at the dog-leg of the CTF3 linac, before the start of the beam-loading experiment. This prototype of TW structures is made from disk cells which are bonded together. The structure has a total of 26 regular cells and 2 coupling cells. It is tapered with an iris aperture

decreasing from 6.3 to 4.7 mm, and each cell includes HOM damping waveguides for wakefield suppression. This prototype was conditioned with pulse lengths of 100, 150 and 200 ns and increasing automatically the accelerating gradient up to 100 MV/m with the Xbox-1 conditioning algorithm. During this process, the BDR was restricted to a maximum level of 3×10^{-5} bpp.

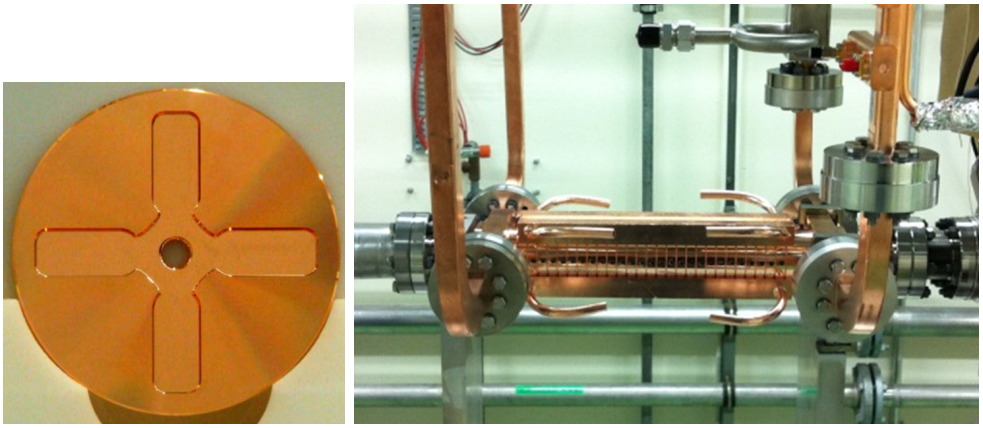

Figure 4.7: Picture of the TD26CC disk (left) and full prototype (right) tested at Xbox-1.

The distribution of time delays t_d^{edge} obtained with the edge method, from Eq. (4.1), is shown in Fig. 4.8(a). The conversion of these measured timings to the corresponding cell position is made by interpolating Eq. (4.2), and the resulting distribution is shown in Fig. 4.8(b). The results show that the breakdowns are spread uniformly along the structure, which means that all the cells are contributing with the same weight to the overall BDR performance of the structure. A fraction of the breakdown events exceeds the expected timing limits of the structure and are consequently detected outside. This could be either due to arcs in the input or output waveguides or due to failure of the automatic edge detection of the signals. The time resolution becomes critical for the first cells of the structure since time delays between consecutive cells are smaller than the sampling rate of the log-detector signals. This implies an experimental error in the estimation of the breakdown cell position in the structure. In particular, one can notice in Fig. 4.8(b) that the breakdowns occurred at cell number 1 can not be determined because the limited time resolution makes that the measured time delays falls into the adjacent cells. Despite this uncertainty, this method is still valuable to verify the uniformity of the breakdown distribution along the structure.

When applying the correlation method for the same set of breakdowns, the measured distribution determined by time delays $t_d^{\text{corr}}$and given by Eq. (4.3), is shown in Fig. 4.9(a). The corresponding cell number position, also interpolated from Eq. (4.2), is shown in Fig. 4.9(b). This distribution typically shows a greater concentration

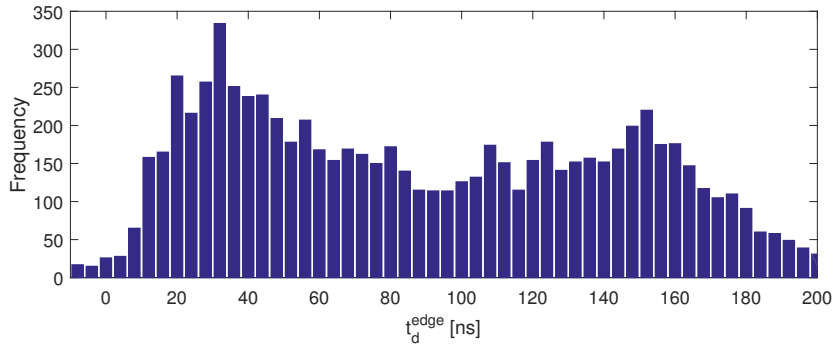

(a)

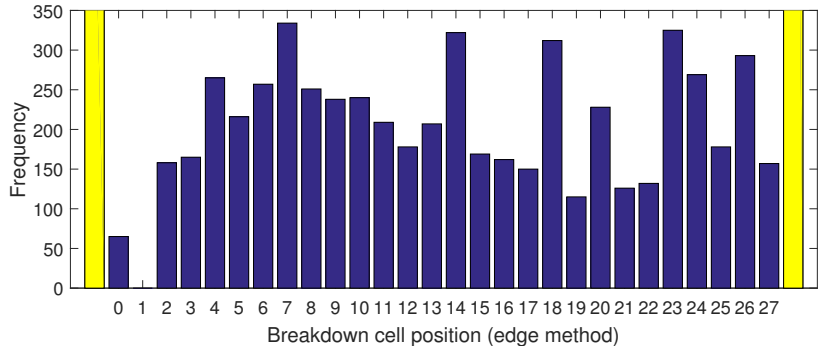

(b)

Figure 4.8: Results of the edge method for breakdown localization in (a) time delays between reflected and transmitted signal edges and (b) converted cell position. Yellow bars correspond to the discarded breakdowns that result outside the structure.

of breakdowns at the beginning of the structure, in contrast to the obtained with the edge method. The origin of this difference may be that the correlation of the signals is evaluated at the tail of the pulse after the breakdown ignition, while the edge method determines the position at the onset of the breakdown. The migration or expansion of the breakdown area within the structure, or even the formation of a secondary breakdown at the same pulse, would explain the drift of the calculated breakdown position with the correlation method towards the front of the structure.

The breakdown phase ϕ_{BD} has been calculated, using Eq. (4.7), from the signals of the same subset of events in the TD26CC structure. The algorithm has found stable breakdown phase measurements in only 22% of the total number of breakdowns. The resulting phase distribution is represented in Fig. 4.10(a). Breakdown phases are distributed in three distinct populations separated by about 120 degrees, as it is expected for the phase advance per cell of the TD26CC prototype. The fact that the

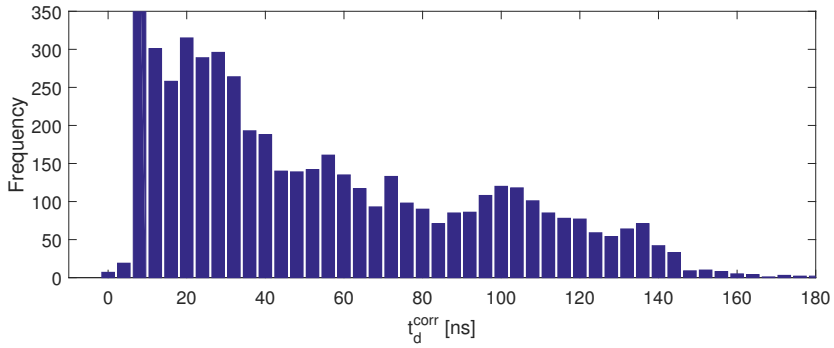

(a)

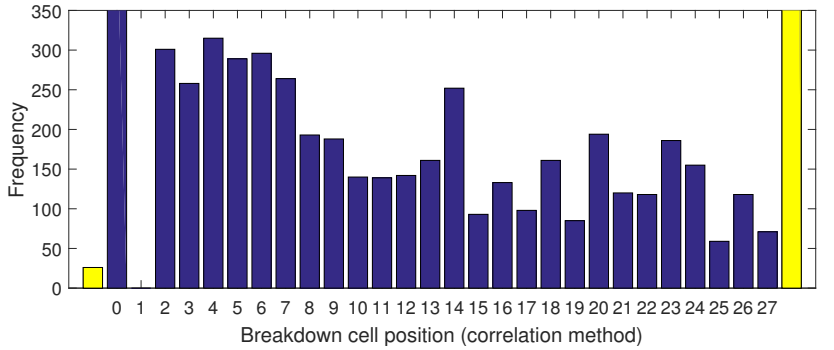

(b)

Figure 4.9: Results of the correlation method for breakdown localization in (a) time delays between correlated incident and reflected signals and (b) converted cell position. Yellow bars correspond to the discarded breakdowns that result outside the structure.

three populations are clearly separated, compared with the distributions obtained by the edge and correlation methods, means that the breakdown phase method provides much better resolution than using timing information. The reflected phase returns to the same value after three cells due to the 120 degrees phase advance, so timing complement each other to provide the best resolution. A specific value of $\phi_0 = 80$ deg has been chosen in Eq. (4.8) to define the most suitable phase limits of the cells according to the three phase distributions in Fig. 4.10(a).

As the measurements of phase are wrapped into the interval between 0 and 360 degrees, two different breakdowns separated by a distance of 3 cells would result into the same breakdown phase. For this reason, a combination of the phase and time delays, obtained by either the edge or the correlation method, is made in order to best determine the breakdown cell number. Figure 4.10(b) shows the correlation between the measured phase ϕ_{BD} and edge time delay t_d^{edge}, together with the bin

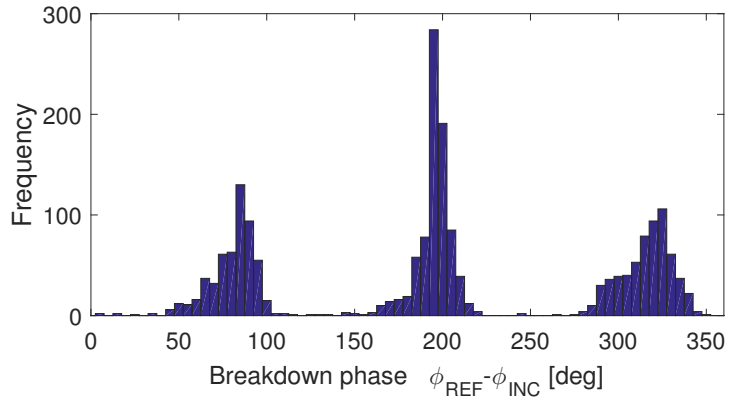

(a)

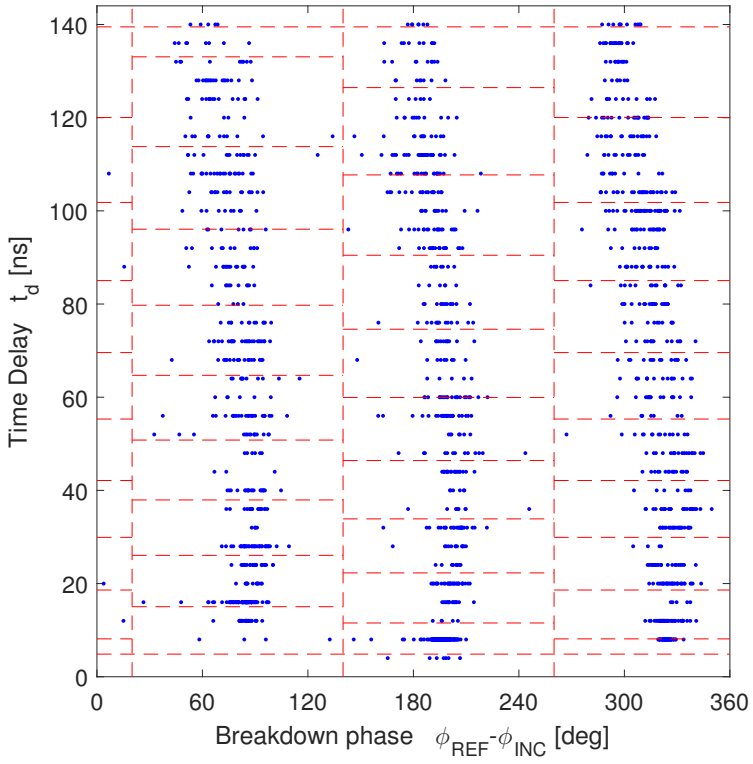

(b)

Figure 4.10: Distribution of (a) breakdown phase measurements and (b) combination of breakdown phase and correlation time delay, obtained from a subset of 1986 breakdowns recorded at Xbox-1 during the test of the TD26CC when it was installed at dogleg.

limits that defines each cell number. The cell number increases with the time delay and the measured breakdown phase changes from cell to cell in steps of 240 degrees.

One can notice a tilt of the measured breakdown phase compared to its cell position, showing a small drift of the phase advance towards the end of the structure. This could be explained by thermal and mechanical stresses during high-power performance that could possibly affect the geometry of the cells and modify the phase advance per cell. The error in phase is consequently accumulated as the RF wave travels through each cell.

4.2 Statistical analysis of breakdown events

The overall performance of a HG accelerating structure is commonly evaluated by counting the number of breakdowns that are detected during many RF pulses at a specific gradient, giving an average BDR during the period of measurement that can be calculated using Eq. (2.1). The statistical behavior of the occurrences of breakdowns during HG operation can be studied as a probabilistic scenario, in which the structure presents a certain probability to develop a vacuum arc for each pulse. A statistical analysis of the breakdown probability has been made to characterize the distribution of breakdown events in time.

4.2.1 The Poisson model

If we assume, initially, that breakdowns are uncorrelated random events, then they can be described by the probability function of a Poisson distribution. This distribution assumes that the probability of an event within a certain interval is independent of the probability of an event in any other non-overlapping interval, and this probability does not change over different intervals. The probability of experiencing a total number of N_{BD} breakdown events within an interval of n_{pulses} is given by:

$$\mathcal{P}(N_{BD};\mu) = \frac{\mu^{N_{BD}} \cdot e^{-\mu}}{N_{BD}!} \tag{4.9}$$

where μ is the only parameter of the Poisson function, which corresponds to the mean value of the number of breakdowns that follows this distribution:

$$\mu = \langle N_{BD} \rangle = \text{BDR} \cdot n_{\text{pulses}} \tag{4.10}$$

The standard deviation of this distribution, associated to the statistical error of the number of detected breakdowns, is also related to the mean value:

$$\sigma(N_{BD}) = \sqrt{\langle N_{BD} \rangle} = \sqrt{\text{BDR} \cdot n_{\text{pulses}}} \tag{4.11}$$

From the discrete Poisson function of a number of events one can derive [96] that the probability of experiencing two consecutive poissonian breakdowns within an interval of pulses Δn_{pulses} is given by an exponential Probability Density Function (PDF):

$$f(\Delta n_{\text{pulses}}) = \begin{cases} 0 & \Delta n_{\text{pulses}} \leq 0 \\ \text{BDR} \cdot e^{-\text{BDR} \cdot \Delta n_{\text{pulses}}} & \Delta n_{\text{pulses}} > 0 \end{cases} \tag{4.12}$$

where the inverse of the BDR gives the average number of pulses between each pair of consecutive breakdowns:

$$\langle \Delta n_{\text{pulses}} \rangle = \frac{1}{\text{BDR}} \tag{4.13}$$

4.2.2 Experimental results of the breakdown probability density function

The statistics of breakdown events have been experimentally investigated by analysing the data of two HG structure tests at the Xbox test stands: the TD26CC prototype tested at Xbox-1 (see picture in Fig. 4.7), with a total of 677 breakdowns recorded during the conditioning process at 250 ns pulse length, from November to December 2013 [76]; and the T24-OPEN prototype tested at Xbox-2 (see picture in Fig. 4.11), which accumulated 869 breakdowns during its conditioning with 200 ns-long pulses, from November 2015 to February 2016 [97]. The field parameters of these prototypes were summarized in Table 2.1 and their performances in Table 3.1. The TD26CC structure, made of 26 regular cells and 2 coupling cells, was manufactured in disks which are etched and bonded together, while the T24-OPEN was fabricated in two halves, with 24 regular cells made by milling, and brazed together.

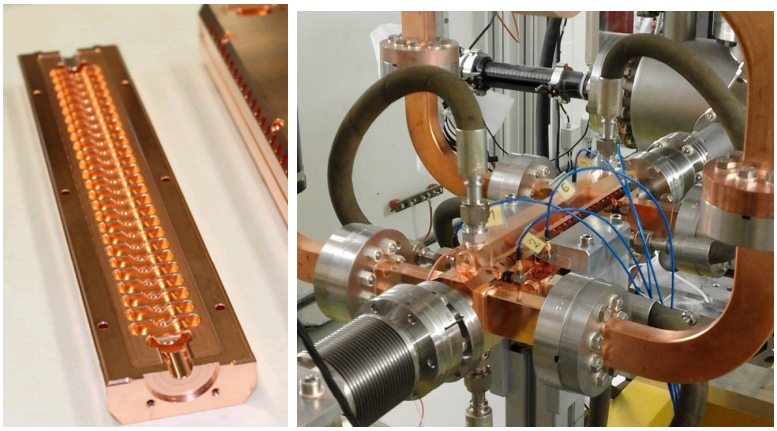

Figure 4.11: Picture of the T24-OPEN half milled piece (left) and full prototype (right) tested at Xbox-2.

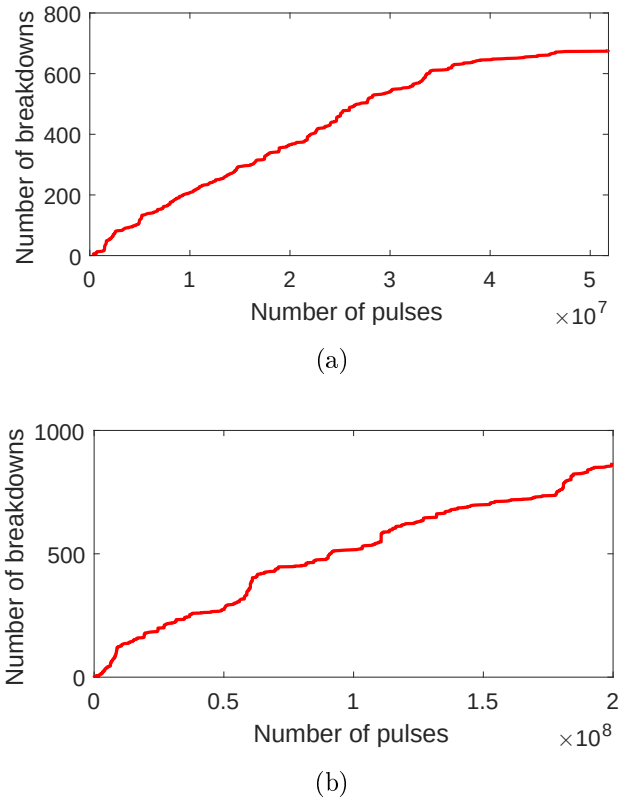

Figure 4.12: History of the cumulative number of breakdowns with respect to the number of triggered pulses recorded during a period of the test of (a) a TD26CC prototype at Xbox-1 and (b) a T24-OPEN prototype at Xbox-2.

Figure 4.12 shows the cumulative number of breakdowns with respect to the number of pulses observed for the TD26CC and T24-OPEN prototypes. The variation in the slope of the curve indicates the variation of the BDR during the HG operation, resulting an average value of 1.3×10^{-5} and 4.4×10^{-6} bpp, respectively. A stair-case pattern is visible due to the experience of 'clusters' of several breakdowns that have been triggered in short intervals of time.

The PDF $f(\Delta n_{\text{pulses}})$ from the acquired data is obtained by first calculating the number of pulses between each pair of consecutive breakdowns, Δn_{pulses}. The resulting array of values are then represented in a discrete histogram, with a finite number of bins. Each bin i is centered at a defined position $\Delta n_{\text{pulses},i}$ and with a bin width $\Delta_{bin,i}$ so that it contains the same number of events N_{bin} as all the other bins of the histogram. The PDF is calculated by the number of events per unit of bin:

$$f(\Delta n_{\text{pulses},i}) = \frac{1}{\sum_j \left(N_{bin}/\Delta_{bin,j}\right)} \frac{N_{bin}}{\Delta_{bin,i}} \tag{4.14}$$

where a normalization factor has been included so that the integral of the PDF is equal to 1.

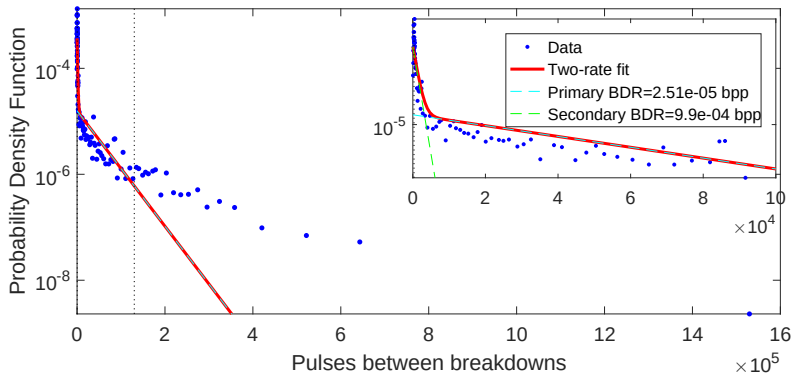

(a)

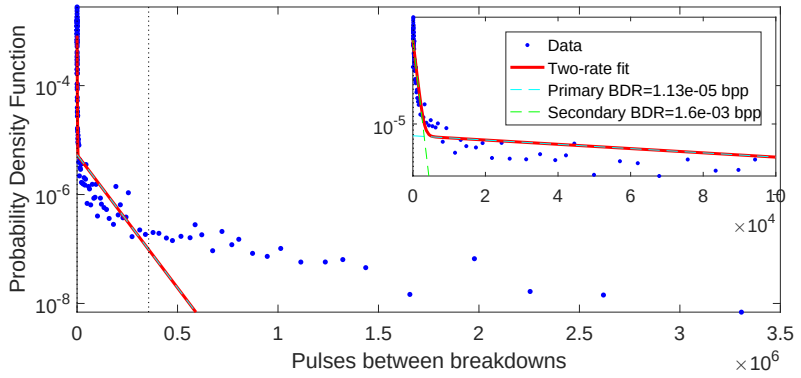

(b)

Figure 4.13: PDF distribution of the number of pulses between two consecutive breakdowns obtained from (a) a TD26CC structure tested at Xbox-1 and (b) a T24-OPEN structure tested at Xbox-2. A fit to a double-exponential function of the data delimited in dotted vertical lines is included.

The PDF of the TD26CC and T24OPEN data is shown in Fig. 4.13. Using a logarithmic scale for the y-axis, the expected exponential function formulated in Eq. (4.12) is linear in the graph. However, the data shows a probability function that clearly differs from the Poisson model. The variation of the slope of the resulting PDF suggests that there is a superposition of different BDR terms.

The first consequence of the discrepancy with a Poisson distribution is that breakdowns can not be randomly independent events, but they are excited by other mechanisms that have been triggered in previous occurrences. Nor would it be a

superposition of independent poissonian events that are triggered at different rates, since this would result effectively in another Poisson distribution with a combined BDR. For this reason, there must exist a correlation between the accumulated breakdowns that take place during the history of the structure test.

4.2.3 The two-rate model and data fit analysis

A double-exponential function is suggested to fit the resulting PDFs shown in Fig. 4.13, in which we distinguish a change of trend in the downward slope at about 10^3 pulses. Based on the Poisson model of Eq. (4.12), the new hypothesis function considers a superposition of two correlated BDR terms [98]:

$$g(\Delta n_{\text{pulses}}) \equiv \begin{cases} 0 & \Delta n_{\text{pulses}} \leq 0 \\ A_1 e^{-\text{BDR}_1 \cdot \Delta n_{\text{pulses}}} + A_2 e^{-\text{BDR}_2 \cdot \Delta n_{\text{pulses}}} & \Delta n_{\text{pulses}} > 0 \end{cases} \tag{4.15}$$

where the normalization is determined by the following expression:

$$\frac{A_1}{\text{BDR}_1} + \frac{A_2}{\text{BDR}_2} = 1 \tag{4.16}$$

The physical origin of a two-rate statistical behavior of breakdowns could be explained by the distinction of two kind of occurrences:

1. A number of 'primary' breakdowns are triggered by a process that may be considered as random poissonian occurrences, which are independent of the rest of events. This process corresponds to the intrinsic BDR of the structure, represented by the term BDR_1, that contains the limiting performance of the high-field surfaces of the structure.

2. A second set of 'follow-up' or 'secondary' breakdowns that are triggered as a consequence of the damage or residue that is left by the previous arc. These occurrences populate the high-BDR term, named BDR_2, of the resulting PDF distribution since they present a higher probability per pulse to develop a breakdown.

The TD26CC and T24-OPEN data have been fitted to the double-exponential function using the Maximum Likelihood Estimation (MLE) method [99], implemented in MATLAB [100], which consists of finding the function parameters (A_1, BDR_1, BDR_2) that maximizes the likelihood $\mathcal{L}$, defined by:

$$\mathcal{L}(A_1, \text{BDR}_1, \text{BDR}_2 \mid \{\Delta n_{\text{pulses},i}\}_{i=1}^{N_{BD}}) = \prod_{i=1}^{N_{BD}} g(\Delta n_{\text{pulses},i}) \tag{4.17}$$

where $\{\Delta n_{\text{pulses},i}\}_{i=1}^{N_{BD}}$ is the array of pulses between consecutive breakdowns and N_{BD} is the number of events. For the sake of a good fit of the data, the fit region has been restricted to the first data points that include the 85% of the smallest values of Δn_{pulses}. The study of longer pulses between breakdowns needs to be further investigated. For the moment, we aim at making a novel qualitative description of the experimental results. The resulting fit, together with the superposed exponentials of the primary and secondary BDR terms, have been included in Fig. 4.13.

Table 4.1: Fit results of the PDF distributions of the number of pulses between breakdowns to the two-rate model.

Parameter	**Units**	**TD26CC**	**T24-OPEN**
BDR_1	[bpp]	2.5×10^{-5}	1.1×10^{-5}
A_1		1.6×10^{-5}	5.4×10^{-6}
$\mathcal{P}_1$		0.63	0.48
BDR_2	[bpp]	9.9×10^{-4}	1.6×10^{-3}
A_2		3.7×10^{-4}	8.5×10^{-4}
$\mathcal{P}_2$		0.37	0.52
$\text{BDR}_1/\text{BDR}_2$		39.6	145
$\mathcal{P}_2/\mathcal{P}_1$		0.59	1.1
$\hat{n}_{\text{pulses}}$	[pulses]	3259	3129

The results of the fitted parameters can be found in Table 4.1. One can distinguish between the number of primary and secondary breakdowns by evaluating the integrated probability, $\mathcal{P}_1$ and $\mathcal{P}_2$ respectively, of each term of the PDF:

$$\mathcal{P}_1 = \int_0^\infty A_1 e^{-\text{BDR}_1 \cdot \Delta n_{\text{pulses}}} d(\Delta n_{\text{pulses}}) = \frac{A_1}{\text{BDR}_1} \tag{4.18}$$

$$\mathcal{P}_2 = \int_0^\infty A_2 e^{-\text{BDR}_2 \cdot \Delta n_{\text{pulses}}} d(\Delta n_{\text{pulses}}) = \frac{A_2}{\text{BDR}_2} \tag{4.19}$$

The crossing point of both exponentials, in which the probability of experiencing a primary and a secondary breakdown is the same, can also be evaluated:

$$\hat{n}_{\text{pulses}} = \frac{\ln(A_1/A_2)}{\text{BDR}_1 - \text{BDR}_2} \tag{4.20}$$

These calculations have been included in Table 4.1 for comparison between the two different structures. A similar trend of the PDF is observed in the statistics of both structures, being the primary rate of the order of 10^{-5} bpp and the secondary one of the order of 10^{-3} bpp. The two exponentials intersect at about 3000 pulses for

both structures. This number can be used as an estimated reference to distinguish between primary and secondary breakdowns, meaning that those breakdowns that have been triggered after less than 3000 pulses are more likely to be follow-up events. A difference in the ratio $\mathcal{P}_2/\mathcal{P}_1$ is observed between the two structures. This number gives an estimation of the number of follow-up breakdowns that are produced per each primary event during the HG test of the structure.

4.2.4 Spatial displacement of breakdown 'clusters'

The hypothesis postulated here of the existence of 'follow-up' breakdowns would imply that these have been triggered at the same iris or at the vicinities of the previous event. The analysis techniques developed in Section 4.1 are a helpful tool to determine the correlation between consecutive breakdowns and to check the validity of the arguments given above.

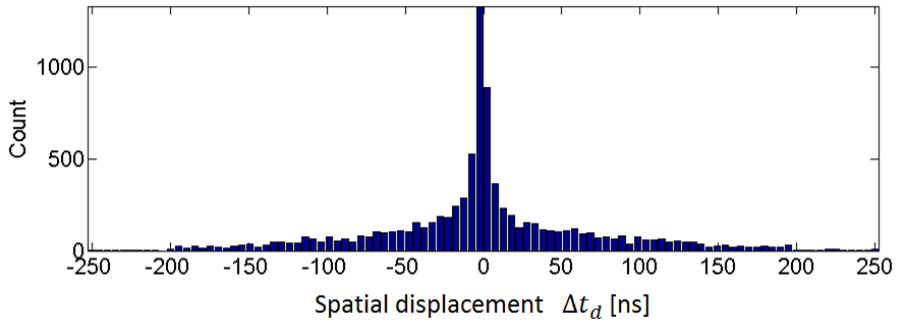

Figure 4.14: Distribution of the spatial displacement of consecutive breakdowns, in terms of the difference in time delays t_d obtained with the correlation method [101].

A set of breakdown events recorded during the test of the TD26CC prototype have been analysed [102] to determine both the number of pulses in the interval preceding the breakdown event and the cell position inside the structure where the arc was detected. Figure 4.14 shows the histogram of the difference of breakdown position between two consecutive events, represented with the time delays t_d obtained by correlation method. A triangular shape is expected for a random distribution of independent breakdowns confined within the length of the structure, but the histogram shows a larger concentration of secondary breakdowns around the same cell position as the previous one.

A good confirmation of the two-rate hypothesis is found in Fig. 4.15, where the spatial displacement of consecutive breakdowns has been represented with respect to the number of pulses of separation between both breakdowns. A contour plot of the distribution indicates the intervals of the spatial displacement distribution that

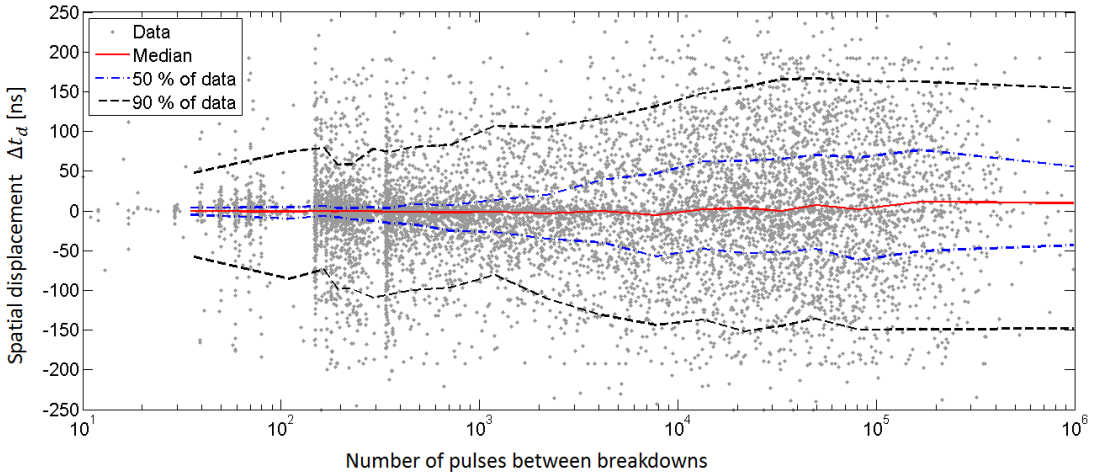

Figure 4.15: Correlation between the number of pulses between two consecutive breakdowns and the spatial distance inside the structure between the same pair of breakdowns [101]. The breakdown cell position displacement has been represented by the difference in time delay t_d obtained with the correlation method.

contains the 50% and 90% of the data for different number of pulses between consecutive breakdowns. The plot shows that those breakdowns that take place sooner in time after another one also occur closer in spatial position, and the distribution becomes more uniform and wider as the number of pulses between breakdowns is larger.

The analysis of the breakdown performance of a HG structure shows that it carries a memory of previous breakdowns for typically 3000 breakdowns. These 'clusters' of breakdowns are created in a small region of the structure during short periods of the order of 1000 pulses, which is in agreement with the formation of secondary breakdowns postulated in the two-rate model. The observation of an inter-correlation between breakdown occurrences needs to be considered as a self-exciting process that is relevant for the ultimate performance of the structure.

4.2.5 Error estimation of the breakdown rate

The standard error estimation of the BDR measurement is usually made assuming that the number of detected breakdowns follow a Poisson distribution and its standard deviation is given by Eq. (4.11):

$$\sigma(\mathrm{BDR}) = \frac{\sigma(N_{BD})}{n_{\mathrm{pulses}}} = \frac{\sqrt{\langle N_{BD} \rangle}}{n_{\mathrm{pulses}}} \tag{4.21}$$

However, a double-BDR PDF has been observed in the number of pulses between

consecutive breakdowns. Consequently, the statistical distribution of the number of breakdowns detected during the interval of pulses differs from the Poisson function.

A Monte Carlo simulation of 10000 experiments has been made to obtain such distribution and evaluate the statistical dispersion of the number of detected breakdowns. A double exponential function has been assumed using the obtained parameters from the fit of the TD26CC data (see Table 4.1). The "inverse transform method" [99] has been used in a MATLAB script for generating the number of pulses Δn_{pulses} that are triggered before the following breakdown:

1. A uniform random value x_0 between 0 and 1 is generated.

2. The number of pulses Δn_{pulses} before the next breakdown is solved from the following equation:
$$F(\Delta n_{\text{pulses}}) = x_0 \tag{4.22}$$
where $F(\Delta n_{\text{pulses}})$ is the cumulative density function (CDF) of the PDF defined by:
$$\begin{aligned} F(\Delta n_{\text{pulses}}) &= \int_{-\infty}^{\Delta n_{\text{pulses}}} f(x)dx = \\ &= \frac{A_1}{\text{BDR}_1}\left(1 - e^{-\text{BDR}_1 \cdot \Delta n_{\text{pulses}}}\right) + \frac{A_2}{\text{BDR}_2}\left(1 - e^{-\text{BDR}_2 \cdot \Delta n_{\text{pulses}}}\right) \end{aligned} \tag{4.23}$$

3. Steps 1 and 2 are iteratively repeated until the total cumulative number of pulses reaches the target:
$$n_{\text{pulses}} = \sum_i \Delta n_{\text{pulses},i} \tag{4.24}$$

The simulation has been performed for an interval of 5×10^6 and 2×10^7 pulses. Figure 4.16 shows the cumulative number of breakdowns that have been simulated for a set of 20 experiments of 2×10^7 pulses.

The results of the statistical distribution of the detected number of breakdowns during the run of two intervals are summarized in Table 4.2 and shown in Fig. 4.17. The obtained histogram has been compared to a nominal Poisson distribution, using Eq. (4.9), with an equivalent average number of breakdowns to the simulation. For both intervals of pulses, the two-rate model presents a wider distribution than the poissonian, hence the error given by the Poisson distribution is underestimated by a factor close to 2 compared to the real measurement.

It can also be noticed that the error of the BDR measurement is enhanced for longer intervals of pulses, as it is the case of poissonian events that reduces the error with the inverse of the square root of the number of breakdowns. An equivalent

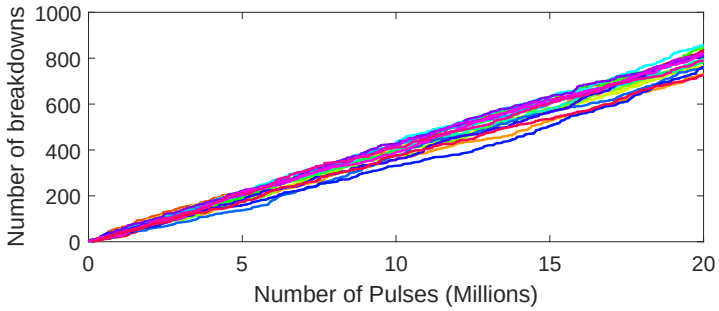

Figure 4.16: Cumulative number of breakdowns with respect to the number of pulses from a set of 20 Monte Carlo simulations following a two-rate PDF as obtained from the TD26CC data, for an interval of 2×10^7 pulses.

reduction is observed in the Monte Carlo simulations of Table 4.2, in which the BDR error is a factor 2 smaller for an interval of pulses 4 times longer.

This simulation assumes a simplistic scenario in which the breakdown probability function does not change during the period of measurement. As we will describe in the following section, conditioning tends to slowly decrease BDR during the operation of the structure. This means that the breakdown PDF would change depending on the conditioning state. If conditioning is still present while operating at constant gradient, as it happened in [87], the measurement of BDR would be affected, thus its error estimation would be larger. The effect of conditioning on the breakdown probability function needs further investigation.

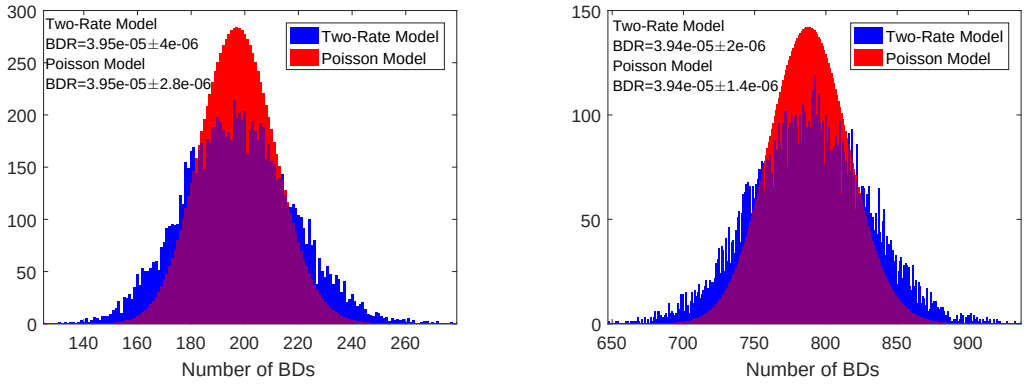

(a) (b)

Figure 4.17: Monte Carlo simulation of the number of detected breakdowns (blue) during an interval of (a) 5×10^6 pulses and (b) 2×10^7 pulses, and comparison to the Poisson distribution (red) with the same average number of breakdowns as the simulation.

Table 4.2: Results of the Monte Carlo simulations using the two-rate PDF obtained from the TD26CC data, and comparison with a nominal Poisson process.

	Simulation 1	**Simulation 2**
Number of experiments	10000	10000
n_{pulses}	5×10^6	2×10^7
$\langle N_{BD} \rangle$	197.5	788.2
$\sigma(N_{BD})$ (Monte Carlo)	20.2	40.3
$\sigma(N_{BD})$ (Poisson)	14.1	28.1
BDR (Monte Carlo) [bpp]	$(3.94 \pm 0.40) \times 10^{-5}$	$(3.94 \pm 0.20) \times 10^{-5}$
BDR (Poisson) [bpp]	$(3.94 \pm 0.28) \times 10^{-5}$	$(3.94 \pm 0.14) \times 10^{-5}$

4.3 Comparative analysis of RF structure conditioning

The ultimate performance of the recent HG prototypes is close to being acceptable for the CLIC requirements of BDR below 3×10^{-7} bpp/m. However all the structures tested so far have required a lengthy, three to four month, RF conditioning period to arrive to the target performance. Since such a long conditioning period would represent a significant contribution to the total cost of the structures, reducing the conditioning time is an important priority for the CLIC study. A better understanding of this process has been achieved from the comparative study of the available conditioning data of similar RF design CLIC prototypes [77], collected from the high-power test at the Xbox test stands (CERN) and the NEXTEF facility (KEK), which allows to find the best strategies in order to reduce the conditioning time.

4.3.1 Characterization of the conditioning level

Different conditioning parameters (gradient, pulse length and BDR) are followed during the test of CLIC prototypes. In order to directly compare the behaviour of the two structures throughout their operating history, the data must be scaled to account for the differing operating conditions. This can be done using experimental dependencies of BDR on gradient and pulse length, formulated in Eq. (2.11). By rearranging terms of this equation, we can define a **scaled gradient** E^*_{acc} as:

$$E^*_{acc} = \frac{E_{acc} \cdot t_p^{1/6}}{\text{BDR}^{1/30}} \tag{4.25}$$

The conditioning history of the TD26CC structure tested at Xbox-1 has been already presented in Fig. 2.13, in which the gradient has been increased in different

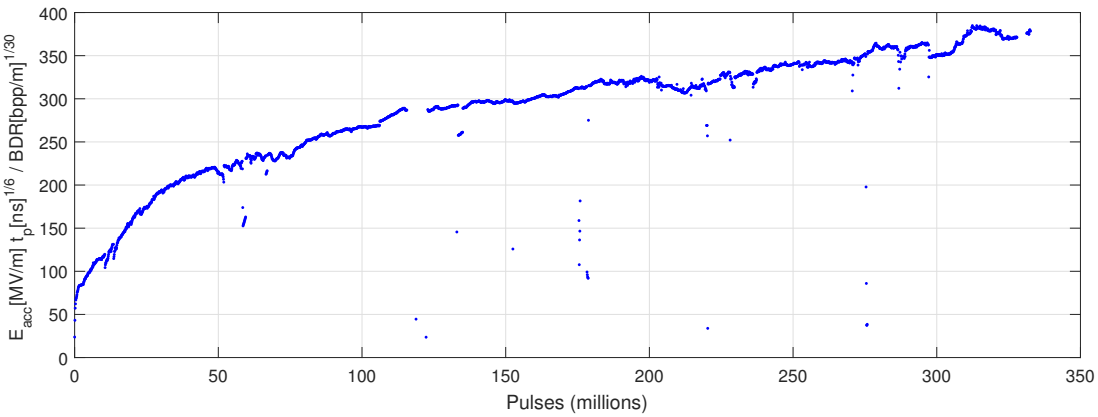

Figure 4.18: Scaled gradient vs number of accumulated pulses for the structure TD26CC tested at CERN. The rescaling has been done applying the definition in Eq. (4.25).

stages of pulse lengths from 50 to 250 ns using an automatic algorithm that keeps the BDR constant at 2×10^{-5} and 7×10^{-5} bpp. Equation (4.25) has been applied to the TD26CC data and the result is shown in Fig. 4.18. What emerges is a rather smooth curve which increases steadily over the course of the experiment and is no longer segmented by the different operating conditions. The smoothness of the scaled gradient curve indicates that the quantity represents a well-defined physical state of the structure, and the steady rise that it represents the conditioning state of a structure. The scaled gradient also allows a direct comparison of different processed structures.

The gradient can be also scaled to a reference pulse length and BDR, labeled as

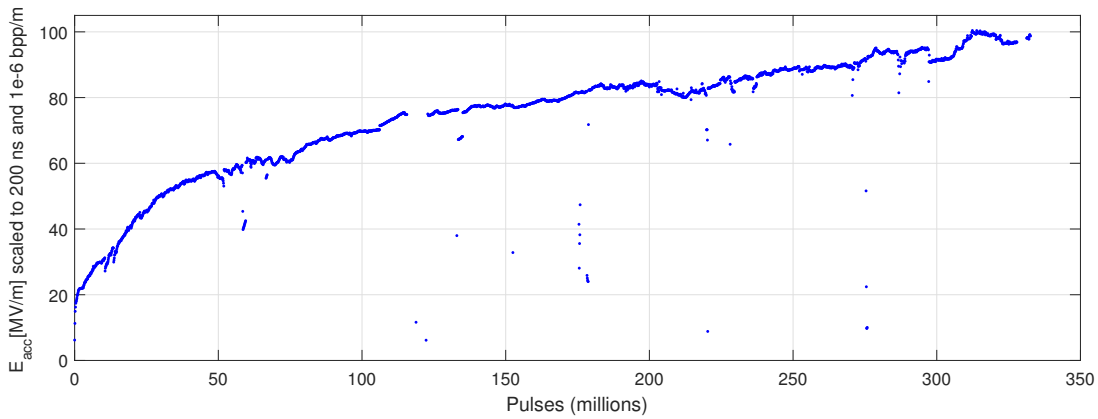

Figure 4.19: Scaled gradient to a BDR of 10^{-6} bpp/m and pulse length of 200 ns for the structure TD26CC tested at CERN.

$t_{p,0}$ and BDR_0, by using the following expression:

$$E_{acc}\{t_{p,0}, \mathrm{BDR}_0\} = E_{acc}\left(\frac{t_p}{t_{p,0}}\right)^{1/6}\left(\frac{\mathrm{BDR}}{\mathrm{BDR}_0}\right)^{-1/30} = E^*_{acc}\cdot t_{p,0}^{-1/6}\cdot \mathrm{BDR}_0^{1/30} \quad (4.26)$$

which represents the maximum gradient that is expected to be achieved by the structure at a fixed operating conditions of pulse length and BDR. As shown in Fig. 4.19, in which Eq. (4.26) has been applied, the expected achievable gradient with 200 ns-long pulses and a BDR of 10^{-6} bpp/m is around 70 MV/m after the first 100 million pulses, and it is enhanced up to 100 MV/m at the end of the test.

Analogous analysis can be made by scaling the measured BDR, using Eq. (2.11), in order to define a **scaled BDR**:

$$\mathrm{BDR}^* = \frac{\mathrm{BDR}}{E_{acc}^{30}\cdot t_p^5} \quad (4.27)$$

which is related to the scaled gradient by the following expression:

$$\mathrm{BDR}^* = (E^*_{acc})^{-30} \quad (4.28)$$

Assuming the operation of the structure running at a fixed gradient $E_{acc,0}$ and pulse length $t_{p,0}$, one can evaluate an expected BDR performance by using:

$$\mathrm{BDR}\{E_{acc,0}, t_{p,0}\} = \mathrm{BDR}\left(\frac{E_{acc}}{E_{acc,0}}\right)^{-30}\left(\frac{t_p}{t_{p,0}}\right)^{-5} = \mathrm{BDR}^*\cdot E_{acc,0}^{30}\cdot t_{p,0}^5 \quad (4.29)$$

The scaled BDR to a reference of 100 MV/m and 200 ns pulses is calculated using Eq. (4.29) for the TD26CC structure data, and it is shown in Fig. 4.20. One

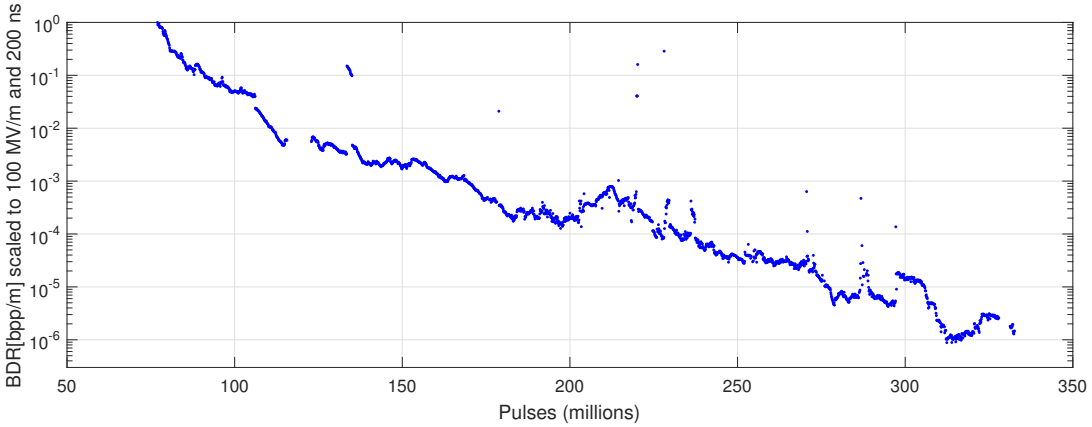

Figure 4.20: Scaled breakdown rate to an operation of 100 MV/m gradient and 200 ns pulse length for the structure TD26CC tested at Xbox-1.

can see how the probability of triggering a breakdown is reduced by several orders of magnitude for a given gradient as the structure runs more pulses, which is the same feature observed in the experiments for long runs at constant gradient and pulse length [87].

4.3.2 Conditioning comparison of CLIC-G damped structures

The scaled gradient can now be used to directly compare conditioning data from different structures so that, for example, the conditioning rate can be quantitatively compared independently of the particular operational parameters of an experiment. The scaled gradient as a function of the number of pulses has been compared for four similar structures (damped CLIC-G design): a TD26CC [76] and TD24R05 tested in Xbox-1, and two TD24R05s tested at NEXTEF [103]. The latter prototypes are a 11.4 GHz version of the TD24R05 design adapted to the operating frequency of the NEXTEF facility.

The testing protocols at the two test facilities are similar. Breakdowns in both facilities are detected by a combination of measurement of current bursts via Faraday cups and measurement of increased reflected RF power. HG operation in Xbox-1 is controlled by an automated conditioning algorithm, which ensures a fixed BDR, with operator intervention necessary only to set pulse length and target BDR. The NEXTEF conditioning control is based on a user-defined power ramping rate which is typically updated daily to maintain a safe BDR level.

The conditioning data of these prototypes have been scaled with the same analysis as used in Section 4.3.1. The results of this analysis have been collected in Appendix A and have been used for the comparative analysis of the conditioning histories.

The first type of comparison, shown in Fig. 4.21(a), is a plot of the scaled gradient vs. the number of pulses, in which it is observed that the conditioning behaviour of the four structures is remarkably similar. The second type of comparison, shown in Fig. 4.21(b), is a plot of the scaled gradient versus the number of accumulated breakdowns. In this case there is a significant divergence in the behaviour of the four structures. This probably reflects the different target BDR (selected through the values of the parameters of the operational algorithm) used at the two test areas. The Xbox-1 target rate was roughly a factor of 5 to 10 higher than the NEXTEF rate, and this is reflected in the accumulated number of breakdowns to reach the same scaled gradient. All structures have reached the same conditioning level after the same time of operation despite operating at very different BDRs and accumulating a statistically different number of breakdowns.

The stronger correlation of scaled gradient as a function of the number of pulses compared to the number of breakdowns indicates that **the structures condition**

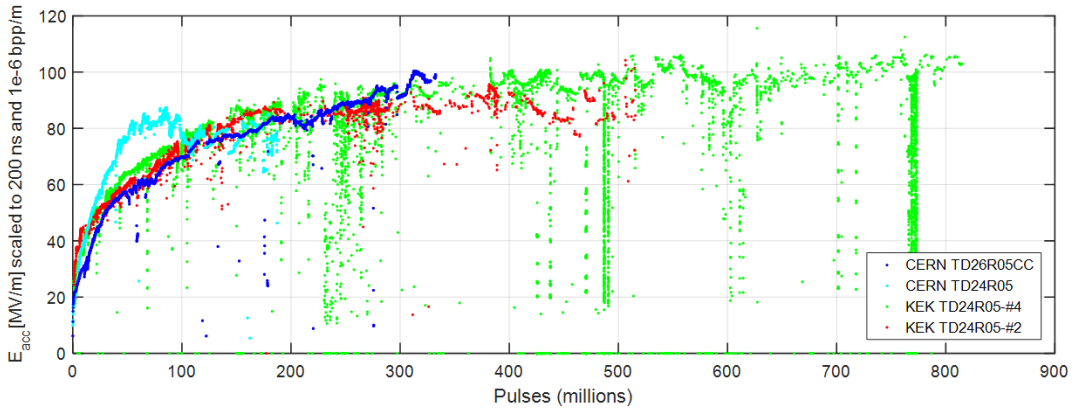

(a)

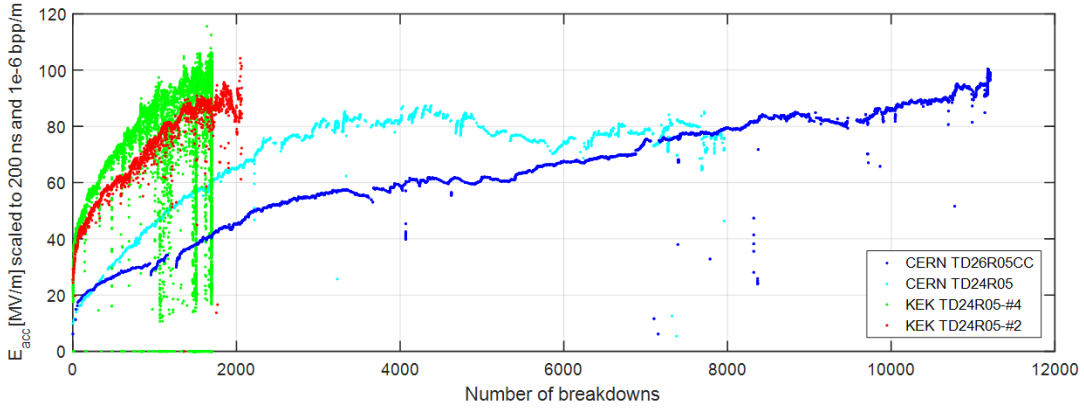

(b)

Figure 4.21: Comparison of the conditioning evolution of a TD26CC (blue) and TD24R05 (cyan) tested at Xbox-1, and two TD24R05s (red and green) tested at NEXTEF, represented by the scaled gradient to pulse length of 200 ns and BDR of 10^{-6} bpp/m versus (a) the accumulated number of RF pulses and (b) the accumulated number of breakdowns.

with the **number of accumulated RF pulses** and not with the **number of accumulated breakdowns**. In other words, breakdowns occur during conditioning but they are not the cause of it.

One conclusion is that conditioning at a low BDR does not take longer than at high BDR, and certainly reduces the risk of accumulated damage to the structure by limiting the number of breakdowns. This observation needs to be verified by the test of many different conditioning strategies to have better statistics than the four structures presented here. The high-repetition infrastructure offered by the Xbox-3 for testing simultaneously four structures would provide a massive amount

of relevant data for this study. The DC Large Electrode System is also a good source of data capable of conditioning a pair of electrodes in an equivalent time of 1-2 weeks.

Another consequence of this new insight in the conditioning mechanism is that each RF pulse appears to act to modify the structure surface to strengthen it against high fields and reduce or eliminate potential breakdown sites in a way which does not result in a fully-evolved and detectable breakdown event. Identifying the relevant strengthening mechanisms would be particularly valuable since it would open the possibility of developing, in a targeted way, a surface treatment procedure which reproduces the effect of RF conditioning but at a lower cost. Indeed, new experiments in the DC LES [104] shows that hard copper samples, which have not been processed through a heat treatment, condition much faster than soft copper ones and then reach a saturation in which the BDR can't be decreased anymore. This suggests that conditioning may be a hardening process of the surface that allows to sustain higher fields without breaking down.

4.3.3 Evolution of limiting RF quantities during conditioning

The present formalism has allowed to compare the conditioning behavior of prototypes with similar RF design, as it is the case of the TD26CC and the TD24R05 families. Other structures with completely different designs in the framework of the CLIC study have been manufactured and tested at the Xbox test stands and NEXTEF. It is the case of undamped prototypes such as the T24, made of 24 bonded-disks, and the T24-OPEN, made of two halves that have been brazed together. Field quantities have been previously summarized in Table 2.1. A Crab cavity for CLIC, made of 10 disks, was also fabricated and tested [81] to be operated in deflecting (dipole) mode. Due to the high fields present on the surface, a conditioning strategy was required to minimize the probability of breakdowns.

As discussed in Chapter 2, the accelerating gradient is not a relevant parameter to predict the best performance of the structure. A more clear relationship is found between the breakdown mechanism and other quantities such as the surface electric field and the modified Poynting vector. The description of these quantities during the conditioning process with equivalent scaling laws allows a comparison of the test of prototypes with different RF designs.

Given the proportionality between the gradient and the surface electric field $E_{acc} = k_E E_s$ and the square root of the modified Poynting vector $E_{acc} = k_S \sqrt{S_c}$,

being k_E and k_S constants, the following scaled quantities are defined:

$$E_s^* = \frac{E_s \cdot t_p^{1/6}}{\mathrm{BDR}^{1/30}} \tag{4.30}$$

$$S_c^* = \frac{S_c \cdot t_p^{1/3}}{\mathrm{BDR}^{1/15}} \tag{4.31}$$

Since the profile of these fields is not uniform along the structure, the peak value is taken as it is more relevant for the BDR limit. The maximum surface fields that

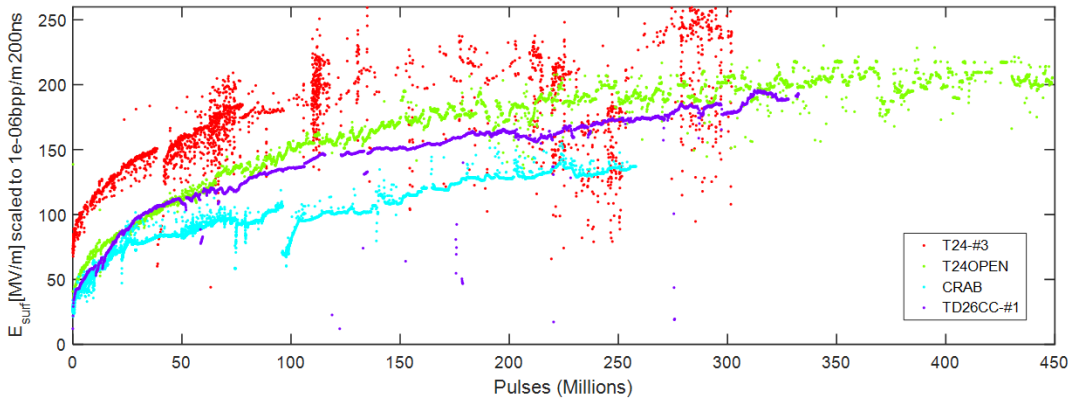

(a)

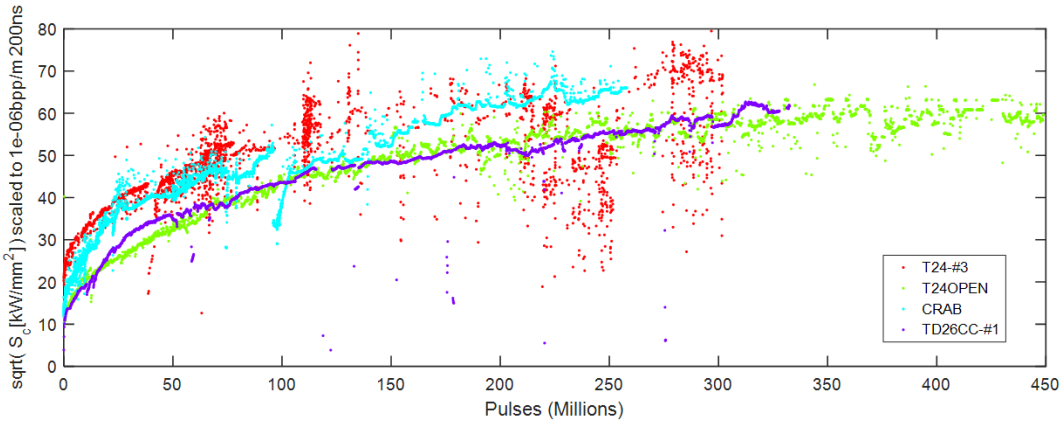

(b)

Figure 4.22: Conditioning histories of three undamped structures—T24-#3 (red), T24-OPEN (green) and Crab cavity (cyan)— and one damped structure—TD26CC (violet)—tested at Xbox and NEXTEF, compared by (a) the scaled peak surface electric field and (b) the scaled peak modified Poynting vector. Since $S_c \propto E_s^2$, the square root of the scaled S_c is represented in order to allow a linear comparison with the scaled E_s.

are expected for a certain performance of pulse length and BDR can be calculated as:

$$E_s\{t_{p,0}, \mathrm{BDR}_0\} = E_s^* \cdot t_{p,0}^{-1/6} \cdot \mathrm{BDR}_0^{1/30} \tag{4.32}$$

$$S_c\{t_{p,0}, \mathrm{BDR}_0\} = S_c^* \cdot t_{p,0}^{-1/3} \cdot \mathrm{BDR}_0^{1/15} \tag{4.33}$$

A comparison of the conditioning histories between undamped and damped structures is shown in Fig. 4.22, using the scaled quantities of Eq. (4.32) and (4.33). The T24-#3 structure was tested at NEXTEF and achieved the best performance so far for a BDR below 3×10^{-7} bpp/m, with an operational gradient of 120 MV/m and pulse length of 180 ns. The Crab and the T24-OPEN structures were tested at Xbox-2, and their conditioning histories were compared with the undamped T24-#3 and the damped TD26CC prototypes. The scaling of the conditioning data of the mentioned prototypes can be found in Appendix A.

All different designs show a smaller discrepancy when comparing the peak modified Poynting vector with respect to the peak surface electric field. The scaled S_c data of the T24-#3 history lies remarkably well on top of the Crab cavity, despite the significant differences in the surface electric fields. The data of the damped TD26CC prototype remains slightly below than the data of the T24-#3 when comparing the achieved S_c, but still in better agreement than the surface electric field.

These results are good indicators that the electric field is not a suitable limiting quantity related to the structure behavior, and the modified Poynting vector may point towards the actual constraint that predicts the ultimate performance.

4.3.4 Long-term trends of conditioning

The conditioning curves seen in Fig. 4.21(a) present a characteristic behavior with the accumulated number of pulses, in which the ramping speed becomes slower as time passes through. There is a special interest in studying the long-term trend of these curves, in order to find whether there is a saturation in the maximum gradient that a structure can sustain or not. It would also help to have an estimation of the time that a structure needs to complete the conditioning process and achieve the target performance.

Plots of the scaled BDR, defined in Eq. (4.27), of the TD26CC and TD24R05 histories tested at Xbox-1 and NEXTEF, respectively, are shown in Fig. 4.23 as a function of the number of pulses in double-logarithmic scale. A linear trend is observed and data has been fit to a power law function:

$$\mathrm{BDR}^* = B \cdot n_{\mathrm{pulses}}^{-A} \tag{4.34}$$

which is equivalent to:

$$\log_{10} \mathrm{BDR}^* = -A \log_{10} n_{\mathrm{pulses}} + \log_{10} B \tag{4.35}$$

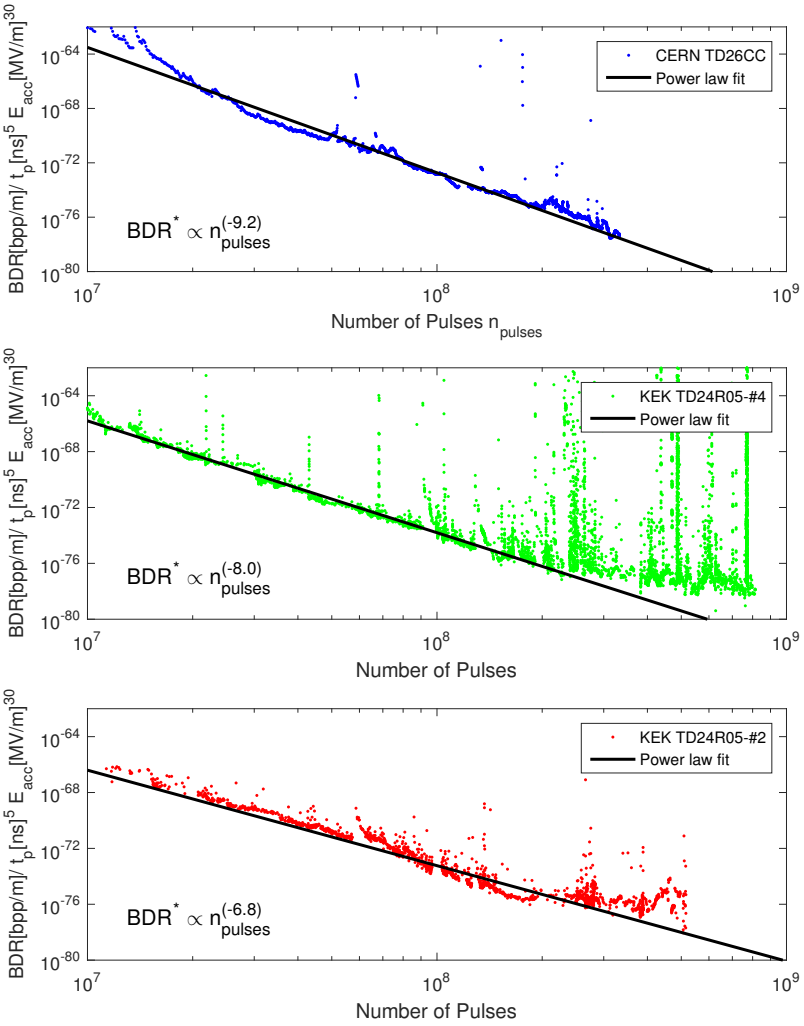

Figure 4.23: Evolution of the scaled BDR with the accumulated number of pulses and power law fit of the data of the TD26CC tested at Xbox-1 and the TD24R05s tested at NEXTEF.

where n_{pulses} is the accumulated number of pulses and (A, B) are the fit parameters. The exponent A can be used to quantify the conditioning speed of the structure, and the fit to the power law function results in similar values between [6.8–9.2] among the different structures.

For the case of the TD24R05-#4 structure tested at NEXTEF, the one that has been tested for the longest time, one can observe that the conditioning trend starts to diverge from the power law fit at about 4×10^8 pulses, possibly showing that its conditioning state is no longer improving. This saturation would imply that there is a lower limit to the achievable BDR.

The evidence of a conditioning limit in RF structures needs to be further investigated with longer tests that accumulates more pulses and breakdowns at very low BDR regimes. Since this would require years of operation and data collection at the existing RF test stands, a high repetition rate system such as the pulsed-DC LES (see Section 3.3) is very important to explore the long-term trends of conditioning.

Conditioning algorithm in the pulsed-DC Large Electrode System

In 2014, the automatic conditioning algorithm that is used in the Xbox test stands [82] was implemented into the existing LabVIEW program of the pulsed-DC LES in order to control the electrode voltage ramp-up attending to the breakdown rate performance of the system. The conditioning algorithm functions by increasing the voltage if a given number of pulses have occurred without breakdown. The algorithm also reduces the voltage if the breakdown occurs very early either after the preceding breakdown or after the voltage increase.

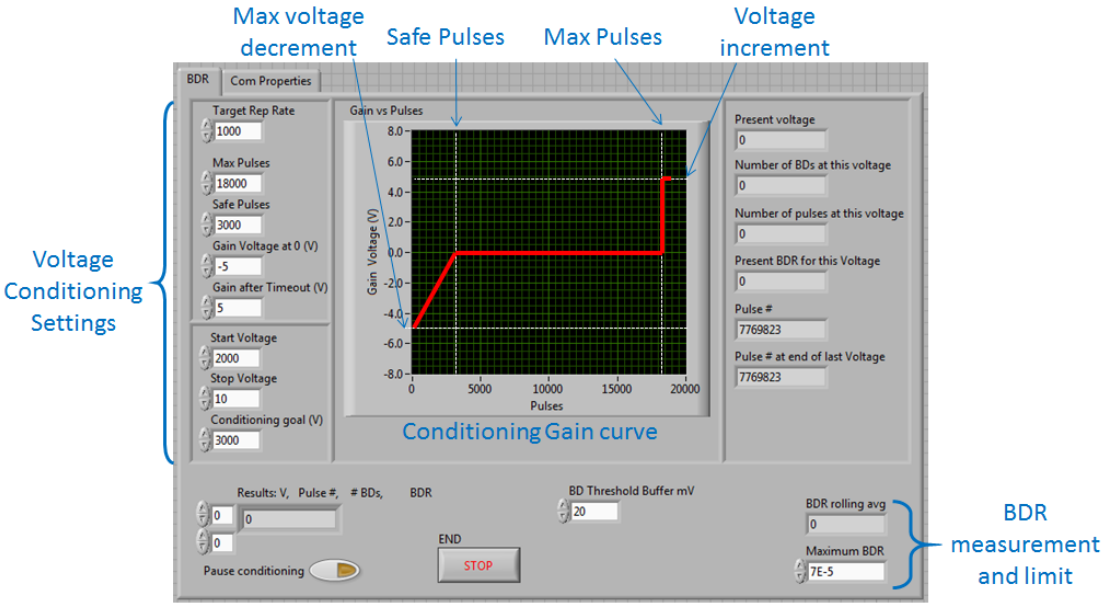

Figure 4.24: LabVIEW's VI front panel of the conditioning algorithm implemented in the LES.

A screenshot of the LabVIEW's VI front panel is shown in Fig. 4.24, and the algorithm is summarized in the following steps:

1. The conditioning algorithm parameters are initially set:

    - Max Pulses t_{max} : maximum number of pulses at the same voltage level without detecting a breakdown.

- Safe Pulses t_{safe} : maximum number of pulses which decreases the voltage if a breakdown is detected.
- Voltage increment ΔV^+ : increment in voltage if no breakdown has been detected after t_{max}.
- Max voltage decrement ΔV^- : maximum decrement of voltage after detecting a breakdown.
- BDR_{max} : maximum BDR as limit in the breakdown performance of the electrodes.

2. The switch starts pulsing at an initial voltage V_i, with the previously defined settings of pulse length and repetition rate, and counts the number of pulses that are being triggered. At the same time, a counter measures the number of breakdowns detected in a window of the last 1 million pulses and calculates the present BDR:
$$\text{BDR} = \frac{\#\text{BDs (last } 10^6 \text{ pulses)}}{10^6 \text{ pulses}}$$

3. If no breakdown is detected after triggering more pulses than t_{max}, the voltage is incremented only if the BDR is lower than the previously defined limit $\text{BDR} < \text{BDR}_{max}$:
$$V_{i+1} = V_i + \Delta V^+$$
If $\text{BDR} > \text{BDR}_{max}$, the voltage remains at the same level, $V_{i+1} = V_i$, to wait for the BDR to be diminished. The algorithm is back to step 2.

4. If a breakdown takes place within the defined period $t_{BD} < t_{max}$, the voltage is either decremented or unchanged depending on how early the breakdown has been triggered and following the gain curve of Fig. 4.24:

   - If $t_{BD} < t_{safe}$ (early breakdown), the voltage is decremented proportionally to t_{BD} and the algorithm is back to step 2:
   $$V_{i+1} = V_i - \Delta V^- \left(1 - \frac{t_{BD}}{t_{safe}}\right)$$
   - If $t_{BD} > t_{safe}$ (late breakdown), the voltage setpoint is not changed for the next iteration, $V_{i+1} = V_i$, and the algorithm is back to step 2.

The result of this algorithm is a slow increase of the voltage that keeps the BDR about constant. The conditioning history of a pair of soft-copper electrodes can be seen in Fig. 4.25. The voltage is increased and decreased in short-term periods of time according to the occurrences of breakdowns, but the long-term trend shows

an increase of the surface field keeping a constant BDR of 10^{-5} bpp. One can also notice that the system has produced a total of 10^9 pulses in about three weeks of operation, compared to an RF test stand that would require more than a year for the same number of pulses.

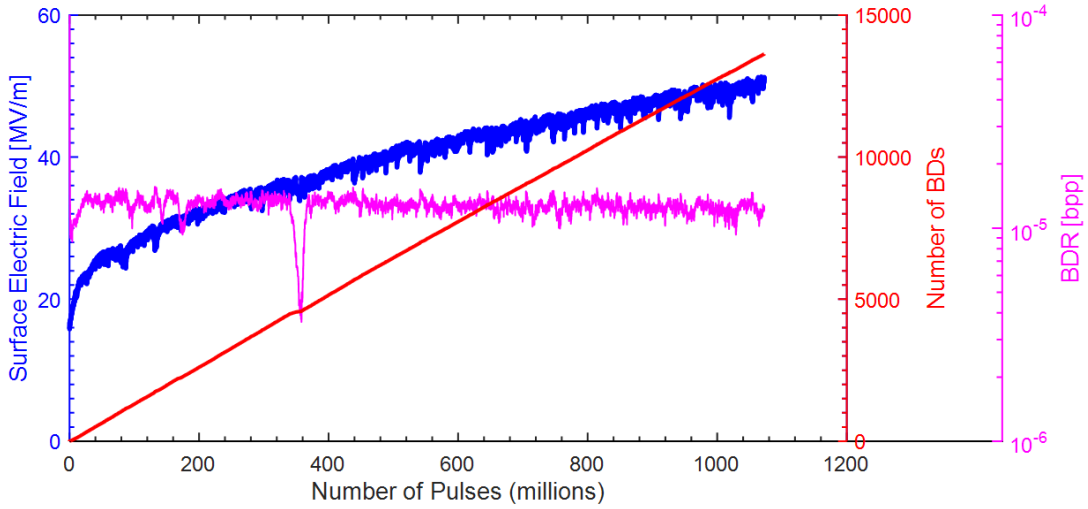

Figure 4.25: Conditioning history, with respect to the accumulated number of pulses, of a pair of soft-copper electrodes in the LES. Blue dots represent the electric field in the gap, red line is the accumulated number of breakdowns and pink line is the BDR.

Long conditioning trends in the pulsed-DC Large Electrode System

The same analysis of the conditioning history has been made for the test of soft-copper electrodes in the DC LES [105], as shown in Fig. 4.26. The scaling of the BDR of the electrodes has been made by replacing the gradient with the surface field in Eq. (4.27). The data from the test of RF structures has been included for comparison using the same scaling with surface fields.

A total of 2.5×10^9 pulses were recorded during the test of the pair of electrodes taking advantadge of the 1 kHz repetition rate pulsed system. A power law dependence is also apparent in the DC data and it has similar slope (or conditioning speed) as RF accelerating structures. After 10^9 pulses, the electrodes are no longer conditioning and BDR is settled down to a saturation level. The behavior observed in Fig. 4.26 also proves that breakdown studies can be performed in DC systems as the LES to be translated to RF structures and that the conditioning mechanisms in the two cases are similar.

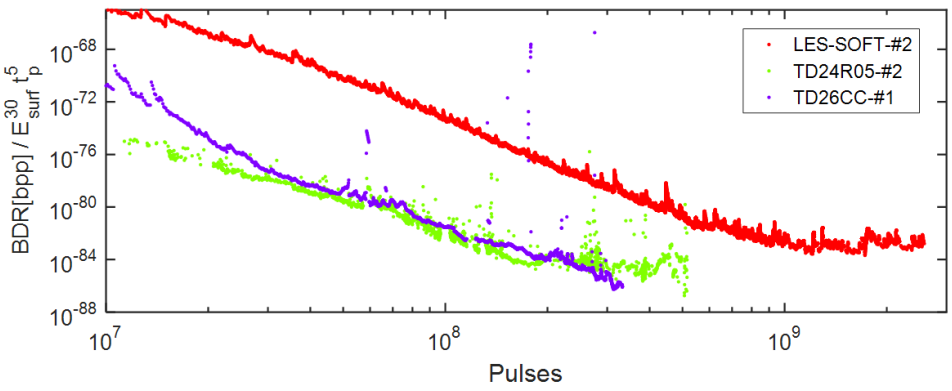

Figure 4.26: BDR, scaled to the pulse length and surface electric field, with respect to the accumulated number of pulses measured at a pair of soft-copper electrodes tested at the DC LES, and comparison with RF structures tested at Xbox-1 and NEXTEF.

4.4 Breakdown rate dependence on the pulse shape

While the NEXTEF facility combines the power of two klystrons to reach up to 100 MW power, the Xbox test stands at CERN make use of a pulse compressor after the klystron to increase the peak power up to 140 MW. During the time while the compressor cavities are being filled, the charging stage, some power is reflected towards the structure under test. The stored energy is later delivered to the structure with a 180 deg phase flip and, when the input RF pulse ends, the compressor slowly discharges the remaining energy. The resulting pulse that is sent to the structure is shown in Fig. 3.4(c).

In this section we aim to study the magnitude of a possible negative effect on the BDR performance caused by the pre-pulse and post-pulse which is present when operating with pulse compressor. Since the actual pulse is longer than the typical 200 ns-long pulses that are used to test the prototype, the structure dissipates more extra energy by resistive heating and the temperature rise of the copper surface is larger. A simulation of the temperature rise in the T24-OPEN structure, tested in Xbox-2, has been made using Eq. (2.18) with a real power pulse shape at a level of 30 MW compressed flat-top of length 200 ns. The result, shown in Fig. 4.27, has been compared to the expected surface heating produced with a standard flat rectangular pulse at the same power level and pulse length.

The maximum temperature rise results 7.5% higher for a structure driven by a compressed pulse compared to the obtained with a regular pulse. The initial stage of charging of the pulse compressor cavities produces a pre-heating effect on the structure, which is around 2 K warmer at the start of the compressed pulse. If the pulse surface heating is contributing to the occurrence of breakdowns, the full pulse

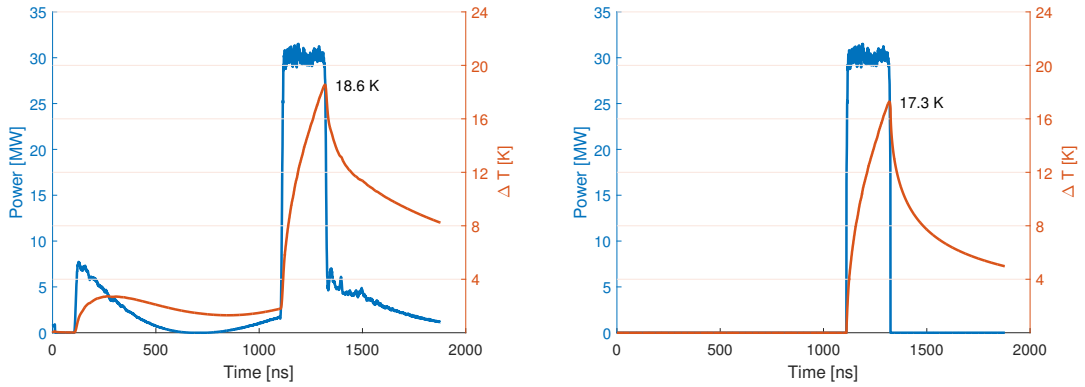

(a) (b)

Figure 4.27: Simulation of the maximum temperature rise of the copper surface of the T24-OPEN structure tested at Xbox-2 when operated (a) with pulse compressor and (b) without pulse compressor (flat pulse).

provided by the pulse compressor would slightly aggravate the BDR performance of the structure. Consequently, the gradient that the structure would achieve with a regular pulse would be 3.7% higher than with a pulse compressor shape.

The pulsed surface heating is at the moment the only physical quantity, that the author is aware of, which makes an explicit prediction of the dependency of breakdown rate on pulse length and shape. An analogous expression to Eq. (2.18) can be defined to study other scaling law between field and pulse length different from the obtained with the pulsed surface heating. The following integral is used in [106]:

$$I_\alpha = \int_0^t \frac{1}{(t-t')^\alpha} P(t')dt' \tag{4.36}$$

where α is a free parameter. Notice that, for $\alpha = 1/2$, the integral represents the same formula given by the temperature rise in Eq. (2.18). In addition, for $\alpha = 2/3$ and a flat pulse of length t_p, the integral yields $Pt_p^{1/3}$ as it results from the experimental scaling law in Eq. (2.11) for a fixed BDR. The statistical analysis made in [106] of the experimental BDR results with different pulse shapes shows the agreement with a parameter α in the range of 0.4–0.7.

The calculation of this integral, with $\alpha = 2/3$, has been made for the pulse shapes considered before with and without pulse compressor during the test of a T24-OPEN structure at a flat-top power of 30 MW and 200 ns pulse length. The results, represented in Fig. 4.28, show a difference of 4% higher for the compressed pulse shape due to the delivery of some power at the charging stage of the compressor. If we scale the BDR with the integral as BDR $\propto I_\alpha^{15}$, this would imply an increase

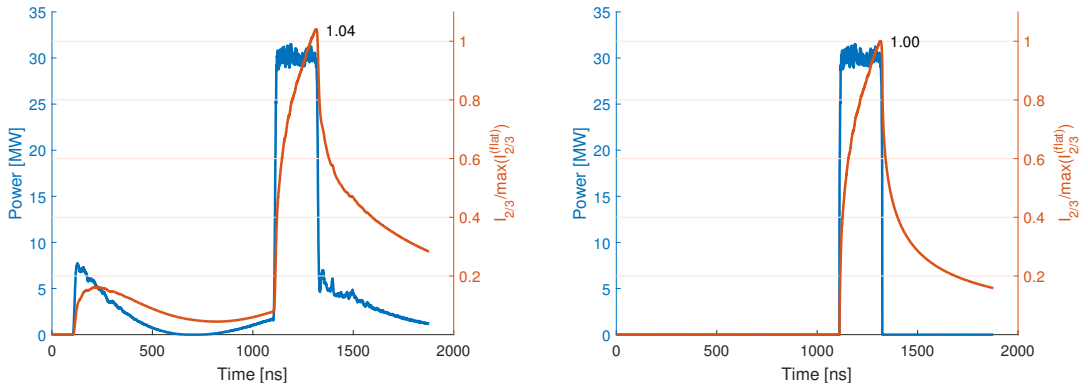

(a) (b)

Figure 4.28: Simulation of the integral $I_{2/3}$ of the T24-OPEN structure tested at Xbox-2, using Eq. (4.36), when operated (a) with pulse compressor and (b) without pulse compressor (flat pulse). The integral has been normalized to the peak value obtained with a flat pulse.

of the BDR of 80%. Equivalently, the achievable gradient would be reduced a 2% using a pulse compressor.

A first verification of the estimated effect of breakdown rate with and without pulse compressor has been made with experimental data taken from the test of the T24-OPEN prototype in Xbox-2. The cavities of the compact pulse compressor, made at CERN and installed in Xbox-2, include a tuning piston at one end of each cavity that can be manually moved to two fixed positions in order to vary their internal geometry. One position of the pistons is set at the 'tuned mode', so that the resonance frequency of the cavities is tuned to the 11.994 GHz RF frequency of the klystron output power. The second piston position is out of tune and no storage of RF energy is made in the cavities, thus the pulse compressor is effectively removed from the circuit. Hence, the Xbox-2 high-power system can deliver the two simulated pulse shape configurations that have been simulated in this section.

The first measurements of the BDR has been made in the T24-OPEN prototype with the two mentioned pulse shape configurations manipulated by tuning and detuning the Xbox-2 pulse compressor [107]. Both the compressed pulse and the regular flat pulse have been configured to have the same flat-top pulse length of 200 ns, for the sake of a good comparison between each other and the simulations. The results of the BDR measurements at different average flat-top power levels, between 30 and 42 MW, are shown in Fig. 4.29.

As expected from the simulations, the BDR is higher when the pulse compressor is tuned and this case results about an average factor 4 higher than the regular flat

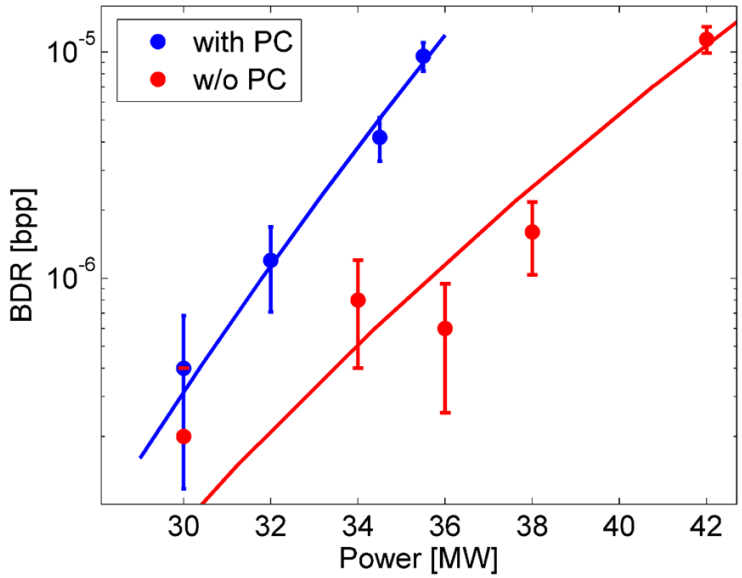

Figure 4.29: Measurements of the BDR at different average flat-top power levels made at the test of the T24-OPEN prototype in Xbox-2, using two different pulse shapes: a regular flat pulse (red) and the output pulse of the pulse compressor (blue). Data has been fit to a power law function [107].

pulse shape. Nevertheless the large measurement errors of the BDR does not allow to have a good estimation of the difference between both measurements. A fit of the data to a power law function has also been made, and the dependence between BDR and input power results slightly steeper in the case of pulse compression, but close to the expected scaling law with P^{15}.

More experiments need to be performed with better statistics in order to evaluate the effect of using pulse compressors for feeding the HG structures. If the negative effects observed in the presented preliminary results of the BDR performance were verified, the HG constraints of accelerating structures would need to be revisited for the particular case of linacs powered with pulse compressor systems.

Chapter 5

Breakdown rate studies in the beam-loading experiment at CTF3

In this chapter, we will describe in detail the beam-loading experiment for the study of the breakdown performance of a CLIC HG structure in the presence of an electron beam. A big part of this work is focused on the stability of the experiment during the measurement periods. First results of the BDR measurements and breakdown position are also presented.

5.1 Motivation of the experiment

The nominal CLIC performance requires the acceleration of a 156 ns-long train of bunches, with a beam current of 1.2 A, at an accelerating gradient of 100 MV/m and allowing a maximum BDR of 3×10^{-7} bpp/m. The HG testing programme carried out by the CLIC study has demonstrated the feasibility of accelerating gradients of 100 MV/m at this low BDR to limit the luminosity loss of the collider due to transverse kicks on the beam. Nevertheless, all HG tests performed so far, summarized in Fig. 3.1, have been made without taking into account the loading introduced in the structure by an accelerating beam.

The unloaded and beam-loaded accelerating gradient profiles have been calculated using Eq. (1.39) with the design parameters of a CLIC TD26CC prototype, as shown in Fig. 5.1. The iris aperture of this structure is tapered so that it provides an approximately constant unloaded gradient profile. An average gradient of 100 MV/m corresponds to an input power of 43.3 MW. When the beam is present the gradient is loaded, that is, it is lowered towards the end of the structure because power is absorbed by the beam, thus the average gradient is reduced to 81 MV/m. Consequently, the energy gain of the electron beam, given by Eq. (1.1), is smaller and needs to be compensated with higher input power. Figure 5.1 also shows the

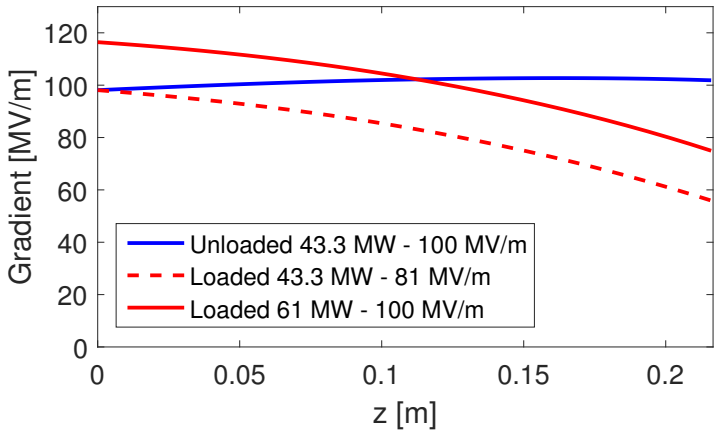

Figure 5.1: Gradient profile along a CLIC TD26CC accelerating structure when operated at input RF power of 43.3 MW, without beam (solid blue line) and with a CLIC nominal beam (dashed red line). The average gradient is reduced from 100 to 81 MV/m. To recover the average gradient to 100 MV/m, higher power of 61 MW should be fed to the structure (solid red line).

loaded gradient profile in the same structure at an input power of 61 MW, which corresponds to the desired average value of 100 MV/m. The problem is that the front of the structure needs to sustain a gradient of around 120 MV/m. In this region, the surface electromagnetic fields and power flow are much more intense than the specified at 100 MV/m unloaded operation.

The effect of the field profile change on the breakdown behaviour is hard to predict. The BDR of the whole structure varies approximately with the gradient as E_{acc}^{30}, given by Eq. (2.11), while the longitudinal dependency of the breakdown rate with the field is approximately linear, as given by the distribution of the longitudinal position of the breakdowns. The first experimental verification of the beam-loading effect on the BDR performance has been made at CTF3. A CLIC prototype has been tested in HG operation using Xbox-1 as the 12 GHz high-power source, while an electron beam produced at the CTF3 Drive Beam generation is delivered to load the structure.

Any advances in understanding this effect are crucial for the future directions of the CLIC study as they provide input for a full optimization of its design. In addition, beam-loading results are also of general interest for the HG community for different applications that requires similar beam-loading conditions, for instance, in FELs.

5.2 Experimental setup

The beam-loading experiment is carried out at CTF3 [108], the electron beam facility which is used to prove the key feasibility issues of the CLIC two-beam acceleration scheme. A layout of the facility is shown in Fig. 5.2.

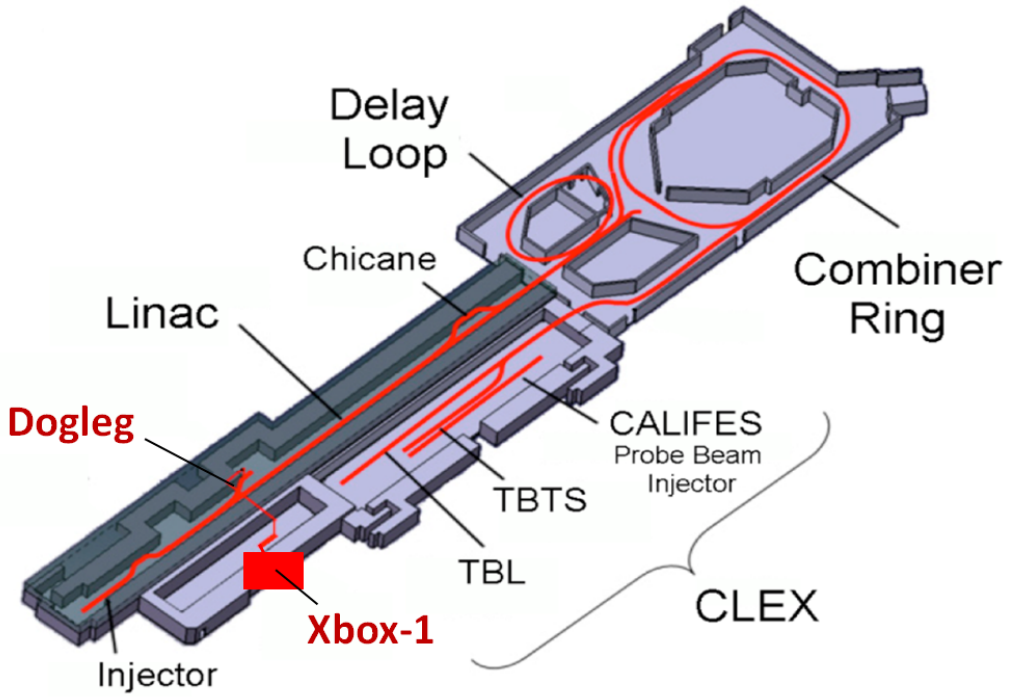

Figure 5.2: Layout of the CTF3 facility indicating the present subsystems and experiments.

One of the objectives of the CTF3 facility is the generation of a high-current electron Drive Beam needed for the production of the 12 GHz high-power to feed the HG accelerating structures of the CLIC Main Linac. The beam is accelerated in the CTF3 Linac TW structures in full-loading mode to maximize power efficiency, and is later manipulated in a series of delay lines and combiner rings, using injections by RF deflectors, in order to multiply the bunch frequency and achieve a current of 30 A with 140 ns-long trains of bunches. A second objective of the facility consists of testing the CLIC two-beam acceleration concept. The Drive Beam is delivered to an experimental area (CLEX) to be decelerated in the PETS and test the production of 12 GHz RF power. The Drive Beam can also be sent to the module of two PETS used to accelerate a probe electron beam with a dedicated injector (CALIFES) using four HG accelerating structures, in order to perform the two-beam acceleration.

The beam-loading experiment is placed at the dog-leg beam line that branches off

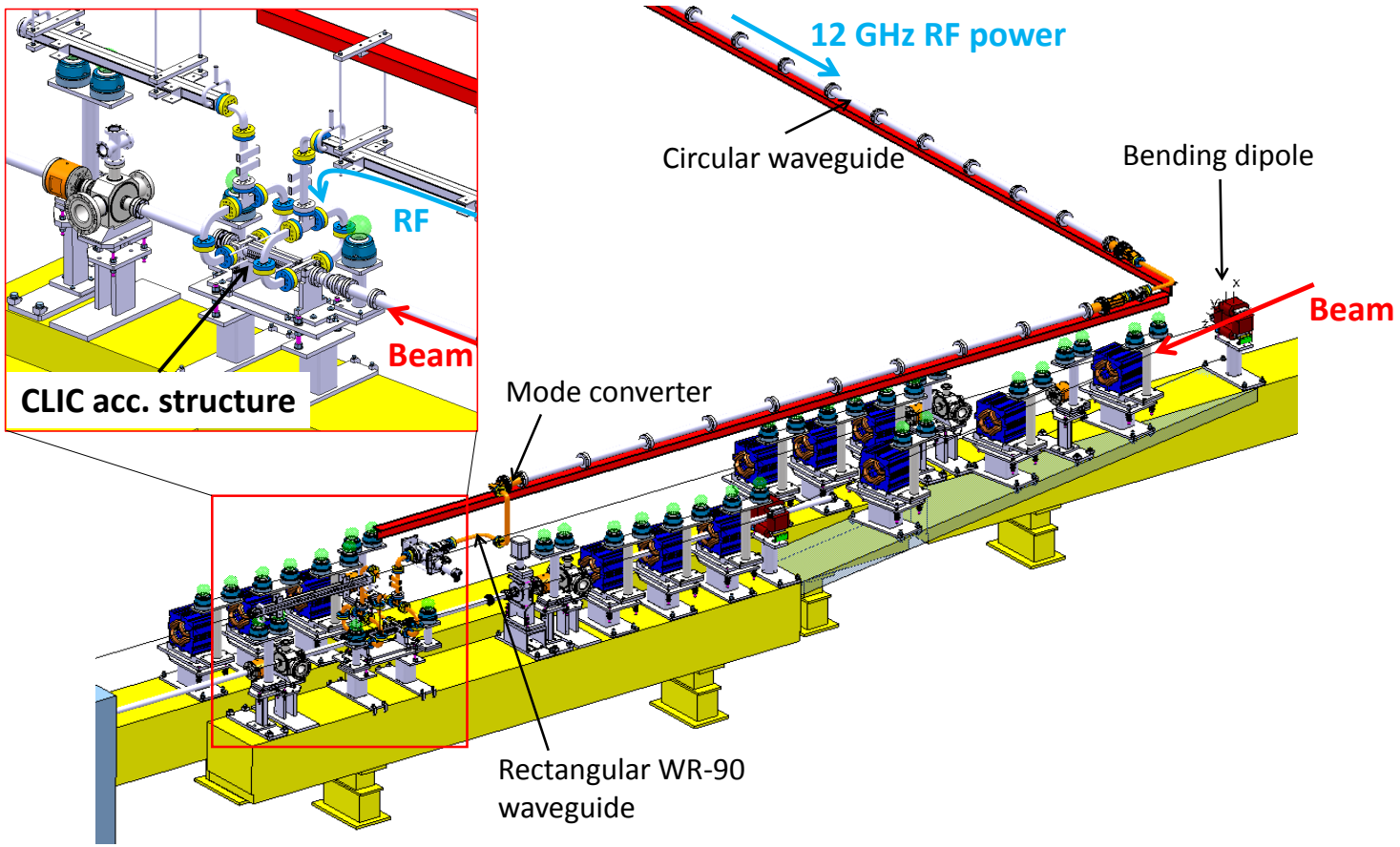

Figure 5.3: Drawing of the Dog-leg beam line at the CTF3 linac and experimental setup for the beam-loading experiment.

part-way along the CTF3 Linac to transport the beam to a HG prototype connected to the Xbox-1 RF source. The drawing of the dog-leg integration at the CTF3 Linac and the RF network installation are shown in Fig. 5.3.

5.2.1 The high-gradient structure under test

The beam-loading experiment presented here was done using a 12 GHz CLIC prototype, a TD26CC, consisting of a TW structure made of 26 regular cells and 2 coupling cells that include damping waveguides for HOM suppression [6].

An initial run of the experiment was already made in July 2014 with the first test of a T24 prototype [74], a TW 24-cell structure made in disks without damping waveguides for HOM suppression. A hot spot, that is an area where almost all the breakdowns occurred, was found at the front of the structure when the beam measurements started. A misalignment of the collimator before the structure was found, and the hot spot may have been produced by beam losses that damaged the surface of the front of the prototype. Since most of the breakdowns were triggered at the same region, the T24 prototype was not suitable for the experiment in order to distinguish the effect of the beam-loaded scenario with respect to the unloaded. For this reason, the T24 was replaced by the mentioned TD26CC structure in June 2015. This prototype had been previously conditioned and tested without beam at Xbox-1, when it was installed at the CTF2 bunker [76].

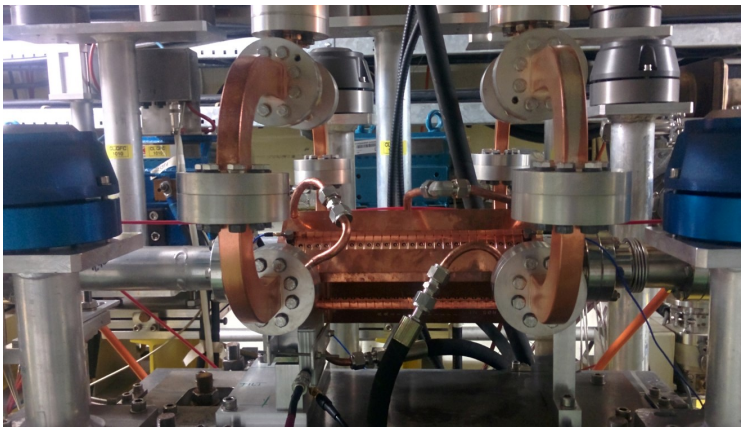

Figure 5.4: Picture of the TD26CC prototype installed at the dog-leg beamline in CTF3.

The TD26CC prototype was fully conditioned during 5 months in 2013 and, as already shown in Table 3.1, achieved an ultimate performance of 100 MV/m with 250 ns-long pulses at a BDR of 7×10^{-6} bpp/m. Unfortunately, the structure was accidentally vented to air for few weeks at the testing place because of a vacuum leak produced during the dismantling of the waveguide network. In order to remove

oxides which formed while the structure was exposed to air, the prototype was shortly baked-out at 650°C in the oven used for the thermal treatment of new HG structures. The prototype still showed a reduction of its performance when it was initially installed at the dog-leg beam line of CTF3 (see picture in Fig. 5.4). A reconditioning of the prototype was made from August to December 2015 using the standard automatic algorithm used in Xbox-1 [77].

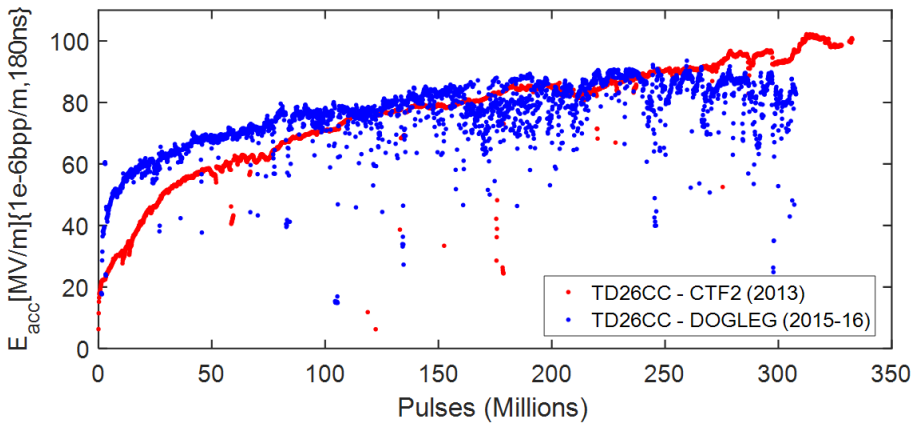

Figure 5.5: Conditioning histories of the TD26CC when tested at CTF2 (red) and at the dog-leg beam line (blue), represented by the accelerating gradient scaled to a constant pulse length of 180 ns and BDR of 10^{-6} bpp/m.

The TD26CC prototype requires 43.3 MW of input power to produce the nominal average accelerating gradient of 100 MV/m without beam. Figure 5.5 shows the conditioning history of the structure in terms of the scaled gradient with respect to the number of pulses and compared to the first conditioning made at CTF2 in 2013. After the bake-out the conditioning level of the prototype dropped to about 40%. The conditioning speed of the TD26CC prototype at the dog-leg was also observed to be slower than in the previous test. In addition, the structure showed a saturation of the conditioning level with a BDR of about 7×10^{-5} bpp/m when running at a gradient of 100 MV/m and pulse length of 180 ns. This corresponds to a maximum achievable accelerating gradient of only 84 MV/m at CLIC requirements of BDR and pulse length.

Despite the performance degradation, a conditioning saturation allows BDR measurements to be made during long periods of time assuming that the conditioning level will not change. Moreover, as the BDR is higher, more breakdown events are recorded and provides better statistics for the sake of a good comparison with the beam-loading conditions.

5.2.2 The CTF3 beam

The beam produced in the CTF3 Linac is used for the loading of the HG structure. It is generated from a thermo-ionic gun, which is capable of producing 4.5 A beam current in 1.5 μs-long pulses. The beam is bunched with a frequency of 3 GHz and is then accelerated up to 130 MeV using eight S-band TW structures powered by four 3 GHz klystrons, which are equipped with pulse compressor systems. A magnetic chicane, with a slit, between the second and third structure is used to reduce energy spread. A dipole magnet is located 20 m after the gun and diverts the beam to the dog-leg line towards the CLIC HG structure. A lattice of quadrupole magnets are used to focus the beam and optimize the beam transmission through the structure under test.

In order to measure the energy and beam optics along the line, a spectrometer and screen are installed further down the linac after the dog-leg dipole. The Twiss parameters are measured by a quadrupole scan, in which the beam size is measured at the screen while the quadrupole strength is varied. The nominal design of the optics was made in MAD-X to fulfill the beam requirements for the experiment [110]. The measured horizontal and vertical β functions and the horizontal dispersion are shown in Fig. 5.6. The configuration of the optics is designed to cancel the horizontal dispersion in the straight part of the dog-leg line and to minimize the beam size at the structure so that the beam transmission is maximized. Since the structure is tapered from an aperture diameter of 6.3 mm to 4.7 mm, the beam is squeezed towards the downstream end to ensure a good transmission. Moreover, an 8 mm-diameter collimator was installed before the structure at an optimized longitudinal position in order to protect it from energy spread induced beam losses. The present configuration offers operation flexibility to provide beam pulses of up to 1.6 A, 250 ns and 130 MeV, with a maximum repetition rate of 50 Hz. A regular operation at 25 Hz is performed at full maximum RF power into the structure of 43.3 MW, for the sake of stability from the Xbox-1 RF system.

A series of inductive Beam Position Monitors (BPM) [111] are installed along the linac and dog-leg lines in order to measure the beam current and its transverse (horizontal and vertical) position. These measurements are necessary for the evaluation of the beam transmission to the HG prototype and guarantee a stable beam-loading. One BPM is located upstream the structure before the collimator (BPM1) and another one downstream (BPM2). Figure 5.7 shows the acquired BPM1 and BPM2 signals for the loading with a beam current of 1.6 A and pulse length of 200 ns.

5.2.3 The RF system

After the conclusion of the first HG test of the TD26CC prototype [76], the Xbox-1 network was prepared for the beam-loading experiment. In 2014, the waveguide

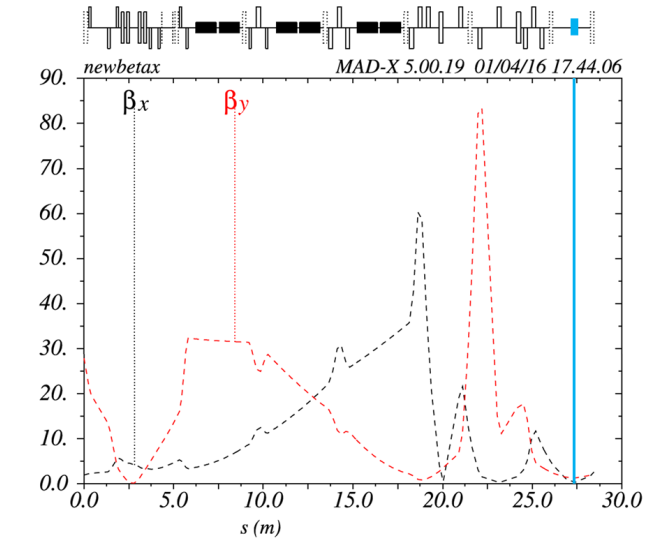

(a)

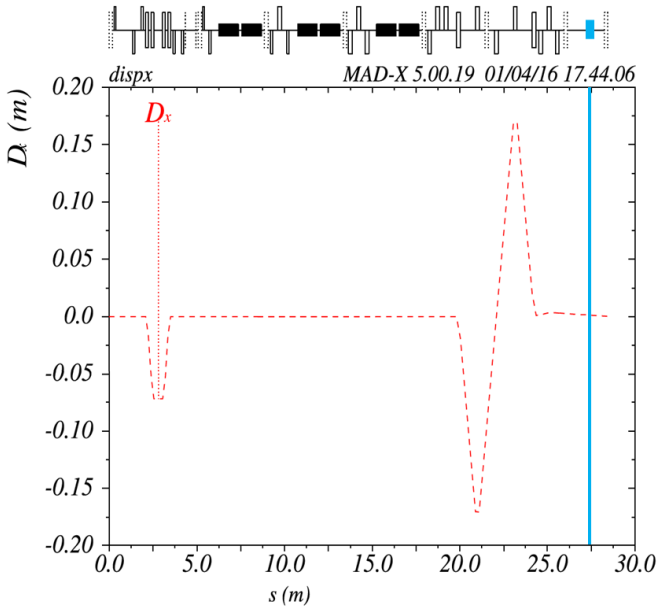

(b)

Figure 5.6: Reconstruction of the (a) horizontal and vertical β functions and (b) horizontal dispersion function from the injector to the end of the dog-leg beamline, from the beam measurements performed in April 2016 [109]. The position of the structure under test is indicated with a blue line. The dotted elements on top represent the position of the BPMs.

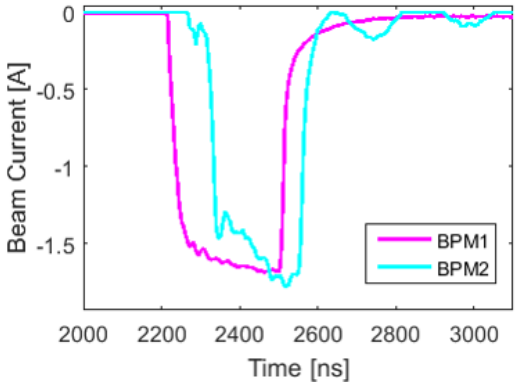

Figure 5.7: Beam current measured at the BPMs, upstream (BPM1) and downstream (BPM2) the structure under test.

network was disconnected from the prototype in CTF2 and extended towards the CTF3 linac in order to connect to the HG prototype installed in dog-leg [112].

Figure 5.8 shows the full diagram of the RF and controls systems that is used for operating the beam-loading experiment. The low-level and high-level RF systems (yellow box) have been already described in Section 3.2.1. The X-band klystron combined with the SLED-I pulse compressor is capable of providing up to 140 MW in 250 ns-long pulses.

The experiment also makes use of the Xbox-1 control and acquisition system (green box) employed for the test of HG structures, based on National Instruments electronics. The NI PXI controller is equipped with FPGA-based digitizers for the signal reading and interlocking. The system is integrated in the main CTF3 trigger board so that the RF pulses are synchronized with the beam pulses at the same repetition rate.

The 35 m-long waveguide network from the pulse compressor to the structure is composed of different sections of WR90 rectangular waveguides and circular over-moded waveguides, the latter being subject to smaller power losses. One straight circular-waveguide section, installed between the klystron gallery and CTF2, needed to be replaced by a new rectangular waveguide due to strong breakdown activity observed in one of the mode converter components. The total attenuation of the waveguide network to the input coupler of the structure was measured by the reflectometry technique using one-port Vector Network Analyzer (VNA) measurements. A value of 61% of power transmission was obtained, which means that 72 MW are needed from the pulse compressor output to feed the structure with the required power of 43.3 MW. The optimization of the pulse compressor operation will be described in more detail in Section 5.3.2.

Along the waveguide network, several ion pumps and vacuum gauges are installed

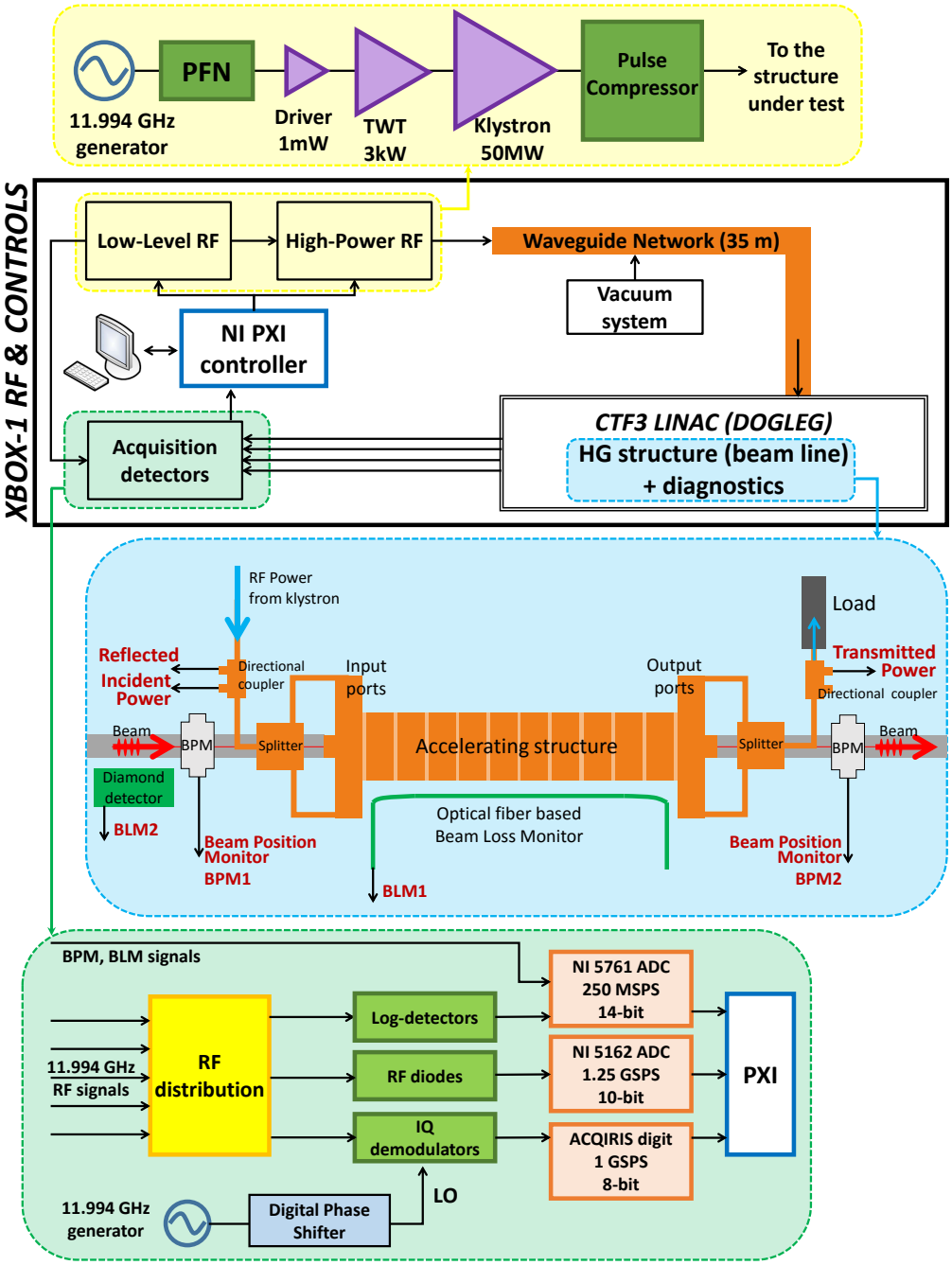

Figure 5.8: Layout of the RF system, controls and diagnostics for the beam-loading experiment, including the low-level and high-power RF components (yellow box), hardware for breakdown studies (blue box) and data acquisition system (green box).

and connected to the waveguide network through RF pumping ports in order to preserve and monitor the ultra-high vacuum at the waveguides and the structure. The measurement of ion pump current and the gauges signals are connected to the Xbox-1 acquisition system for on-line measurement and data logging. Ion pumps are located at the klystron output and close to the pulse compressor to monitor the vacuum level in the components in order to assure their good performance. Further pumps are strategically installed to cover long straight sections and close to the mode converters between circular and rectangular waveguides. The high peak power that is required to test the structure is high enough to occasionally produce a strong breakdown activity in the RF components and waveguides. Ion pumps ensure the recovery of the vacuum to 10^{-7} mbar at the waveguides and below 10^{-9} mbar at the structure. The occurrences of vacuum arcs at the waveguide network results into a sharp jump of the pressure, and its measurement at the different stations can be used to estimate the position of such breakdowns.

5.2.4 Structure breakdown diagnostics

A complete setup has been installed around the structure for the detection and analysis of breakdown events during the high-power operation with beam-loading. The employed instrumentation is based on the same high-power test setups that are used at the Xbox test stands, adapted for the beam-loading experiment. A layout of the acquired signals from the structure is shown in Fig. 5.8 (blue box).

As is standard in testing TW structures, three RF power signals are acquired to evaluate the performance of the structure: incident to (INC), reflected from (REF) and transmitted through (TRA) the prototype. These signals are extracted at two bi-directional couplers located in the waveguide network before and after the structure. The signals are delivered to the acquisition rack via N-type coaxial cables. The RF power is split to be detected with log-detectors, RF diodes and IQ-demodulators, and the signals are digitized in different ADCs that are processed by the LabVIEW software in the PXI controller. The signals of beam current measured at the BPMs located before (BPM1) and after (BPM2) the structure are also sent to the PXI controller to be recorded. Additionally, two Beam Loss Monitors, consisting of an optic fiber (BLM1) extended in parallel to the prototype [88] and a diamond detector (BLM2) located close to the input beam pipe, were installed to measure the possible beam losses in the structure. These systems can also be used for the dark current and breakdown current measurement when the experiment is operated without beam. A TDMS-file is built every 8 hours with the acquired signals of all detected breakdown events, and regular pulses are also stored every minute even when no breakdown has been detected.

5.3 The Xbox-1 operation

The Xbox-1 software and pulse configuration has been adapted for the beam-loading experiment. We will present here the modifications and upgrades of the system that were required for the experiment, such as the configuration of the RF waveform, the tuning of the pulse compressor, the RF phase feedback loop and the breakdown detection logics.

5.3.1 The incident RF waveform

The TD26CC prototype was initially reconditioned, from August 2015, at the dog-leg beam line with rectangular-shaped pulses of 100, 150 and 200 ns. In November 2015, the incident RF power was configured to reproduce the CLIC nominal pulse shape that would be formed at the PETS of the two-beam scheme. This pulse is characterized, as seen in Fig. 5.9, by a linear ramp of about 90 ns rising time before achieving the flat-top level. This profiled initial fill of the structure is needed in order to compensate the bunch-to-bunch energy gain variation due to the transient of the beam-loading [13]. This pulse shape was chosen to test the HG structure with beam.

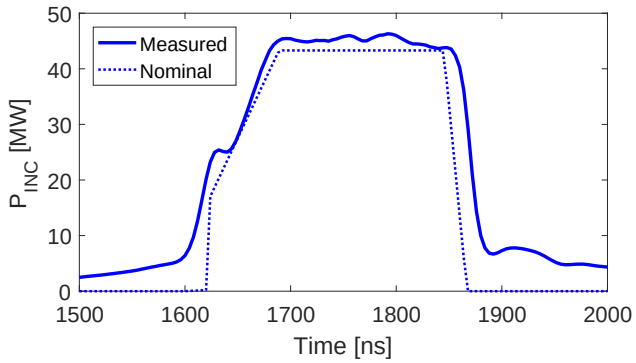

Figure 5.9: Pulse of the incident RF power to the structure for the beam-loading experiment, measured at the input directional coupler with log-detectors (solid line) and compared with the CLIC nominal pulse shape (dotted line) from [13].

Since the phase of the RF waveform is manipulated to perform the RF compression at the pulse compressor system, the phase of the incident RF waveform had to be matched with the phase of the train of bunches in order to produce a constant beam loading. The manipulation of the RF phase is done at the low-level RF stage by controlling the fast analogue phase shifter of the Pulse Forming Network (PFN). The phase waveform that controls the phase shifter is represented in Fig. 5.10, which

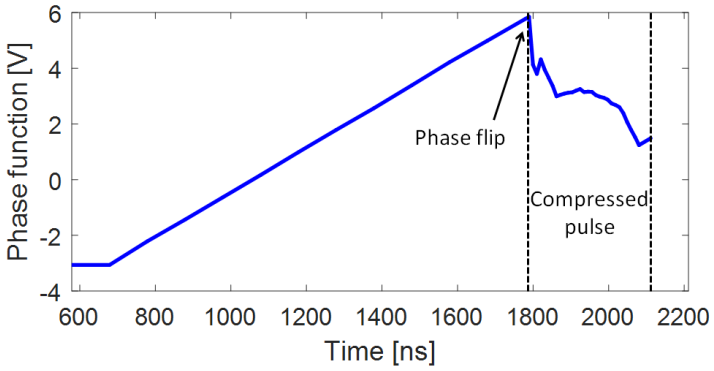

Figure 5.10: Phase function (voltage signal), configured in the analog phase shifter of Xbox-1, that is applied to the RF pulse waveform generator.

remains unchanged during the full experiment, and has been optimized for a constant beam-loading in time. A linear ramp of the phase is made during the charging stage of the pulse compressor cavities and a phase flip is applied for the start of the compressed pulse. The phase profile of the compressed pulse is then configured to obtain the nominal pulse shape. This profile guarantees a good phase match with the train of bunches, which present the same phase sag.

Maximum beam-loading is achieved when all bunches of the pulse are on the crest of the RF wave, where the acceleration is maximum. The strongest loading is found by a scan in phase with the digital phase shifter, at the low-level RF PFN of Xbox-1. The RF phase is varied to minimize the transmitted power at the output coupler of the structure after the structure. This is the condition when the absorption of RF power by the beam is maximum. The result of the **loaded** mode is a low, flat transmitted power signal, as shown in Fig. 5.11(a), due to a constant beam-loading of the full RF pulse. When this phase is inverted by 180 degrees, the beam is decelerated and produces RF power that is detected at the transmitted power channel, as can be observed in Fig. 5.11(b). The maximum decelerating mode, also called the **anti-loaded** mode, is also under study for the experiment to analyse its effect on the BDR performance.

5.3.2 Tuning of the pulse compressor

The 35 m-long waveguide network that connects the high-power source to the HG prototype generates a power loss of about 39%. For this reason, a pulse compressor system is necessary to provide sufficient power to the structure and achieve the nominal 100 MV/m. At least 72 MW of peak power in 200 ns-long pulses are required from the pulse compressor to receive 43.3 MW in the HG prototype. The SLED-I type pulse compressor (see picture in Fig. 5.12(a)) consists of two high-

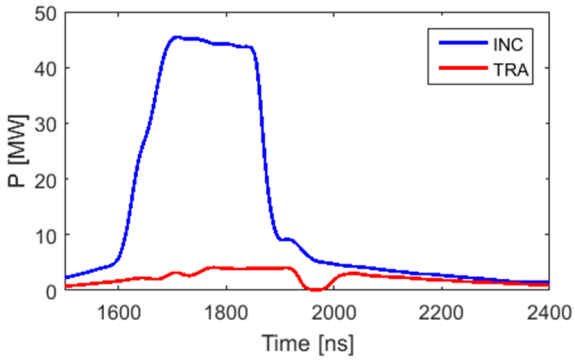

(a)

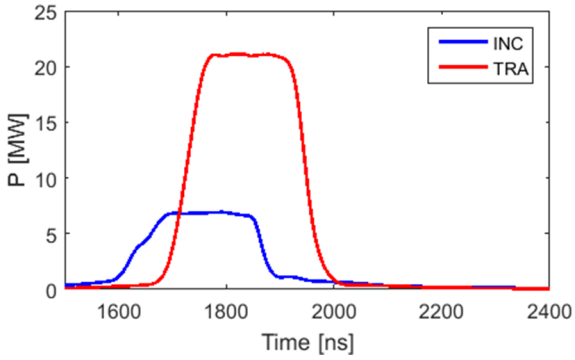

(b)

Figure 5.11: Signals of the compressed pulse of the incident (INC) and transmitted (TRA) RF power, acquired by log-detectors, when operating in (a) loaded mode for 43.3 MW incident power and (b) anti-loaded mode for 6.5 MW incident power.

Q resonant cavities overcoupled to the waveguide system by a 3 dB hybrid. The incoming RF power is split to feed both cavities while the reflected power from each cavity is combined and redirected to the output port of the system. The phase manipulation provides a higher peak power at the expense of pulse width [113]. An important fraction of the RF power is dissipated in the cavities of the pulse compressor and the excess of power heating deforms their geometry. The resonant frequency of the cavities is very sensitive to geometry variations due to their high intrinsic quality factor of the order of 10^5. The frequency mismatch between the input RF and the resonant cavities produces high reflections towards the klystron.

A good stability of the pulse compressor operation is crucial for the development of the experiment. Strong fluctuations in temperature due to variations of the operated power affect to the pulse compression, specially when either the structure or the waveguide network suffers from a cluster of several breakdowns. In this case,

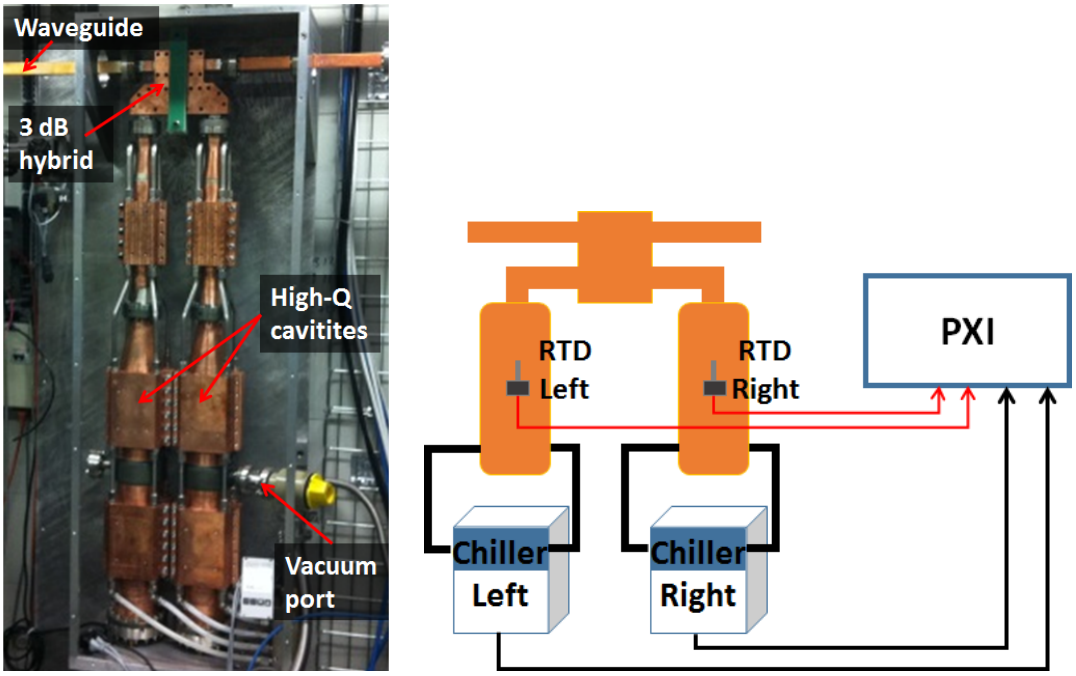

Figure 5.12: Pulse compressor system installed at Xbox-1: (a) picture of the system inserted at the Xbox-1 network and (b) scheme of the temperature control with water-cooling chillers and measurement of temperature at the walls of each cavity with RTDs.

the system interlocks and waits after 3 seconds to restart the pulsing, thus the cavities cool down and get detuned. For this reason, a tuning algorithm of the pulse compressor has been implemented to compensate the deformation of the cavities due to temperature variations.

Initially, the pulse compressor cavities were tuned with pistons integrated at the bottom end, moved by stepper motors in order to compensate the variations in volume by thermal effects [81]. At the start of the beam-loading experiment, a strong vacuum activity in the pulse compressor was found due to the need of higher peak power and, possibly, a poor thermal contact of the moving part of the pistons. In 2015, the pistons were removed and the system was tuned by the temperature control of the cavities using SMC water-cooling chillers. The control of the temperature of the chillers is done by the NI PXI controller, communicated by serial connection as schematized in Fig. 5.12(b), and can be changed via the LabVIEW's user interface at the computer. The temperature of the cavities is also acquired with Resistance Temperature Detectors (RTD) attached to the outer copper walls of each cavity. An automatic control of the chillers temperature has been implemented to compensate the temperature variations in the cavities due to changes of driving power.

The tuning algorithm is based on the flattening of the incident power pulse, $P_{INC}(t)$, to the structure and the reduction of the reflected power from the pulse compressor to the klystron, $P_{KR}(t)$. The algorithm evaluates numerically two quantities: the slope S of the incident flat-top pulse, and the ratio K between the integral of two parts of the reflected power signal, and both are given by the following expressions:

$$S = \sum_{t_1}^{t_2} \Delta P_{INC}(t) \tag{5.1}$$

$$K = \frac{\sum_0^{t_c} P_{KR}(t)}{\sum_{t_c}^{t_{end}} P_{KR}(t)} \tag{5.2}$$

where ΔP_{INC} is the variation of the incident power between two consecutive signal samples, (t_1, t_2) is the range of the pulse flat-top to calculate the slope, t_c is chosen at the start of the compressed pulse (phase flip) and t_{end} is the last acquired sample of the signal. The timing parameters t_1, t_2 and t_c are optimized by the operator. The goal of the algorithm consists of keeping both S and K parameters within an acceptance range in which the pulse compressor is well tuned. The boundaries of this range are defined by the user according to the obtained experience during the operation.

On one hand, the parameter S is obviously a good indicator of the pulse flatness. On the other hand, the parameter K is correlated to the amount of energy that is reflected from the pulse compressor to the klystron. When this parameter is either very large or very small, the reflection becomes very large because the resonant frequencies of each cavity move away in opposite directions, resulting in a phase mismatch that transmits part of the RF power towards the klystron. The acceptance band of the slope S is centered at zero, since we aim at achieving a flat pulse, and the parameter K is usually set in the interval $[0.8, 4]$.

When the temperature of the cavities is varied by, for example, chiller water temperature, the reaction in the parameters S and K is observed after about a minute, as the thermal processes changes the cavity geometry very slowly. The correction of the slope S and the parameter K, in steps of 0.1°C for each chiller, is made every 1 minute and 3 minutes, respectively. In order to avoid a excess of correction of the slope and an unstable feedback, the algorithm calculates a projection S^* of this parameter after 3 minutes based on the trend that is followed in the previous pulses. This is very useful, for instance, when S is increasing faster but is not in the acceptance range yet, in order to stop varying the chiller temperatures as it assumes that the slope will keep increasing for some more time. The projection is calculated as follows:

$$S^* = S + \frac{\mathrm{d}S}{\mathrm{d}t} \cdot T \tag{5.3}$$

where $T = 3$ minutes is the projection time and the derivative $\mathrm{d}S/\mathrm{d}t$ is calculated numerically from the slope of the last 25 s.

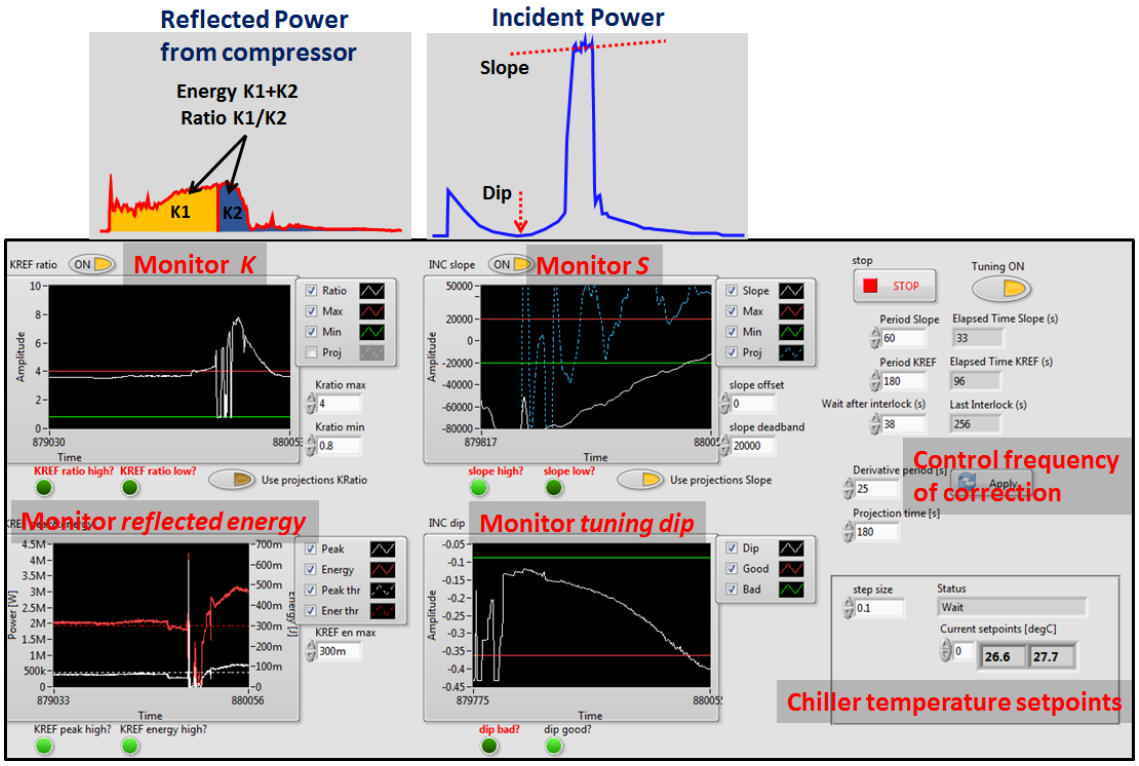

Figure 5.13: LabVIEW's VI front panel of the automatic pulse compressor tuning algorithm implemented in the Xbox-1 operation software.

The screenshot of the front panel of the software, made in LabVIEW, in which the tuning algorithm has been implemented can be found in Fig. 5.13. It calculates the slope S and the ratio K of the acquired pulses and checks whether they are within the acceptance ranges. In case one of the parameters is out of range, the algorithm applies a correction of the chiller temperature in steps of 0.1°C. The direction (increment or decrement) of the temperature correction is summarized in Table 5.1. When the slope S is positive and too large, the resonant cavities of the pulse compressor are too warm and the algorithm decreases the temperature of both chillers. Conversely, when the slope is negative and too small, the temperature of both chillers is increased. In the case that the parameter K is too large, the the left chiller temperature is increased and the right one is decreased, and viceversa.

The tuning algorithm has allowed the pulse compressor detuning to be compensated with an automatic control of the temperature of the cavities that follows the fluctuations of the room temperature and also the big variations in power that is

Table 5.1: Criterion for the temperature correction of the water chillers in the pulse compressor system, implemented in the tuning algorithm.

Chiller	**Parameter** S		**Parameter** K	
	Too large	Too small	Too large	Too small
Left cavity	↓	↑	↑	↓
Right cavity	↓	↑	↓	↑

dissipated in the compressor. In the case of strong detuning produced by a large rate of interlocks in the system, the algorithm needs at least 3-5 minutes to retune the pulse compressor and recover the original state. The operation at the nominal power of 43.3 MW in the structure and at a repetition rate of 50 Hz has been often dominated by periods in which the pulse compressor is detuned. The repetition rate has been lowered to 25 Hz for the beam-loading experiment in order to be less sensitive to power variations, and the tuning stability has proven to be satisfactory. A better thermal design of the pulse compressor has been implemented in subsequent versions of pulse compressor.

5.3.3 Phase feedback loop

The generated RF must be stable both in power and in phase in order to ensure that the beam-loading of the structure, thus the field profile, is constant during the measurement period. The klystron is a non-linear RF system and the phase of the output wave changes when varying only the amplitude of the input wave from the low-level RF system. For this reason, a phase feedback loop has been implemented to the Xbox-1 software in order to control and keep the phase of the incident RF power to the structure constant.

A screenshot of the LabVIEW's VI front panel of the phase feedback loop is shown in Fig. 5.14. The algorithm consists of a 'proportional-gain' loop which iteratively controls the digital phase shifter at the PFN of the low-level RF system based on the acquired phase of the incident RF pulse to the structure. The measurement is made by IQ demodulators and an average of the phase during the pulse flat-top is taken. The algorithm evaluates the error of this measured phase ϕ_{meas} with respect to the target phase ϕ_{sp}, and the control V_i of the digital phase shifter is varied according to the following formula:

$$V_{i+1} = V_i + k_p \cdot (\phi_{\text{sp}} - \phi_{\text{meas}}) \tag{5.4}$$

where k_p is the proportional gain factor of the iteration, defined by the operator. The higher the phase error $(\phi_{\text{sp}} - \phi_{\text{meas}})$, the bigger the step made at the phase

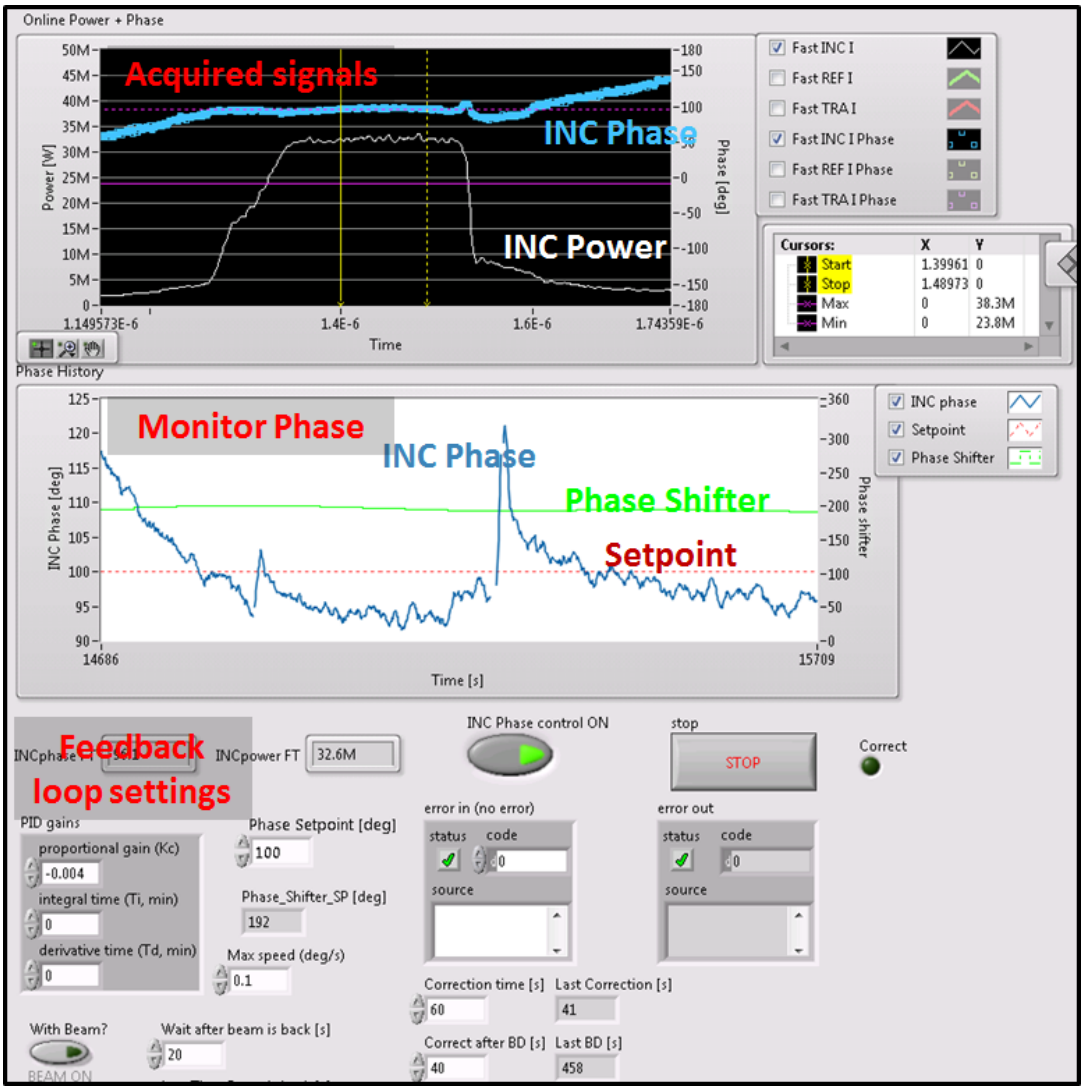

Figure 5.14: LabVIEW's VI front panel of the automatic phase feedback loop implemented in the Xbox-1 operation software.

shifter to correct the RF phase. The current algorithm only works at one iteration per minute, since it is designed to correct possible phase drifts due to the detuning of the pulse compressor. The loss in the compression ratio should be compensated with more power from the klystron and, consequently, a drift in the RF phase. The phase loop follows the slow tuning variations controlled by the tuning algorithm.

The history of the experiment operation during a 24 h-run is shown in Fig. 5.15, with the deceleration of a 1.6 A beam (anti-loaded). It can be noticed that the RF phase of the incident power is kept constant, with fluctuations of ± 3 deg, and the

transmitted power after the structure is stable. This proves that the feedback loop allows optimizing the loading conditions for the experiment.

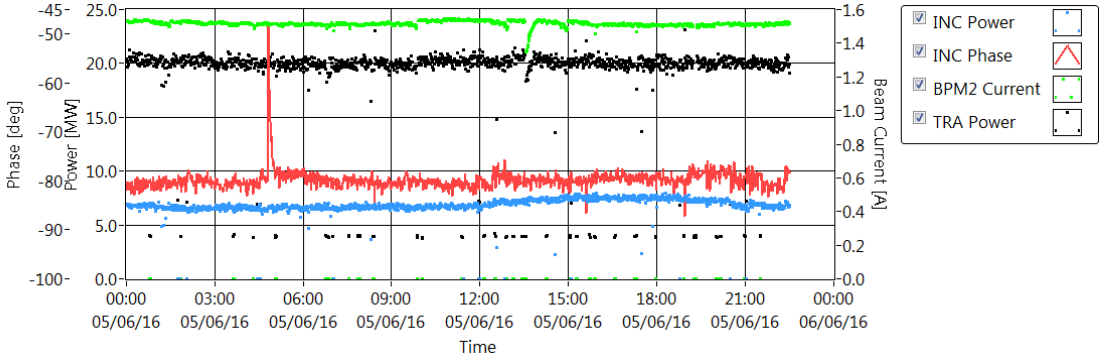

Figure 5.15: History of a 24 h-run of the beam-loading experiment (in anti-loaded mode) at 6.5 MW incident power to the structure. The figure represents the peak incident power (blue dots), peak transmitted power (black dots), beam current (green dots) and the incident RF phase (red line). The phase feedback loop was active during this run to keep a stable RF phase with maximum fluctuations of ± 3 deg.

5.3.4 Breakdown detection

The techniques employed for the detection of breakdowns in HG tests [93] are based on the rise of the reflected power and the breakdown currents measured with Faraday cups at both ends of the structure (see Chapter 3). However, for the beam-loading experiment, there is no possibility to insert Faraday cups in the beam line as diagnostics for breakdown detection. Other external current detectors, such as the Beam Loss Monitors (BLM), are blind for measuring breakdown currents because of the intense beam currents during the experiment.

We have modified the software for breakdown detection to react only to the incident, reflected and transmitted RF signals, acquired via bi-directional couplers before and after the structure. The three RF signals are processed in logarithmic detectors and digitized at the NI-5761 FPGA-based ADC integrated in the PXI controller. The ADC obtains the voltage signals of the incident $V_{INC}(t)$, reflected $V_{REF}(t)$ and transmitted $V_{TRA}(t)$ RF power, shown in Fig. 5.16(a). The FPGA configures the logics to interlock the system when a breakdown is detected by these signals.

A breakdown in one cell iris of the structure produces the rise of the reflected power and the drop of the transmitted power, as observed in the event of Fig. 5.16(b). Taking this into account, three criteria are implemented in the FPGA logics to interlock the system when at least one of them is satisfied:

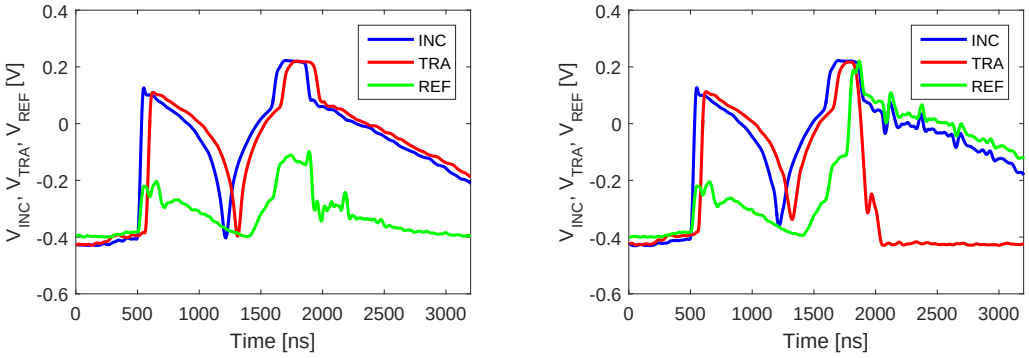

Figure 5.16: Raw signals from log-detector of the incident (INC), reflected (REF) and transmitted (TRA) power of (a) a regular event and (b) a breakdown event.

1. **Peak reflected power**: when the waveform of the reflected signal $V_{REF}(t)$ exceeds a certain threshold I_1^{max}.

$$I_1[\mathrm{V}] = \max(V_{REF}(t)) > I_1^{max}[\mathrm{V}] \tag{5.5}$$

2. **Reflected energy**: when the energy of the reflected signal $V_{REF}(t)$ is greater than a certain threshold I_2^{max}.

$$I_2[\mathrm{bits}\cdot\mathrm{samples}] = \sum_{0}^{t_{end}} V_{REF}(t) > I_2^{max}[\mathrm{bits}\cdot\mathrm{samples}] \tag{5.6}$$

3. **Missing transmitted energy**: when the transmitted signal decreases $V_{TRA}(t)$ and its energy is lower than the incident one $V_{INC}(t)$, based on a certain threshold I_3^{max}.

$$I_3[\mathrm{bits}\cdot\mathrm{samples}] = \sum_{t_0}^{t_{end}} (V_{INC}(t) - V_{TRA}(t + t_{fill})) > I_3^{max}[\mathrm{bits}\cdot\mathrm{samples}] \tag{5.7}$$

   Here, the integration of the signals is made from the start of the compressed pulse t_0, and the transmitted signal is shifted one filling time t_{fill} to be aligned with respect to the incident signal. Notice that no power calibration is made in the FPGA level due to excessive processing time. Extra interlocks are adopted for safety purposes, such as vacuum level and reflections to the klystron.

In order to test the effectiveness of the interlock system presented here, a statistical analysis of breakdown and non-breakdown events has been made. Figure 5.17

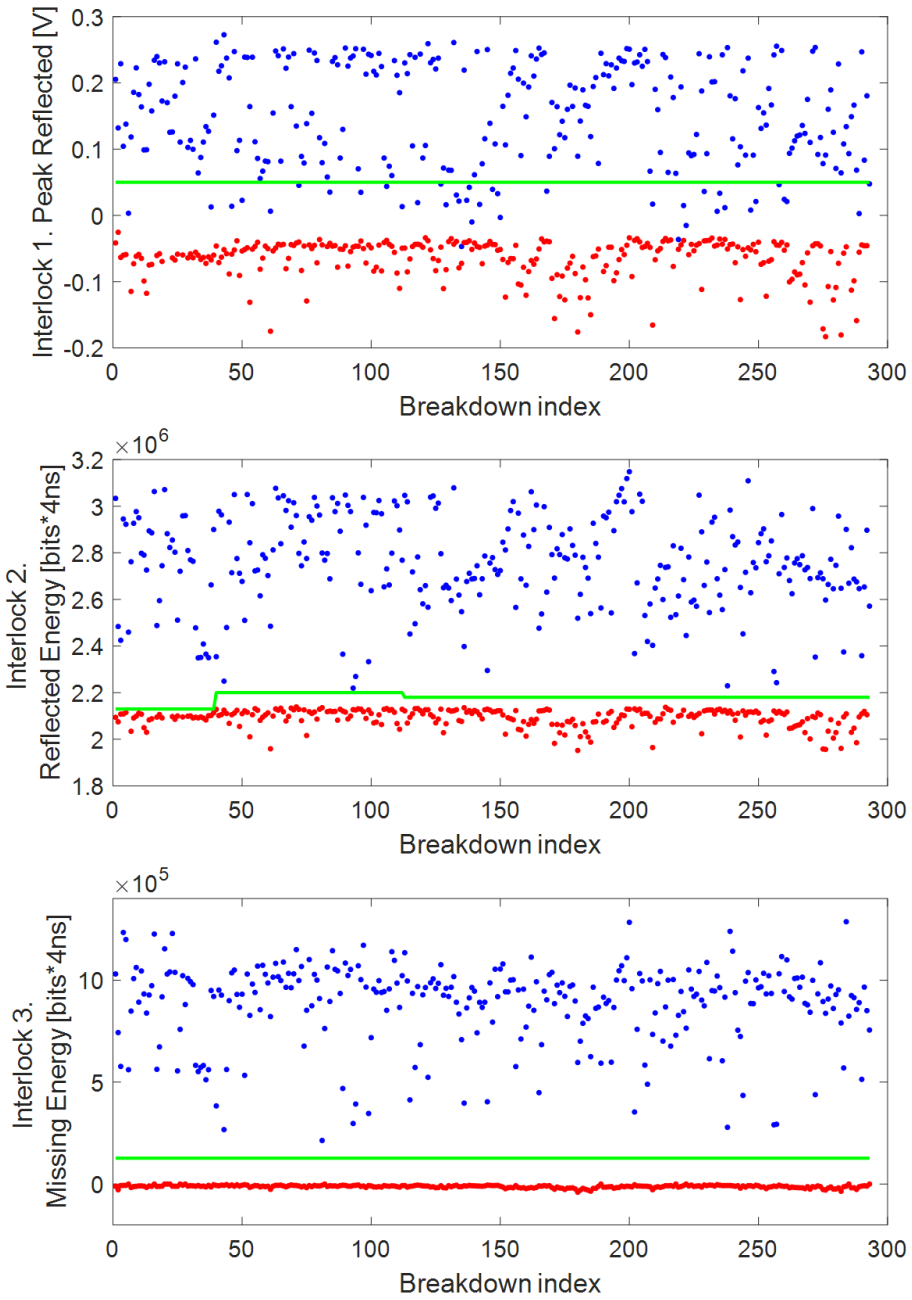

Figure 5.17: Interlock values of peak reflected power, reflected energy and transmitted missing energy, given by Eqs. (5.5), (5.6) and (5.7), for a set of 293 breakdown pulses (blue dots) and the previous non-breakdown pulses (red dots) in a TD26CC structure under test. The threshold set for each interlock is also shown (green solid line).

shows the interlock values given by Eqs. (5.5), (5.6) and (5.7) for a subset of 293 breakdown pulses, together with their non-breakdown previous pulse, recorded during the conditioning of the TD26CC structure. The peak reflected power interlock I_1, calculated from the voltage signal of the log-detector, shows a smaller difference between breakdown and non-breakdown pulses. This is explained by the logarithmic conversion made by the log-detectors. As the reflected power increases with the incident power level, this interlock needs to be adjusted depending on the operating power. Nevertheless, interlocks I_2 and I_3 are proposed to better detect breakdowns with low reflections. The interlock values of the reflected energy and the missing transmitted energy have been calculated in Fig. 5.17 by the integration of the acquired bits in the ADC over all the samples (with a time resolution of 4 ns). For these interlocks, the distinction between breakdown and regular pulses is bigger hence they represent a good criterion to detect vacuum arcs. As the measured transmitted energy drops when the structure is loaded with the beam, the transmitted missing energy I_3 increases and the threshold needs also to be adjusted to a higher level. Interlock thresholds are revisited before every measuring period. I_1, I_2 and I_3 values are calculated on-line from the acquired signals and the breakdown thresholds are set slightly above. A margin of about 4-5 standard deviations is usually left in order to take into account possible fluctuations of the measured values.

The interlock values of a larger subset of 579 breakdowns, occurred during February 2016, are plotted in a histogram in Fig. 5.18 to analyse the statistical distribution of all the events. A total of 9555 regular pulses without breakdown, recorded every minute, have been also represented for comparison in the same figure. One can observe that the interlocks based on the reflected energy and missing transmitted energy present better resolution than the peak reflected power to distinguish between breakdowns and non-breakdown events. Consequently, the lack of Faraday cup signals in the beam-loading experiment can be compensated by the use of interlocks I_2 and I_3.

Due to their good resolution, they represent good extra criteria in breakdown detection for other high power RF tests, and will be implemented in the near future for Xbox-2 and Xbox-3. The redundancy given by different criteria would ensure that the system is not missing any event of potential interest. For the same subset of 579 breakdowns, nearly 90% of the events have been detected by all three interlock criteria I_1, I_2 and I_3. For the rest of the events, interlock I_1 was missed because the threshold in the reflected signal was set too high. This proves that the redundancy of the interlock logics works effectively and reinforces the capabilities of detecting a vacuum arc if any of the other interlocks fails.

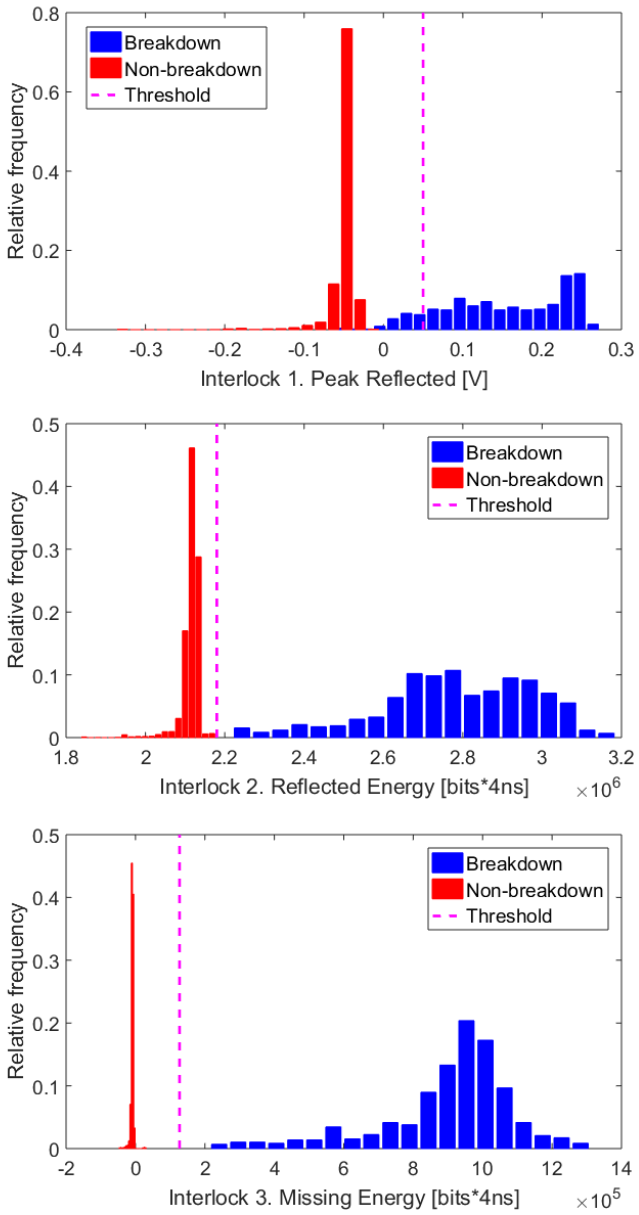

Figure 5.18: Histograms of interlock values of peak reflected power, reflected energy and missing transmitted energy, calculated on a set of 579 breakdown (blue bars) and 9555 non-breakdown (red bars) events recorded in a TD26CC structure under test during February 2016 run, and threshold (pink line) settings of breakdown detection.

5.4 Beam-loading measurements and results

After finishing the conditioning process of the TD26CC prototype, beam-loading measurements started in March 2016. Running was subject to the availability of the CTF3 electron beam at the dog-leg beam line. The beam was fully dedicated to the beam-loading experiment during the weekends and other extended week days. The Xbox-1 software was in charge of the automatic control of pulse triggering, RF power and phase, pulse compressor tuning, breakdown detection and interlocking, and data logging. A fixed beam current and pulse length was set from the CTF3 control system.

5.4.1 Breakdown rate measurements

A summary of the measurement runs performed with and without beam can be found in Table 5.2, including the measurement dates, the input power, the beam current and the count of triggered pulses and detected breakdowns for each period. A statistical measurement of breakdowns was made in unloaded, loaded and anti-loaded conditions, using a beam current of 1.6 A. This current is intentionally higher than the nominal CLIC current to increase the loading and to amplify an eventual effect on the BDR. The structure was strategically tested with 43.3 MW input power without and with beam, corresponding to an average gradient of 100 MV/m (unloaded) and 75 MV/m (loaded), in order to compare BDR performances at the same incident power. For the sake of completeness, the structure was also tested with an unloaded gradient of 75 MV/m, at 24.6 MW input power. Finally, a test of the prototype at 6.5 MW input power was performed in anti-loaded (decelerating)

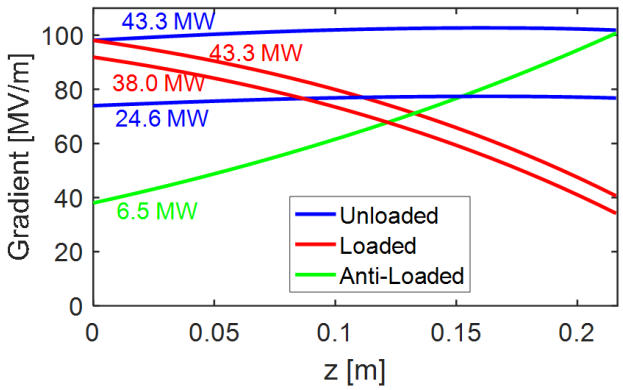

Figure 5.19: Longitudinal accelerating gradient profile for the CLIC structure under test unloaded (blue lines) at 43.3 and 24.6 MW input power, with 1.6 A of beam loaded (red line) at 43.3 and 38.0 MW, and anti-loaded (green line) at 6.5 MW input power.

mode by inverting the RF phase by 180 degrees, as explained in Section 5.3.1. This measurement provides the same gradient of 100 MV/m at the last cell of the structure, to be compared with the unloaded case at 43.3 MW. Figure 5.19 shows the accelerating gradient steady-state profile, calculated using Eq. (1.39), of each of the performed measurements.

Table 5.2: Experimental conditions of input RF power P_{in}, repetition rate, beam current I_{beam} and loading scenario, for the various BDR measurements in the beam-loading experiment. The accumulated number of pulses n_{pulses} and detected breakdowns N_{BD} have been included for each measurement period.

Period	P_{in}**[MW]**	**Rep.Rate[Hz]**	I_{beam}**[A]**	**Loading**	n_{pulses}	N_{BD}
24/02-01:00 01/03-12:00	43.3	50	0	Unloaded	22517650	368
04/03-19:30 07/03-08:00	43.3	10	1.6	Loaded	1057750	12
22/03-19:00 24/03-15:00	43.3	50	0	Unloaded	7279050	113
24/03-18:30 30/03-16:00	43.3	10	1.6	Loaded	4070150	52
30/03-20:00 31/03-17:00	24.6	50	0	Unloaded	3672400	5
31/03-18:00 04/04-02:00	43.3	25	1.6	Loaded	6007950	174
04/04-18:30 08/04-16:00	6.5	25	1.6	Anti-loaded	8112500	76
08/04-17:30 09/04-21:15	38.0	25	1.6	Loaded	2242600	4
15/04-18:45 16/04-17:00	43.3	25	1.6	Loaded	1338800	12
22/04-18:00 25/04-10:00	43.3	25	1.6	Loaded	4222050	32
29/04-17:00 30/04-11:30	43.3	25	1.6	Loaded	1339500	12
04/05-18:20 09/05-09:30	43.3	25	1.6	Loaded	8391700	128

Some of the measurements have been repeated in order to have more statistics of breakdown events and have a better estimation of the BDR. Table 5.3 shows the results of the BDR averaged from the total number of breakdowns and pulses measured during the periods with the same conditions of input power and loading. The results of BDR are shown in Fig. 5.20 with respect to the average gradient in

the structure and the peak gradient at the cell which supports higher fields. Error bars are also included, calculated by standard error mechanism, and result larger for measurements of low-BDR due to lack of statistics in the number of breakdown events.

Table 5.3: Average of the BDR results for repeated measurements of input power P_{in} and loading.

P_{in}**[MW]**	$E_{acc}^{\text{average}}/E_{acc}^{\text{peak}}$ **[MV/m]**	**Loading**	n_{pulses}	N_{BD}	**BDR** [$\times 10^{-5}$ **bpp**]
43.3	100 / 103	Unloaded	29796700	481	1.61±0.07
24.6	75 / 77	Unloaded	3672400	5	0.14±0.06
43.3	75 / 98	Loaded	26427900	422	1.60±0.08
38.0	68 / 92	Loaded	2242600	4	0.18±0.09
6.5	66 / 100	Anti-loaded	8112500	76	0.94±0.11

A first comparison can be made between the BDR measurements for unloaded and loaded conditions at 43.3 MW input power, and anti-loaded at 6.5 MW. Despite the very different longitudinal gradient profiles and average gradients, the peak value of the accelerating gradient inside the structure is very similar, in the range of 98–103 MV/m, but at different cell location (see Fig. 5.19). The resulting BDR is also very similar for these three measurement points and show better correlation with the peak gradient in Fig. 5.20(b), rather than the average gradient in Fig. 5.20(a). Furthermore, we can compare the measurements between the unloaded and loaded operation at 24.6 and 43.3 MW, respectively, which have the same average gradient of 75 MV/m along the structure. The BDR clearly differs about one order of magnitude between both measurements, and supports the idea that there is no correlation between the BDR and the average gradient.

5.4.2 Breakdown positioning analysis

The analysis of breakdown positioning, previously described in Section 4.1, has been made to determine the behavior of each cell under beam-loading conditions. This study is important to understand the different BDR results obtained in the experiment and allows to find the regions of the structure where the breakdown activity is more frequent.

The distribution of breakdowns in longitudinal position inside the structure has been analysed for each scenario and is shown in Fig 5.21. The technique used for the localization of breakdowns is the 'edge method' [93], based on the timing differences between the rising edge of the reflected signal and the falling edge of the

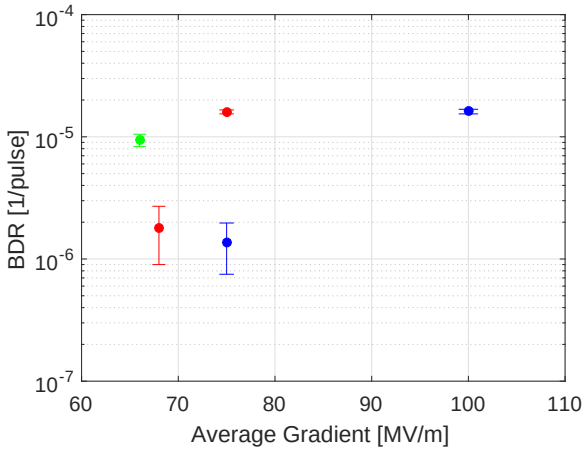

(a)

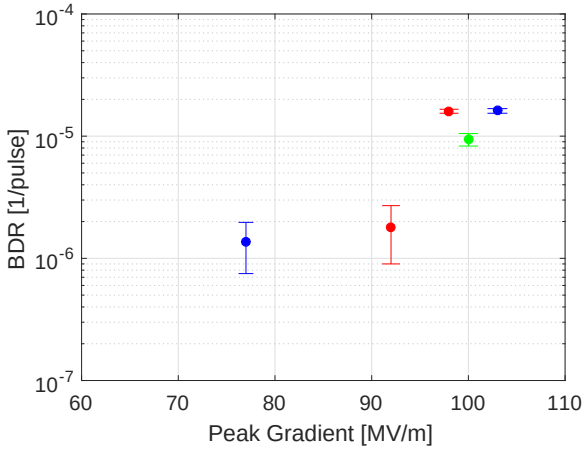

(b)

Figure 5.20: Results of BDR for the unloaded (blue), loaded (red) and anti-loaded (green) measurements with respect to (a) the average accelerating gradient and (b) the peak accelerating gradient.

transmitted signal. For the unloaded measurements, the breakdown distribution is approximately uniform along all the cells of the structure. In the loaded case, there is a reduction of the number of breakdown events detected at the last cells of the structure, as it is expected from the accelerating gradient profile when the beam loads the structure. And for the anti-loaded case, in which the beam produces RF power instead of absorbing it and increases the gradient towards the end of the structure, breakdowns mostly occur in the last cells. The distributions of breakdowns per cell are correlated to the strength of the fields in the cells of the

structure according to the gradient profile of Fig. 5.19. This result further supports the hypothesis of a **BDR dominated by peak gradient rather than by the average gradient**. One can notice that there is an excess of breakdowns around the cell number 14 for the loaded measurement. The reason of this result is still unclear, though we might think that the conditioning state of each individual cell is not uniform along the structure and may not preserve the E_{acc}^{30} scaling law equally in all cells. The repetition of measurements and collection of more data will help to find if it corresponds to an statistical fluctuation or a development of a 'hot cell' that is visible in loaded mode.

If these results are confirmed, it may be possible to optimise the structure tapering for the loaded field profile to be flat, rather than the unloaded, giving better performance under beam-loaded conditions. However, these new designs would require the infrastructure to perform the conditioning of the fresh structure with the presence of beam, in order to avoid that the last cells conditions faster than the first. In addition, running this type of structure without beam would create a different longitudinal field profile and create stress areas at the end of the structure.

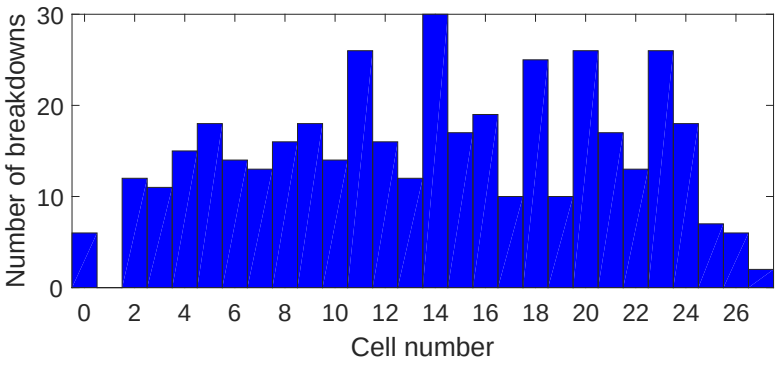

(a)

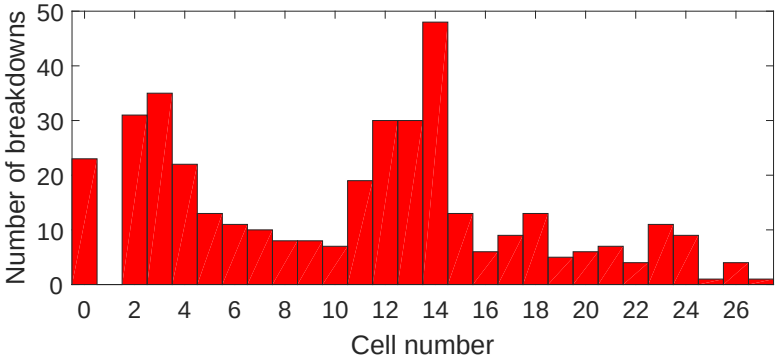

(b)

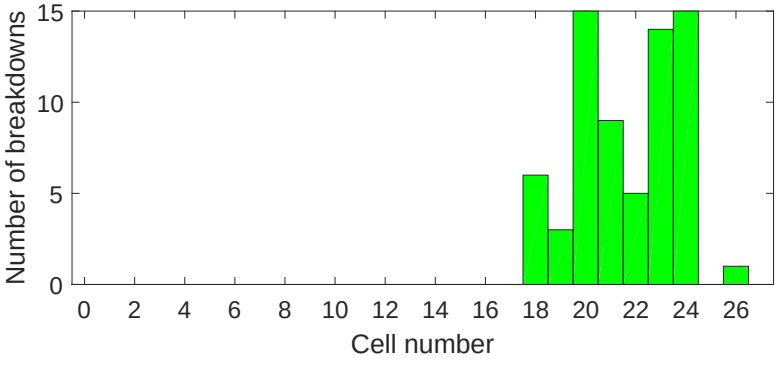

(c)

Figure 5.21: Longitudinal distribution of breakdowns per cell inside the structure under test for the (a) unloaded, (b) loaded and (c) anti-loaded measurement runs.

Chapter 6

S-band high-gradient developments for hadron therapy

There is special interest in the use of linacs for hadron therapy accelerators due to their advantages in modularity and fast control of the beam. The utilisation of HG technology offers compactness and cost-effective solutions for hadron therapy linacs to promote the worldwide construction of accelerator facilities dedicated to cancer treatment. In this chapter, we will review the current developments in HG linacs for hadron therapy carried out at CERN and the future contributions of the new IFIC HG-RF laboratory in Valencia (Spain).

6.1 High-gradient developments for hadron therapy at CERN

There is a long tradition at CERN in the development of medical accelerators applied to hadron therapy. The European Network for Light Ion Hadron Therapy (ENLIGHT) [114] was established in 2002 in order to coordinate the efforts of a multidisciplinary community of professionals in the field of hadron therapy. CERN has recently participated in different European (EU) projects under the umbrella of the ENLIGHT network: PARTNER (Particle Therapy Network for European Radiotherapy) [115], ENVISION (European Novel Imaging Systems for Ion therapy) [116], ENTERVISION (European training network in digital medical imaging for radiotherapy) [117] and ULICE (Union of Light Ion Centres in Europe) [118]. A joint PhD project [25] between the Instituto de Física Corpuscular (IFIC) [119] and TERA Foundation [120] was already carried out within the framework of the PARTNER EU training program for the study of HG accelerating structures and their application in hadron therapy.

6.1.1 Turning Linac for Proton therapy

The CLIC collaboration supports the study of HG technology to be exported to hadron therapy accelerators and, particularly, is involved on the linac design of the Turning Linac for Proton therapy (TULIP) project. TULIP is a project on design development [121] patented by TERA Foundation that would benefit from HG technology in order to build a compact single-room proton therapy facility, in which the main linac can be directly mounted on the rotating gantry. The 'single-room' approach is adopted as an alternative of the only existing 'multi-room' proton therapy facilities, with typically three treatment rooms, in order to offer more proximity of this service to more people around the world [27]. The goal is the design of a compact proton accelerator complex capable of producing beam currents of few [nA] at an energy range between 70 and 230 MeV, and implement innovative treatment techniques such as fast active spot scanning with tumor multipainting (see Section 1.2.2).

A layout of the last version of the accelerator design is shown in Fig. 6.1. Protons are initially accelerated in a high-frequency (750 MHz) Radio Frequency Quadrupole (RFQ), designed by CERN [123], up to 5 MeV and later in an S-band SCDTL (Side-Coupled Drift Tube Linac), patented by ENEA [124], up to 70 MeV. The beam is then accelerated in the S-band main linac up to 230 MeV. One distinctive feature of this design is the mechanical infrastructure capable of moving around the patient both the linac and the magnets of the gantry. The main linac is made up

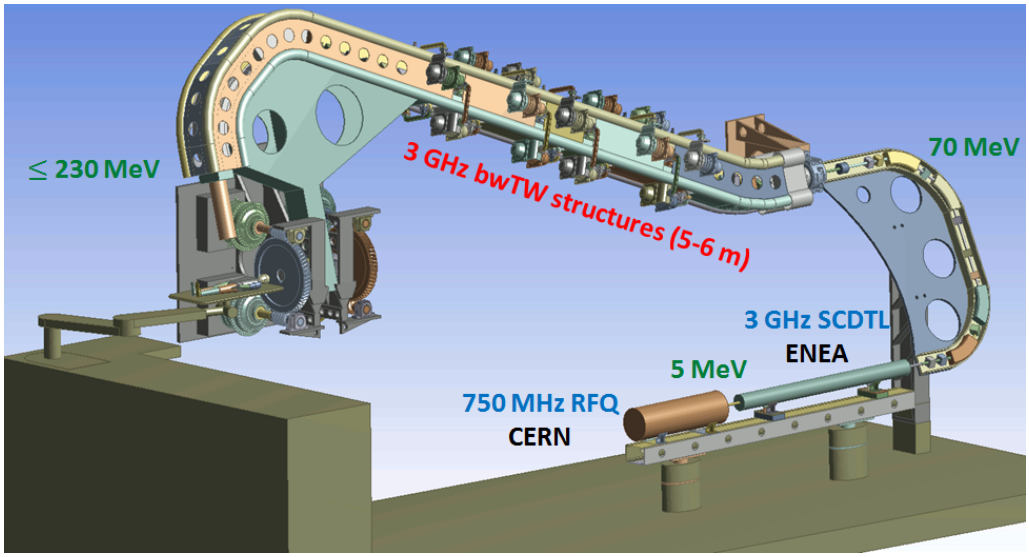

Figure 6.1: Artistic view of TULIP's single-room proton therapy facility. Taken from [122].

of accelerating tanks that are individually fed by klystron units. The control of the accelerating gradient of each tank with high repetition rate of 200 Hz allows the fast variation of the final energy in the linac, so that fast active scanning techniques can be employed to irradiate the tumor of the patient.

The length and weight of the main linac is restricted to the feasibility of the gantry infrastructure, hence very high gradients are required in order to efficiently accelerate the beam.

6.1.2 S-band backward traveling wave structure for a high-gradient proton linac

The design and fabrication of a HG prototype for medical proton linacs have been funded by the Knowledge and Transfer (KT) group at CERN under the project 'High-gradient accelerating structures for proton therapy linacs' [125]. The goal is to double the current state-of-the art accelerating gradient for hadron therapy linacs to achieve about 50 MV/m. With this upgrade, the length of the TULIP's linac would be reduced to 6 m for a final energy of 230 MeV and would ease its integration on the gantry with a total weight of approximately 12 tons.

The KT fund project has been developed to build two prototypes of the first HG accelerating structure of the proton linac, corresponding to an energy of 70 MeV and a particle velocity of 38% of the speed of light. The prototype consists of a novel

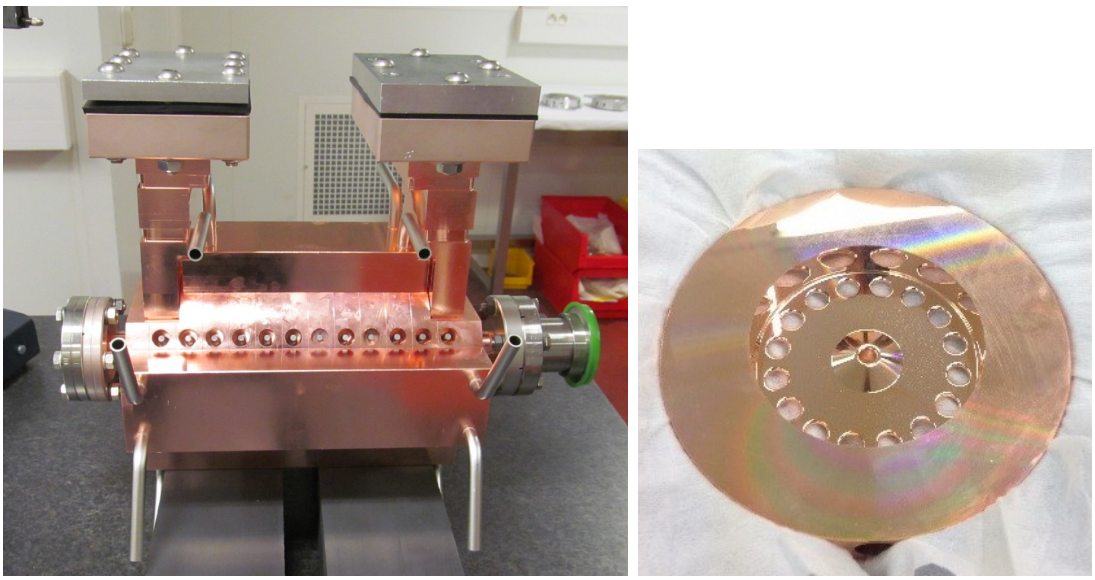

Figure 6.2: Picture of the first fully-assembled prototype (left) and single regular cell (right) of a HG backward TW structure for a medical proton linac.

design [126] that has been developed by members of the CLIC study and TERA Foundation. It is a 2.9985 GHz backward TW structure, in which the RF power that fills the structure flows in the opposite direction than the beam, and with a designed phase advance per cell of 150 deg. The RF design of the structure is based on the test of S-band single-cell cavities made at CERN [25,59] and the experimental RF and mechanical constraints inherited from the CLIC study (see Section 2.5.4).

A picture of the first prototype is shown in Fig. 6.2. The prototype has been fabricated and assembled in disks and it is made of 10 regular cells and 2 coupling cells with an aperture diameter of 5 mm. Each disk has 16 magnetic coupling holes at the periphery to allow the RF coupling between cells. The disks were bonded and all cells of the fully-assembled prototype were tuned at CERN [127] by means of bead-pull measurements [128]. The high-power test of the prototype will be performed at the end of 2016 at the CTF2 bunker by members of the CLIC RF group and IFIC's Group of Accelerator Physics. The main goal consists of testing the HG performance of the structure limited by breakdowns and verify the specifications of gradient at 50 MV/m and a maximum BDR of 10^{-6} bpp/m.

6.1.3 S-band rotary joint for medical applications

The high-power RF produced by klystrons needs to be carried through an efficient waveguide network to feed the HG structures of the TULIP's turning linac, mounted on the gantry. About 15 MW per linac structure are needed to achieve a maximum gradient of 50 MV/m. CERN proposed the design of a compact 3 GHz rotary joint to transport such high power at different rotating angles without major losses and without phase shifts over the rotation range. The novel design consists of the

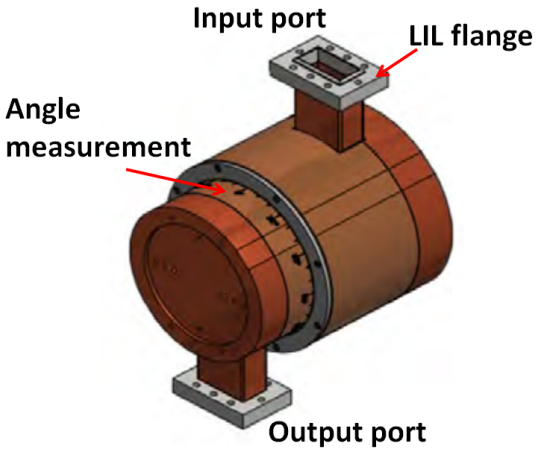

Figure 6.3: Image of the S-band rotary joint designed at CERN. Taken from [59].

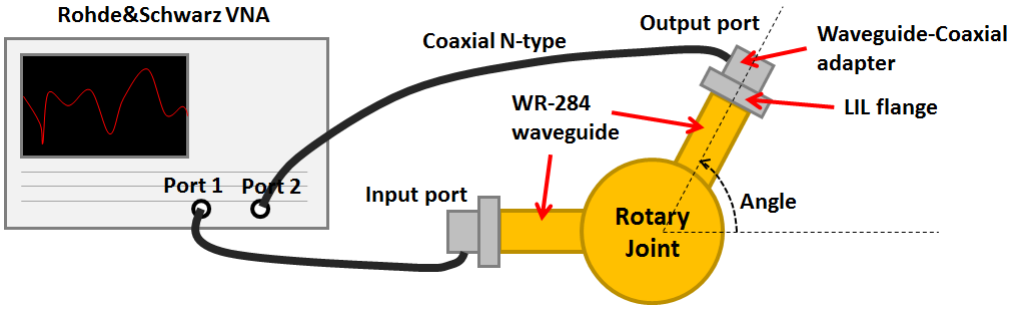

Figure 6.4: Scheme of the setup for the low-power measurements of the rotary joint.

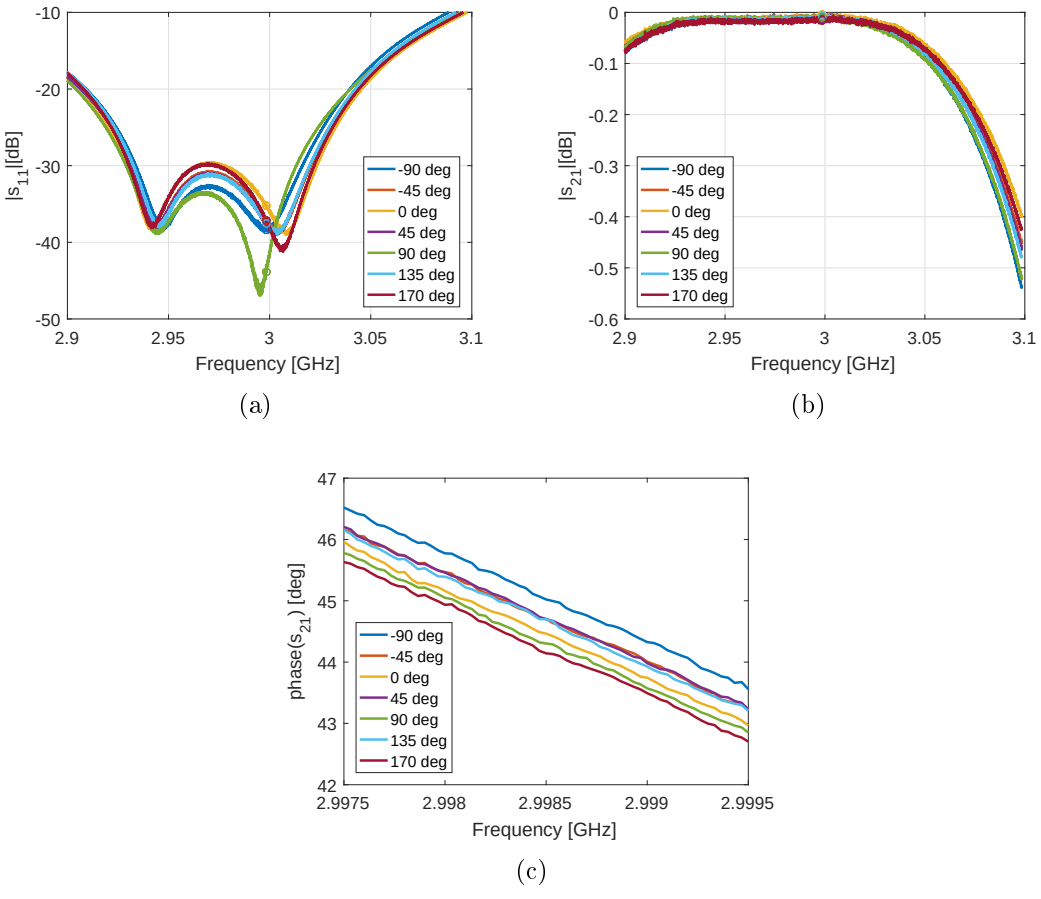

Figure 6.5: Low-power measurements of the complex scattering parameters of the S-band rotary joint at different rotating angles: (a) magnitude of s_{11}, (b) magnitude of s_{21} and (c) phase of s_{21} zoomed in the central frequency of 2.9985 GHz.

conversion from rectangular H-type waveguide to circular waveguide and then back to rectangular, which is made by double chocked mode converters from rectangular TE_{10} to circular TM_{01} mode. In order to test the high-power behavior of the device, a prototype has been fabricated at CERN [129] to be connected to standard WR-284 waveguides equipped with LIL flanges. A 3D-image of the design of the S-band rotary joint is shown in Fig. 6.3.

Low-power measurements of the RF rotary joint were made at the CLIC RF laboratory at CERN, in October 2014, to characterize the RF properties. A two-port Vector Network Analyser (VNA) [130] was used and connected to the input and ouput ports of the rotary joint, as shown in the scheme of Fig. 6.4. Figure 6.5 shows the measurement of the complex scattering parameters s_{11} and s_{21}, corresponding to the reflection and transmission coefficients, at different angle positions between the input and output ports of the rotary joint in the range of $(-90, 170)$ deg. The magnitude of s_{11} results smaller than -35 dB at the central frequency of 2.9985 GHz for the different angle positions. The transmission of the RF power is also satisfactory since the phase of s_{21}, shown in Fig. 6.5(c), varies a maximum of ± 0.5 deg when rotating the output port at different angles.

A high-power test of the RF rotary joint was performed in March 2015 at the CTF2 bunker using the S-band klystron MKS14 of the CTF3 linac as the power source. A picture of the experimental setup in CTF2 is shown in Fig. 6.6. A long WR-284 waveguide network, under SF6 gas, was installed to connect the klystron to the rotary joint at CTF2. A ceramic window was used to isolate the section under

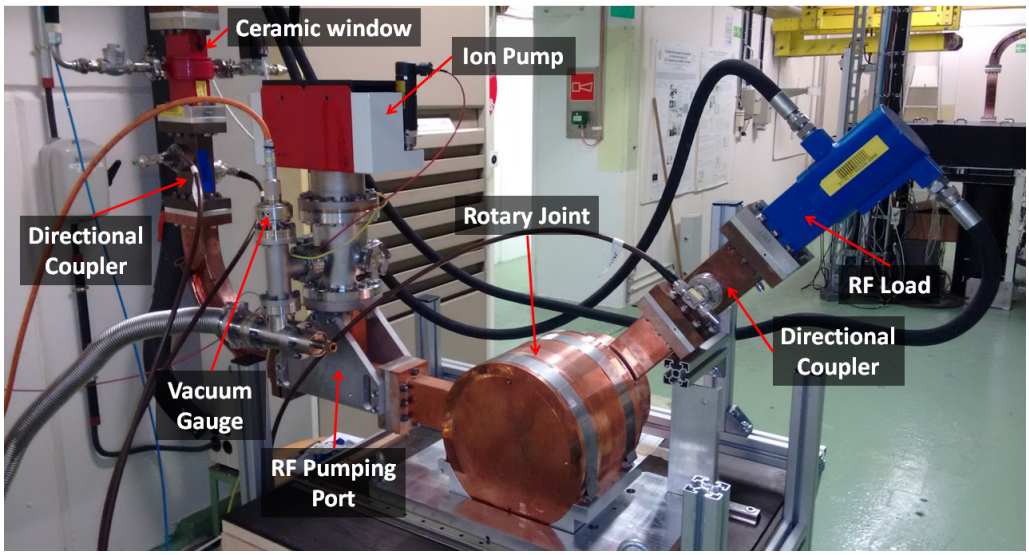

Figure 6.6: Picture of the high-power test setup of the 3 GHz rotary joint at the CTF2 bunker of the CLIC Test Facility.

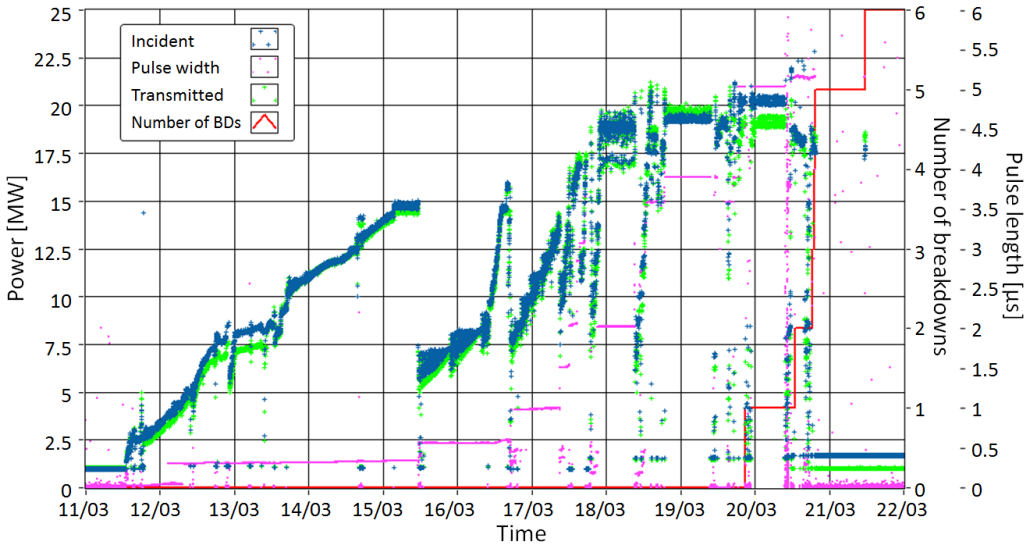

(a)

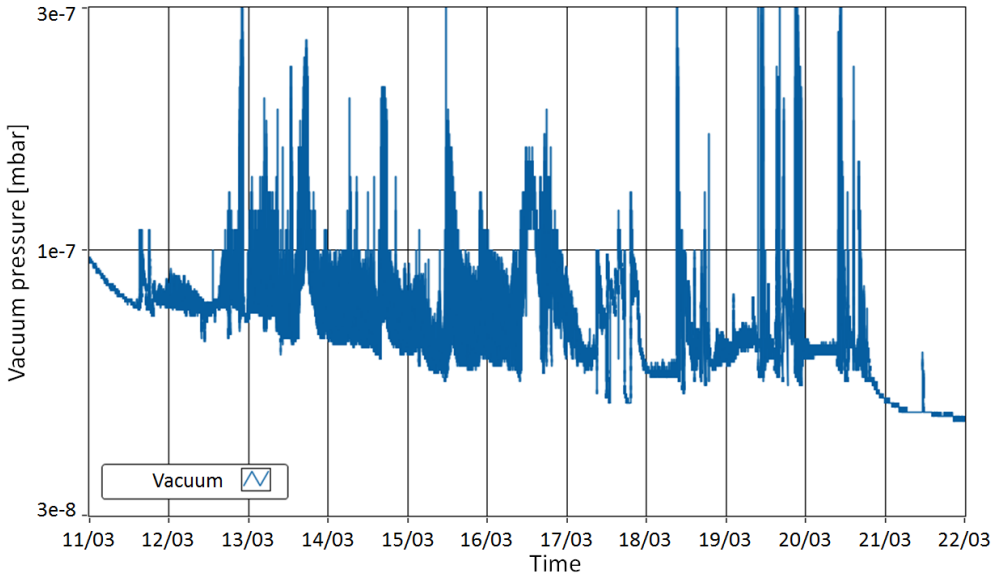

(b)

Figure 6.7: History of the high-power test of the S-band rotary joint, which shows the (a) measured incident (blue dots) and transmitted (green dots) power, pulse width (pink dots) and number of breakdowns (red line), and (b) measured vacuum levels (blue line).

vacuum of the rotary joint. An RF pumping port was inserted in this section in order to install the pumping network in which a primary group, an ion pump and a vacuum gauge were connected. This system allowed to achieve and measure pressure levels below 10^{-7} mbar. Two bi-directional couplers were installed before and after the rotary joint to acquire the incident, reflected and transmitted power RF signals. A water-cooled RF load was used to damp the rotary joint output power.

The control and acquisition systems used for the operation of the high-power test was managed by a NI PXI controller, which communicated with the klystron through the CTF3 Technical Network. The RF signals from the directional couplers were digitized in a NI-5761 ADC (14-bits, 250 Msamples/s). The software for the high-power operation is based on a simplified version of the Xbox-2 LabVIEW software [81].

The high-power test was performed in ten days (11th–21st March 2015) and the full history is summarized in Fig. 6.7. The rotary joint, positioned at a fixed rotating angle, was conditioned starting with a pulse length of 100 ns which was gradually increased up to 5 μs. The limitations of the rotary joint performance were given by a strong vacuum activity, thus the conditioning algorithm was configured to vary the incident power in a feedback loop based on the measured pressure and a fixed setpoint of 10^{-7} mbar. The best performance achieved by the rotary joint was a maximum power of 20 MW with a pulse length of 5 μs, at a repetition rate of 50 Hz, and it was tested at different rotating angle positions.

The successful results of the behavior of the rotary joint means that the RF network can be designed to bring the power to the linac structures mounted on the rotating gantry support. All the details of this work are published in [129]. A recent proposal is adopted instead to simplify the overall design by making use of the new compact and more efficient Multi Beam Klystrons (that can operate at 52 kV without need of oil tank) [131] mounted directly close to the accelerating structure, as it integrated in the layout of Fig. 6.1.

6.2 The IFIC high-gradient RF laboratory

The IFIC HG-RF laboratory is under construction at the Parc Científic of the University of Valencia and the Instituto de Física Corpuscular (IFIC), in Valencia (Spain), under a FEDER-funded collaboration agreement between the University of Valencia and the Spanish General Administration (MINECO) for the building integration and the equipment of scientific instrumentation.

The main objective of the laboratory is the study of vacuum breakdown phenomenology in S-band HG accelerating structures. In particular, one of the most important applications of these studies is in hadron therapy linacs. The current activities of the HG-RF laboratory in Valencia are developed in collaboration with

the CLIC RF group under the contract "IFIC-CSIC collaboration on CLIC" (CERN collaboration agreement KE2638/BE, 526980 Euros, from 2015 to 2018). The first prototypes to be tested in this test bench will be the two backward TW accelerating structures fabricated at CERN within the KT project, described in Section 6.1.2.

6.2.1 The S-band test facility

The IFIC HG RF laboratory is under construction since 2015 and has been designed to host the high-power infrastructure for testing HG normal-conducting RF accelerating structures and develop the necessary instrumentation and diagnostic techniques for breakdown studies in the S-band frequency [132].

The design has been made through a close collaboration between the IFIC's Group of Accelerator Physics (GAP) and the CLIC RF group at CERN. The layout is inspired by the scheme of the Xbox-3 test facility (see Section 3.2.3), which is currently under commissioning at CERN, and it has been adapted to a frequency of 2.9985 GHz. The system will be prepared for the conditioning and test of two S-band TW structures.

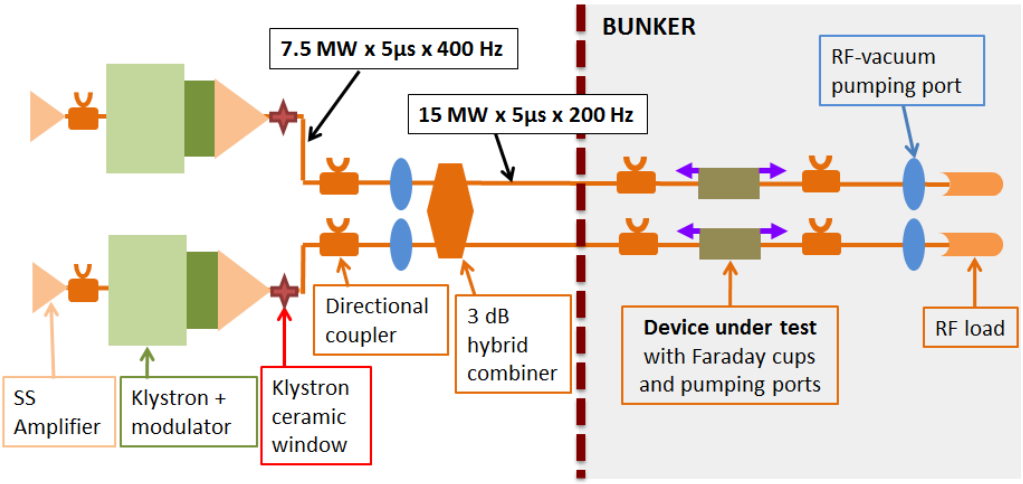

Figure 6.8: Layout of the high-power subsystem of the IFIC HG RF laboratory. Taken from [132].

A scheme of the high-power components of the test facility is shown in Fig. 6.8, and the 3D integration of the network at the IFIMED building can be seen in Fig. 6.9. The system makes use of two S-band (2.9985 GHz) klystrons, CPI model VKS-8262G1 [133], powered by two solid-state 150 kV modulators, provided by JEMA [134]. These units are capable of providing a maximum RF power of 7.5 MW with a pulse length of up to 5 μs and a repetition rate of up to 400 Hz. The output power of both klystrons is combined in a 3 dB hybrid that can deliver the sum of

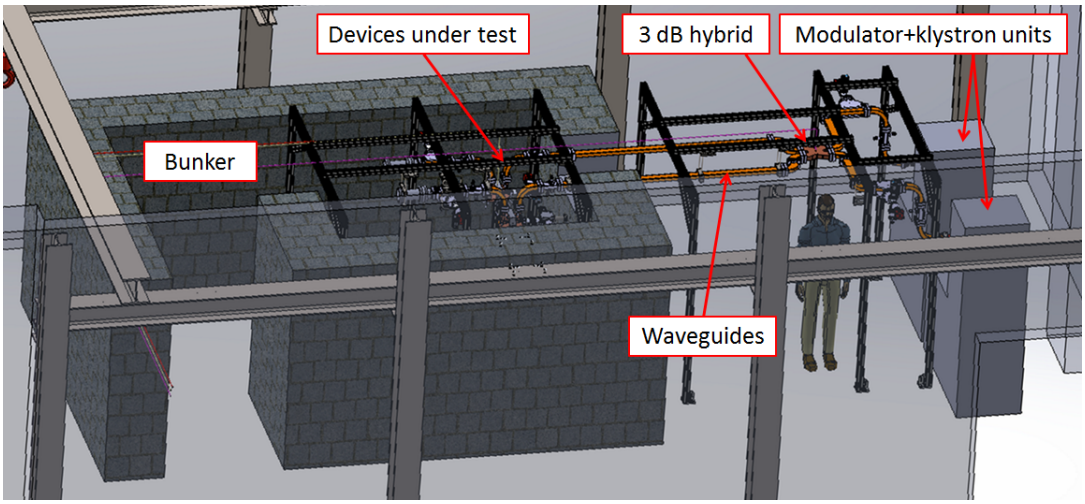

(a)

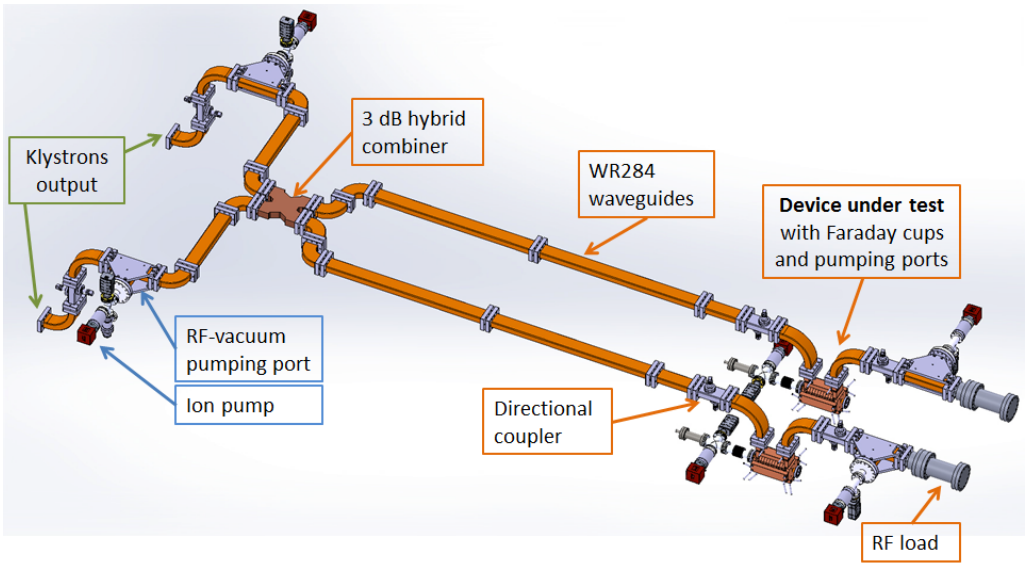

(b)

Figure 6.9: Integration 3D of the high-power network of the IFIC HG RF laboratory: (a) integration in the laboratory enclosure of the building and (b) detail of the assembly of the high-power and vacuum components from the klystron output. Taken from [132].

power, up to 15 MW, to two different lines depending on the relative phase between the two incoming RF waves. The power of each line is sent through WR-284 copper-made waveguides to the structures under test, installed inside the bunker, which will be equipped with the experimental setup required for breakdown studies. Two RF

pumping ports are installed for each line, equipped with ion pumps, to ensure the ultra-high vacuum below 10^{-7} mbar along the waveguide network and the structures. The facility will be controlled by a National Instruments [135] PXI real-time system in charge of the low-level RF generation, the acquisition of signals for diagnostics, the signal processing and the trigger control and interlock of the hardware.

Experimental capabilities

The combination of the two klystron with a 3 dB hybrid is a cost-effective design of the test facility, proven by Xbox-3 [91], for the optimization of both peak power and repetition rate. The operation of the modulator units that drive the 7.5 MW klystrons with 150 kV, 5 μs-long pulses improves the feasibility of a repetition rate of 400 Hz, compared with the single-klystron scheme of Xbox-1 and Xbox-2 which are capable of operating at 50 Hz. The output power of both klystrons is then combined to double the peak power, up to 15 MW, to be delivered to the HG structure under test. HG prototypes need of the order of 10^8–10^9 pulses to be conditioned so that they achieve their best performance of accelerating gradient, pulse length and BDR, which typically last about four months in 50 Hz systems. The optimization of the repetition rate up to 400 Hz implies an important reduction of the time required to condition and test a structure.

Another advantage of the 'two-klystron' scheme is the possibility of testing two different prototypes simultaneously. The manipulation of the two klystrons output RF phase, from the low-level RF electronics, allows to control the amount of power that is delivered to each output branch of the 3 dB hybrid [81]. If the two input wave signals differ +90 deg in phase, the full combined power exits through the first output of the hybrid. In case that the phase difference between both input signals is −90 deg, the full power exits through the second output of the hybrid. This phase difference can be alternated pulse-to-pulse in order to test independently the two prototypes at the same time, with an effective repetition rate of 200 Hz for each structure. The RF power amplitude of each klystron can be also controlled pulse-to-pulse, which offers the required flexibility to test different prototype designs or structures that present different conditioning states.

RF breakdown studies

The facility will also open the possibility of several RF breakdown studies in S-band HG accelerating structures to complement the recent progress in the understanding of vacuum arcs by the CLIC study that has been discussed in this thesis. The main objectives of the IFIC HG RF laboratory will be the following:

- The HG performance of S-band accelerating structures will be evaluated by measuring the accelerating gradient, pulse length and BDR. An average BDR

will be calculated using Eq. (2.1) from the count of the number of breakdowns and number of pulses during a certain period of measurement. Breakdowns will be detected from the combined measurements of the reflected RF power from the structure with a directional coupler and the breakdown currents with Faraday cups.

- The measurement of BDR at different gradients and pulse lengths will be used to test the experimental scaling laws of Eq. (2.11). These studies will allow to investigate the physical mechanisms that validate the observed dependencies between the BDR and the operation settings of the structure, such as surface fields, pulsed temperature rise, pulse shape and/or repetition rate.

- The instrumentation for breakdown detection will be used to develop the best techniques to localize vacuum arcs inside the structure. This analysis is also essential for the evaluation of the performance of the HG structure, since it is required that breakdowns are distributed uniformly along all the cells.

- Dark current measurements will be made with Faraday cups that are attached to both ends of the structure. In addition to test the validity of surface field emission theory in RF structures, this measurement will provide a better understanding of the breakdown mechanism and will possibly allow to find their precursors.

As already mentioned, the 'two-klystron' scheme is adopted to double the testing capabilities, thus different strategies and experimental setups can be employed and developed for breakdown studies. Future results and progress provided by this laboratory will be of special interest for the HG community, not only for hadron therapy but also for the design of HG linacs with applications in Medicine, colliders and high-energy light sources.

Chapter 7

Summary and conclusion

HG RF technology offers the possibility of constructing very compact linear accelerators destined for different applications. However, the performance of HG linacs is limited by the occurrences of vacuum arcs. The Xbox test facilities and the pulsed-DC LES at CERN have supported the development of a wide experimental programme of testing HG accelerating structures and breakdown phenomenology studies. Furthermore, the ongoing construction of the IFIC HG-RF test facility in Valencia will complete the efforts in breakdown studies for S-band HG linacs. In this chapter we will summarize the main contribution of this thesis work to this field.

7.1 Main contribution and future work

7.1.1 X-band high-gradient studies in CLIC

The operation of the HG RF test stands, Xbox-1 and Xbox-2, and the pulsed-DC laboratory at CERN, described in Chapter 3, has allowed the collection of significant amount of data to evaluate the HG performance of different CLIC accelerating prototypes and to make a phenomenological study of the formation of vacuum arcs. Accelerating gradients of 100 MV/m have been accomplished in the new CLIC designs, with RF pulse lengths over the nominal 180 ns, and operating at low BDRs close to the CLIC requirements of 3×10^{-7} bpp/m.

Different studies have been carried through Chapter 4 to provide a better understanding of the breakdown limitations in HG accelerating structures. Breakdown localization techniques have been developed to monitor the good performance of the structure under test. Three methods, named 'edge', 'correlation' and 'breakdown phase' methods, are used to localize the cell in which breakdowns are initiated inside the structure. A uniform distribution of breakdowns along all the cells of the struc-

ture is the signature of a good HG performance. The damage caused by breakdowns is observed at the irises during the post-mortem optical inspection. The statistical analysis of breakdown events in RF structures and pulsed-DC systems has revealed new insights in the underlying mechanism of vacuum arc formation. The occurrences of breakdowns during operation have been described with a probability density function (PDF) of the number of pulses in the interval preceding each breakdown event. This PDF shows that **breakdowns are not poissonian or uncorrelated random events**, but they can be described by a **'two-rate' process** which assumes the existence of 'follow-up' breakdowns as a consequence of the damage or residue that is left by the previous arc. This is supported by the breakdown localization analysis, which shows that the formation of breakdown 'clusters' is more concentrated in small regions within the structure. A consistent physical model needs to be investigated to explain the self-exciting behavior of breakdowns that leads to the observed two-rate PDF. Further studies have been carried out concerning the conditioning process that is required in fresh structures after their fabrication in order to achieve their best performance. The scaled gradient and scaled BDR have been used to directly compare the conditioning histories obtained from different structures tested at the Xboxes and NEXTEF (KEK) so that they can be quantitatively compared independently of the particular operational parameters of the experiment. The comparative analysis have shown a similar progression with the number of pulses, despite the different conditioning strategies of gradient, BDR and pulse length, and **the conditioning state improves with the number of RF pulses and not with the number of breakdowns**. These new insights are very important for the future optimization of conditioning strategies and the development of fabrication techniques of RF structures that will allow to reduce the conditioning time. The study of different conditioning strategies must be a priority in the future plans of the Xbox-3 and the pulsed-DC LES due to their multiple testing slots and their high pulsing repetition rates. The latter is capable of triggering over 10^9 pulses in few weeks, at 1 kHz, which makes it the best candidate to study the existence of a lower limit in the achievable BDR. Other studies have been performed at Xbox-2 concerning the possible negative effect of the pulse shape driven by the pulse compressor on the BDR performance of the structure under test. Simulations have been performed to analyse the excess of pulsed surface heating that is produced during the charging stage of the pulse compressor cavities, and first preliminary results obtained at Xbox-2 with a T24-OPEN structure have shown an **increase of the BDR when operating with pulse compressor**. Further measurements need to be made with different pulse shapes, that can be configured from the Xbox control system, and analyse the time distribution of breakdowns within the pulse. In parallel, time-resolved measurements of dark current are of special interest to find if there are hints of breakdown precursors within the pulse.

The CLIC beam-loading experiment has started to measure the effect of the beam on the BDR of a HG accelerating structure at the dog-leg beam line of CTF3. The Xbox-1 network and software have been adapted to the experimental requirements of the study, and it has been described in detail in Chapter 5. The experiment has tested the breakdown performance of the structure under loading (accelerating) and anti-loading (decelerating) conditions to be compared with the unloaded performance. The first results show a **BDR dominated by the maximum peak gradient inside the structure rather than by the average gradient** for all unloaded, loaded and anti-loaded cases. Consistently, it has been shown that breakdowns are accumulated at the cells which have higher fields. Further measurements are required to confirm these results with more statistics in order to have a better estimation of the BDR for each loading scenario. As the presence of the accelerated beam does not seem to impact the BDR for the same input power, one may consider the possibility of optimizing the structure tapering for the loaded, rather than the unloaded, field profile in future designs.

7.1.2 S-band high-gradient studies for hadron therapy

There is an active support of the CLIC study to develop HG technology for future hadron therapy linacs at CERN, which has been discussed in Chapter 6. Regarding the work of this thesis, a first prototype of a compact S-band rotary joint, designed and built at CERN, has been high-power tested at CTF3. This test has proven the feasibility of transporting about 15 MW of power at different angles in order to feed accelerating structures directly mounted on the gantry of the hadron therapy room facility. A backward TW structure has been also designed and two prototypes have been built at CERN for a medical proton linac, aiming at doubling the current state-of-the-art accelerating gradient. A high-power test is ongoing at CTF3 to evaluate the breakdown performance in one of these prototypes. If the results confirm the expected performance of 50 MV/m gradient, medical proton linacs could be reduced to only 6 m-long to achieve beam energies up to 230 MeV.

The IFIC HG-RF laboratory is under construction since 2015 in Valencia to support the development of HG technology in the S-band frequency. The high-power testing infrastructure is inspired in the design of the Xbox-3 at CERN, and has been adapted to the frequency of 2.9985 GHz. The facility will be capable of testing two HG accelerating structures at the same time with a maximum power of 15 MW and a maximum repetition rate of 400 Hz. Furthermore, the experimental equipment for breakdown diagnostics will help to draw further conclusions about the breakdown limitations in HG RF structures.

Appendix A

Analysis of conditioning histories

The conditioning histories of different HG RF prototypes tested at the Xbox and NEXTEF test facilities, and a pair of soft copper electrodes tested at the pulsed-DC LES, have been analysed by a scaling of the data to normalize the different operation settings and strategies. The accelerating gradient, peak surface electric field and peak modified Poynting vector have been scaled to a reference pulse length and BDR, using Eqs. (4.26), (4.32) and (4.33). The BDR has been also scaled to a fixed gradient and pulse length, using Eq. (4.29).

The following figures show the resulting conditioning histories, represented by these scaled quantities, of a collection of tested prototypes: a TD26CC and a TD24R05 tested at Xbox-1; a Crab cavity and a T24OPEN tested at Xbox-2; two TD24R05s and one T24 tested at NEXTEF; and a pair of soft-copper electrodes tested at the pulsed-DC LES.

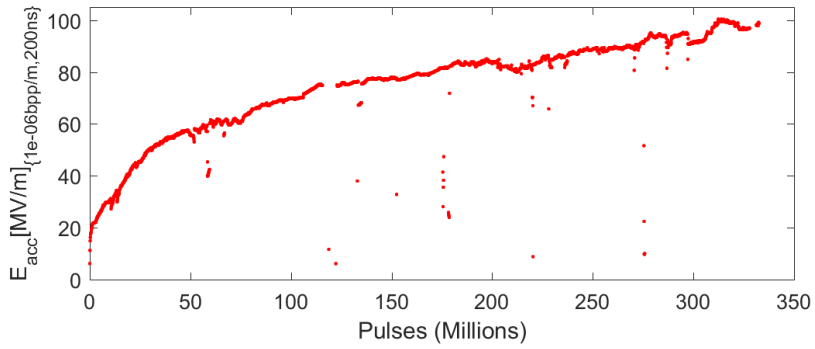

(a)

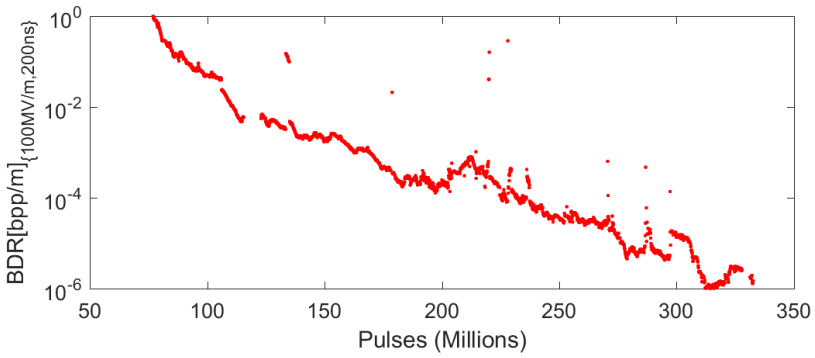

(b)

Figure A.1: Conditioning history of the TD26CC prototype tested at Xbox-1, represented as the (a) scaled accelerating gradient to $\mathrm{BDR}_0 = 10^{-6}$ bpp/m and $t_{p,0} = 200$ ns, using Eq. (4.26), and (b) scaled BDR to $E_{acc,0} = 100$ MV/m and $t_{p,0} = 200$ ns, using Eq. (4.29).

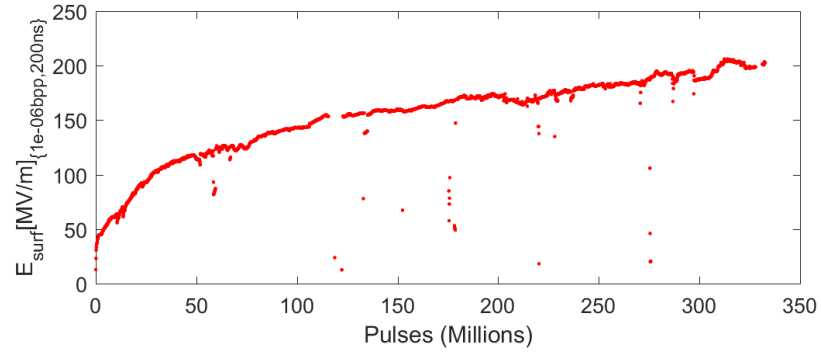

(a)

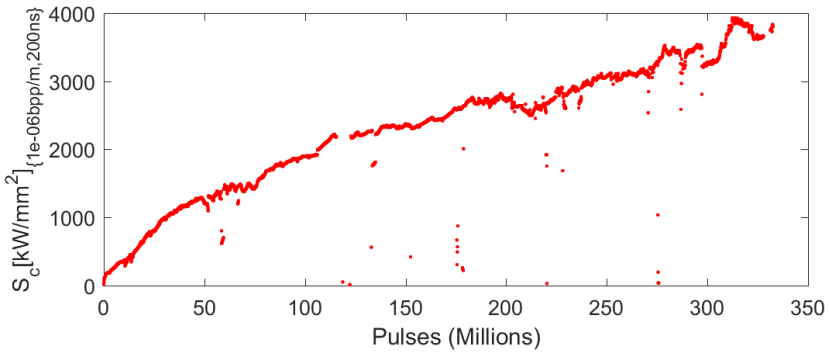

(b)

Figure A.2: Conditioning history of the TD26CC prototype tested at Xbox-1, represented as the (c) scaled peak surface electric field and (d) scaled peak modified Poynting vector to $\mathrm{BDR}_0 = 10^{-6}$ bpp/m and $t_{p,0} = 200$ ns, using Eqs. (4.32) and (4.33), respectively.

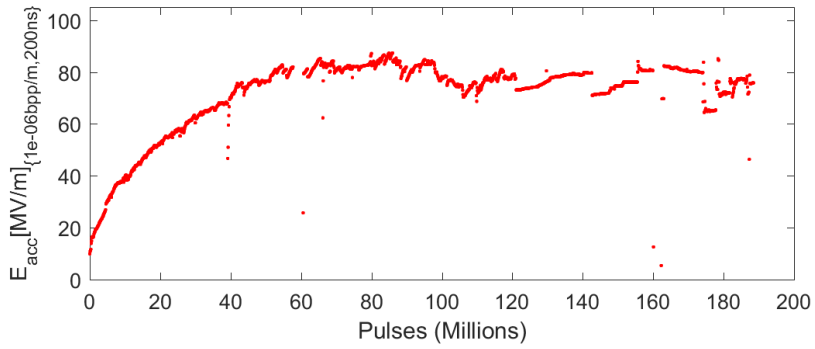

(a)

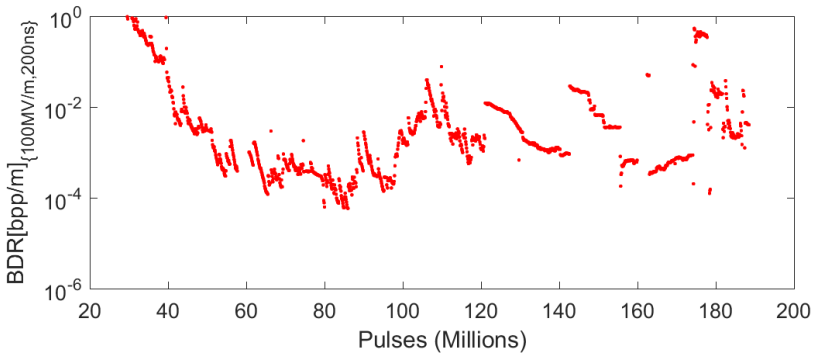

(b)

Figure A.3: Conditioning history of the TD24R05 prototype tested at Xbox-1, represented as the (a) scaled accelerating gradient to $\mathrm{BDR}_0 = 10^{-6}$ bpp/m and $t_{p,0} = 200$ ns, using Eq. (4.26), and (b) scaled BDR to $E_{acc,0} = 100$ MV/m and $t_{p,0} = 200$ ns, using Eq. (4.29).

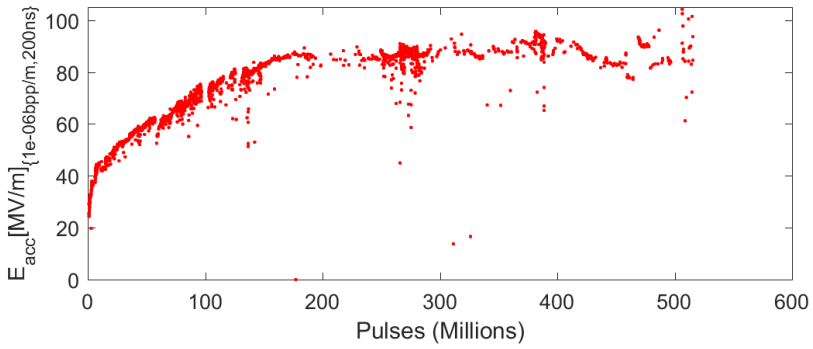

(a)

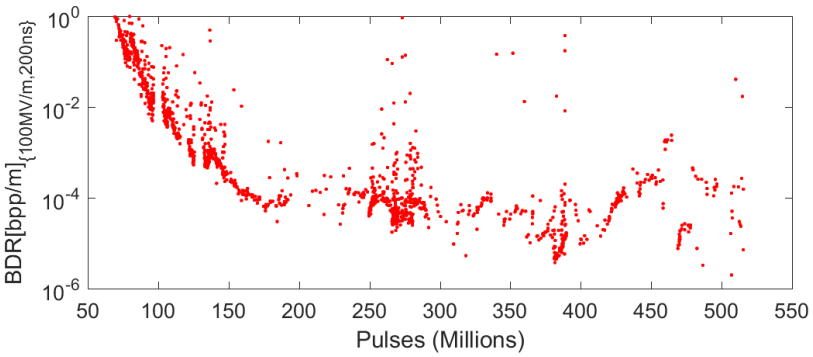

(b)

Figure A.4: Conditioning history of the TD24R05-#2 prototype tested at NEXTEF (KEK), represented as the (a) scaled accelerating gradient to $\mathrm{BDR}_0 = 10^{-6}$ bpp/m and $t_{p,0} = 200$ ns, using Eq. (4.26), and (b) scaled BDR to $E_{acc,0} = 100$ MV/m and $t_{p,0} = 200$ ns, using Eq. (4.29).

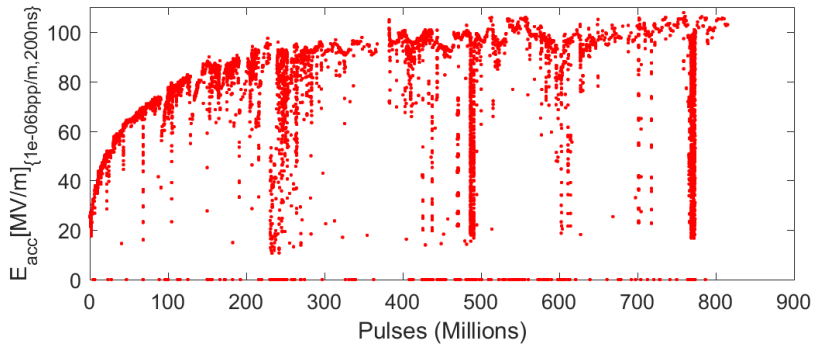

(a)

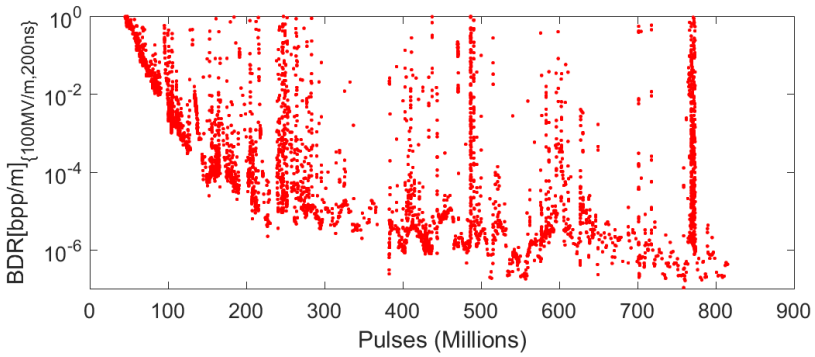

(b)

Figure A.5: Conditioning history of the TD24R05-#4 prototype tested at NEXTEF (KEK), represented as the (a) scaled accelerating gradient to $\mathrm{BDR}_0 = 10^{-6}$ bpp/m and $t_{p,0} = 200$ ns, using Eq. (4.26), and (b) scaled BDR to $E_{acc,0} = 100$ MV/m and $t_{p,0} = 200$ ns, using Eq. (4.29).

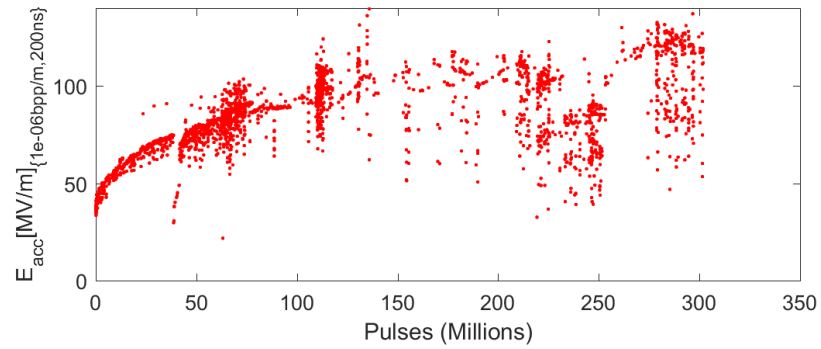

(a)

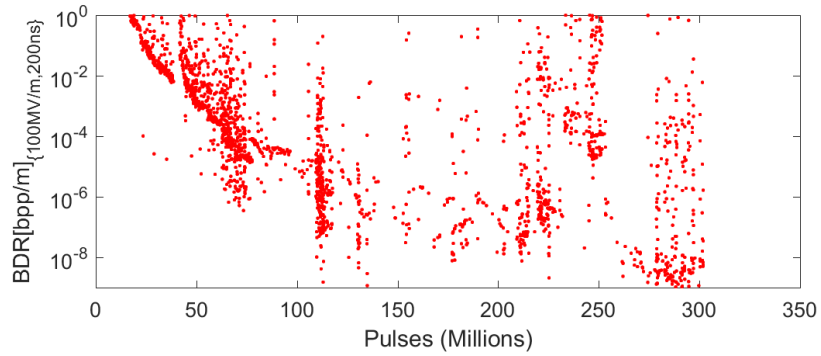

(b)

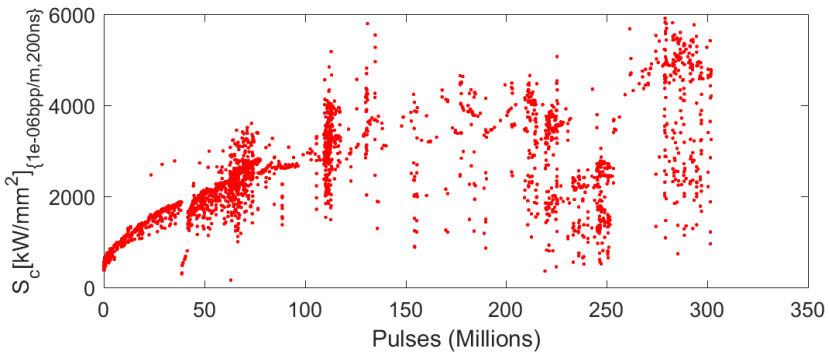

(c)

Figure A.6: Conditioning history of the T24-#2 prototype tested at NEXTEF (KEK), represented as the (a) scaled accelerating gradient to $\mathrm{BDR}_0 = 10^{-6}$ bpp/m and $t_{p,0} = 200$ ns, using Eq. (4.26), (b) scaled BDR to $E_{acc,0} = 100$ MV/m and $t_{p,0} = 200$ ns, using Eq. (4.29), and (c) scaled peak modified Poynting vector to $\mathrm{BDR}_0 = 10^{-6}$ bpp/m and $t_{p,0} = 200$ ns, using Eq. (4.33).

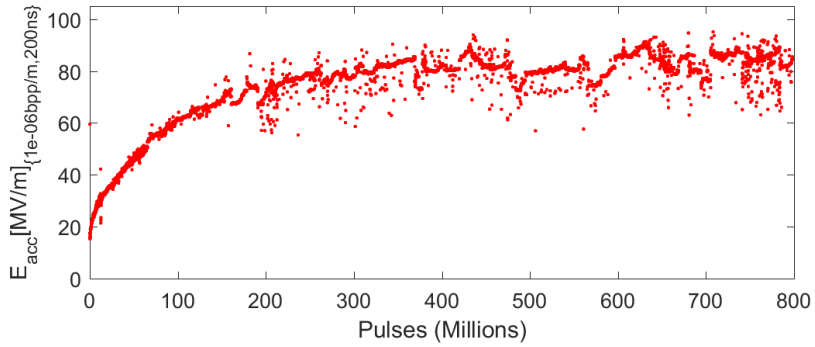

(a)

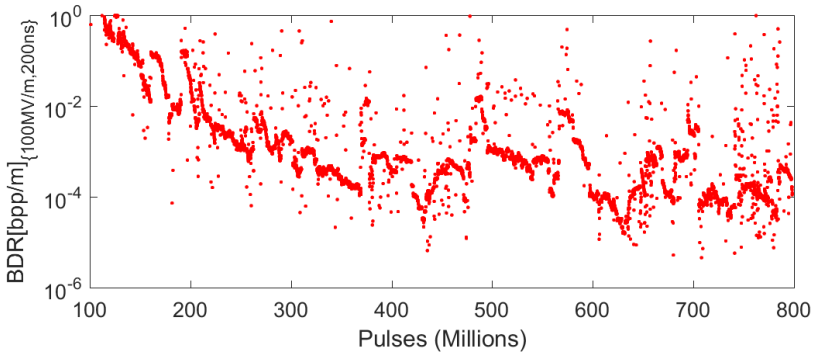

(b)

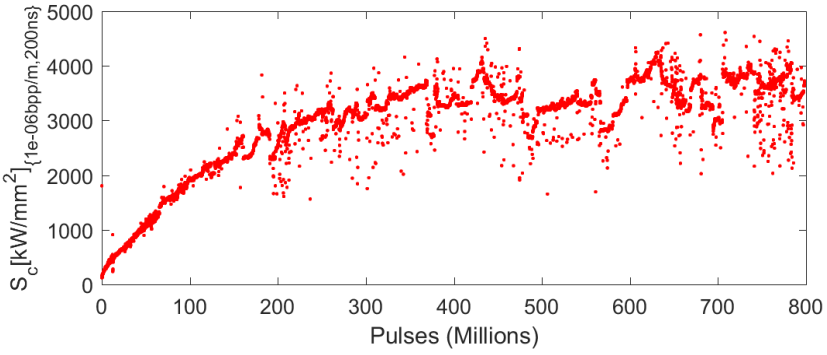

(c)

Figure A.7: Conditioning history of the T24OPEN prototype tested at Xbox-2, represented as the (a) scaled accelerating gradient to $\mathrm{BDR}_0 = 10^{-6}$ bpp/m and $t_{p,0} = 200$ ns, using Eq. (4.26), (b) scaled BDR to $E_{acc,0} = 100$ MV/m and $t_{p,0} = 200$ ns, using Eq. (4.29), and (c) scaled peak modified Poynting vector to $\mathrm{BDR}_0 = 10^{-6}$ bpp/m and $t_{p,0} = 200$ ns, using Eq. (4.33).

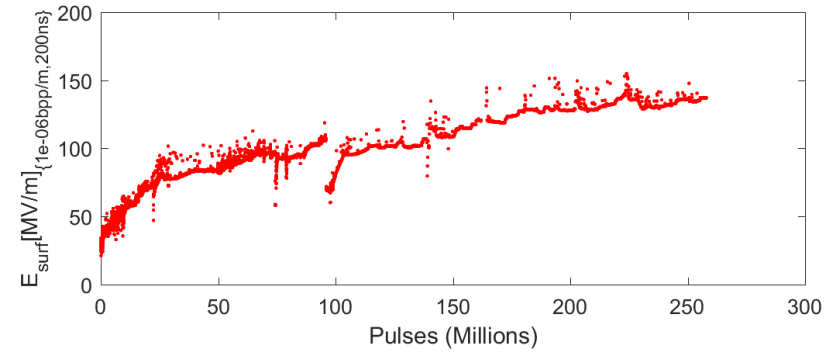

(a)

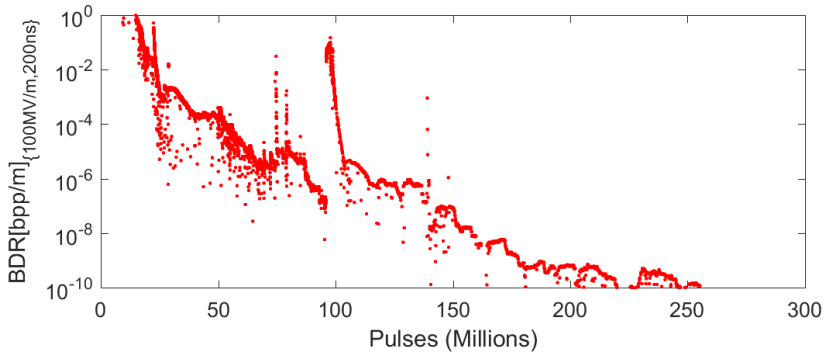

(b)

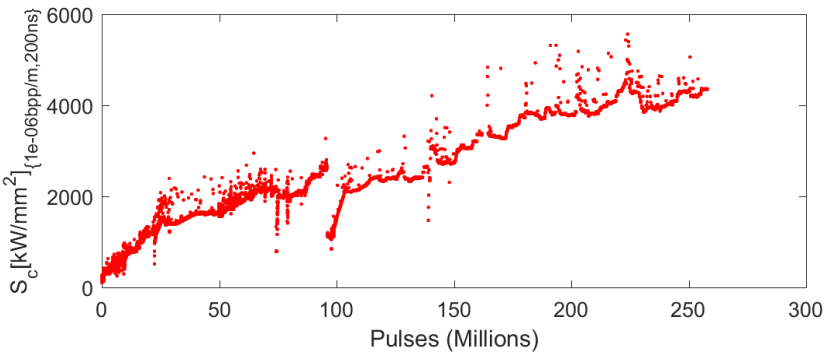

(c)

Figure A.8: Conditioning history of the Crab cavity prototype tested at Xbox-2, represented as the (a) scaled peak surface electric field to $\mathrm{BDR}_0 = 10^{-6}$ bpp/m and $t_{p,0} = 200$ ns, using Eq. (4.32), (b) scaled BDR to $E_{s,0} = 100$ MV/m and $t_{p,0} = 200$ ns, and (c) scaled peak modified Poynting vector to $\mathrm{BDR}_0 = 10^{-6}$ bpp/m and $t_{p,0} = 200$ ns, using Eq. (4.33).

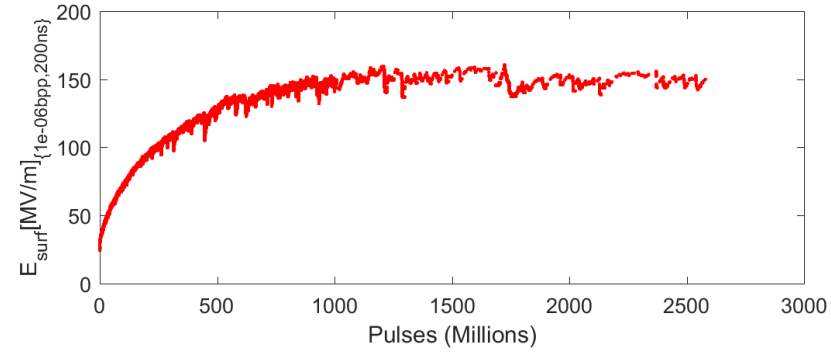

(a)

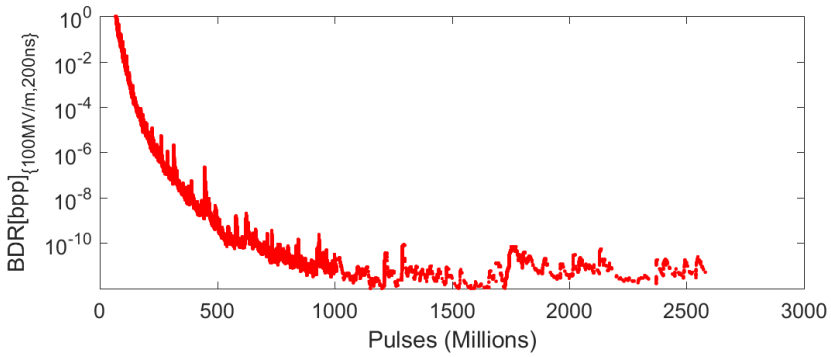

(b)

Figure A.9: Conditioning history of the pair #2 of soft-copper electrodes tested at pulsed-DC LES, represented as the (a) scaled surface electric field to $\mathrm{BDR}_0 = 10^{-6}$ bpp and $t_{p,0} = 200$ ns, using Eq. (4.32), and (b) scaled BDR to $E_{s,0} = 100$ MV/m and $t_{p,0} = 200$ ns.

Bibliography

[1] W.K.H. Panofsky. Linear accelerator beam dynamics. *University of California Radiation Laboratory Report*, UCLR-1216, 1951.

[2] W. Wuensch. Normal-conducting RF. 9th Accelerator School for Linear Colliders, Whistler (Canada), 2015. `http://agenda.linearcollider.org/event/6906/`.

[3] T. Wangler. *Principles of RF Linear Accelerators*. John Wiley and Sons, 1st edition, 1998.

[4] F. Gerigk. Cavity types. *Proceedings of the CERN Accelerator School CAS 2010*, 2011. Presented at the CAS 2010: RF for accelerators, Ebeltoft, 8-17 June 2010; CERN-2011-007.

[5] P.B. Wilson. Transient beam loading in electron-positron storage rings. Technical Report SLAC-PEP-0276, CERN-ISR-TH-78-23, Stanford Linear Accelerator Center, 1978.

[6] A. Grudiev and W. Wuensch. Design of the CLIC Main Linac accelerating structure for CLIC Conceptual Design Report. In *Proceedings of Linear Accelerator Conference LINAC2010*, pages 211–213, Tsukuba (Japan), 2010.

[7] J.-Y. Raguin and M. Bopp. The Swiss FEL C-band accelerating structure: RF design and thermal analysis. In *Proceedings of the Linear Accelerator Conference LINAC2012*, pages 501–503, Tel-Aviv (Israel), 2012.

[8] T. Inagaki, C. Kondo, H. Maesaka, T. Ohshima, Y. Otake, T. Sakurai, K. Shirasawa, and T. Shintake. High-gradient C-band linac for a compact X-ray free-electron laser facility. *Phys. Rev. ST Accel. Beams*, 17(8):080702, Aug 2014. doi:10.1103/PhysRevSTAB.17.080702.

[9] H.-S. Lee, Y.J. Park, Y.-D. Joo, H. Heo, K.-M. Oh, S.-J. Noh, W.H. Hwang, S.-D. Jang, S.-S. Park, H. Matsumoto, H.-S. Kang, J.Y. Huang and I.-S. Ko. PAL-XFEL accelerating structures. In *Proceedings of the International Particle Accelerator Conference IPAC2013*, pages 2806–2808, Shanghai (China), 2013.

[10] D. Alesini, S. Bini, R. Di Raddo, V. Lollo, L. Pellegrino, L. Ficcadenti, V. Pettinacci, L. Palumbo and L. Serafini. Design and RF test of damped C-band accelerating structures for the ELI-NP linac. In *Proceedings of the International Particle Accelerator Conference IPAC2014*, pages 3856–3859, Dresden (Germany), 2014.

[11] ThomX Technical Design Report. LAL/RT 14-21, SOLEIL/SOU-RA-3629, April 2014. `http://hal.in2p3.fr/in2p3-00971281`.

[12] B. Aune et al. Superconducting TESLA cavities. *Phys. Rev. ST Accel. Beams*, 3(9):092001, September 2000. doi:10.1103/PhysRevSTAB.3.092001.

[13] A. Lunin, V. Yakovlev, and A. Grudiev. Analytical solutions for transient and steady state beam loading in arbitrary traveling wave accelerating structures. *Phys. Rev. ST Accel. Beams*, 14(5):052001, May 2011. doi:10.1103/PhysRevSTAB.14.052001.

[14] ATLAS Collaboration. Observation of a new particle in the search for the Standard Model Higgs boson with the ATLAS detector at the LHC. *Physics Letters B*, 716(1):1 – 29, 2012. ISSN 0370-2693, doi:10.1016/j.physletb.2012.08.020.

[15] CMS Collaboration. Observation of a new boson at a mass of 125 GeV with the CMS experiment at the LHC. *Physics Letters B*, 716(1):30 – 61, 2012. ISSN 0370-2693, doi:10.1016/j.physletb.2012.08.021.

[16] Linear Collider Collaboration homepage. `http://www.linearcollider.org/`.

[17] International Linear Collider Technical Design Report. ILC-REPORT-2013-040, June 2013. `https://www.linearcollider.org/ILC/Publications/Technical-Design-Report`.

[18] ILC Global Design Effort. International Linear Collider Reference Design Report. ILC-REPORT-2007-1, August 2007. `http://www.linearcollider.org/ILC/Publications/Reference-Design-Report`.

[19] CLIC Collaboration. A Multi-TeV Linear Collider based on CLIC technology, CLIC Conceptual Design Report. CERN-2012-007, October 2012. `http://clic-study.web.cern.ch/content/conceptual-design-report`.

[20] CLIC and CLICdp Collaboration. Updated baseline for a staged Compact Linear Collider. Technical Report arXiv:1608.07537, CERN-2016-004, CERN, August 2016. `http://cds.cern.ch/record/2210892`.

[21] A. Palaia, M. Jacewicz, T. Muranaka, R. Ruber, V. Ziemann and W. Farabolini. RF-breakdown kicks at the CTF3 Two-Beam Test Stand. In *Proceedings of the International Particle Accelerator Conference IPAC2012*, pages 73–75, New Orleans (USA), 2012.

[22] Zeroth-order Design Report for the Next Linear Collider. SLAC-474, May 1996. `http://www-project.slac.stanford.edu/lc/ZDR/Zeroth.html`.

[23] JLC Design Study. KEK-Report-97-1, April 1997. `http://lss.fnal.gov/archive/other1/kek-report-97-1.pdf`.

[24] J.W. Wang, J.R. Lewandowski, J.W. Van Pelt, C. Yoneda, G. Riddone, D. Gudkov, T. Higo and T. Takatomi. Fabrication technologies of the high gradient accelerator structures at 100MV/m range. In *Proceedings of the International Particle Accelerator Conference IPAC2010*, pages 3819–3821, Kyoto (Japan), 2010.

[25] S. Verdú-Andrés. *High-gradient accelerating structure studies and their application in hadrontherapy.* PhD thesis, Universitat de València, 2012.

[26] Particle Therapy Co-Operative Group homepage. `http://www.ptcog.ch/`.

[27] U. Amaldi and A. Degiovanni. Proton and Carbon linacs for hadron therapy. In *Proceedings of the Linear Accelerator Conference LINAC2014*, pages 1207–1212, Geneva (Switzerland), 2014.

[28] U. Amaldi, R. Bonomi, S. Braccini, M. Crescenti, A. Degiovanni, M. Garlasché, A. Garonna, G. Magrin, C. Mellace, P. Pearce, G. Pitta, P. Puggioni, E. Rosso, S. Verdú Andrés, R. Wegner, M. Weiss and R. Zennaro. Accelerators for hadrontherapy: From Lawrence cyclotrons to linacs. *NIM A*, 620:563 – 577, 2010. doi:10.1016/j.nima.2010.03.130.

[29] R.W. Hamm, K.R. Crandall, and J.M Potter. Preliminary design of a dedicated proton therapy linac. In *Proceedings of the IEEE Particle Accelerator Conference PAC'91*, pages 2583–2585, San Francisco (USA), 1991.

[30] U. Amaldi and B. Larsson. *Hadron Therapy in Oncology.* Elsevier, 1994.

[31] U. Amaldi, P. Berra, K. Crandall, D. Toet, M. Weiss, R. Zennaro, E. Rosso, B. Szeless, M. Vretenar, C. Cicardi, C. De Martinis, D. Giove, D. Davino, M.R. Masullo, and V. Vaccaro. LIBO a linac-booster for protontherapy: construction and test of a prototype. *NIM A*, 521:512 – 529, 2004. doi:10.1016/j.nima.2003.07.062.

[32] A.D.A.M. SA homepage. http://adam-geneva.com/.

[33] S. Verdú-Andrés, U. Amaldi, and A. Faus-Golfe. CABOTO, a high-gradient linac for hadrontherapy. *Journal of Radiation Research*, 54:155–161, 2013. doi:10.1093/jrr/rrt053.

[34] H. Motz. Applications of the Radiation from Fast Electron Beams. *Journal of Applied Physics*, 22(5):527–535, 1951. doi:10.1063/1.1700002.

[35] Linac Coherent Light Source II (LCLS-II) Conceptual Design Report. SLAC National Accelerator Laboratory, April 2011. SLAC-R-978.

[36] XFEL/SPring-8 Beamline Technical Design Report Ver. 2.0. SPring-8 Joint Project for XFEL, February 2010. http://xfel.riken.jp/eng/.

[37] Linac Coherent Light Source (LCLS) Conceptual Design Report. Stanford Linear Accelerator Center, April 2002. SLAC-R-593.

[38] SwissFEL Conceptual Design Report. Paul Scherrer Institut, March 2011. http://www.psi.ch/swissfel/.

[39] European XFEL Technical Design Report. DESY XFEL Project Group, July 2007. http://www.xfel.eu/.

[40] X-band FEL Collaboration homepage. http://xbandfel.web.cern.ch/.

[41] EuroGammaS Collaboration. Technical Design Report EuroGammaS proposal for the ELI-NP Gamma beam System. arXiv:1407.3669, July 2014.

[42] T. Obina et al. Recent developments and operational status of the Compact ERL at KEK. In *Proceedings of the International Particle Accelerator Conference IPAC2016*, pages 1835–1838, Busan (Korea), 2016.

[43] R.H. Fowler and L. Nordheim. Electron Emission in Intense Electric Fields. *Proceedings of the Royal Society A*, 119(781):173–181, 1928. doi:10.1098/rspa.1928.0091.

[44] J.W. Wang and G.A. Loew. Field Emission and RF Breakdown in High-Gradient Room-Temperature Linac Structures. *Stanford Linear Accelerator Center Technical Report*, 1997. SLAC-PUB-7684.

[45] K. Nordlund and F. Djurabekova. Defect model for the dependence of breakdown rate on external electric fields. *Phys. Rev. ST Accel. Beams*, 15:071002, Jul 2012. doi:10.1103/PhysRevSTAB.15.071002.

[46] E. L. Murphy and R. H. Good. Thermionic emission, field emission, and the transition region. *Phys. Rev.*, 102(6):1464–1473, Jun 1956. doi:10.1103/PhysRev.102.1464.

[47] H. Timko. *Modelling vacuum arcs: from plasma initiation to surface interactions*. PhD thesis, Helsinki University, 2011.

[48] J.W. Kovermann. *Comparative studies of high-gradient RF and DC breakdowns*. PhD thesis, RWTH Aachen University, 2010.

[49] H. Timko, K. Ness Sjobak, L. Mether, S. Calatroni, F. Djurabekova, K. Matyash, K. Nordlund, R. Schneider and W. Wuensch. From field emission to vacuum arc ignition: A new tool for simulating copper vacuum arcs. *Contributions to Plasma Physics*, 55:299–314, 2015. doi:10.1002/ctpp.201400069.

[50] A.T. Perez Fontenla. SEM images review on CLIC structures after testing. 5th International Workshop on Mechanisms of Vacuum Arcs (MeVArc 2015), September 2015. `https://indico.cern.ch/event/354854/contributions/834778/`.

[51] C. Adolphsen. Normal-conducting RF structure test facilities and results. In *Proceedings of the Particle Accelerator Conference PAC2003*, pages 668–672, Portland (USA), 2003.

[52] S. Doebert, C. Adolphsen, G. Bowden, D. Burke, J. Chan, V. Dolgashev, J. Frisch, K. Jobe, R. Jones, J. Lewandowski, R. Kirby, Z. Li, D. McCormick, R. Miller, C. Nantista, J. Nelson, C. Pearson, M. Ross, D. Schultz, T. Smith, S. Tantawi, J. Wang, T. Arkan, C. Boffo, H. Carter, I. Gonin, T. Khabiboulline, S. Mishra, G. Romanov, N. Solyak, Y. Funahashi, H. Hayano, N. Higashi, Y. Higashi, T. Higo, H. Kawamata, T. Kume, Y. Morozumi, K. Takata, T. Takatomi, N. Toge, K. Ueno and Y. Watanabe. High-gradient performance of NLC/GLC X-band accelerating structures. In *Proceedings of the Particle Accelerator Conference PAC2005*, pages 372–374, Knoxville (USA), 2005.

[53] W. Wuensch, H. H. Braun, G. Carron, R. Corsini, S. Dobert, R. Fandos, A. Grudiev, E. Jensen, T. Ramsvick, J. Rodriguez, J. Sladen, I. Syratchev, M. Taborelli, F. Tecker, P. Urschuetz, I. Wilson, H. Aksakal and O. Mete. A high-gradient test of a 30 GHz Molybdenum-iris structure. In *Contributions to the Proceedings of EPAC2006*, pages 801–803. European Physical Society Accelerator Group (EPS-AG), 2006.

[54] A. Grudiev, S. Calatroni, and W. Wuensch. New local field quantity describing the high gradient limit of accelerating structures. *Phys. Rev. ST Accel. Beams*, 12:102001, October 2009. doi:10.1103/PhysRevSTAB.12.102001.

[55] V.A. Dolgashev, S.G. Tantawi, Y. Higashi and B. Spataro. Study of basic RF breakdown phenomena in high gradient vacuum structures. In *Proceedings of the Linear Accelerator Conference LINAC2010*, pages 1043–1047, Tsukuba (Japan), 2010.

[56] N. Shipman. *Experimental study of DC vacuum breakdown and application to high-gradient accelerating structures for CLIC.* PhD thesis, University of Manchester, 2014.

[57] T. Higo, T. Abe, Y. Arakida, S. Matsumoto, T. Shidara, T. Takatomi, M. Yamanaka, Y. Higashi, A. Grudiev, G. Riddone and W. Wuensch. Comparison of high gradient performance in varying cavity geometries. In *Proceedings of the International Particle Accelerator Conference IPAC2013*, pages 2741–2743, Shanghai (China), 2010.

[58] W. Wuensch. Advances in the Understanding of the Physical Processes of Vacuum Breakdown. Technical Report CERN-OPEN-2014-028. CLIC-Note-1025, CERN, May 2013.

[59] A. Degiovanni. *High Gradient proton linacs for medical applications.* PhD thesis, École Polytechnique Fédérale de Laussane, 2014.

[60] W. Wuensch. Study of the Conditioning of RF Structures. Oral presentation at 5th International Workshop on Mechanisms of Vacuum Arcs (MeVArc 2015), 2015. `https://indico.cern.ch/event/354854/`.

[61] W. D. Kilpatrick. Criterion for vacuum sparking designed to include both rf and dc. *Review of Scientific Instruments*, 28(10):824–826, 1957. doi:10.1063/1.1715731.

[62] T.J. Boyd, Jr. Kilpatrick's Criterion. Technical Report AT-1:82-28, Los Alamos Group AT-1, February 1982.

[63] A. Descoeudres, T. Ramsvik, S. Calatroni, M. Taborelli, and W. Wuensch. DC breakdown conditioning and breakdown rate of metals and metallic alloys under ultrahigh vacuum. *Phys. Rev. ST Accel. Beams*, 12:032001, Mar 2009. doi:10.1103/PhysRevSTAB.12.032001.

[64] A. Descoeudres, F. Djurabekova, and K. Nordlund. DC breakdown experiments with cobalt electrodes. Technical Report CERN-OPEN-2011-029, CLIC-Note-875, CERN, Jun 2009. `https://cds.cern.ch/record/1355401`.

[65] M. Aicheler. Thermal fatigue of polycrystalline copper in CLIC accelerating structures: surface roughening and hardening as a function of grain orientation. In *Proceedings of the Linear Accelerator Conference LINAC2010*, pages 214–216, Tsukuba (Japan), 2010.

[66] M. Aicheler. TD18 post-mortem summary. Oral presentation at CLIC RF Structure Development Meeting, 2011. `http://indico.cern.ch/event/106251/`.

[67] D.P. Pritzkau. *RF pulsed heating*. PhD thesis, Stanford University, 2001.

[68] J.D. Jackson. *Classical electrodynamics; 3rd ed.* Wiley, New York, NY, 1999.

[69] A. Grudiev. RF constraints. Update 2013 for CLIC rebaselining. Presented at the 6th CLIC design meeting, CERN, April 2013.

[70] W. Wuensch. Observations About RF Breakdown From the CLIC High-Gradient Testing Program. *AIP Conference Proceedings*, 877(1):15–21, 2006. doi:10.1063/1.2409116.

[71] ANSYS HFSS: High Frequency Electromagnetic Field Simulation. `http://www.ansys.com/Products/Electronics/ANSYS-HFSS`.

[72] A. Grudiev. RF design and parameters of 12 GHz TD26-vg1.8-R05-CC. CERN EDMS Document, June 2010. `https://edms.cern.ch/document/1078698/1`.

[73] H. Zha and A. Grudiev. RF design and parameter of (2015) 3 TeV CLIC main linac AS at 12 GHz with compact couplers: CLIC-G-star or TD26_vg1.8_R1_CC. CERN EDMS Document, August 2015. `https://edms.cern.ch/document/1524527/1`.

[74] R. Zennaro, A. Grudiev, G. Riddone, A. Samoshkin, W. Wuensch, S. Tantawi, J. W. Wang and T. Higo. Design and fabrication of CLIC test structures. In *Proceedings of the Linear Accelerator Conference LINAC2008*, pages 533–535, Victoria (Canada), 2008.

[75] H. Zha, A. Grudiev and V. Dolgashev. RF design of the CLIC structure prototype optimized for manufacturing from two halves. In *Proceedings of the International Particle Accelerator Conference IPAC2015*, pages 2147–2149, Richmond (USA), 2015.

[76] A. Degiovanni, S. Doebert, W. Farabolini, A. Grudiev, J. Kovermann, E. Montesinos, G. Riddone, I. Syratchev, R. Wegner, W. Wuensch, A. Solodko and B. Woolley. High-gradient test results from a CLIC prototype accelerating

structure: TD26CC. In *Proceedings of the International Particle Accelerator Conference IPAC2014*, pages 2285–2287, Dresden (Germany), 2014.

[77] W. Wuensch, A. Degiovanni and J. Giner Navarro. Comparison of the conditioning of high gradient accelerating structures. *Phys. Rev. Accel. Beams*, 19:032001, Mar 2016. doi:10.1103/PhysRevAccelBeams.19.032001.

[78] S. Matsumoto, M. Akemoto, S. Fukuda, T. Higo, N. Kudoh, H. Matsushita, H. Nakajima, T. Shidara, K. Yokoyama and M. Yoshida. The status of NEXTEF: the X-band test facility in KEK. In *Proceedings of the Linear Accelerator Conference LINAC2008*, pages 906–908, Victoria (Canada), 2008.

[79] F. Peauger, A. Hamdi, S. Curt, S. Doebert, G. McMonagle, G. Rossat, K.M. Schirm, I. Syratchev, L. Timeo, S. Kuzikhov, A.A. Vikharev, A. Haase, D. Sprehn and A. Jensen. A 12 GHz RF power source for the CLIC study. In *Proceedings of the International Particle Accelerator Conference IPAC2010*, pages 3990–3992, Kyoto (Japan), 2010.

[80] L. Mercadé Morales. Study of the conditioning process and breakdown rate dependencies in a pulsed DC system. Master's thesis, Universitat de València, 2016.

[81] B.J. Woolley. *High Power X-band RF Test Stand Development and High Power Testing of the CLIC Crab Cavity*. PhD thesis, Lancaster University, 2015.

[82] N. Catalan-Lasheras, A. Degiovanni, S. Doebert, W. Farabolini, J. Kovermann, G. McMonagle, S. Rey, I. Syratchev, L. Timeo, W. Wuensch, B. Woolley and J. Tagg. Experience operating an X-band high-power test stand at CERN. In *Proceedings of the International Particle Accelerator Conference IPAC2014*, pages 2288–2290, Dresden (Germany), 2014.

[83] J. Kovermann. News from Xbox-1. Oral presentation at 7th International Workshop on Breakdown Science and High Gradient Technology (HG2013), 2013. `https://indico.cern.ch/event/231116/contributions/1542964/`.

[84] A. Degiovanni. Structure deformation: comparative analysis of RF and dimensional measurements. Oral presentation at CLIC Workshop 2015, 2015. `https://indico.cern.ch/event/336335/contributions/789043/`.

[85] Z.D. Farkas, H.A. Hoag, G.A. Loew, and P.B. Wilson. SLED: A Method of Doubling SLAC's Energy. In *Proceedings of 9th International Conference on High-Energy Accelerators*, Stanford (USA), 1974. `http://inspirehep.net/record/94052/files/HEACC74_597-604.pdf`.

[86] S.W. Ellingson. Correcting I-Q Imbalance in Direct Conversion Receivers. Virginia Polytechnic Institute and State University, 2013. Online resource `http://www.faculty.ece.vt.edu/swe/argus/iqbal.pdf`.

[87] B. Woolley, P. Ambattu, R. Apsimon, G. Burt, A.C. Dexter, A. Grudiev, I. Syratchev, R. Wegner and W. Wuensch. High gradient testing of an X-band crab cavity at Xbox2. In *Proceedings of the International Particle Accelerator Conference IPAC2015*, pages 3242–3245, Richmond (USA), 2015.

[88] M. Kastriotou, E. Nebot del Busto, S. Doebert, W. Farabolini, E.B. Holzer, F. Tecker and C. P. Welsch. A versatile beam loss monitoring system for CLIC. In *Proceedings of the International Particle Accelerator Conference IPAC2016*, pages 286–289, Busan (Korea), 2016.

[89] M. Jacewicz. Breakdown Tomography with Emitted Electrons. Oral presentation at CLIC Workshop 2016, 2016. `https://indico.cern.ch/event/449801/contributions/1945272/`.

[90] G. McMonagle, N.Catalan Lasheras, C. Eymin, S. Rey, A. Solodko, I. Syratchev, B. Woolley, W. Wuensch, J. Giner Navarro, D. Esperante Pereira, T. Argyropoulos and J. Tagg. Construction and commissioning Xbox3: a very high capacity X-band test stand. In *Proceedings of the 2016 IEEE Power Modulator and High Voltage Conference*, Los Angeles (USA), 2016.

[91] N. Catalan Lasheras, C. Eymin, G. McMonagle, S. Rey, I. Syratchev, B. Woolley, W. Wuensch, J. Giner Navarro, D. Esperante Pereira, T. Argyropoulos, M. Volpi and J. Tagg. Commissioning of Xbox3: a very high capacity X-band RF test stand. In *Proceedings of the Linear Accelerator Conference LINAC2016*, East Lansing (USA), 2016.

[92] FuG Elektronik GmbH. `http://www.fug-elektronik.de/en/`.

[93] A. Degiovanni, S. Doebert, W. Farabolini, I. Syratchev, W. Wuensch, J. Giner-Navarro, J. Tagg and B. Woolley. Diagnostics and analysis techniques for high power X-band accelerating structures. In *Proceedings of the Linear Accelerator Conference LINAC2014*, pages 490–492, Geneva (Switzerland), 2014.

[94] A. Palaia, V. Dolgashev, J. Lewandowski and S. Weathersby. Diagnostics of RF breakdowns in high-gradient accelerating structures. In *Proceedings of the International Particle Accelerator Conference IPAC2013*, pages 527–529, Shanghai (China), 2013.

[95] LabVIEW, National Instruments. `http://www.ni.com/labview/`.

[96] A.G. Frodesen, O. Skjeggestad and H. Tofte. *Probability and statistics in particle physics*. Universitetsforlaget, 1979.

[97] N. Catalan Lasheras, A. Grudiev, G. Mcmonagle, I. Syrachev, B. Woolley, W. Wuensch, H. Zha, G. Bowden, V. Dolgashev, A. Haase, T. Argyropoulos, J. Giner Navarro, D. Esperante Pereira, R. Rajamaki, X. Stragier, P.J. Giansiracusa, T.G. Lucas and M. Volpi. Fabrication and high-gradient testing of an accelerating structure made from milled halves. In *Proceedings of the Linear Accelerator Conference LINAC2016*, East Lansing (USA), 2016.

[98] A. Korsbäck, W. Wuensch, A. Degiovanni, R. Rajamäki and J. Giner Navarro. Statistics of vacuum breakdown in the high-gradient and low-rate regime, 2016. To be published: Phys. Rev. Accel. Beams.

[99] G.D. Cowan. *Statistical Data Analysis*. Oxford University Press, 1998.

[100] MATLAB, Mathworks. `http://www.mathworks.com/products/matlab/`.

[101] R. Rajamaki. Private communication, 2015.

[102] R. Rajamaki. Breakdown Positioning. Oral presentation at CLIC Workshop 2016, 2016. `https://indico.cern.ch/event/449801/contributions/1945265/`.

[103] T. Higo, T. Abe, Y. Arakida, S. Matsumoto, T. Shidara, T. Takatomi, M. Yamanaka, Y. Higashi, A. Grudiev, G. Riddone and W. Wuensch. Comparison of high gradient performance in varying cavity geometries. In *Proceedings of the International Particle Accelerator Conference IPAC2013*, pages 2741–2743, Shanghai (China), 2013.

[104] W. Wuensch. Results from the CERN Pulsed DC System and comparison to RF. Oral presentation at 9th International Workshop on Breakdown Science and High Gradient Technology (HG2016), 2016. `https://indico.hep.anl.gov/indico/conferenceDisplay.py?confId=963`.

[105] A. Korsback. Private communication, 2015.

[106] X. Wu, J. Shi, H. Chen, A. Grudiev, W. Wuensch, B. Spataro, Y. Higashi and V. Dolgashev. New quantity describing the pulse shape dependence of the high gradient limit in single cell standing-wave accelerating structures. In *Proceedings of the International Particle Accelerator Conference IPAC2016*, pages 3878–3880, Busan (Korea), 2016.

[107] T. Argyropoulos. High-power test of a structure built from halves. Oral presentation at 9th International Workshop on Breakdown Science and High Gradient Technology (HG2016), 2016. https://indico.hep.anl.gov/indico/conferenceDisplay.py?confId=963.

[108] CLIC Collaboration. CTF3 Design Report. CERN/PS 2002-008, CTF3 Note 2002-047, LNF-02/008, 2002. http://clic-study.web.cern.ch/sites/clic-study.web.cern.ch/themes/cliccern/pdfs/notes/CTF3DesignReport.pdf.

[109] F. Tecker. Private communication, 2016.

[110] F. Tecker, R. Corsini, M. Dayyani Kelisani, S. Doebert, A. Grudiev, J.L. Navarro Quirante, G. Riddone, I. Syratchev, W. Wuensch, O. Kononenko, A. Solodko and S. Lebet. Experimental study of the effect of beam loading on RF breakdown rate in CLIC high-gradient accelerating structures. In *Proceedings of the International Particle Accelerator Conference IPAC2013*, pages 1691–1693, Shanghai (China), 2013.

[111] M. Gasior. An inductive pick-up for beam position and current measurements. In *Proceedings of the European Workshop on Beam Diagnostics and Instrumentation for Particle Accelerators DIPAC2003*, pages 53–55, Mainz (Germany), 2003.

[112] J.L. Navarro Quirante, R. Corsini, A. Degiovanni, S. Doebert, A. Grudiev, G. McMonagle, S. Rey, I. Syratchev, F. Tecker, L. Timeo, W. Wuensch, O. Kononenko, A. Solodko, J. Tagg, B. Woolley and X.W. Wu. Effect of beam-loading on the breakdown rate of high-gradient accelerating structures. In *Proceedings of the Linear Accelerator Conference LINAC2014*, pages 499–501, Geneva (Switzerland), 2014.

[113] A. Fiebig and C. Schieblich. A SLED type pulse compressor with rectangular pulse shape. In *Proceedings of the European Particle Accelerator Conference EPAC90*, June 1990. CERN-PS-90-13-RF, https://cds.cern.ch/record/209756.

[114] The European Network for LIGht ion Hadron Therapy (ENLIGHT) homepage. http://enlight.web.cern.ch/.

[115] Particle Training Network for European Radiotherapy (PARTNER) homepage. http://partner.web.cern.ch/partner/cms/?file=home.

[116] European NoVel Imaging Systems for ION therapy (ENVISION) homepage. http://envision.web.cern.ch/ENVISION/.

[117] European training network in digital medical imaging for radiotherapy (ENTERVISION) homepage. http://entervision.web.cern.ch/ENTERVISION/.

[118] Union of Light Ion Centres in Europe (ULICE) homepage. http://ulice.web.cern.ch/ULICE/cms/index.php?file=home.

[119] Instituto de Física Corpuscular (IFIC) homepage. http://webific.ific.uv.es/web/.

[120] Fondazione per la Adroterapia Oncologica (TERA) homepage. http://www.tera.it/tera/.

[121] A. Degiovanni, U. Amaldi, D. Bergesio, C. Cuccagna, A. Lo Moro, P. Magagnin, P. Riboni and V. Rizzoglio. Design of a Fast-cycling High-gradient Rotating Linac for Protontherapy. In *Proceedings of the International Particle Accelerator Conference IPAC2013*, pages 3642–3644, Shanghai (China), 2013.

[122] S. Benedetti. Update on the TULIP Backward-Traveling Wave Linac Design. Oral Presentation at CLIC Beam Physics Meeting, CERN, 2015. http://indico.cern.ch/event/456216/.

[123] M. Vretenar, A. Dallocchio, V. A. Dimov, M. Garlasché, A. Grudiev, A. M. Lombardi, S. Mathot, E. Montesinos and M. Timmins. A compact high-frequency RFQ for medical applications. In *Proceedings of the Linear Accelerator Conference LINAC2014*, pages 935–938, Geneva (Switzerland), 2014.

[124] L. Picardi, C. Ronsivalle, and A. Vignati. Progetto del top linac. ENEA, Dip. Innovazione, RT/INN/97/17, 1997. http://www.iaea.org/inis/collection/NCLCollectionStore/_Public/29/029/29029212.pdf.

[125] E Chesta, F Caspers, W Wuensch, S Sgobba, T Stora, P Chiggiato, and M Taborelli. Overview of CERN Technology Transfer Strategy and Accelerator-Related Activities, May 2013.

[126] S. Benedetti, A. Degiovanni, A. Grudiev, W. Wuensch and U. Amaldi. RF design of a novel S-band backward travelling wave linac for proton therapy. In *Proceedings of the Linear Accelerator Conference LINAC2014*, pages 992–994, Geneva (Switzerland), 2014.

[127] S. Benedetti, T. Argyropoulos, N. Catalan Lasheras, A. Degiovanni, M. Garlasché, J. Giner Navarro, A. Grudiev, G. Mcmonagle, A. Solodko, R. Wegner, B. Woolley, W. Wuensch. Fabrication and testing of a novel S-band backward

travelling wave accelerating structure for proton therapy linacs. In *Proceedings of the Linear Accelerator Conference LINAC2016*, East Lansing (USA), 2016.

[128] J. Shi, A. Grudiev and W. Wuensch. Tuning of x-band traveling-wave accelerating structures. *Nuclear Instruments and Methods in Physics Research Section A: Accelerators, Spectrometers, Detectors and Associated Equipment*, 704:14–18, 2013. doi:10.1016/j.nima.2012.11.182.

[129] A. Degiovanni, U. Amaldi, S. Benedetti, M. Garlasché, J. Giner-Navarro, P. Magagnin, G. McMonagle, I. Syratchev, W. Wuensch. Design and high power measurements of a 3 GHz Rotary Joint for medical applications. Technical Report To be published: CLIC-Note-1071, CERN, 2016.

[130] Rohde&Schwarz Vector Network Analyzer, Model ZVA24 (2 ports, 24 GHz). `https://www.rohde-schwarz.com/us/product/zva-products_63492-9660.html`.

[131] I. Syratchev. First commercial (VDBT Moscow) prototype of the high efficiency klystron. Oral Presentation CLIC Project Meeting 24. `https://indico.cern.ch/event/516216/contributions/2039566/attachments/1263206/1868345/CLIC_M_04_2016.pdf`.

[132] D. Esperante Pereira and C. Blanch Gutierrez. Valencia's S-Band RF Laboratory: Status and Plans. Oral presentation at 9th International Workshop on Breakdown Science and High Gradient Technology (HG2016), 2016. `https://indico.hep.anl.gov/indico/conferenceDisplay.py?confId=963`.

[133] Communications and Power Industries (CPI) homepage. `http://www.cpii.com/`.

[134] JEMA Energy homepage. `http://www.jemaenergy.com/en/`.

[135] National Instruments homepage. `http://www.ni.com/`.

Acknowledgments

Firstly, I would like to express my sincere gratitude to IFIC and CERN for letting me participate in the project and learn from many experts in the field of Accelerator Physics. Special thanks to my Ph.D. supervisors in this long journey, Dr. Ángeles Faus-Golfe and Dr. Nuria Catalan-Lasheras, who have supported me with their expertise and valuable guidance and have helped me to develop my career in this field. I am also very grateful to Dr. Walter Wuensch for his coordination of the many studies presented in this thesis work.

I take the opportunity to thank the valuable help that I received from Ben Woolley and Alberto Degiovanni who have been by my side during many moments to share their expertise in the operation of the Xboxes test stands. I am also grateful to all the Xbox colleagues that have worked with me during these years, Theo Argyropoulos, Robin Rajamaki, Xiaowei Wu, Xavier Stragier, Tom Lucas, Paul Giansiracusa and Matteo Volpi, for the fruitful discussions during the meetings and coffee breaks. Special thanks to Gerry Mcmonagle, for his constant help in the technical aspects of the operation of the Xboxes and his assistance during the preparation of the S-band high-power tests of the medical rotary joint and accelerating structure at CTF3. I would also like to acknowledge the help of Igor Syratchev in the first designs of the IFIC high-gradient RF laboratory, as well as his help in the high-power operation of the Xbox components. Many thanks to my IFIC colleagues, Daniel Esperante and César Blanch, that joined the Xbox team to give their technical support and make a great job in the development of the future IFIC high-gradient RF laboratory. Thanks to the full team involved in the beam-loading experiment, specially to the CTF3 operators that have closely worked with me, Frank Tecker, Luis Navarro, Davide Gamba and Eugenio Senes, for letting me learn directly from the operation control room about the measurement and control of the beam properties.

I am very grateful of the experience with the team of the DC Spark laboratory at CERN, from which I significantly learned about breakdown phenomenology. Thanks to Anders Korsback, for his fruitful collaboration study between the Xbox and the Large Electrode System, Nick Shipman, for his help in programming the conditioning algorithm of the Large Electrode System, and the rest of colleagues Sergio Calatroni, Iaroslava Profatilova, Tomoko Muranaka, Laura Mercade, Anité Pérez and Enrique Rodríguez.

I must also acknowledge my officemates Roberto Torres, Karim Gibrán and Natalia Galindo, among many other colleagues of building 252, because of their friendship and kindness that made me feel extremely comfortable during these years.

Dejo para el final una dedicatoria especial para mis padres, Juan y Soledad, y para mi hermano Juan a los que debo enormemente haber llegado hasta aquí gracias a su educación y esfuerzo, y que desde la distancia no han parado de mostrar su apoyo en lo que me apasiona. Y por último, agradecer a Cristina, mi futura compañera de vida, por su paciencia durante estos años separados y en los momentos más difíciles de esta relación, y por apoyarme en finalizar esta etapa para dar comienzo a las próximas vivencias juntos.